A FRAMEWORK FOR FAN STAGE CONCEPTUAL DESIGN UNDER DISTORTION INDUCED BY BOUNDARY LAYER INGESTION

A Thesis
Presented to
The Academic Faculty

by

Manish Pokhrel

In Partial Fulfillment
of the Requirements for the Degree
Doctor of Philosophy in the
School of Aerospace Engineering

Georgia Institute of Technology
December 2020

A FRAMEWORK FOR FAN STAGE CONCEPTUAL DESIGN UNDER DISTORTION INDUCED BY BOUNDARY LAYER INGESTION

Approved by:

Professor Dimitri Mavris, Advisor
School of Aerospace Engineering
Georgia Institute of Technology

Professor Lakshmi N. Sankar
School of Aerospace Engineering
Georgia Institute of Technology

Professor Dewey H. Hodges
School of Aerospace Engineering
Georgia Institute of Technology

Dr. Jonathan Gladin
School of Aerospace Engineering
Georgia Institute of Technology

Dr. Mohit Gupta
Department of Aerospace Engineering Sciences
University of Colorado Boulder

Date Approved: October 14th 2020

Set thy heart upon thy work, but never on its reward.

Bhagavad Gita

To my family...

ACKNOWLEDGEMENTS

My lab is like a football team. If I do not need a goalie and you are not flexible to play as a midfielder or a defender, then you are not the right fit in my lab regardless of how good of a goalie you are. These words were part of the first conversation I had with my future advisor, Prof. Dimitri Mavris. It was at that moment I knew I could call ASDL my second home. Over the course of my Ph.D., he has been a constant source of inspiration not only to me but also to many around me in ASDL. I want to sincerely thank Prof. Mavris for providing a unique and wonderful graduate school experience where I could explore so many enriching research avenues in the last six years at Georgia Tech.

I would also like to thank Dr. Jonathan Gladin for helping me navigate through my Ph.D. journey from Day 1. Whether it was explaining about inlet distortion at Starbucks or helping me fix NPSS codes at my desk, he has been a great mentor and a knowledge source whose doors were always open for me.

My especial thanks also goes to Dr. Mohit Gupta, who helped me understand all that I know about VABS and GEBT. His insights on the structural analysis part challenged me and helped me speed up the work. I would also like to thank Prof. Sankar whose questions and comments directed me to look at the problem from different perspectives. I also appreciate the time and feedback that Prof. Hodges provided towards the end of the work and want to thank him for that.

I am grateful to be surrounded by amazing people at ASDL. I want to acknowledge the support of Mr. Russ Denney, who was instrumental in helping me understand OTAC and explaining various turbomachinery concepts to me that made my path relatively easier. Thanks also goes to Mr. Andrew Yatsko, who was always excited to

hear the progress in my work and pointed me to specific papers he remembered from the top of his head.

I would also like to thank some wonderful friends I made at ASDL. Thanks to Roger for being the incredibly weird, funny, and true friend he is. Thanks to Melek for our interesting lunch conversations and for making my TA life memorable. And thanks to Wenxin for being a part of the squad and for his unintentional dry humor. Thanks to Dushhyanth for the random coffee walks and our childish, yet effective, strategy to propose and defend around the same time. Thank you also goes to Darshan and Mingxuan who helped to co-author several papers. David for helping me fix the screen on my phone to the random bugs in my codes. I would also like to thank Mayank and Arturo for being a part of my quals group and making the qualifying exams less stressful than it's supposed to be. And I cannot forget to thank the espresso machine in the lab whose productivity was strongly correlated to my everyday efficiency.

As I near the completion of my graduate school, I reflect upon those moments that brought me to where I am today. Thank you to my mom, Anjana Pokharel, for instilling in me the desire to learn something new every day. Thank you to my dad, Nilmani Pokharel, for believing in me no matter what I pursued. Thank you to my sister, Manisha, for being my role model as I grew up. Finally, thank you to my wonderful wife, Manjari, who went through this journey with me. Her captivating smile and positive attitude provided me with confidence when I needed it the most. Without her support, I would be nowhere close to finishing this dissertation. To my wife, this dissertation is as equally yours as it is mine.

Manish Pokhrel

Atlanta, GA

November, 2020

TABLE OF CONTENTS

LIST OF TABLES

LIST OF FIGURES

SUMMARY

Various tightly integrated aircraft concepts have emerged as a result of aggressive performance goals set forth by various organizations. One technology common in most integrated aircraft systems is the concept of Boundary Layer Ingestion (BLI). BLI is a concept in which a set of propulsors on a vehicle ingest a portion of that vehicle's viscous boundary layer. The result is typically that the propulsive efficiency of the device is improved, thereby reducing fuel burn. However, a number of significant challenges - both on the modeling and design fronts - appear as a result of BLI. This dissertation deals with the impacts on the fan stage due to BLI induced circumferential flow distortion.

In BLI propulsor modeling, many studies use representative fan maps and scale them accordingly. This dissertation argues that instead of using the conventional maps, we must first design fans for non-uniform flows and replace the maps by a fan design/analysis method integrated with the thermodynamic cycle analysis tools. Distortion introduces extra losses in both rotors and stators in addition to increased unsteady rotor response. In presence of large incidence swings, conventional conceptual design tools are inadequate to design optimal rotor blades and generate non-axisymmetric stators, a concept that has shown promise in alleviating stage losses due to distortion. Besides, concerns of structural integrity also arise for rotor blades due to the unsteady loading they experience when rotating in a distorted flow field. This dissertation aims to quantify the parametric effects of these phenomena on the stage losses with varying levels of flow distortion and recover a significant portion of these losses using the framework introduced and formulated here.

For the aerodynamic design of the fan stage, several elements are added as extensions to the conventionally used meanline and multi-meanline methods. For modeling asymmetry, the flow field is divided into various sectors based on the distortion profile and each sector is treated with the assumption of axial symmetry. Parametric variation of blade angles to control the incidence and deviation is used to minimize the losses in the rotor and stator rows. An analytical formulation is employed to transform rotor's quasi-steady performance to unsteady performance using the behavior of the 2-D airfoil in the blades. Similarly, a multi-point multi-meanline design approach is used to design non-axisymmetric stators in terms of blade metal angles. An aerodynamic design framework to encapsulate the aforementioned effects is also developed as a part of this dissertation.

The aerodynamic framework is used in the analysis of Rotor 67 to verify the results of the flow profile at the rotor exit under distorted inflow by comparing with the CFD results. The aerodynamic design framework is then used to illustrate the effects of parametric rotor blade angle optimization, unsteady rotor response, and non-axisymmetric stator design on the stage performance. For various intensities and types (total pressure, swirl, and mixed) of distortion, the stage losses are computed with and without the application of these modeling effects and the contribution of each modeling element on the overall recovery is quantified.

Variational Asymptotic Method (VAM) is proposed as a computationally efficient method to perform transient structural analysis of rotor blades. The stresses and natural frequencies of the blades are computed to extract the vibratory stresses and resonance margins of the blades under the application of the loads computed using the flow profile at the exit and inlet of the rotor. The validation of VAM as an efficient technique for dynamic structural analysis of fan blades is performed by comparing the results from VAM with that of 3-D FEM method on a variety of loading scenarios. As a part of this thesis, a parametric environment is built that can take arbitrary

cross-section parameters and loads from the aerodynamic design framework, mesh the cross-sections, and perform transient analysis. The structural analysis framework is used to demonstrate the nature of vibratory stresses and the concerns of resonance on a test case.

The design framework encapsulating both the aerodynamic design and structural analysis is leveraged to explore the design space to minimize the vibratory stresses present in the blades with a small trade off in the stage efficiency. The fan stage design resulting from the framework introduced and developed in this dissertation aims to serve as a starting point for the preliminary design of a distortion-tolerant fan.

CHAPTER I

INTRODUCTION

In the past 50 years, advances in gas turbine engines have led to a 90% improvement in flight safety, a 350% increase in thrust to weight ratio, a 45% decrease in fuel consumption, and a 35 dB decrease in engine noise [35]. Continuous attempts to reach newer aviation horizons are in progress with desires for cleaner, safer, and more efficient designs.

1.1 Future Aviation Goals

Analyzing global trends, NASA's ARMD (Aeronautics Research Mission Directorate) has set forth goals for improved noise, emissions, field length, and energy efficiency for future subsonic transport aircraft. Table 1 lists the improvement goals in the system-level metrics of subsonic transport for noise, emissions, and energy consumption for different time frames: near-term, mid-term, and far-term [140].

Table 1: NASA targets for subsonic transport system-level metrics.

Technology Benefits	**Near-term** (2015 - 2025)	**Mid-term** (2025 - 2035)	**Far-term** (Beyond 2035)
Noise (cum. below Stage 4)	22 - 32 dB	32 - 42 dB	42 - 52 dB
LTO NOx Emissions (below CAEP 6)	70 - 75%	80%	80%
Cruise NOx Emissions (relative to 2005 best in class)	65 - 70%	80%	80%
Aircraft Energy Consumption (relative to 2005 best in class)	40 - 50%	50 - 60%	60 - 80%

Advisory Council for Aviation Research and innovation in Europe (ACARE) has set similarly aggressive goals for aircraft whose Entry into Service (EIS) is 2050. The targets set in Flightpath 2050 are a 75% reduction in energy consumption and CO_2 emissions, a 90% reduction in total mission and cruise NO_X, and a 65% reduction in perceived noise level compared to the technology level of EIS2000 [92].

1.2 Towards Novel Configurations

Tube-and-wing configurations with podded engines have been predominant in the commercial aviation industry for decades. However, stringent aviation goals, such as the N+3 targets put forth by NASA and other entities, necessitate configuration changes for the current aircraft fleet [127]. As a consequence, newer concepts have emerged as potential solutions to meet these targets. We provide a summary of a few novel configurations here.

(a) D8 (credit: Aurora) **(b)** N3-X (credit: NASA)

(c) STARC-ABL (credit: NASA) **(d)** NOVA (credit: ONERA)

Figure 1: Advanced N+3 configurations.

Aurora D8

Aurora D8 is a concept with capabilities similar to the Boeing 737 and Airbus A320. The D8 was originally designed by Mark Drela [38]. Fig. 1a shows the Aurora Double Bubble D8 concept whose EIS is the 2030 - 2035 time frame. The D8 is a modified tube and wing configuration with an unconventional wide lifting fuselage formed by joining two traditional fuselages. The concept also features smaller and lighter wings and a pi-tail empennage. The most important feature of the D8 concept is the aft-mounted Boundary Layer Ingesting (BLI) propulsion system. The D8 configuration can reduce fuel consumption by 52% and significantly reduce the community noise impacts as well [165].

NASA N3X

The NASA N3X is a Hybrid Wing Body (HWB) concept that employs a Turbo-electric Distributed Propulsion (TeDP) system. Fig. 1b shows a concept sketch of the N3X. N3X has a mission similar to the Boeing 777-200LR and cruises at 0.84 Mach with a 7500 nm range [4]. The distinguishing feature of N3X is its propulsion system - it has two gas turbine engines at the wingtips that electrically drive the distributed array of fans placed on the upper aft of the fuselage. This architecture is possible due to the flexibility enabled by the electric power transmission. The 15 propulsors ingest the boundary layer generated through the fuselage surface to create a substantial benefit for the aircraft system [45]. Based on the preliminary studies, the N3X concept can lower the fuel burn by 72% [4].

NASA STARC-ABL

The Single-aisle Turboelectric Aircraft with an Aft Boundary Layer Propulsor (or STARC-ABL) is another concept by NASA that could enter into service in 2035. Like the Aurora D8, the STARC-ABL has a mission similar to Boeing 737 and Airbus

A320. The concept is still a tube-and-wing configuration, as shown in Fig. 1c. However, it uses a turboelectric propulsion system architecture that flexibly enables the distribution of power. The shaft power from the two underwing turbofans is converted into electrical power by a generator. The generator then transmits the electrical power through wires to the aft-mounted fan that ingests the boundary layer generated over the fuselage [153]. The STARC-ABL concept can reduce the design mission block fuel burn by 7% compared to an N+3 Conventional Configuration (N3CC) [153].

NextGen ONERA Versatile Aircraft (NOVA) Concept

NOVA is a concept of medium haul transport aircraft by ONERA, the French Aerospace Lab. With an expected entry into service in 2030, NOVA has a mission similar to the Boeing 737-900 designed to carry 180 passengers with a cruise Mach of 0.82 on a 3000 nm range [154]. NOVA is a BLI configuration that has two partially embedded rear engines that ingest the side-wall boundary layer generated over the fuselage (Fig. 1d). While the propulsive efficiency is likely higher for this concept, the quantitative benefits of NOVA over the baseline configurations were not available to the author in the open literature.

A commonality in the configurations presented here is the presence of tight integration of different systems involved. Besides, all these configurations utilize the concept of Boundary Layer Ingestion (BLI) to attain fuel-burn benefits.

1.3 Boundary Layer Ingestion

Originally proposed by Smith in the 1940s, the concept of BLI is not new [142]. It has been the focus of research for maritime applications since the 1960s and only recently has the research interest been focused on BLI for transport aircraft [52, 156].BLI improves the propulsive efficiency by re-energizing the low momentum flow ingested into the propulsor. Depending on the type of configuration studied, Liu reported fuel burn savings of anywhere between 3 - 10% based on the system level benefit established by several studies [102].

BLI Benefits

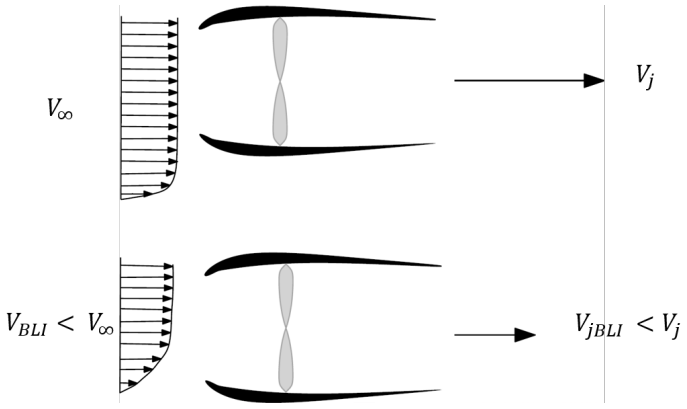

Figure 2: Schematic illustrating BLI benefit.

Simple equations involving propulsive power and thrust can demonstrate the benefit provided by BLI. For an isolated engine ingesting freestream flow, Eq.1 represents the net momentum flux (or net thrust). The difference in the kinetic energy rate of the flow at the exit and the propulsor's entrance is the power provided by the engine to produce this thrust. This power is proportional to the net momentum flux, as shown by Eq. 2. For the BLI case, Eqns. 3 and 4 represent the net momentum flux and propulsive power requirements.

$$F_N = \dot{m}(V_j - V_\infty) \tag{1}$$

$$P = \frac{\dot{m}}{2}(V_j^2 - V_\infty^2) = \frac{F_N}{2}(V_j + V_\infty) \tag{2}$$

$$F_{N_{BLI}} = \dot{m}_{BLI}(V_{j_{BLI}} - V_{BLI}) \tag{3}$$

$$P_{BLI} = \frac{\dot{m}_{BLI}}{2}(V_{j_{BLI}}^2 - V_{BLI}^2) = \frac{F_{N_{BLI}}}{2}(V_{j_{BLI}} + V_{BLI}) \tag{4}$$

In Fig. 2, the inlet velocity for the BLI case is lower than the freestream velocity ($V_{BLI} < V_\infty$). Let us assume that the BLI propulsor is sized to ingest the same mass flow rate as the non-BLI engine ($\dot{m}_{BLI} = \dot{m}$). In that case, the jet velocity for the BLI case must be lower than the jet velocity for the non-BLI case ($V_{j_{BLI}} < V_j$) to produce the same net momentum flux across the propulsor ($F_{N_{BLI}} = F_N$). Consequently, this leads to a lower gross thrust requirement as the ram drag decreases. Thus, a BLI configuration requires a lower propulsive power to produce the same net momentum flux across the propulsor since $V_{j_{BLI}} + V_{BLI} < V_j + V_\infty$. The result is ultimately a reduction in the fuel burn.

In addition to increased propulsive efficiency due to reduced jet dissipation, BLI configurations also decrease the mixing losses of wake due to the flow's ingestion that would otherwise dissipate in the wake. Many configurations that propose partially embedded engines also benefit from the reduced area losses from nacelle and pylon.

BLI Modeling

The presence of propulsion-airframe interaction makes the modeling of BLI challenging. BLI leads to an inherently coupled aero-propulsive interaction. On the one hand, the airframe flow affects how the propulsion system operates, and on the other, the design and/or the engine's operation affects the flow distribution upstream [59]. For conventional configurations, the airframe designs and the propulsion system are

generally decoupled from each other. The companies that design the airframe are usually not the companies that design the aircraft engines. So, from a practical viewpoint, the successful design of a BLI configuration needs collaboration from several entities. From a modeling viewpoint, there are no established guidelines or methods for propulsion-airframe integration, and this is currently an area of active research.

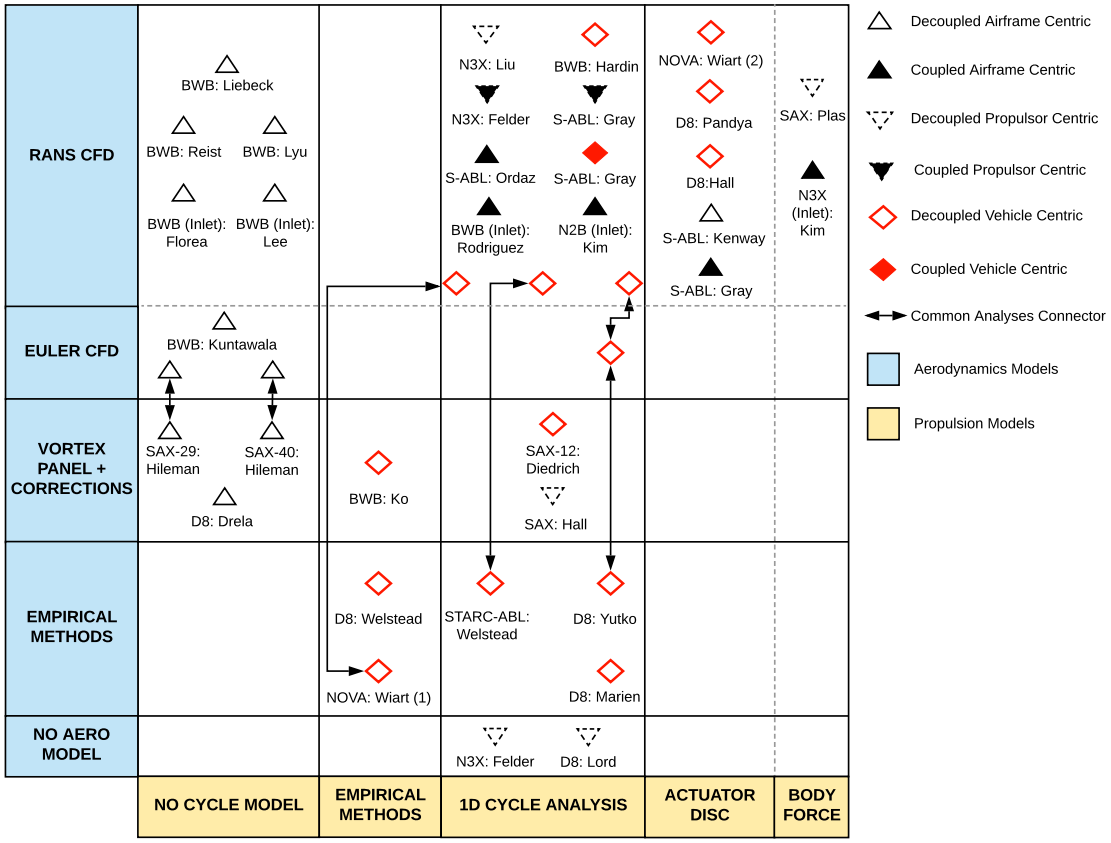

Figure 3: Summary of BLI modeling approaches, reproduced from [1].

The inclusion of the BLI effect can either be modeled as a reduction in ram drag component (computed from the aerodynamics module), ultimately lowering thrust requirement for the thermodynamic cycle or as an increase in thrust production (in the propulsion module) compared to a uniform inflow. As long as the bookkeeping is made consistent, both approaches can model these effects satisfactorily. Fog. 3 shows a review of several aerodynamic and propulsion modeling approaches used for BLI studies,

provided by Ahuja [1]. While several modeling approaches are used for aerodynamic modeling, the propulsion model is generally a 1-D cycle analysis [81]. The widespread use of 1-D thermodynamic cycle analysis is due to the computational efficiency and reasonable accuracy of these cycle models. Therefore, 1-D thermodynamic cycle analysis can be considered the most appropriate method for analyzing the propulsion system at the conceptual level.

Since 1-D cycle analysis methods are consistently used as the propulsion models in the BLI domain, it begs the question as to how the treatment for BLI is made in such models. Fig. 4 shows the schematic of a generic propulsion system architecture for a 1-D cycle analysis. This architecture is used for uniform flow because it represents the flow as a point mass at any station. As mentioned previously, the BLI effect can be modeled as a reduction in ram drag or a reduction in required thrust in these models. Changes can be made in the inlet component to account for reduction in ram drag from the analysis of the incoming boundary layer flow. Besides modeling the BLI effect on thrust reduction, another concern brought forth by the ingestion of the boundary layer is the fan stage's impact due to flow non-uniformity. The fan is the first component that the flow encounters as it enters the engine; therefore, the harsh conditions of non-uniformity impact the fan stage, and care should be taken to account for these effects.

A fan is simply a component for a 1-D cycle analysis. Each component in Fig. 4 can be represented via a set of thermodynamic equations, and the flow at the exit of the component can be solved to result in a physically converged solution. Components, such as fans, also use maps to represent the component's performance under a set of operating conditions. For uniform flow modeling, a fan map represented by pressure ratio and efficiency in the corrected speed and mass flow space is used to predict the component's performance. Scaling laws are used to scale such maps within reason to alleviate the need for requiring an extensive data set of maps. Fig. 5 shows a

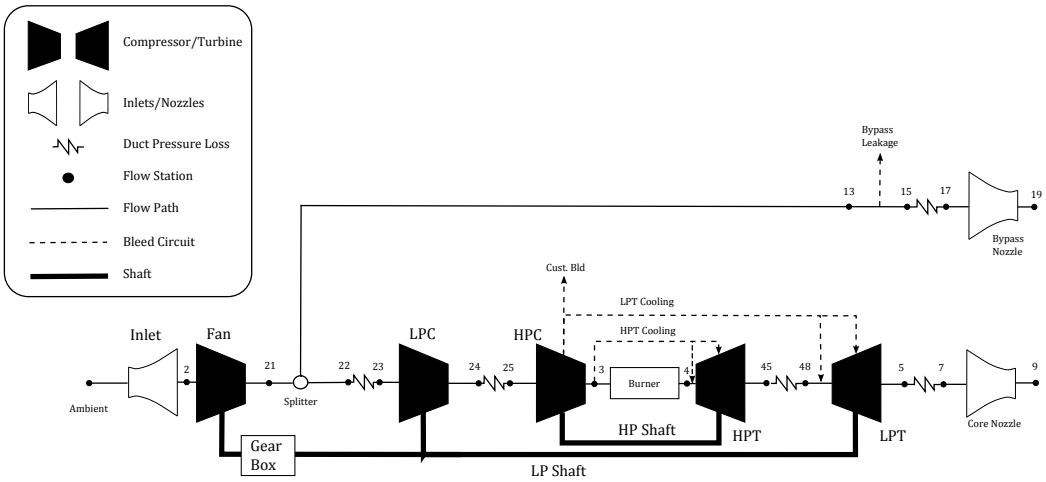

Figure 4: Schematic of propulsion system modeling for uniform flow.

notional example of a fan map consisting of pressure ratio and efficiency values as functions of corrected inlet flow. The ability to use such maps dramatically reduces the computational expense and generally provides a reasonable estimate of the overall engine performance.

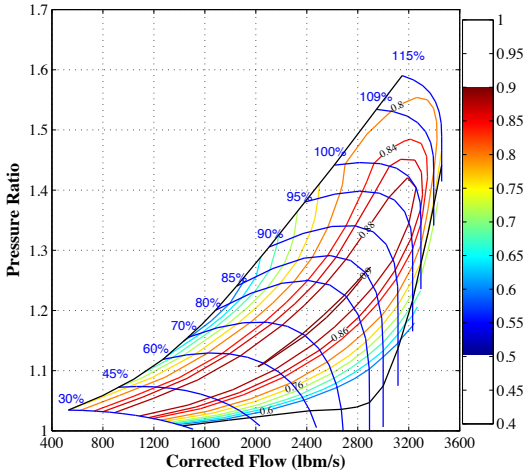

Figure 5: Map based fan representation (notional).

It can be argued that using conventional maps in the 1-D thermodynamic cycle is not sufficient to model BLI induced distortion that negatively affects the fan's performance. While relatively more straightforward in terms of implementation, using map based fan representation has several drawbacks for distortion analysis. First,

it cannot correctly account for variations in swirl flow i.e., the effect of co-swirl or counter-swirl distortion offsets the map to a certain degree. Second, it represents a quasi-steady performance of the fan. Third, in the case of non-axisymmetric stators, discussed in the next chapter, the representation of a stage map becomes non-trivial. Finally, using fan maps implies a fixed design of a fan. If these maps come from the design of uniform flow, then their effectiveness should be reevaluated. Also, in cases of distorted inflow, the fan stage design relies heavily on the nature of distortion, which is also affected by the propulsor.

The significant impacts of distortion are reducing efficiency and stall margin and the fan's structural integrity problems. In several BLI studies, the flow is averaged, and a drop in fan efficiency is specified to model the losses due to BLI. Using this approach does not consider the actual design of the fan being used. Another approach is modifying the 1-D thermodynamic cycle and using a map-based approach to model the losses due to BLI. For example, Fig. 6 shows splitting the flow at the inlet into two fans and using the same map for performance prediction [56]. Using such architecture in 1-D cycle analysis models is very useful in obtaining a reasonable estimate in fan performance degradation without compromising the cycle analysis solvers' computational expense. However, these methods also suffer from the general drawbacks of using map-based approaches. A review of the literature in chapter 2 will show that in studies where map based approaches are not used, the computational costs tend to pose hurdles to be used in the conceptual design phase. In addition, they are incompatible with 1-D cycle analysis tools.

1.4 Need for a Fan Stage Conceptual Design Method for Distorted Flows

A cursory review of the literature shows that several methods have been used to analyze the fan stage's performance in the presence of in-homogeneous inlet flow conditions. Often, the sensitivities of various design parameters on fan performance are also

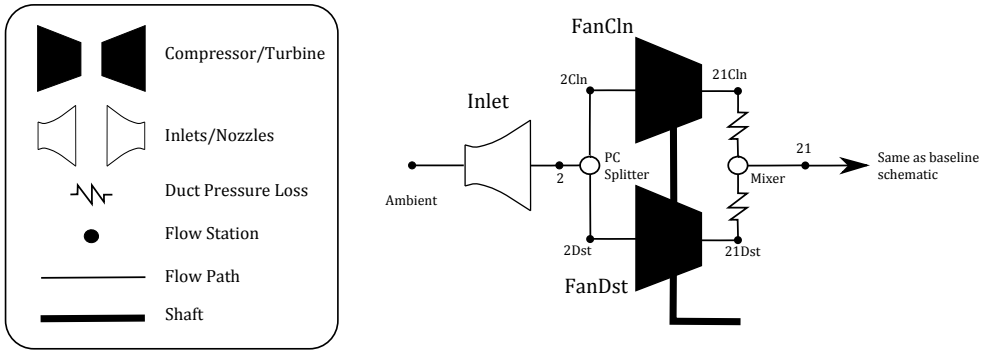

Figure 6: Fan modeling for inlet distortion, reproduced from [56].

explored. While some of the models used require relatively lower computational power, they are still not suitable for exploring and optimizing thousands of design iterations in the conceptual phase. Also, they are not compatible with 1-D thermodynamic cycles. Using the maps generated for a specific inlet distortion in the thermodynamic cycle analysis is not recommended since any change in the cycle design changes the inlet flow due to aero-propulsive coupling. Once the flow changes, the map is not suited for that application anymore. Strong reliance on higher fidelity tools motivates the need to rethink the current design process. An environment for rapid fan design and assessment that can interact with 1-D thermodynamic cycles will alleviate this highly integrated problem's computational burden and help bring knowledge forward in the design process. From a practical viewpoint, engines, let alone fans, are generally not designed for a specific aircraft. With that argument, it is natural to question the need of a fan design framework. But, since distortion presents a unique set of problems, engines should very likely be different for different configurations as they lead to different flow profiles. If only a few number of aircraft are designed, then designing a separate engine does not make practical and financial sense. However, if hundreds of BLI aircraft are to be designed, then it is not unreasonable to demand a new fan/engine combination for the fleet. In such cases, the need of a fan design framework is warranted that can integrate with the propulsion and the aircraft design

modules to enable conceptual/early sizing and optimization exercises, similar to ones in [11, 17, 131]. We thus establish a high-level motivating question at this point.

Motivating Question

What is an appropriate fan stage design framework for distorted flow applications that is compatible with the conceptual level analysis/design of 1-D thermodynamic cycles?

This dissertation tries to identify gaps in the current literature for the conceptual design of fan for BLI applications. It proposes a framework for designing fans under distortion that captures both aerodynamic and structural effects.

1.5 Document Outline

The structure of the thesis presented here is as follows:

- Chapter 2 provides a review of relevant literature regarding distortion. It sets up the background by introducing distortion descriptors. Following this, the effects of flow non-uniformity on the fan stage are discussed. Then, several methods that have been used to model flow distortion on fan stages are presented. The chapter also provides an idea of the current state of structural analysis methods for BLI fans.

- Chapter 3 draws upon the observations from the literature review and identifies observed gaps. Requirements for the conceptual design framework are established. Then, a discussion of key research questions and corresponding hypotheses are detailed.

- Chapter 4 formally introduces the proposed framework for aerodynamic design and structural analysis of the fan stage. Detailed descriptions of all steps are also provided here.

- Chapter 5 presents a verification of the proposed aerodynamic model on a practical distortion problem. It then details the experimental efforts conducted to analyze the effectiveness of various modeling effects on recovering losses due to circumferential flow distortion.

- Chapter 6 describes the validation efforts conducted to establish the relevance of the Variational Asymptotic Method as a computationally efficient and accurate method for structural analysis of rotor blades. Then, it also uses the method to perform structural analysis of rotor blades generated from the aerodynamic design framework proposed in this work.

- Chapter 7 provides a summary of the work presented in this thesis. Finally, the key contributions and potential future work are discussed.

CHAPTER II

LITERATURE REVIEW

2.1 Chapter Overview

The discussions in Chapter 1 established motivation for a fan stage design framework for distorted flow applications that is compatible with the conceptual level analysis/design of 1-D thermodynamic cycles. In this chapter, a review of some basic distortion descriptors is provided first. Next, the flow physics of distortion and its impacts on the fan stage are discussed. Following that, we present the hierarchy for fan design and modeling approaches for distortion.

2.2 Distortion Descriptors

Flow distortion is defined as any non-uniformity in the thermodynamic properties of the flow. Typically, distortions in total pressure, swirl, and temperature are essential to the operation of a gas turbine engine and its turbomachinery components. In the case of BLI, distortion is primarily produced by a large pre-entry surface producing friction on the flow before entering the engine.

Based on the directional nature, distortion can be divided into two types: circumferential and radial. These two types can be easily understood by looking at the compressor annulus in cylindrical coordinates. Circumferential distortion is the variation along the tangential direction in axial velocity, pressure, or swirl, while radial distortion is the variation relative to the radial direction (along the blade span).

There are several different methods by which the propulsor can ingest the boundary layer of an air vehicle. However, the most typical one involves embedding the engine or

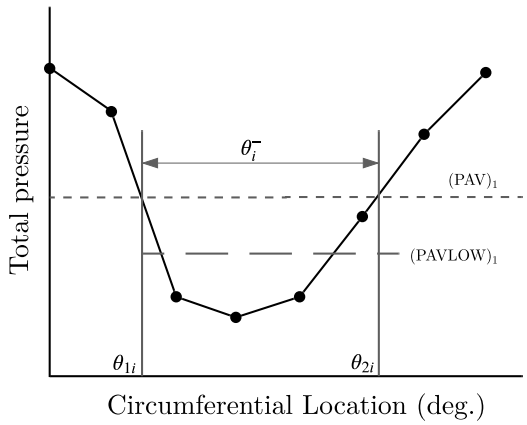

Figure 7: One-per-rev circumferential distortion pattern.

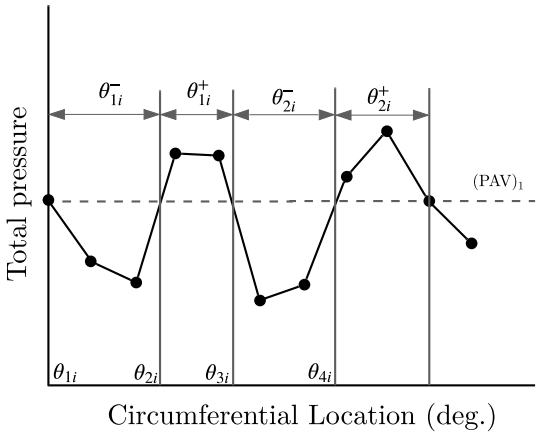

Figure 8: Multi-per-rev circumferential distortion pattern.

the propulsor on the aerodynamic surface itself. This placement leads to a large build-up of low momentum flow in one annulus sector and a high amount of circumferential distortion. Since a boundary layer is present and is, by definition, accompanied by a velocity gradient normal to the wall, radial distortion will typically be present in these cases as well.

A commonly adopted guideline for describing distortion intensity is given in ARP 1420 [23]. These were produced by SAE in collaboration with many companies over several decades of distortion research and were found to be the most robust procedures for measuring and determining distortion. Typical circumferential distortions at the fan face can be either one-per-rev (Fig. 7) or multi-per-rev (Fig. 8) depending on the configuration. Ultimately, it is dependent on the curvature of the fuselage surface and the inlet that defines how the flow reaches the fan face. By virtue of the velocity gradient developed on the boundary layer, a typical radial distortion profile can be seen in Fig. 9.

Descriptors have been defined for both circumferential distortion and radial distortion. For example, the circumferential extent and intensity (also called DPCP) are defined in Eq. 5 and Eq. 6 respectively. Here, θ refers to the angle in the circumferential

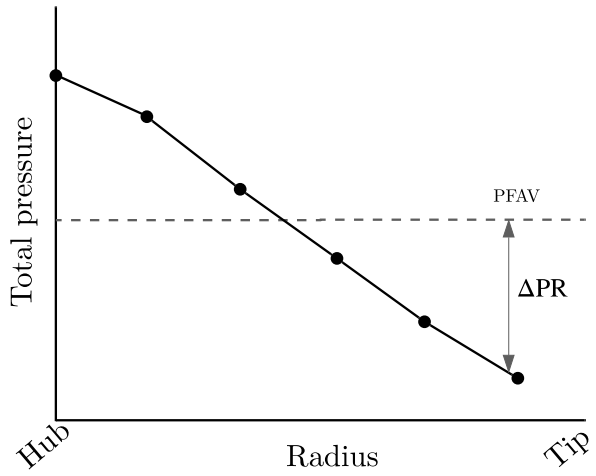

Figure 9: A typical radial distortion pattern.

direction that contains the lower than average flow properties (total pressure in this case). Radial distortion intensity (also called DPRP) is defined in Eq. 7.

$$\text{Ring Extent} = \theta_i^- = \theta_{2i} - \theta_{1i} \tag{5}$$

$$\text{Ring Intensity} = (\frac{\Delta PC}{P})_i = (\frac{PAV - PAVLOW_i}{PAV})_i \tag{6}$$

$$\text{Radial Intensity} = (\frac{\Delta PR}{P})_i = (\frac{PFAV - \Delta PR}{PFAV})_i \tag{7}$$

2.3 Effects of Flow Non-uniformity

Based on several experimental inlet designs studied at the NASA Langley Research Center Transonic Tunnel, a S-duct inlet (Inlet A) was defined as a baseline for BLI inlets [13]. This study's experimental results indicated that the inlet's pressure recovery generally decreased with the increase in the distortion at the inlet entrance. The inlet distortion increased with the increase in Mach number. Ingesting a larger portion of the boundary layer also showed a decrease in inlet recovery. Increasing the Reynolds number showed a negligible effect on inlet distortion but increased the inlet recovery

slightly. This work's crucial contribution was a common baseline for future BLI inlet flow studies that involve high Reynolds number cases with a large amount of boundary layer ingestion. Besides, it still serves as a validation tool for many CFD studies.

Instrumentation data recorded in experiments conducted on Inlet A were reduced to inlet pressure recovery, $P_{T1}/P_{T\infty}$, and average circumferential distortion intensity, $DPCP_{avg}$ as discussed in Section 2.2. The cases were run for several flight conditions from Mach 0.25 to Mach 0.83. At high Mach numbers, the distortion intensity was approximately 0.055. However, this study did not provide any information on distortion extents and the intensity of swirl distortion [46].

In an experimental test, a Pratt & Whitney JT15D-1 fan was subjected to a distortion profile similar to the pressure profile at NASA Inlet A from the study in [58]. Instead of an averaged circumferential distortion intensity, the intensity of each ring at the AIP was provided. Besides, the magnitudes of radial distortion intensity and the extents of circumferential distortion intensity were also provided. The circumferential extents, described in Eq. 6, ranged from 138° to 162°. The radial distortion intensity was an order of magnitude lower than the circumferential distortion intensity. The intensities of distortion and circumferential extents were maximum at the tip, which makes sense given the slowest part of the boundary layer being ingested at the tip.

The studies mentioned above did not consider the presence of swirl distortion, which is inherently the secondary flow developed through the inlet. The fan's physical presence affects the fan face flow distortion. Numerical simulation by Giulaini et al. [54] showed that the height of distortion and the intensity of total pressure distortion are reduced in the fan's presence compared to the inlet-only case. An understanding of the distortion flow physics is necessary to develop a design framework. In this section, several aspects of distortion impact are discussed, as listed below.

1. Upstream flow redistribution

2. Stall margin loss

3. Rotor losses

4. Unsteady rotor response

5. Stator losses

6. Unsteady structural effects

2.3.1 Upstream Flow Redistribution

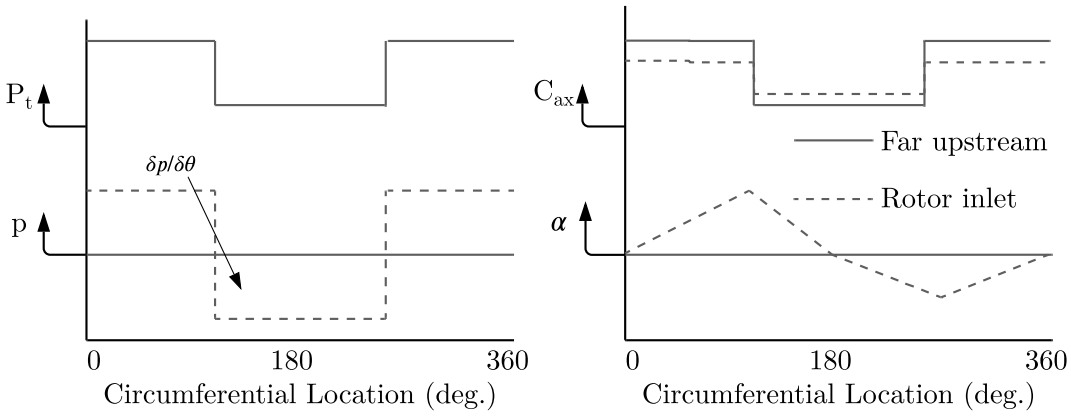

Figure 10: Explanation of circumferential redistribution, adapted from [114].

The thick boundary layer developed on the fuselage surface, in addition to the complex inlet aerodynamics and the presence of the rotor itself, defines the distortion at the fan face. As the flow moves from the inlet entrance to the fan, three-dimensional flow distribution is observed, which leads to swirl distortion and attenuation of non-uniformity in axial velocity at the fan face [48, 50, 65]. Longley et al. [103] used a simple parallel compressor to investigate flow redistribution ahead of the rotor. In Fig. 10, the circumferential distribution of total and static pressure, axial velocity, and swirl are shown at the inlet entrance (far upstream) and rotor inlet. The inlet

entrance flow is generally non-uniform in terms of total pressure only (a square wave is shown here for clarity). The static pressure variation is non-existent; therefore, the axial velocity non-uniformity follows the total pressure profile. Constant static pressure also implies no movement of flow in the circumferential direction, therefore no swirl. The lower velocity (consequently, lower mass flow) sector undergoes a larger change in the pressure across the stage. Under the assumption of constant static pressure exit at the fan exit, it becomes clear that the static pressure at the rotor inlet should be non-uniform. Therefore, in Fig. 10, static pressure non-uniformity is present in the rotor inlet. The axial velocity non-uniformity is attenuated since some of the non-uniformity is present in the form of static pressure differences. Variation in the static pressure causes the circumferential distribution of the flows around the annulus, causing co-swirl on one side and counter-swirl. It is to be noted here that constant static pressure at the exit of the stage is not necessarily accurate and is a more conservative estimate.

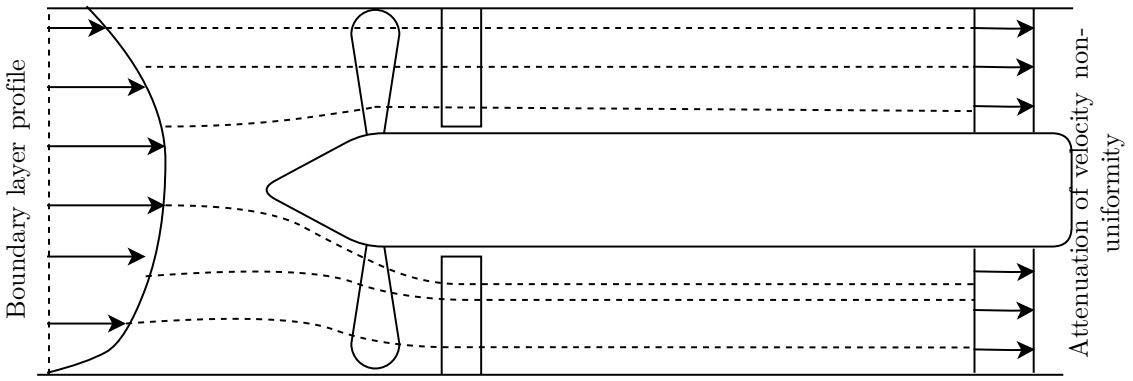

Figure 11: 3D flow redistribution from inlet entrance to rotor inlet, adapted from [65].

Fig. 11 shows a basic sketch of how mass flow redistribution occurs in a BLI fan as the flow progresses from the inlet entrance to the fan face. Far upstream of the rotor, the flow can be assumed to be uniform in static pressure with a smooth axial flow. However, the rotor induces a static pressure non-uniformity as the flow nears the fan because of the uneven work input in the rotor, as discussed above. The flow exits the

fan at almost uniform static pressure, and the slower moving fluid experiences larger work from the rotor. In these regions, low static pressure is induced. The consequent pressure gradients cause a redistribution of mass from the upper side to the lower side. This mass flow redistribution phenomenon reduces the non-uniformity in the mass flow around the annulus at the fan face; however, it results in non-uniformity in swirl angle and radial angle distribution [65]. The fan's presence creates a 3-D flow redistribution of the mass flow, which becomes more prominent for fans with lower hub-to-tip ratios. The contributions of several flow features of BLI at the rotor inlet is shown in Fig. 12. Three dominant features of BLI induced distortion at the rotor inlet can be established:

- attenuation of axial velocity
- stream tube contraction
- increased swirl distortion

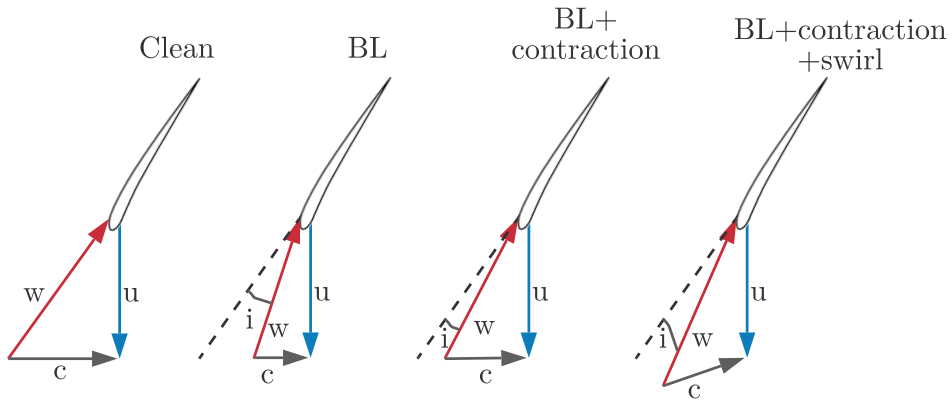

Figure 12: Velocity triangles at the rotor inlet due to various distortion induced flow phenomena, adapted from [115].

In the study by Gunn et al., the swirl angles around the circumference range from $-7°$ to $+7°$, with lower variations observed near the tip [65]. The higher swirl

distortion near the hub can be attributed to the spinner's presence that creates more redistribution towards the hub region. Similarly, in an integrated inlet/rotor design process conducted by UTRC under the BLI2DTF group [27], several iterations between the inlet and rotor design were conducted. The inlet design started with Inlet A, and it was observed that the distortion created by the inlet was not aero-mechanically sustainable for the fan. The distortion pattern produced at the fan face by the optimized Inlet A is a reasonable distortion pattern to be considered for the BLI fan design. The optimized Inlet A resulted in a $DPCP_{avg}$ of 0.1 and $DPRP_{avg}$ of 0.04 with an average circumferential extent of 125°. The swirl angle distribution ranged from +16° to −24°.

The distortion intensities observed in the studies above are similar to the ones observed in Plas et al. [123], Yao et al. [160], Bakhle et al. [7, 8], Giulaini [55], and Ferrar [47].

2.3.2 Stability of the Fan

The ranges of non-uniformity in the total pressure and swirl profiles in the flows described in the preceding paragraphs have consequences on the fan's operability. These large variations in total pressure and swirl can lead to fan stall, and if severe, to surge. A discussion on the initiation of a stall is presented here.

The stall of a compressor occurs during the initiation of an aerodynamic instability that produces a loss in total and static pressure ratio across the compressor. On a compressor map, the stall region of a compressor is typically denoted by a "stall line." It is the stability boundary for that particular machine in corrected flow and pressure ratio space. The "stall margin" is the metric by which a compressor performance engineer can measure the operating point's distance from the stall line. The stall margin at constant flow is typically used and is defined in Eq. 8, where OL and SLL denote operating line and stability limit line, respectively. The stall margin

is generally defined as the percentage of the pressure ratio at the stall between the current operating line of the compressor and the stall line.

$$\text{SMW} = \frac{PR_{SLL} - PR_{OL}}{PR_{OL}} \times 100 \tag{8}$$

A larger stall margin means more margin for things like thermal and other types of transients, engine deterioration, and other features that affect compressor operability. The required stall margin is typically determined through the means of a stall margin "stack-up", whereby the performance engineer determines all of the sources of stall margin reduction and estimates the required margin to prevent surge during the full envelope of operations for the engine.

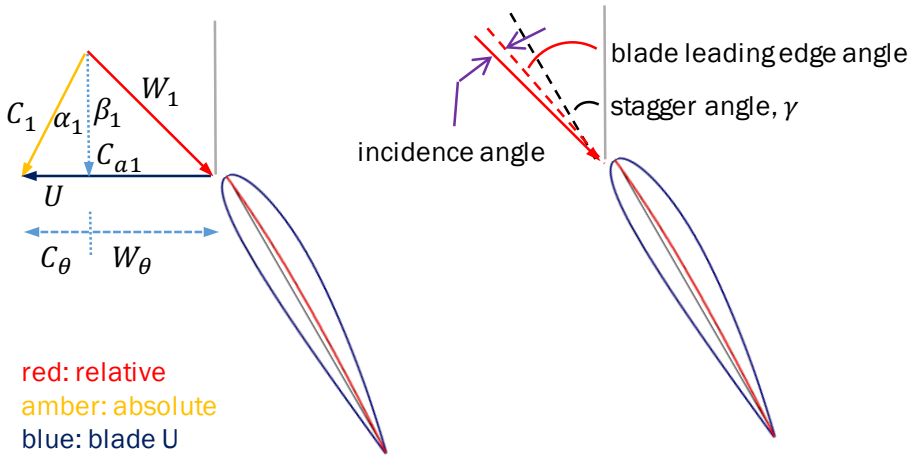

Figure 13: Dependence of incidence angle on axial velocity and swirl angle.

For fans not designed for BLI purposes, during the boundary layer's ingestion, the fan departs from its normal operating condition. Swirl and total pressure distortion lead to incidence angle variations on the fan. In the hub region, due to more redistribution of mass flow, the axial velocity distortion is attenuated compared to the inlet entrance; however, the hub's spinning creates more swirl distortion. So, swirl distortion is mainly responsible for large incidence variations on the fan at the hub region. Near the tips, the total pressure distortion is more dominant, creating a large axial velocity non-uniformity, which is responsible for incidence swings. Either swirl or total pressure

distortion translates into incidence variations for the fan. Swirl angle, axial velocity, and blade metal leading edge angle combined determine the blade's incidence angle. Fig. 13 provides a schematic description of the incidence angle ($ß_1$, blade leading edge angle (κ_1), stagger angle (γ), relevant relative and absolute flow velocities (C_1, W_1), and blade speeds (U). Fig. 14 illustrates the isolated effects of swirl and total pressure distortion on velocity triangles and, consequently, on the incidence angles.

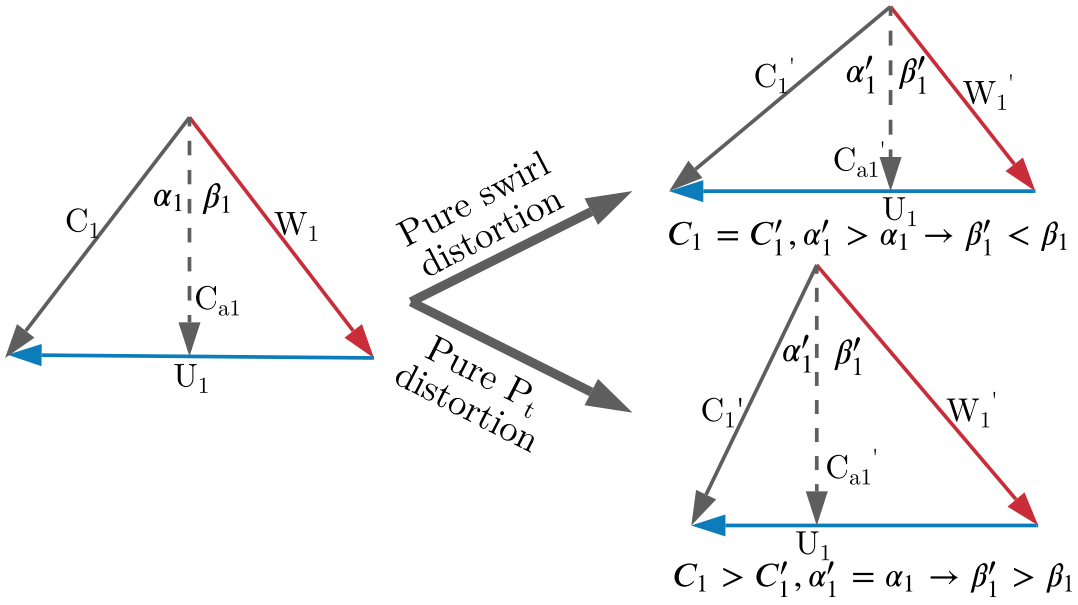

Figure 14: Effect of pure swirl and total pressure distortion on velocity triangles.

In the presence of distortion, the fan imparts unequal work at various locations. With high loading at some part in the annulus, the blades may operate at angles beyond stall at those locations. The initiation of a stall may grow bigger and lead to a catastrophic surge in the engine. When the inlet's mass flow is reduced, and the fan operates towards the stall point, the distortion intensity grows, leading to an additional increase in the fan leading edge incidence angle [46]. Ferrar et al. provide a simple explanation based on parallel compressors' theory for unequal work input [46].

The magnitude of stability loss due to distortion is dependent on various factors: (i)

total pressure distortion intensity (circumferential and radial), (ii) extent of distortion, (iii) distorted sectors per-rev (one-per-rev or multi-per-rev), (iv) swirl distortion intensity, and (v) the blade geometry itself.

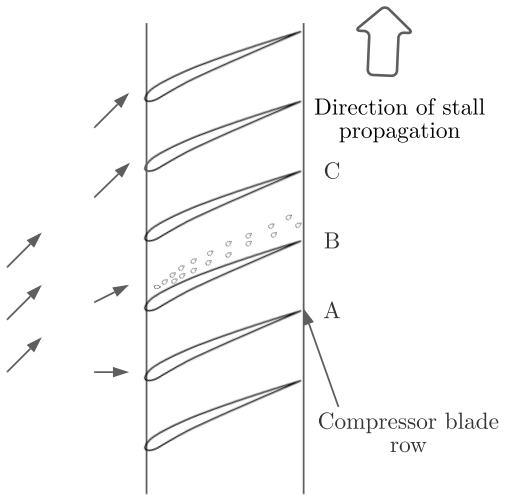

Figure 15: Physical phenomena for stall initiation, adapted from [61]

While the exact computation of the loss in stability margin is a non-trivial task, Fig. 15 attempts to explain the physical phenomenon for the initiation of stall [61]. In a row of rotor blades, the presence of non-uniformity causes the local angle of attack to be higher at some location (say, B) at a time t_1. If the angle of attack at B is sufficient enough to stall the blade, flow separation occurs at B, such that the flow is pushed towards the neighboring blades (suction surface of A and pressure surface of C, in this case). Consequently, the angle of attack reduces on A and increases on C at time $t_1 + \delta t$, causing blade C to operate near stall and A to recover from the stall. A rotating stall is thus initiated because of this local instability. Often, this local instability translates to system-level instability and can lead to surge, which is considered to be a catastrophic failure for engine operation. For this thesis, stall margins will be limited to discussing local instabilities or the initiation of a stall.

Perovic et al. calculated that the stability margin caused by BLI was only 1-2% of

the flow coefficient [121]. Other studies, however, have shown that the loss in stability pressure ratio can vary anywhere from 2% - 8% [79, 104].

2.3.3 Loss in Efficiency and Pressure Rise Capacity

Besides concerns of stability, BLI also leads to fan efficiency loss and a reduction in the pressure rise. Gunn [65] points out that pressure rise reduction is small compared to fan efficiency reduction - the reason being that the non-uniform work distribution tries to offset the reduction in pressure rise across the fan. The reason why fan imparts unequal work can be understood simply by considering a fan map. If we assume that a fan's response is instantaneous, at regions of low momentum flow, the operating point on the map changes, and the fan imparts higher pressure rise to that region. (Fig. 16)

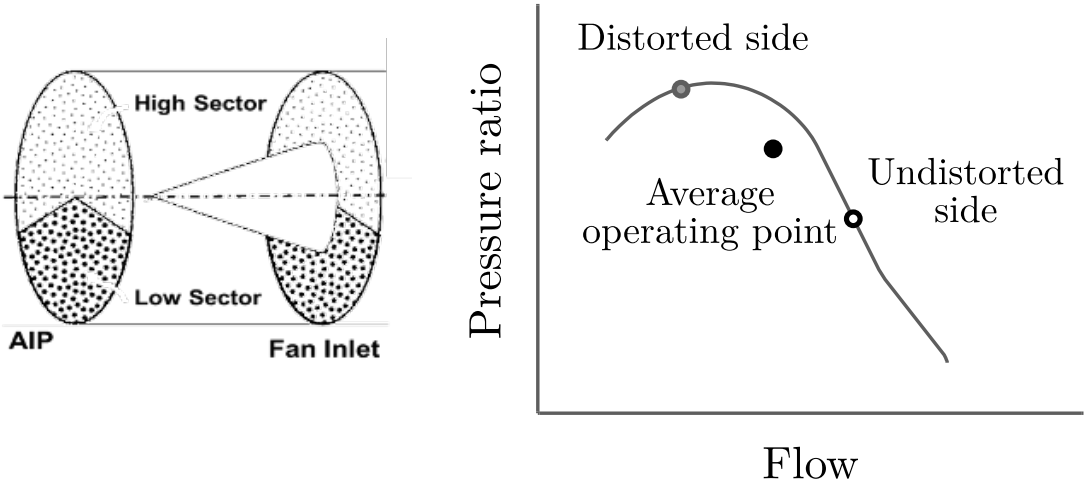

Figure 16: Parallel compressor analysis: unequal pressure rise, adapted from [111].

At the micro-level, fan efficiency reduction is related to one of the various loss sources. Instead of breaking down the losses and tracking the streamlines, for a general correlation, Lieblein's Diffusion Factor (DF) (Eq. 9) can be used as a surrogate for fan efficiency [101]. The second term in Eq. 9 accounts for bulk diffusion, and the third

term accounts for the flow turning.

$$\mathrm{DF} = 1 - \frac{V_2}{V_1} + \frac{\Delta V_\theta}{2\sigma V_1} \tag{9}$$

Various BLI studies, depending on the configuration studied and the inlet distortion pattern, estimate an efficiency loss of 1% - 4%. A study on the vehicle-level system impact of BLI for the ND8 concept used a 3.5% efficiency penalty based on their interaction with the BLI2DTF group [21, 108]. Based on Gunn et al.'s study, an optimistic drop of around 1% was found for the overall stage efficiency [65]. Another study by Florea et al. report the fan efficiency loss due to BLI was 6%, but the optimization of inlet led to a loss of only 0.5% - 1.5% [49]. However, this study did not account for the aeromechanical constraints that might alter the optimal inlet shape and the subsequent fan efficiency drop. These differences also depend on the fan under consideration, its operating condition, and the distortion's nature. Regardless, inlet distortion creates additional losses in the fan, and any fan analysis/design method needs to account for this loss.

2.3.4 Rotor Unsteady Response

The flow in a turbomachine is fundamentally unsteady. Dean [33] first showed that for a turbine or a compressor to provide shaft work or absorb the work, there must exist unsteady local changes in static pressure. The relation can be seen in Eq. 10 [31]. This relation means that the rate of change of stagnation enthalpy of a particle along a pathline is proportional to the partial derivative of the static pressure to time at that instantaneous location. So, without unsteadiness, stagnation enthalpy cannot change in a turbomachine.

$$\frac{Dh_t}{Dt} = \frac{1}{\rho}\frac{\partial p}{\partial t} \tag{10}$$

Although unsteadiness in inherent in a turbomachine, in conceptual designs, the

unsteady flow has found very little consideration in terms of application. It is possible to treat the flow as steady using the Euler turbomachinery equation in the relative frame of reference [31]. If a turbomachine includes only one blade, the flow is uniform, and we analyze it in a relative frame of reference. The problem can be treated as steady by writing the governing equations accordingly [166]. In this thesis, unsteadiness refers to the additional periodic unsteadiness due to distortion and not the inherent unsteadiness that exists in all kinds of flows.

With the ingestion of BLI, the assumption that the flow is steady remains in question even under the relative frame of reference. As the rotor blade rotates around the distorted flow field, the blade's leading edge is exposed to varying axial velocity and swirl angle. Thus, the blade is subjected to varying incidence. Low axial velocity and negative swirl angle (or counter-swirl) increase the incidence angle that the blade sees. The question then becomes if the blade responds instantaneously to the changing flow conditions at its given operating condition. Two types of unsteady effects are relevant to discuss - inviscid and viscous unsteady effects.

A reason why the distorted response is different compared to a uniform flow is because of the inviscid unsteady effects. It deals with the acceleration of the fluid particles such that the difference in the static pressure at the trailing edge is different from the one predicted by the quasi-steady pressure rise characteristic. [111]. On a fan map, the steady pressure ratio characteristic thus changes into an orbit even for a case with no swirl distortion, as shown in the notional representation in Fig. 17. The existence of this unsteady orbit, instead of the steady characteristic, causes the average operating point to be different from the one obtained from the quasi-steady analysis and changes the flow field downstream.

Another effect is due to the unsteadiness of the viscous flows that cause hysteresis in rotor loss coefficients near the stall point. Fig. 18 shows the variation of relative total pressure loss as a function of the inlet flow angle for a uniform flow field and 180°

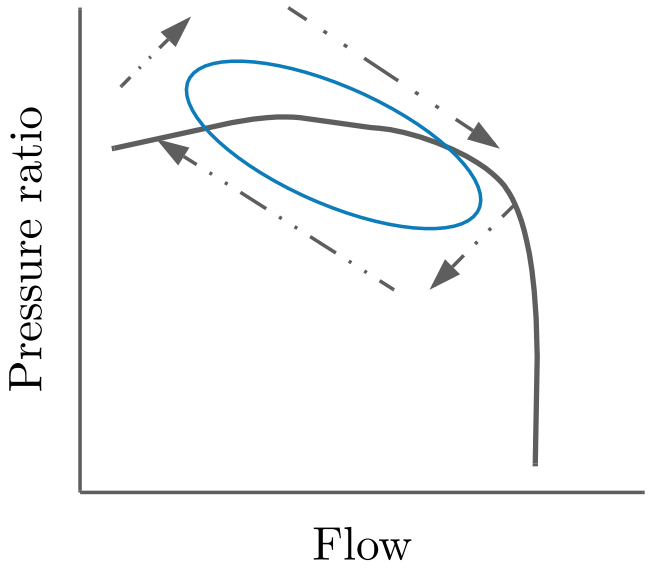

Figure 17: Notional fan map under distortion (including unsteady orbit), adapted from [114].

distortion. The presence of distortion introduces losses that clearly exhibit a hysteresis loop and that the values between steady and unsteady losses depart significantly in magnitude. In the non-uniform flow field, excursions to higher incidence angle than steady stall can also be observed. Greitzer [61] notes that the rotor is operating transiently at flow angles above uniform stall, which is in direct contrast to many quasi-steady models used to treat the problem of inlet distortion.

The phenomenon of rotors transiently operating in some areas beyond stall is what we refer to as "stall delay". The lift increase and the separation delay are the critical features of this phenomenon due to the unsteadiness present in the flow. The problem can be thought, in a similar way, like that of the extra lift produced by insects when flying. When flapping their wings at a specific frequency, an intense leading-edge vortex is generated, acting as a high lift generating mechanism [44]. The same phenomenon is also responsible for generating extra lift on delta wings, where the flow along the span-wise direction stabilizes the vortex.

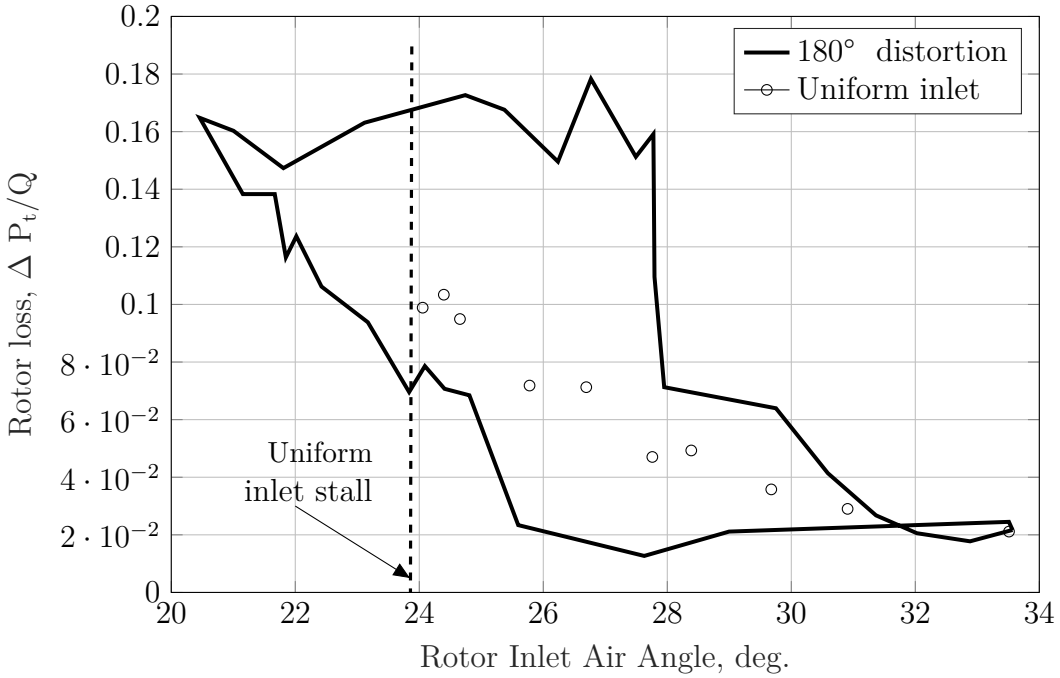

Figure 18: Total pressure loss coefficient for a rotor, digitized from [111].

Fig. 19 shows the unsteady loop in the pressure rise at different passage locations with different corrected mass flow in those regions for three conditions: nominal, closer to choke (1), and closer to stall (2) [50]. The three loops of pressure rise are just the 3 flight conditions. As a result of the unsteadiness in the flow, issues of representing fan maps for distorted flows also arise. In an attempt to understand the dynamic behavior of compressor aerodynamic response, Cousins [24] identified that rotor's blading parameters determine the dynamic response of a compressor system. Cousins [24] determined that the blade's time constant is responsible for the response of a compressor in a distorted flow field.

2.3.5 Stator Losses

The rotor interaction with the non-uniform flow field results in an unsteady rotor response. Consequently, the flow exiting the rotor is also non-uniform in terms of swirl and radial angle. Fig. 20 shows a typical stator exit profile for a propulsor operating in a BLI flow field. These values are deviations from the uniform inflow condition.

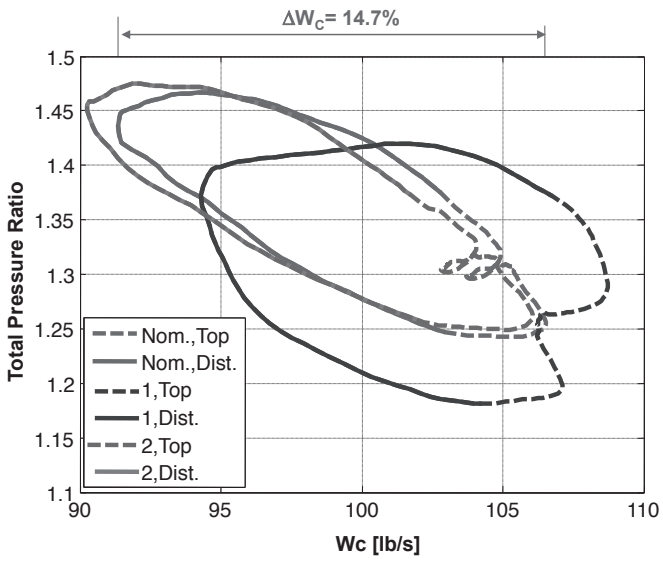

Figure 19: Total pressure rise loop for a fan operating in a distorted flow field, reproduced from [50].

It can be seen that the amplitude in swirl angle variation is dominant towards the tip region. The amplitude of variation is as high as 15° in the tip region compared to ≈5° in the hub. Conventional stator rows are not designed for circumferentially varying flow in terms of swirl and mass flux.

A rotor's presence attenuates the total pressure distortion to a certain extent; however, the mass deficit transfers from the inlet of the rotor to its exit. Low axial velocity regions at the rotor exit result in a shorter vector of the relative velocity. When converted into the absolute frame, this vector is overturned. The result is a positive incidence and, consequently, increases the turning requirement in the stator. This phenomena is highlighted in Fig. 21. Flow turning has the largest effect on the stator diffusion factor [77]. From previous discussions, it is known that reducing the diffusion factor at the exit directly correlates to increasing the stage efficiency. These variations at the stator inlet lead to increased losses in the axisymmetric stator.

Minimizing deviation from "design" incidence angles can mitigate some of the efficiency losses. Various high-fidelity analyses by Hall et al. [77], Cousins et al. [27], Gunn et al. [66] have suggested the need of a non-axisymmetric stator design. In a

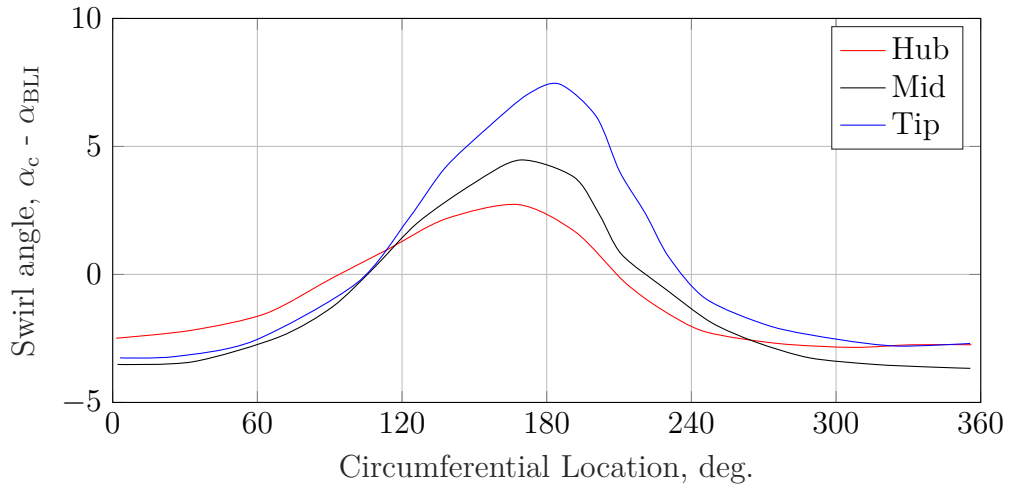

Figure 20: Circumferential variation of swirl angle at stator inlet, digitized from [66].

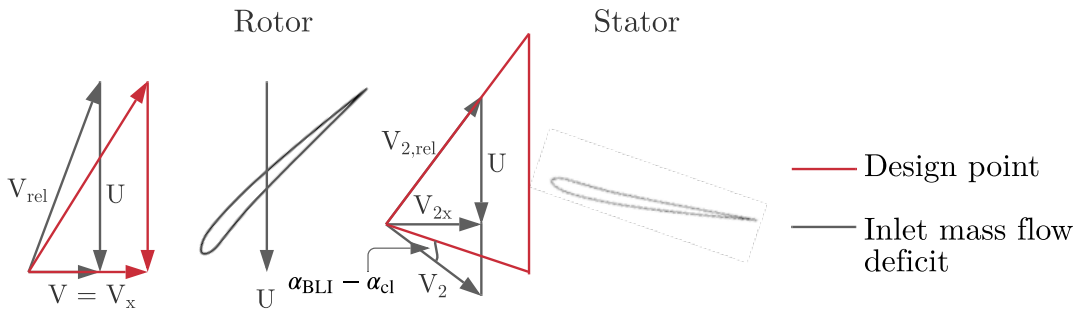

Figure 21: Stator incidence variation due to inlet distortion from BLI, adapted from [65]

study by Gunn et al. [66], as much as 10% in stator losses were recovered by modifying the stator metal angles, chord, and lean.

2.3.6 Mechanical Issues

One issue not discussed in detail so far is the blades' mechanical integrity when operating in a distorted flow field. While the aerodynamic performance of the fan is the objective function, mechanical integrity is a constraint. Major mechanical concerns associated with the fans ingesting the distorted flow are large resonant fan blade response and vibratory stresses caused by high-frequency cyclic loading.

The flow on the blade changes at each circumferential location when they rotate in a distorted flow field. The unsteady pressure loading on each blade acts as an external forcing on the blade [8]. This unsteady loading may result in blade vibration, which further increases the unsteadiness of the flow. The periodic unsteadiness excites the fan at a specific loading frequency. When the excitation frequencies come close to one of the blade's natural frequencies during rotation, resonance may occur. There are two frequencies responsible for resonance to occur during forced oscillations - the blade's natural frequency and the excitation frequency caused by the unsteady loading acting on the blade. The blade's natural frequency is the frequency at which the blade would vibrate" naturally" when subjected to some disturbance and let to vibrate freely. In contrast, the excitation frequency can be determined from the frequency analysis of the blade response when operating in the unsteady loading environment. There are one or more natural frequencies of all mechanical structures, and resonance can be reached when the excitation frequency reaches any of the natural frequencies [78].

While studying the problem of resonance in steam turbines, Campbell [19] introduced, what is called the Campbell diagram, also called an interference diagram. Campbell diagrams still serve as tools to portray potential solutions of blades vibrating with high amplitudes [30]. Fig. 22 shows a Campbell diagram that can be used to explain its application. The horizontal axis is the speed of rotation, and the vertical axis is the frequency. The lines passing through the origin are the excitation frequency lines, and the curves (almost horizontal lines) are the natural frequencies at different modes. At the speeds of operation, if these two curves cross each other at any point, then resonance is likely to happen at that operating condition if that frequency of excitation occurs. Typically, the blades should be designed so that the natural frequency at the design speed should have a safe margin with the frequencies at which the blades are excited.

Cousins et al. [27] analyzed a rotor that was designed for under-wing engines and

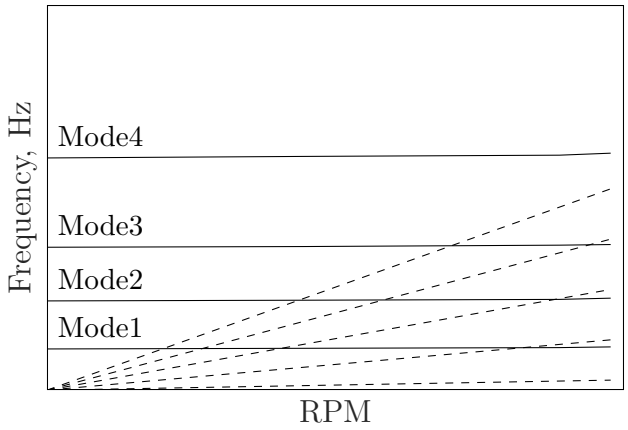

Figure 22: Notional Campbell diagram.

found that there were crossings of concern (or narrow resonance margins) at speeds near the design point. The most significant concerns were the excitation frequencies of lower order. Cumpsty et al. [30] also notes that low-order excitation frequencies pose more concerns than high-order excitation frequencies. To avoid natural frequency and excitation frequency crossing, we can take measures to change these frequencies. The excitation frequency is a function of the blade RPM and the distortion profile. Also, the blade's natural frequency can be increased by increasing its stiffness or reducing its tip mass [30]. The tradeoff in aerodynamic performance and structural integrity becomes very apparent here.

Another concern brought by the unsteady forces acting on the blade is that of high cycle fatigue. The stresses on the blades will be oscillatory - with mean stress and some alternating stress. It is necessary to analyze the pair and determine whether it is in the material's operating limit. The steady stress may be well below the tensile stress of the material. However, the alternating stresses present may cause the fan to operate outside the envelope allowed for safe operation for many cycles [113]. A simple way of representing this envelope is with a Goodman diagram that draws the envelope of when the material fails. Fig. 23 shows a conceptual sketch of a Goodman diagram, where the horizontal axis denotes the static stress, and the vertical axis denotes the

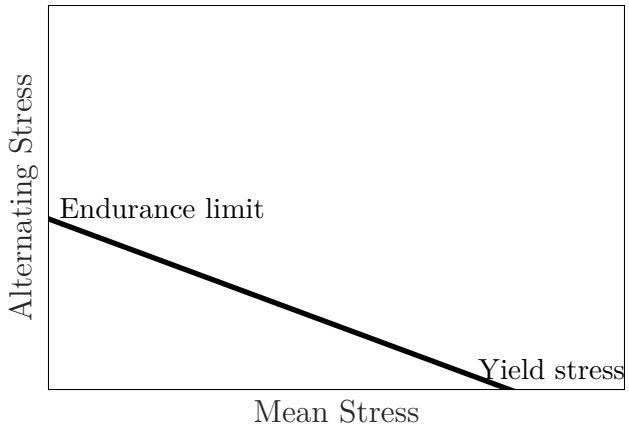

Figure 23: Notional Goodman diagram.

vibratory stress. Loosely speaking, the line joining the endurance limit (vertical axis) and ultimate tensile stress (horizontal axis) forms the Goodman line. Anywhere inside the region bounded by the Goodman line, the abscissa, and the ordinate, the blade can safely operate for a large number of cycles.

In the study done under the BLI2DTF group, it was found that the reference fan (fan for under-wing engine applications) was not able to satisfy the Goodman requirement. However, by modifying the inlet, the distortion extent was increased, and the incidence variation was minimized, which resulted in the fan achieving better results (still over the envelope though) [27]. Some structural changes were made that finally made the blade satisfy the Goodman requirement.

2.4 Fan Modeling Approaches for Distorted Inflow

The preceding section discussed the impacts of distorted inflow. This section focuses on various fan modeling efforts for distorted inflow and examines their computational efficiency, ease of integration with cycle analysis tools, and the effects captured. We discuss the following modeling approaches:

- Parallel compressor theory
- Parallel compressor theory - modifications

- Linearized distortion transfer models
- Semi-empirical approaches
- Actuator disk modeling
- Body force approach
- CFD approach

2.4.1 Parallel Compressor Theory

One of the simplest ways to model the effects of inlet distortion is Parallel Compressor (PC) theory, invented by Pearson, et al. in 1963 [120]. The parallel compressor model treats the incoming flow as two parallel streams: one distorted and the other clean with uniform properties at each stream. This model assumes constant static pressure at the exit of both sectors and sets the compressor map's operating points.

In Fig. 24, point 1 represents the low-pressure region, and point 3 represents the high-pressure region. In the presence of distortion, these two points do not overlap. Since the PC model assumes that both sectors will exit at the same static pressure, they correspond to different points on the compressor map guided by required mass flow and the static pressure convergence requirement. The mean operating point (point 2) is a weighted average of the spoiled and clean sectors.

The classical parallel compressor theory is applicable for steady-state analysis of circumferentially non-uniform but radially uniform flows. While relatively simpler, this model can reflect several distortion features. Upstream flow redistribution in the parallel compressor model can be achieved via constant exit static pressure boundary condition and the satisfaction of mass continuity. A constant exit static pressure implies non-uniform static pressure at the rotor inlet since the two parallel sectors experience unequal pressure rise. Upstream at the inlet entrance, the static pressure is uniform. The result is a mass flow redistribution as the flow propagates from the

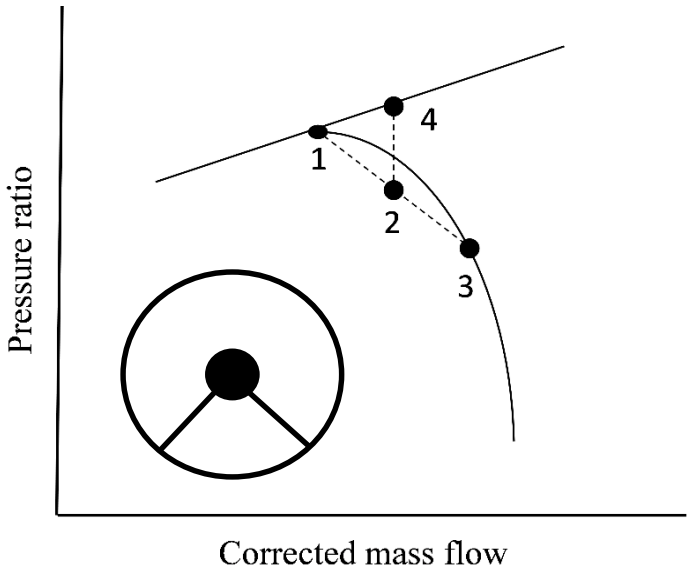

Figure 24: A sketch describing the Parallel Compressor model.

inlet to the fan face. Greitzer et al. [62], Longley et al. [103], and Greitzer [61] have demonstrated this phenomenon using parallel compressor theory.

According to classical theory, the compressor's stability boundary occurs when the low-pressure region reaches a stall stability limit. The spoiled sector is taken to stall, and its exit static pressure is computed. This static pressure requirement helps locate the clean sector's position on the map. The loss in stability pressure ratio (Δ PRS) is computed at a constant flow. This relationship is shown in Eq. 11.

$$\Delta PRS = \frac{PR_4 - PR_2}{PR_4} \tag{11}$$

Similarly, an average operating point can be computed in the presence of low and high-pressure sectors. The loss in pressure ratio and the drop in stage efficiency are computed based on the average operating point's location compared to the clean operating point using the performance maps. This modeling technique captures no unsteady behavior since it uses a quasi-steady map and assumes that the rotor response is instantaneous. The swirl distortion modeling is also not possible by using one performance map as the stage performance characteristic varies with the swirl.

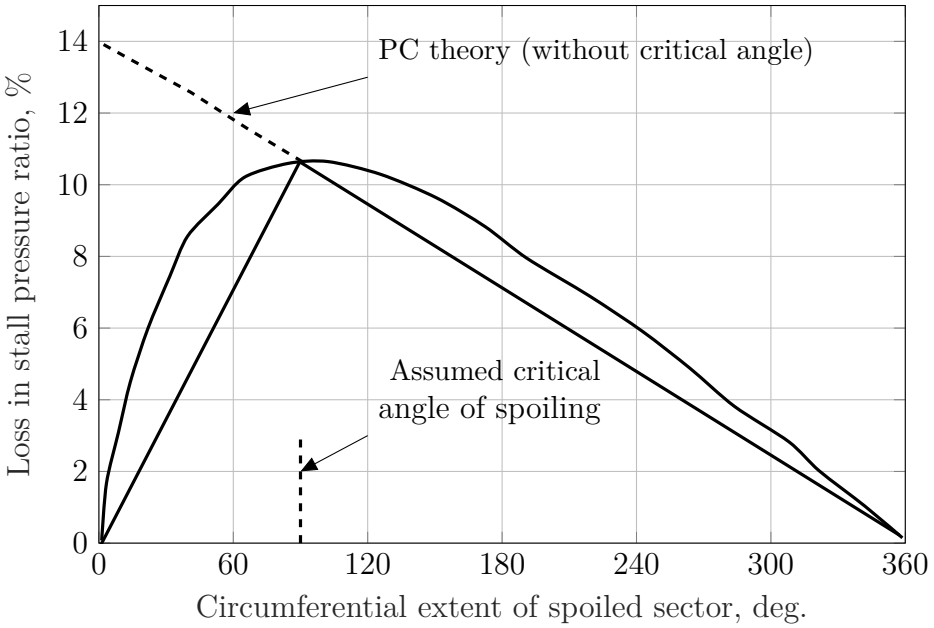

Figure 25: Critical angle concept, digitized from [155].

The individual effect on the rotor and stator cannot be separately identified as it uses a stage map and enforces a boundary condition at the stage exit.

2.4.2 Parallel Compressor Theory - Modifications

The results from basic parallel compressor theory are somewhat inconsistent with experiments. It fails to predict the correct stall margin loss below a certain angle of distortion [134]. Stall pressure ratio loss below this angle is reduced and can be seen in Fig. 25. As the distorted sector's extent goes below a certain angle, the loss in stability pressure ratio goes towards zero, unlike the classical PC model, which predicts a continuous increase.

Reid highlighted this behavior and used the concept of critical angle to mitigate this deficiency [134]. This angle needs to be determined experimentally or with higher fidelity codes for each design. The critical angle is compressor dependent, as different compressors behave differently to different inlet flow conditions as a function of the compressor blading [24].

In an attempt to understand the fundamental physics behind why different compressors respond differently, Cousins analyzed the dynamics of a complete surge cycle for an axial-centrifugal compression system [25, 28]. Different time constants were observed for different portions of the compressor, suggesting that the time constant of a blade and the circumferential extent of the applied distortion are essential parameters required to understand compressors operating in inlet distortion. These observations suggest that Reid's introduction of the critical angle concept is a way to incorporate the unsteady effects in a quasi-steady analysis.

Cousins and Davis used the parallel compressor model and included several other features such as circumferential mass redistribution, swirl effects, and dynamic response [26, 32]. The dynamic response was modeled through the inclusion of time constant. Circumferential mass flow redistribution between the rotor-stator gap was approximated using an orifice analogy. Finally, swirl effects were included by supplying multiple performance maps in the presence of swirl.

Another extension of the basic parallel compressor theory is the multiple parallel compressor theory by Mazzawy [111]. Multiple segment parallel compressor model splits the annulus into multiple segments of equal circumferential width. Similar to the classical theory, the inlet condition of any segment defines the local exit parameters. The extension by Mazzawy accounts for the circumferential crossflow of the fluid within the segments, viscous and inviscid unsteady flow effects, and dynamic instability.

Refs. [**?**,95,124] are some studies that have integrated parallel compressor model for distortion analysis. Some other examples of extending the use of a parallel compressor and combining it with streamline curvature can be found in Refs. [37, 119].

2.4.3 Linearized Distortion Transfer Models

The parallel compressor method has been used primarily to estimate the compressor performance under distorted inflow. With the limitations of parallel compressor theory

realized, several theoretical models were developed to replace or improve the classical parallel compressor theory. However, they rely on a linearized approach where the distortion's amplitude is considered to be sufficiently small such that the non-linear effects could be ignored [103].

A primary advantage of using such an approach is the ability to include several effects such as unsteady losses, deviation, and mass redistribution within the rotor-stator gaps. During the 1970s, major advances in the understanding of distortion transfer were possible because of these linearized models with the assumption of inviscid and incompressible flows [48]. Several studies [18, 41, 60, 63, 80, 85, 144] have used the linearized models and explained the propagation of the non-uniform flow through the blade rows. In addition to the limitation of not modeling 3-D effects, these linearized models are applicable for incompressible flows, high hub/tip ratio machines, and cannot predict the loss in stability margins.

Hall [76] provides a detailed description of the two-dimensional linearized model. The basic idea is to write the equations of continuity and momentum for the mean and perturbation components of the flow separately and neglect any second-order terms. Boundary conditions are then applied to solve differential equations and obtain solutions for the perturbation components at various locations.

2.4.4 Semi-Empirical Approaches

The methods discussed so far account for the fan performance using predefined performance characteristics. Instead of using any performance characteristic, semi-empirical approaches calculate the performance using the incoming flow and empirical correlations developed for the cascade of airfoils used. For uniform flow modeling, semi-empirical approaches are the first set of tools used when designing any component, such as a fan. In uniform inflow modeling, two semi-empirical methods are used: meanline/multi-meanline and throughflow methods. Variations of these methods have

been used in the literature to simulate non-uniformity effects in the flow field. Below, discussions on two such methods from the literature are provided.

2.4.4.1 Empirical Relations with Meanline Method

Valencia et al. [150] discretized the inlet region into radial and circumferential segments. They used the empirical relation and the equations of the meanline to compute the exit flow properties. When comparing to CFD solutions, it was observed that the overall trends of the distortion transfer matched. Fig. 26 shows the authors' algorithm to compute the fan performance characteristics. It can be seen that the velocity triangles obtained from the incoming flow are used to generate the blade geometry. Note that the flow characteristic for the design point is a uniform inflow. The non-uniform flow is passed in the off-design setting, where the off-design incidence and performance are computed.

While this method is efficient computationally and can be easily integrated with the cycle analysis tools, few limitations exist. First, it does not consider design optimization under non-uniform flow. Second, meanline method does not account for any radial equilibrium; therefore, no streamtube contraction can be modeled. A brief description of the meanline is provided below.

Meanline method can be used for either analysis or design. In the analysis phase, the main objective is to compute the change in flow properties across each blade row for a given set of blade row properties. In the design phase, the objective is to develop a set of blade design parameters for a set of desired flow properties. The change in flow properties within the blade rows is not computed, so the detailed geometry is neither required nor computed.

Convergence needs to be achieved in either design or analysis mode for the set of equations being solved. Two sets of equations are considered in the mean line method - one set germinates from fundamental physics while the other from empirical

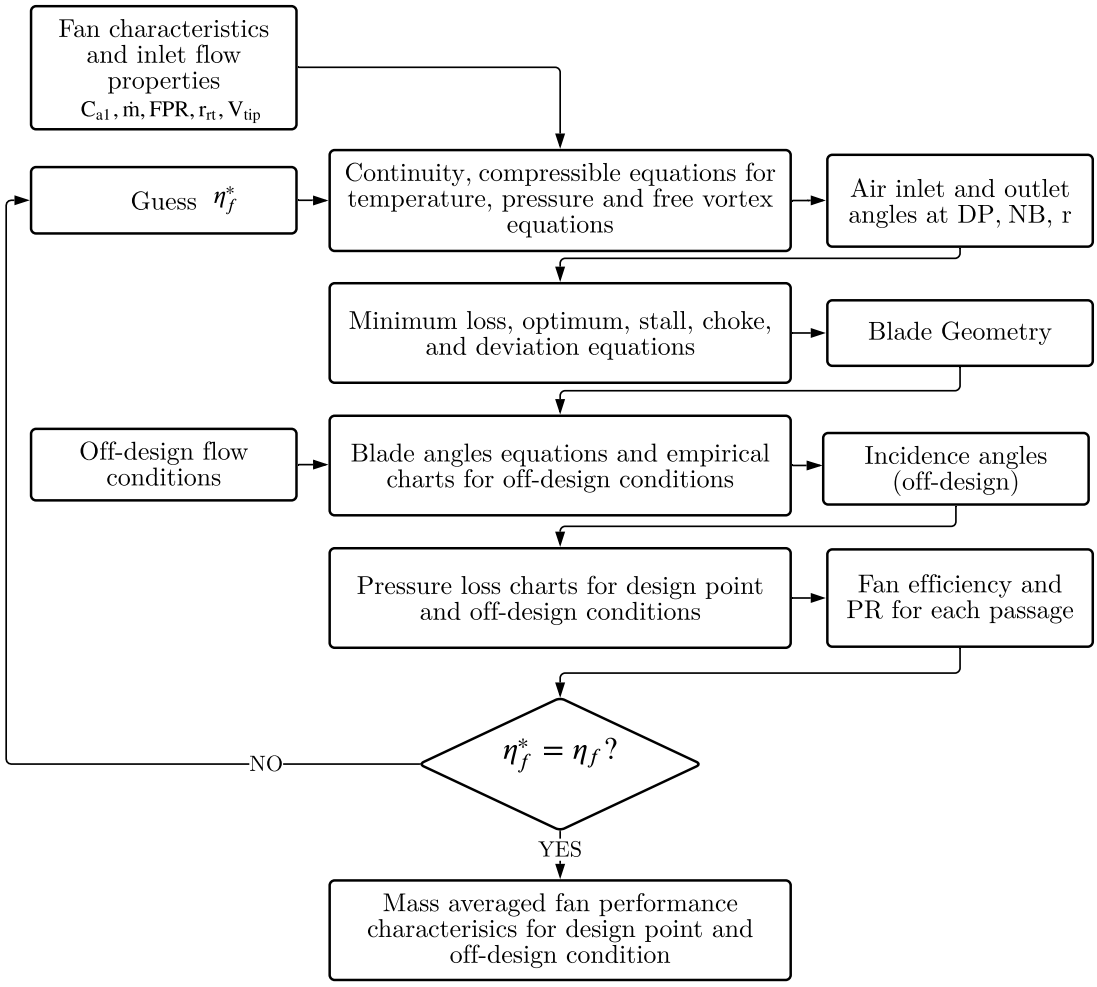

Figure 26: Discretized Miller approach for fan performance analysis, adapted from [150]

relationships. Euler's turbomachinery equation, coupled with the geometric constraints and the conservation of mass, is the set of the physical equations to be solved. These physical equations are solved for ideal flow, and no losses are accounted. Some sets of empirical relations account for the losses. The loss models generally account for the losses as functions of the blade characteristics and flow angles.

A set of seven attributes can completely describe the state of a fluid at any point [89].

(i) the mass flow rate or flux through an area normal to the meridional velocity

(ii) two thermodynamic state properties (pressure, temperature)

(iii) three velocity parameters - eg. swirl (tangential velocity), meridional angle, and axial velocity

(iv) a parameter describing location - eg. radius

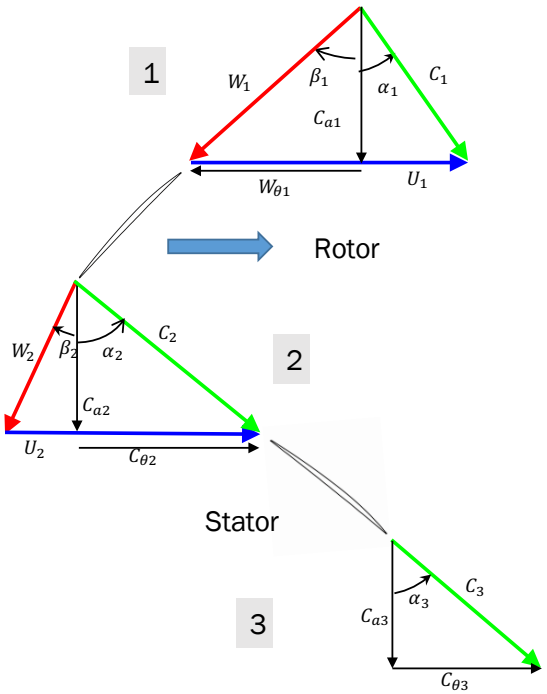

Figure 27: Blade velocity triangles at the meanline: rotor and stator.

Seven equations are needed to evaluate these seven unknowns. These equations are adapted from [89]. Refer to the velocity triangles in Fig. 27 for velocity directions.

$$\dot{m}_{\mathrm{m1}} = \dot{m}_{\mathrm{m2}} \tag{12}$$

$$h_{\mathrm{t2}} - h_{\mathrm{t1}} = \omega(r_2 V_{\theta 2} - r_1 V_{\theta 1}) \tag{13}$$

$$p_{\mathrm{t2}} = p_{\mathrm{t2\ ideal}} - f_{\mathrm{loss}}(\mathrm{args}) \tag{14}$$

$$\beta_2 = \text{blade metal exit angle} + \delta \tag{15}$$

$$r_2 = \text{machine radius at station 2} \tag{16}$$

$$A_{\text{m2}} = \text{machine area at station 2} \tag{17}$$

$$r_2 = \text{machine radius at station 2} \tag{18}$$

$$\Phi_2 = \text{machine annulus angle at station 2} \tag{19}$$

Eq. 12 maintains continuity, Eq. 13 is the Euler turbomachinery equation for enthalpy change, and Eq. 14 can include loss models that cause the actual thermodynamic state variables to differ from ideal calculations. These loss models are empirically defined. Several loss models exist in the literature that can be used as a starting point for many turbomachinery meanline studies. Eq. 15 is the assumed condition that the flow will exit the blade in the direction of the blade metal exit angle with a small adjustment of δ. Eq. 17 - Eq. 19 are the geometric constraints that need to be maintained.

2.4.4.2 Empirical Relations with Throughflow Method

Another example of a semi-empirical approach being used to compute fan performance for distorted inflows is the work by Pachidis et al. [119]. The authors used a multi-fidelity technique to integrate a 1-D thermodynamic cycle model with a 2-D streamline curvature model of the fan. The streamline curvature can handle the radial variation in the incoming flow but assumes circumferential symmetry. The viscous losses are present in the form of empirical correlations. While it can only model radial asymmetry, the streamline curvature method has been combined with the parallel compressor method to account for radial and circumferential distortion [37]. The streamline curvature method is computationally expensive than meanline/multi-meanline methods but

much faster than high fidelity CFD computations. A brief origin and working of the streamline curvature model are presented below.

In 1952, Wu [157] proposed a general theory for the fluid flow through the turbomachine. In Wu's theory, the flow's complete three-dimensional equations are satisfied by iterating between two intersecting stream surfaces. These surfaces are the S1 and S2 surfaces. The sketch of the intersecting S1 and S2 surfaces from Wu's work can be seen in Fig. 28. Although this set of equations and the associated iterations result in fully three-dimensional effects, it has not been a generally adopted method. A more common method is to use a single S2 surface together with several S1 surfaces. This technique of solving the flow using one S2 surface and multiple S1 surfaces is generally known as the quasi-3D methods [88]. In the original theory, the stream surfaces (Fig. 28) can warp and change shapes in each iteration. However, this results in challenges in implementation and computational complexity. A more common method is to make these two surfaces as the blade-to-blade surfaces (loosely, S1) and the mid-pitch meridional plane (loosely, S2). A description is shown in Fig. 29.

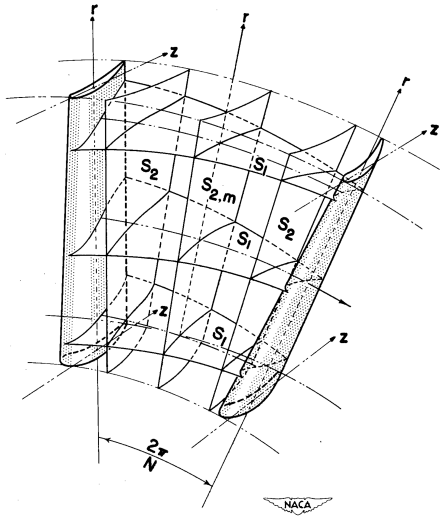

Figure 28: Intersecting S1 and S2 surfaces [157].

Wu's throughflow theory is based on the general theory, but the equations are solved only for the mean S2 stream surface [109]. This S2 stream surface can be

thought of in the pitch-wise averaged sense. The throughflow equations can be solved in multiple ways. Two types of calculations are common - StreamLine Curvature (SLC) and the matrix throughflow [36]. Both methods aim to solve the same set of equations (six equations: 1 continuity, three motion, one energy, one state) to obtain the solution to the equations of motion and the components of velocities in a turbomachine. We will only focus on the streamline curvature method, since it is a more popular approach for solving the throughflow equations in the meridional plane.

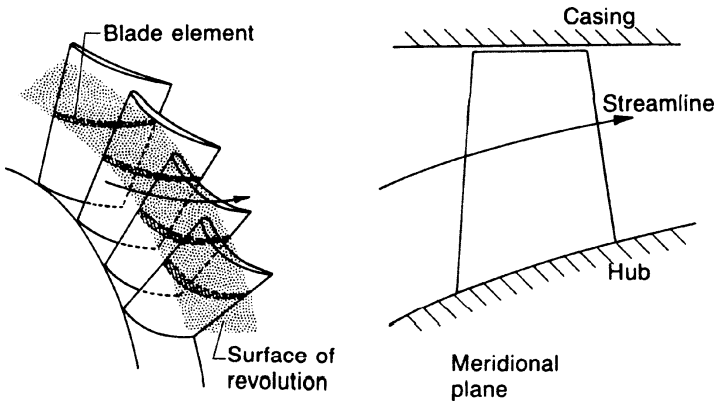

Figure 29: Two fixed surfaces representing approximate S1 and S2 surfaces [30].

The development of the streamline curvature method took place independently by Smith [143], Novak [117], and Silvester [141]. The streamline curvature method's general process is based on the assumption of the axial symmetry of the radial component of the momentum equation. It is referred to as the radial equilibrium equation. The full equation can be reviewed in [87].

The terms that contribute to the radial pressure gradient fall into one of the following categories: [87]

(i) Streamline curvature in the meridional plane

(ii) Centrifugal effect

(ii) Axial pressure gradient

(iv) Blade force effect

(v) Perturbation terms

The most considerable contribution to the radial pressure gradient comes from the fluid's centrifuging, which is the only factor considered in the simple radial equilibrium. So, the full radial equilibrium accounts for more factors to be considered and thus enhances accuracy. However, it has a computational cost associated with it. Streamline curvature computations for throughflow calculation is a widely used tool in turbomachinery design or analysis. While many assumptions and empirical relations of loss models and real gas effects are involved, it still plays a vital role in the preliminary designs of turbomachines.

Computationally, the streamline curvature method is solving a linear differential equation with constant coefficients. Fig. 30 shows a typical grid for solving throughflow equations using the SLC method. The procedure involves starting with guessing a set of meridional streamlines. Mass continuity is maintained at each axial plane, and radial equilibrium is satisfied by varying the velocity and radial location of streamlines [99]. The iterations converge when the radial locations of streamlines at all axial planes do not change further.

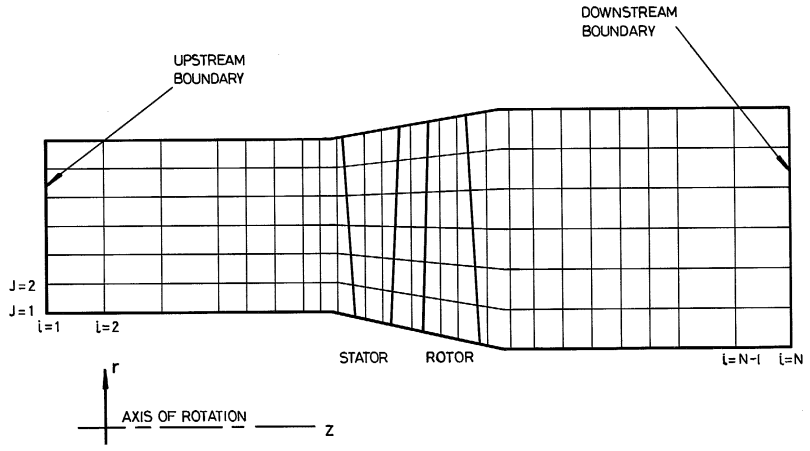

Figure 30: A typical grid for streamline curvature computation [51].

2.4.5 Actuator Disk Method

Instead of using blade rows for simulation, actuator disk theory provides a simpler model by representing the blade row's effects with a disk. The idea goes back to the momentum theory for propeller blades [30]. The earliest work of replacing the turbomachinery blade row by an actuator disk dates back to Dunham [39]. Earlier, Enrich [42], Yeh [161], and Rannie and Marble [106] had provided the solutions for a single two dimensional blade row [146]. Fig. 31 shows a sketch of the representation of the rotor and stator by actuator disks.

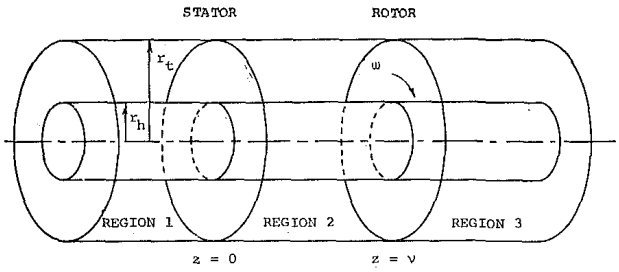

Figure 31: Rotor and stator represented by actuator disks [118].

The actuator disk represents a discontinuity in the flow field. When this concept is applied to an incompressible flow with asymmetry restricted to linearized levels, the flow equations' solution can be written as a series of Bessel functions [90]. If a fan is to be modeled, at some axial location (typically at the trailing edge or the mid-chord location), a plane actuator disk is placed, and the following conditions are applied: [90]

(i) mass continuity

(ii) radial momentum conservation,

(iii) rothalpy conservation,

(iv) specification of flow angle at the exit,

(v) specification of stagnation pressure jump

These conditions are enforces at each location in the grid. Loss and deviation models or the characteristics of the blades must be specified for the last two conditions.

The specification of the second condition implies that the radial forces exerted by the blades are neglected. The first and the third are mere consequences of the disk not storing any mass or energy.

Many studies on inlet distortion employ actuator disk theory to predict fan performance in the presence of inlet distortion, especially to model the propulsor's presence. An example is the use of actuator disk to model the BLI effect for D8 aircraft [75]. Other studies have also used the actuator disk to model fan performance in distorted inflow conditions [76, 97, 112]. However, it is only an analysis tool but can be used to understand the sensitivities of fan parameters on the propulsor performance.

2.4.6 Body Force Method

The concept of replacing the fan blades by a force field enables the lower computational cost of CFD solutions because it eliminates the need to mesh the blade geometry. This concept is the idea behind any body-force method. Fig. 32 shows body force representation of the fan blades in the CFD simulation to generate the exact turning and rise in entropy. The concept of replacing the fan blades by a force field was introduced by Marble [107] in 1964. One way to include the body force is to use the analytical model for the body force itself. The other way is to evaluate the forces via a CFD simulation [149]. The body forces are accounted for by including the source terms in the solver equations. If the analytical model is not used for the body force field, then the force is evaluated from RANS calculation of a single passage of the geometry. In the present day, this method has been extended from 2-D to 3-D modeling.

Many modifications to the body force model have been proposed following Marble's work to assess distortion impacts on fan stage performance. Gong [57] proposed an analytical body force model to assess the compressor stability problem and included unsteady effects near the stall regime. Other modifications to this model include

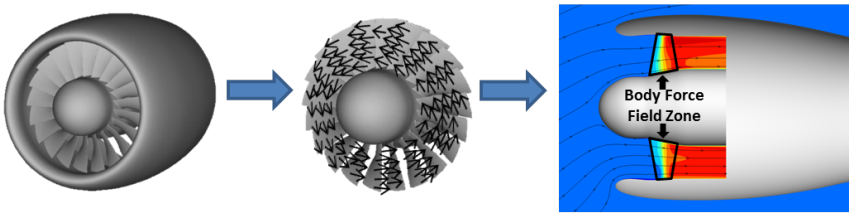

Figure 32: Body force modeling concept, reproduced from [148].

application to an air intake case by Hsiao [86], study of shock noise by Defoe [34], fan/inlet/exhaust interaction study by Peters [122], and the addition of blockage by Thollet [148]. Hall [76] employed a similar concept of non-axisymmetric turbomachinery throughflow analysis to assess the three-dimensional impacts of flow distortion on the fan's response.

2.4.7 3-D CFD Methods

While 3-D CFD methods are computationally costly, most studies focusing on performance analysis of BLI fans rely on them for close to an accurate solution. CFD methods help understand the 3-D flow phenomena that occur during distorted flow ingestion. Some CFD studies [48, 159] have shown the highly 3-D nature of the flow field upstream of the rotor. Gunn et al. [65] performed full annulus unsteady CFD to explain several fluid dynamics and sources of loss at the fan for non-uniform inflows. In another full annulus unsteady CFD study, Gunn et al. [66] showed the benefit of using non-axisymmetric stators. Cousins et al. [27] used URANS CFD solver to model the dynamic response of the blade at each point during rotation and design a distortion tolerant fan, that ultimately led to the design and experimental analysis of a distortion tolerant fan. Advancement in parallel processing and processing speed have led to the discovery of complex flow phenomena through CFD analysis of BLI fans.

2.5 Structural Analysis of BLI Fans

The fan design/analysis methods discussed in the preceding sections did not account for the fans' structural analysis when operating in non-uniform flows. It is evident that the fans operating under non-uniform flows suffer from severe vibratory stresses and may be prone to failure. Using low fidelity tools do not provide adequate results of fan structural performance. A minimal number of studies have performed structural analysis of BLI fans through finite element analysis software or actual experimentation. Bakhle et al. [7] performed aeromechanics analysis of a BLI fan, where they used 3-D RANS CFD for aerodynamic computation. For the structural analysis, the loads were obtained from the aerodynamic analysis, the root of the blade was completely constrained, and the attachment was not included in modeling. 3-D finite element analysis software was used to perform modal analysis and compute static displacement, and the dynamic analysis was based on a normal mode representation. In another study by Min et al. [116], the fan was analyzed using the cyclic symmetry finite element modeling technique. The authors modeled only one bladed disk that reduced the computational expense significantly. Fig. 33 shows the flowchart for the aeromechanics analysis procedures used by the BLI2DTF. It can be seen than the structural analysis is performed after the aerodynamic design is complete, and iterations between the structural analysis and the aerodynamic modules become apparent. The 3-D unsteady pressure forces obtained are used in the aerodamping analysis and forced response analysis to determine whether the designed blade under said operating conditions could satisfy the structural constraints.

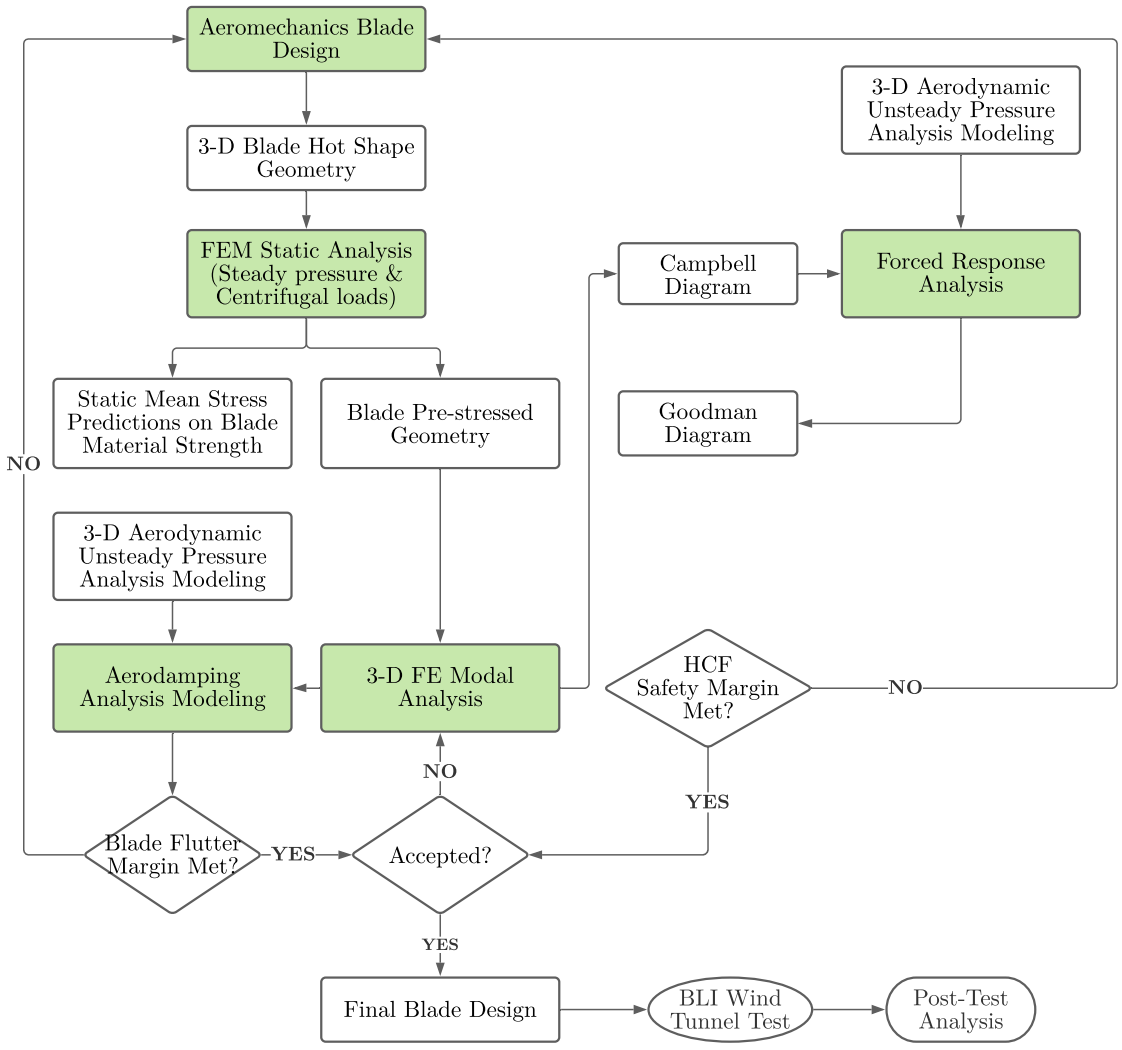

Figure 33: Aeromechanics analysis process for BLI fans, adapted from [116].

CHAPTER III

RESEARCH FORMULATION

3.1 Chapter Overview

Chapter 2 provided details on the distortion descriptors, observed effects of non-uniform flows on the fan stage, and various modeling efforts to simulate the effects. These discussions provide critical observations on the current practices and their limitations. In this chapter, some important observations from the literature are provided first. These observations lead to the gaps in the existing approaches and set requirements for the approach introduced in this thesis. The research questions and their corresponding hypotheses about the overarching research problem are also provided in this chapter.

3.2 Observations from the Literature

Fig. 34 provides a summary of the literature reviewed in Chapter 2. The columns in blue represent the various fan modeling methods. The rows in yellow represent the effects on the fan stage. If a modeling method can capture one of the fan stage (regardless of the fidelity), it is represented by a green dot in the corresponding box. The rows in green represent the capability of the modeling methods. These include if the methods have analysis/design capabilities and if they can be integrated with 1-D thermodynamic cycle tools. A checkbox in the corresponding box indicates that the modeling method is compatible. Compatibility refers not only to the modeling sense but also in the computational sense. If a modeling method is an order of magnitude more expensive than the 1-D thermodynamic cycle analysis in terms of computational time, then it is considered incompatible. Observation 1 is regarding the distortion

effects. Observation 2-5 are regarding aerodynamic modeling methods, and observation 6 is regarding the structural analysis method. Based on the analysis of fan stage effects, the following observation can be made.

	CLEAN MAP	η DROP	PC	PC EXT.	LINEAR-IZED	SEMI-EMPIRICAL	ACTUATOR DISK	BODY FORCE	CFD + 3-D FEM
NO EFFECT	●								
η LOSSES		●	●	●	●	●	●	●	●
UNSTEADY ROTOR (INVISCID)				●					●
UNSTEADY ROTOR (VISCOUS)				●					●
ASYMMETRIC STATOR FLOW					●		●	●	●
LARGE AMPLITUDE		●	●	●		●	●	●	●
DYNAMIC STRUCTURAL EFFECTS									●
DESIGN / ANALYSIS	DESIGN + ANALYSIS	DESIGN + ANALYSIS	ANALYSIS	ANALYSIS	ANALYSIS	DESIGN + ANALYSIS	ANALYSIS	ANALYSIS	ANALYSIS
COMPATIBILITY WITH 1-D CYCLE ANALYSIS	✓	✓	✓	✓		✓			

Figure 34: Summary of modeling methods from literature review.

Observation 1: Ingestion of non-uniform flow introduces several effects on the fan stage that are not present during ingestion of uniform flows

Several studies have highlighted the effects of non-uniform flow on the fan stage. Fans designed for under-wing engine applications do not suffer from the problems that arise when ingesting the boundary layer flow. The non-uniformity at the inlet entrance and the unequal work input by the fan creates a 3-D flow field upstream of the fan. This redistribution from inlet to fan creates attenuation of axial velocity, contraction of streamtube, and swirl distortion. The stability of the fan stage is also a concern for fans operating in the non-homogeneous flow field. The reduction of axial velocity due to the ingested boundary layer increases the blade incidence at some annulus regions and initiates a stall. In the worse case, this stall initiation may lead to a catastrophic failure. Distortion causes the stall to initiate at a larger averaged mass flow, thus reducing the stability margin. It is not only the stability margin that is reduced. For the distorted case, the aerodynamic losses become more pronounced, and the pressure rise capacity is reduced compared to the uniform (averaged) case. This reduction in pressure rise capacity is because of the negative slope of the compressor map.

Another effect of non-uniformity is the rotor unsteady response due to the incidence swings at the rotor inlet. Inviscid unsteadiness causes a non-instantaneous rotor response. Viscous unsteadiness is also responsible for stall delay and can be attributed to the leading-edge vortex. The effect of non-uniformity is not only limited to the rotors but also affects stator blade rows. While the rotor can attenuate some of the swirl distortion present in the flow field, the mass flow deficit persists, requiring higher turning in the stator blades creating increased losses in the stator. Apart from the aerodynamic effects, structural concerns of resonance and vibratory stresses for rotor blades are present when ingesting non-uniform flows. All these effects discussed can be ignored for the conceptual design of a fan stage for clean flows, but cannot be neglected in the design for non-uniform flows since they present as design point

effects. Given that these effects are important to capture, an observation can be made regarding the fan stage's modeling methods for non-uniform flows.

Observation 2: Most conceptual tools for fan distortion modeling are limited to the analysis of degradation in fan performance

Based on the fidelity level and amount of information required, parallel compressor, linearized distortion models, semi-empirical methods, and actuator disk method can be classified as conceptual modeling tools. Parallel compressor and actuator disk methods are useful in conceptual modeling, but they need some fan stage definition. Parallel compressor theory and its several modified approaches rely on a prescribed stage map. While the actuator disk method does not require a map, it nevertheless demands the specification of the stagnation pressure rise and the exit blade angle that can only be available given the fan stage definition. Using these methods provide a good understanding of how distortion affects the fan performance. These methods are also suitable to understand the effects of changing specific fan parameters. For example, the parallel compressor theory analysis suggests that a steeper map is better suited for distortion applications. In the same way, actuator disk methods are helpful to provide, for example, the sensitivities of span-wise variation in pressure rise on fan performance. Nevertheless, these tools are unable to create designs for a given distortion level. A consequent observation can be made regarding the conceptual methods that can design fans for a given level of distortion.

Observation 3: Semi-empirical fan design methods have been demonstrated to be integrated with cycle analysis tools, but do not capture important effects of inlet distortion

Semi-empirical approaches use the combination of physical equations and empirical relationships. The semi-empirical methods used in the literature appear in two forms

- meanline and throughflow. In their conventional form, both methods are used to handle variations in the span-wise direction and assume circumferential symmetry. Valencia et al. [150] discretized the annular area into segments in the radial and circumferential directions and applied the meanline method equations. Pachidis et al. [119] used the throughflow method by integrating with the thermodynamic cycle tool, PYTHIA, to account for radial distortion in the cycle modeling. Doulgeris et al. [37] extended this method by combining with parallel compressor theory to also account for circumferential variation.

In both modeling approaches, the fan is designed for uniform flow and does not consider optimizing the blade angles of both rotor and stator row. Besides, they do not account for rotor unsteady response. While the semi-empirical methods are the most appropriate to be coupled with cycle analysis tools, the approaches currently used do not consider optimizing the designs for distortion purposes.

Observation 4: Body force or CFD methods are mostly used to capture the complex flow phenomena that drive design decisions

Due to the limitations of other modeling approaches, the physics of distorted flows and fan performance can be best understood using high fidelity methods like body force or CFD. While other methods provide a general understanding of the different physical phenomena, high fidelity methods like body force and CFD give insights into the whys and hows of these effects. Using the body force method, Hall [76] identified the attributes of a distortion tolerant fan design by investigating the impacts of design point, span-wise loading distribution, the spacing between rotor and stator, and exit angle distribution of non-axisymmetric stators. Fidalgo et al. [48] and Yao et al. [160] described the upstream flow redistribution using CFD. In another study, Gunn et al. [66] showed the importance of non-axisymmetric stators to minimize losses. The dynamic response of the blade was modeled using URANS CFD by Cousins et al. [27].

Understanding the flow physics from these high fidelity methods helps identify the important factors to be included in the conceptual level designs. Now that we have understood the importance of these high fidelity methods, we can make an observation regarding their computational expense.

Observation 5: Computational expense of body force and CFD methods limit their integration with 1-D thermodynamic cycles and use in conceptual design of fan stage

While advances in parallel processing and computer technology have led to increased use of CFD for complex flow analysis, the computational time required by these tools is still orders of magnitude higher than that of cycle analysis.

Observation 6: The computational complexity of current methods for fan structural analysis render fan aero-structural integration computationally intractable in the conceptual design loop

Discussions from Chapter 2 suggest that most fan design methods do not account for structural analysis of the rotor blades. The concluding passage of Hall [76] states the following:

"*The results in this thesis, both for the external configuration and the internal flow performance, suggest that increased fan losses due to inlet distortion do not represent a significant obstacle to the design of a BLI aircraft configuration. A more important issue may be the aeromechanical behavior of a BLI fan rotor, because the inlet distortion result in unsteady forces on the blades. Balancing requirements between aerodynamic performance and structural integrity may be challenging because the design that produces the most uniform flow may also have the largest variations in blade force...*"

The passage above highlights the need to include the fan rotor's structural analysis

during the design process. Studies by Bakhle et al. [7], Min et al. [116], and Cousins et al. [27] included the dynamic analysis of the rotor blades through 3-D FEM tools combined with CFD methods. CFD is used to extract the unsteady loads, 3-D FEM is used to mesh the blades into finite elements, and modal analysis is used to perform the dynamic analysis. Each step of this process takes time to set up and initialize, making a parametric setup more difficult in the conceptual phase where thousands of designs are explored and analyzed. The finite element equations that are solved at each node for equilibrium, continuity, and energy conservation make the calculation process extremely long and unsuitable for use at the conceptual level.

3.3 Towards a New Approach

Observation 1 indicated that the presence of distortion presents additional impacts on the fan stage. Observation 2-6 led to the conclusion that capturing significant distortion effects in the design phase using conceptual tools were not available in the literature. Besides, high fidelity tools were incapable of performing design trade studies and could not include all these effects during design optimization. Identifying the loss sources in the fan stage and quantifying these impacts from the early design phase will provide a reasonable estimate to evaluate the overall configuration's effectiveness. The absence of parametric studies in the literature accounting for these effects during the fan's design sets the stage for the overarching research question for this thesis.

Overarching Research Question

What are the impacts of ignoring incidence asymmetry, rotor unsteady response, non-axisymmetric stators, and unsteady structural effects on a fan stage design and how much of these losses can be recovered?

Fig. 35 shows a hypothetical scenario where a fan stage is first designed for an averaged uniform flow with some predicted efficiency. Given that the designed fan did

not include the characteristic effects present in a non-uniform flow, it is expected that the fan will experience a drop in stage efficiency when operating in a non-uniform flow. What is the loss in that efficiency? Does a linear increase in distortion intensity translate to a linear drop in stage efficiency? How are the losses distributed between rotors and stators? The first part of this research question asks these questions. When these losses are taken into account, some of these losses are likely to be recovered. However, how much of these losses can be recovered? Can the percent of the losses recovered be higher for the case of higher intensity? Are structural constraints even active? If so, can a structurally sound design be created for distortion applications? The objective of the second part of this research question is to answer these questions.

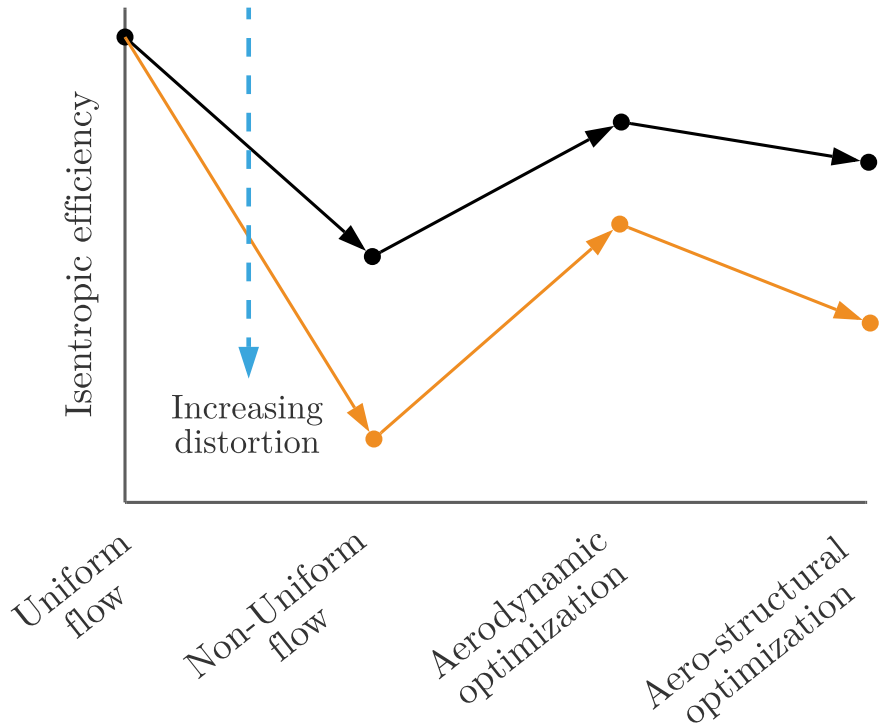

Figure 35: Notional plot showing isentropic efficiency difference through various design processes.

Based upon the discussions in Chapter 2 and the observations made in the preceding section of this chapter, it is evident that a gap exists in the current modeling fidelity

for fan design at the conceptual level. The answer to the overarching research question can be explored with the help of a method that constitutes all modeling elements discussed in the overarching research question, keeping in mind that the framework has to be computationally efficient to enable conceptual design trade-offs. A framework for fan stage conceptual design is needed that can satisfy all of the following requirements.

- **Requirement 1**: Impacts of changing the flow profile, with the same average quantities, at the inlet should be captured in a parametric fashion by the fan design framework.

  $\longrightarrow$ The distortion at the fan face is not only dependent on the flight condition but also on the operating condition of the propulsor and the shape changes in the airframe geometry. It is understood from the literature that different distortion intensities, despite the averaged flow being the same, leads to different fan degradation. Therefore, any framework created to design the fan stage should propagate any variation in the circumferential flow field to the fan performance quantification.

- **Requirement 2**: Effects of incidence swings, unsteady effects, and non-axisymmetric stators must be included and quantified.

  $\longrightarrow$ Observation 1 highlighted the additional effects present during the ingestion of non-uniform flows. Existing methods in the conceptual design do not account for these effects. Therefore, a successful fan design framework should incorporate all the above elements to capture such effects beginning in the early design phase.

- **Requirement 3**: The framework must be compatible with the integration of a 1-D thermodynamic cycle and possess the ability to replace component maps during propulsor modeling.

$\longrightarrow$ The ultimate goal is not only to design a fan stage at the conceptual level but also to integrate this framework with cycle analysis tools. In distortion, it is not convenient to represent the fan stage using conventional fan maps. Therefore, this framework should integrate with existing cycle analysis tools and used instead of the conventional component maps.

- **Requirement 4**: Dynamic structural analysis of rotor blades must be included in the framework and performed in a computationally efficiency manner

  $\longrightarrow$ Although structural concerns are generally neglected even in higher fidelity analysis, the discussions from the literature have highlighted the structural problems that rotor blades face. The design framework should perform the dynamic analysis of the rotor blades and do so in a computationally efficient manner to allow for rapid evaluation and optimization at the early design phase.

The requirements defined above stem from the lack of a parametric modeling method to design the fan stage at the conceptual level for distortion applications. Such a method is important to enabling the integration of the thermodynamic cycle analysis with fan stage design considering non-uniformity. To better understand the necessity, consider a design process for inlet, fan, and overall thermodynamic cycle for a uniform flow case. Fig. 36 shows the design process and the direction of data flow. For a given uniform flow, an inlet with a maximum pressure recovery is designed for a given set of inputs (x_1). Using the output of the inlet design (y_1), namely pressure recovery, and the fan requirements such as pressure rise, RPM, and efficiency, a representative fan map is scaled using map scaling techniques. The performance of the fan stage (y_3) allows the rest of the cycle analysis to be performed for a given set of design inputs, x_3.

The absence of feedback loops in the uniform flow design is because propulsors' presence does not affect the flow upstream. At least, that can be said for conceptual

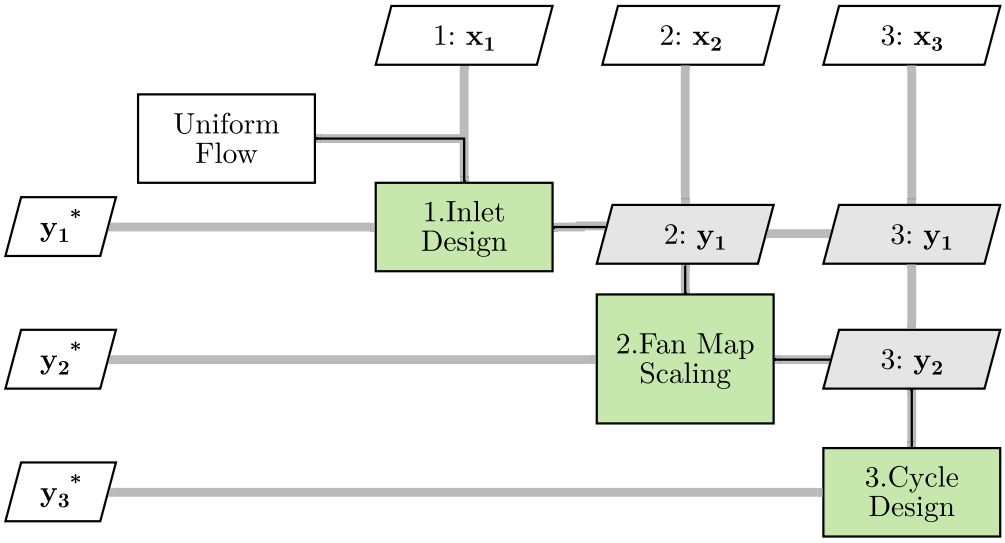

Figure 36: Inlet/Fan/Cycle design process for uniform flow.

modeling. The presence of non-uniformity introduces feedback loops in the design process. Fig. 37 shows the design process for the distorted flow conditions. Unlike the clean flow process, the flow or the inlet distortion needs to converge for the distorted case. Using an initial inlet distortion $y^t(0)$, say for the case without a propulsor, the inlet is designed. The fan stage's inclusion changes the flow redistribution as the flow traverses from the inlet entrance to the rotor inlet. Depending on whether the fan can sustain the incoming distortion level, the inlet may have to be redesigned. The fan design framework (in blue) is the focus of the work in this dissertation. When the fan design has converged, the cycle analysis can be performed. The overall cycle performance is also responsible for changing the inlet distortion at the inlet entrance. The process continues until the convergence in the target flow field (y_3^t) and y_3 can be achieved. The framework for fan design then has to be able to perform off-design analysis when run at off-design conditions instead of using maps because of the presence of non-uniform flow features such as swirl, unsteadiness, and presence of non-axisymmetric stators.

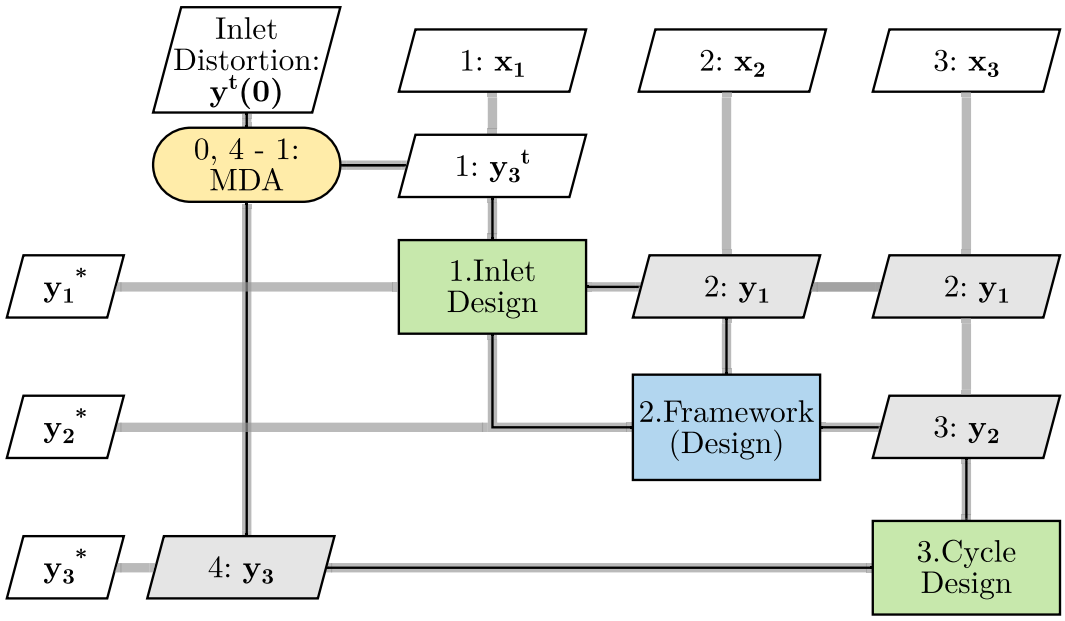

Figure 37: Inlet/Fan/Cycle design process for non-uniform flow.

The proposed framework on this thesis is an enabler for the kind of design process shown in Fig. 37 using extensions on the semi-empirical approaches. Based on the discussions above and the requirements set earlier, the research objective is stated as follows.

Research Objective

To develop a parametric fan stage conceptual design framework for inlet distortion that (i) captures the effect of flow asymmetry, incidence swings, unsteady effects, and non-axisymmetric stators; (ii) can integrate with 1-D thermodynamic cycle analysis as a replacement for component maps; and (iii) incorporates dynamic structural analysis in a computationally efficient manner, thereby allowing for rapid aero-structural trade-offs at the early analysis and design of propulsors for distorted inflows.

Chapter 4 provides a complete description of the framework introduced in this

thesis. This framework will answer the overarching and its subsequent research question and test their corresponding hypotheses. The next section segments the main research question and dissects it further.

3.4 Research Questions and Hypotheses

The overarching research question poses the question in two fronts - aerodynamic design and structural analysis. Therefore, it is natural to segment the framework into these two divisions.

3.4.1 Aerodynamics Module

The overarching research question inquires about the level of losses that the aerodynamic framework can recover. When the recovered losses are computed, the pressure rise in the stage should be equal to the desired pressure rise. Ensuring a target pressure rise is not trivial for a distorted flow field because of the flow experiencing unequal pressure rise at various spatial locations around the annulus. Recovering the losses in the flowfield also means minimizing losses in the non-uniform flow. Therefore, the overarching research question leads to a natural question regarding the design framework, which can be stated as follows.

Research Question 1

What is an appropriate design framework to maximize the stage efficiency of a fan in presence of flow asymmetry?

Observations from the literature suggested some aerodynamic effects of non-uniform flows that need to be captured. As the question suggests, the overall goal is to minimize the losses occurring throughout the stage. It is convenient to follow the fan stage in which the flow traverses through the stage. We will, therefore, first analyze how losses in the rotor could be minimized. In doing so, we will explore the composition of rotor losses and hypothesize based on the discussions on what factors could reduce

losses. As the flow exits the rotor, the rotor exit flow will be analyzed, and qualitative discussions on the need for unsteady response will be made. Finally, approaches to reducing stator losses will also be discussed. Naturally, these three areas directly stem from research question 1.

- Rotor losses
- Rotor unsteady response
- Stator losses

3.4.1.1 Rotor losses

As evident in the literature, the presence of distortion causes incidence swings for the rotor blades. While the rotor cannot control the incidence variation, it can be designed to minimize these losses. How can rotor losses be minimized in the presence of incidence swings?

Let us begin the discussion by defining the composition of rotor losses. In conceptual design, some empirical loss relations are added to describe and include the compressor's losses. The loss models used by turbomachinery companies are proprietary in nature, and although no single loss model exists, there are several loss models available in the literature [2, 5, 29, 40, 91]. All these loss models typically constitute a loss in total pressure and are used in the form of coefficients. Eq. **??**, where ' denotes isentropic quantity.

$$\bar{\omega}_r = \frac{P_{t2',rel} - P_{t2,rel}}{P_{t1,rel} - P_{s1}} \tag{20}$$

This loss term typically arises in rotors from several sources:

1. Profile loss ($\bar{\omega}_p$)
2. Endwall or clearance loss ($\bar{\omega}_{EW}$)

3. Shock loss ($\bar{\omega}_{SH}$)

The majority of the losses in subsonic cascades come from profile loss. Shock losses and endwall losses are almost negligible compared to profile loss. Therefore, we will limit the study of profile losses only when talking about rotor losses for our purposes.

In this work, rotor losses in the non-uniform flow field are analyzed in a mass-averaged sense. Let us say a non-uniform flow field at the AIP is given. The goal is to design a rotor blade that produces the least rotor loss coefficient when operating in the distorted flow field. Intuitively, it can be argued that the design point should be the averaged condition of the non-uniform flow field, where the rotor operates. This argument's rationale is that averaging the flow might minimize fluctuations in the off-design flow that the blade sees. However, before establishing the validity of this idea, let us dissect this further. For this dissertation, an empirical loss model based on the book by Aungier [5] is used.

The design profile loss is an empirical correlation of loss with equivalent diffusion factor as shown in Eq. 21. Further, the equivalent diffusion factor is a function of the design incidence (i^*), design deviation (δ^*), inlet and exit blade metal angles (κ_1, κ_2), solidity (σ), and axial velocity ratio ($\frac{C_{m1}}{C_{m2}}$) as shown in Eq. 22.

$$\frac{\bar{\omega}^* cos\beta_2^*}{2\sigma}(\frac{W_1^*}{W_2^*}) = f(D_{eq}^*) \tag{21}$$

$$D_{eq}^* = (\frac{W_{max}}{W_1})^* \frac{W_1^*}{W_2^*} = f(i^*, \delta^*, \kappa_1, \kappa_2, \sigma, \frac{C_{m1}}{C_{m2}}) \tag{22}$$

Some corrections are also made for Mach number and off-design incidence. A plot of the loss coefficient and incidence angle (in degrees) from [136] is shown in Fig. 38. The loss is not a linear function of incidence (it even seems asymmetric about the vertical axis at the minimum loss point).

Ideally, the preference would be for all off-design points to operate at the design incidence to achieve minimum losses. Since the flow field is not uniform, all off-design

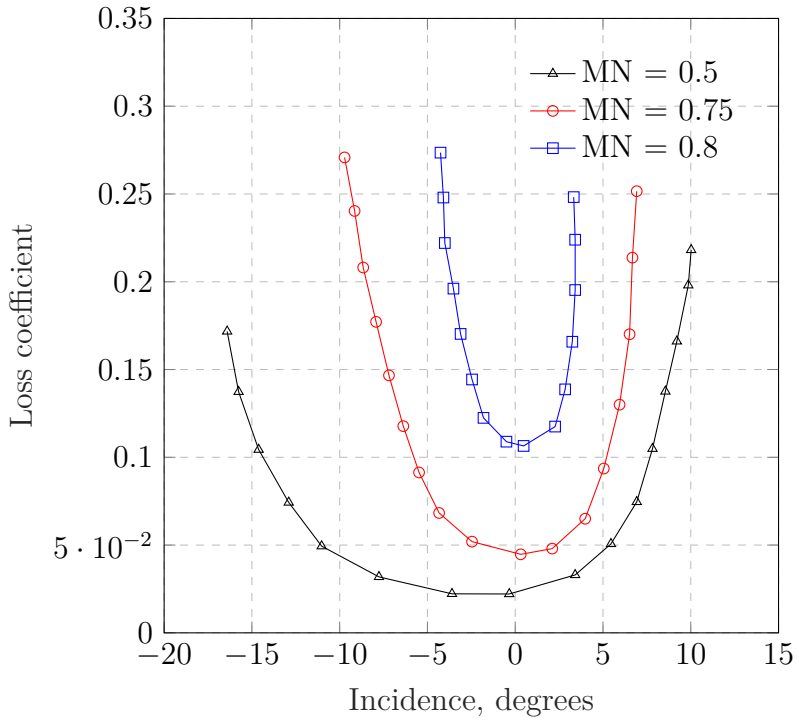

Figure 38: Variation of rotor loss coefficient with incidence angle, reproduced from Saravanamuttoo [136].

incidences cannot be equal to design incidences. An important insight can be gathered from Fig. 38. Had the losses been a linear function and the same magnitude of the slope in either direction of the minimum loss point, the losses in the off-design conditions obtained from operating the blade designed for averaged flow would also be minimal. This argument is true because all circumferential locations would contribute equally to the overall loss per unit mass flow. Because of the loss models' asymmetric and non-linear function on either side of the minimum loss point, some circumferential locations contribute more to the mass averaged rotor loss. These sectors contribute more to the overall loss, and minimizing the losses in those sectors would lead to the minimum overall loss.

From the discussions above, we understand that if designing the rotor for uniform flow, then the design resulting from the averaging the flow field is likely not optimal when operating in the distorted flow. Some other flow field defines the design flow

for the averaged condition. Searching the optimal averaged flow can be challenging. Instead, since the design point for the averaged flow is not the true operating point, we can choose to create a non-optimal rotor at the design point (averaged flow) such that the rotor has optimal performance in the non-uniform flow. This design can be achieved by varying the camber and the blade angles at the design point. We choose the design incidence as a lever that can be used to control the blade camber for simplicity. At the design point, this design incidence is a parameter that can be varied away from its optimal point, only at the design point, to create an optimal design when operating in the non-uniform flow. We expect that if we use this parameter to minimize the rotor losses, the design incidence defined in such fashion will be different for the case of uniform and non-uniform flows. A hypothesis can therefore be stated at this point regarding the minimization of rotor losses. The hypothesis is stated as follows.

Hypothesis 1.1

If the fan is designed for an averaged flow, the minimum loss design incidence for non-uniform flow departs from its optimal value for uniform flow

3.4.1.2 Rotor unsteady response

Next, we investigate the effect of unsteadiness in rotor response. As discussed in the literature, two types of unsteadiness are present in distortion conditions - viscous and inviscid. The viscous unsteadiness leads to the phenomenon of the dynamic stall and stall delay. These are complex phenomena and are challenging to model even with high fidelity tools. Therefore, for conceptual level design, the concept of stall delay is not modeled in this work. By unsteadiness, we, therefore, refer only to the inviscid unsteadiness. Inviscid unsteadiness leads to the difference in the actual response from a quasi-steady response. Fig. 39 shows a hypothetical difference in

steady and unsteady behavior. In the presence of distortion, the operating points may demonstrate a loop even in the case of no swirl distortion, and the average operating point may not lie on the steady map characteristic. Most studies in the literature assume a quasi-steady response and do not consider the effect of this unsteadiness in the modeling process. However, is the effect of unsteadiness essential to be captured for distortion applications?

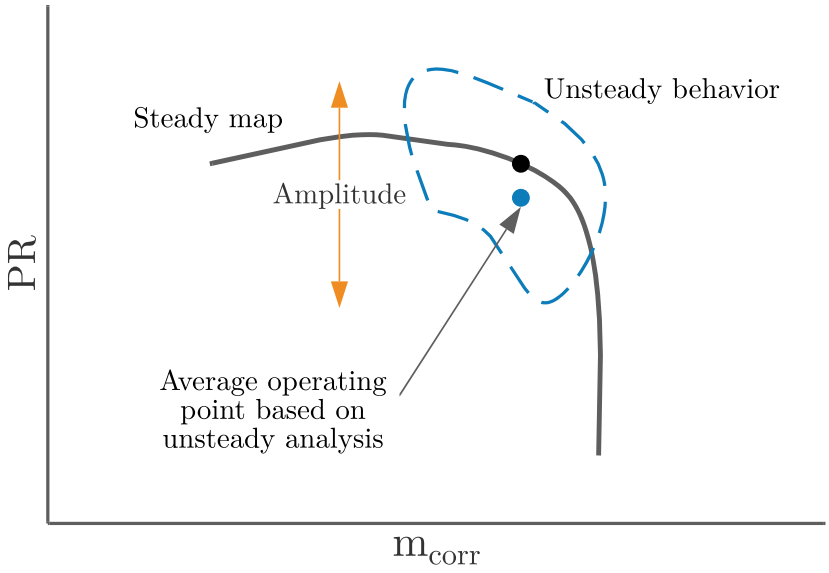

Figure 39: Hypothetical difference in quasi-steady and unsteady behavior for a pure total pressure distortion.

Most distortion type analyses assume the quasi-steady response of the rotor. Parallel compressor theory is a classical example that assumes that the compressor can be divided into two parallel compressors with the uniform incoming flow. Nevertheless, how much of the performance prediction delta is attributed to the unsteady response remains a question. Is it worth adding the complexity in the modeling process if the difference is small? In turbomachinery, the concept of reduced frequency is used to define the level of unsteadiness.

The disturbance is periodic along the circumference. This periodicity has unsteady

effects on the turbomachinery blades. The level of unsteadiness depends on two time scales. The first one is the time scale associated with the angular frequency of the unsteady motion relative to that of the blade rotation (ω). The second time scale is the one that is associated with the motion of the fluid particle to travel through the blade row (c/V), where c denotes the chord length, and V denotes the axial velocity. Instead, if we take it as a half chord, then we call this ratio as the reduced frequency (β), as shown by Eq. 23.

$$\beta = \frac{\omega c}{2V} \tag{23}$$

For a reduced frequency, much less than one ($\beta << 1$), the flow can be treated as quasi-steady - i.e., the fan response instantaneously and the response is a function of only instantaneous flow conditions. However, for higher reduced frequencies, the fan's response is also a function of the history of the flow [166].

An analogy can be made between an airfoil pitching up-down at some constant frequency and the rotor blade rotating in a distorted flow field subjected to varying incidence angles. A rotor blade at an elemental level is an airfoil, after all. Consider an airfoil pitching at an angle α given by Eq. 24. A schematic diagram in shown in Fig. 40.

$$\alpha(t) = \alpha_m + \alpha_a sin(\omega t + \phi) \tag{24}$$

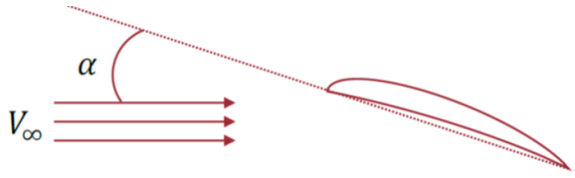

Figure 40: A pitching airfoil.

Eq. 25 shows the relationship between the lift generated per unit span and this is

a function of the circulation (Kutta-Joukowski theorem).

$$L' = \rho V \Gamma \tag{25}$$

However, the circulation, Γ, is the bound circulation, and this relationship does not consider the presence of wake in the domain. Of course, after a while, the wakes will be far downstream that the effect of wakes will be negligible and the lift predicted by Eq. 25 will be reached. When the airfoil pitches up (increases the angle of attack), the lift force takes a specific time to develop as the circulation in the wake tries to counteract the lift force generated by the bound circulation.

This sort of problem was what gave rise to the foundation of the classical theory of unsteady aerodynamics. The solution to this problem was simplified by the foundations of earlier aerodynamic theories and mostly by Prandtl's earlier works. Wagner [151] solved the problem of a step-change in the angle of attack in 1925. Similarly, in 1935, Theoderson [147] solved the same problem in the frequency domain. Von Karman and Sears [93] later, in 1938, provided a more general and elaborate way to solve the classical unsteady aerodynamics problem. All formulations, irrespective of the approach, were based on the concept of replacing airfoil and wake by vorticity distributions that satisfy Laplace's equation. The exception is the surface where singularities are placed. Besides, three other conditions are needed for a closed-form solution: (i) no penetration boundary condition, (ii) Kutta condition, and (iii) conservation of total circulation. The analytical expressions using these theories can only be applied to the flat wake assumption. However, today, many numerical techniques can be used to allow for unconstrained motion of the wakes.

The departure of the unsteady lift from the steady lift can be seen in Fig. 41. This is the same reason why blades do not respond instantaneously to changing flow conditions. While the reduced frequency is highly dependent on the value of rotating speed, when a fan is subjected to a varying level of distortion, the amplitude of the

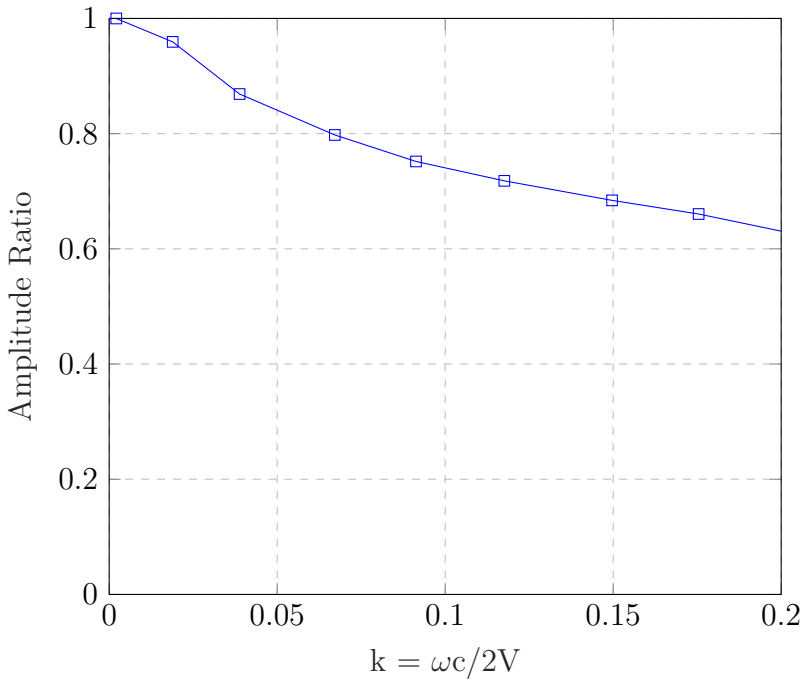

Figure 41: Amplitude ratio vs. reduced frequency for an airfoil, digitized from [10].

variation in the flow profile gets more pronounced at higher intensities. The effect is similar to the increase in α_m in Eq. 24. Li et al. point that increasing amplitude has a monotonic effect on the airfoil force coefficients [100]. Fig. 42 shows that a change of around 4° in the pitching amplitude can have a significant effect on the lift coefficient.

As the distortion intensity increases, the incidence variation that the rotor blade experiences also increases at a constant rotational speed. It can be argued that this is similar to the case of increasing amplitude for the pitching airfoil. In that regard, it makes sense that the effect of the increased distortion will impact the rotor unsteady response as the amplitude of variation changes. We expect that at a given RPM, as the distortion intensity increases, the deviation of rotor quasi-steady and unsteady response starts becoming significant. Not only will this deviation affect the overall flow profile at the rotor exit, but it will also likely increase the fluctuations on the blade forces acting on them. Since the forces take time to develop with increasing unsteadiness, lower lows and higher highs are expected in the blade force

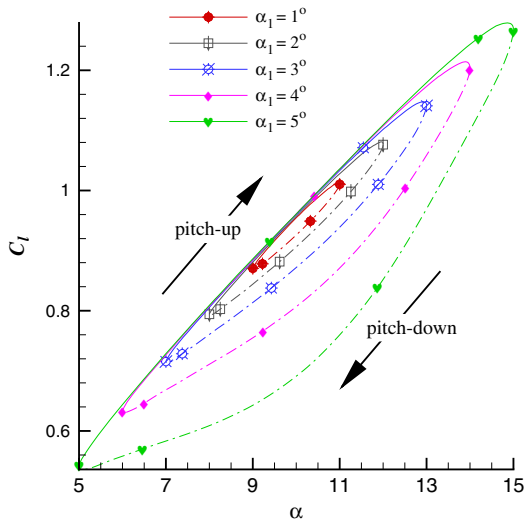

Figure 42: Lift coefficient vs. angle of attack for different amplitudes, reproduced from [100].

differences between the quasi-steady and rotor unsteady response. This qualitative understanding leads to the formulation of a hypothesis regarding rotor unsteady response.

Hypothesis 1.2

The necessity of including rotor unsteady response will be dependent on the intensity of distortion. At high distortion intensities, the effect of unsteady response on pressure rise and the blade normal force will be non-negligible

3.4.1.3 Stator losses

Gunn et al. [66] demonstrated the importance of designing 2-D and 3-D non-axisymmetric stators. While the effects of 3-D changes in lean are not in the current modeling capability of conceptual designs, the 2-D changes certainly are. Nevertheless, it is essential to incorporate the non-axisymmetric design changes in the design framework. Increasing the design degree of freedom provides more knowledge of the final design from the conceptual phase. In the literature, studies that analyze the required variation in stator asymmetry with parametric changes in distortion intensity have not been

conducted.

Non-axisymmetric design is a better design choice to minimize losses. However, how should the degree of asymmetry be enforced in the design loop? The goal is to minimize losses. As noted previously, the losses are strong functions of incidence and deviation angles. The exit swirl angle is generally used to define the span-wise input distribution. Eq. 26 shows the relationship between the flow angles, blade metal angles, incidence, and deviation. Since the flow angles (βs) are non-uniform, the blade metal angles (κs) have to be asymmetric for the incidences and deviations to be around their design values.

$$i - \delta = (\beta_1 - \beta_2) - (\kappa_1 - \kappa_2) \tag{26}$$

This understanding provides us an idea worth exploring. If we use the flow information at the rotor exit and design the stator blade angles while trying to minimize their values from the design values at each sector, non-axisymmetric stators could be achieved. It is argued that the rotor will attenuate the level of incoming swirl distortion if any, but the deficit in mass flow propagates to the stator inlet as well. Rotor blades turn the flow, and the flow exits the rotor in the neighborhood of the blade exit angle. A pure swirl distortion will likely not require a higher level of stator asymmetry, but the total pressure distortion will require stator asymmetry. A hypothesis regarding this is formally stated as follows.

Hypothesis 1.3

If the distortion intensity is higher, a larger increase in the level of required stator asymmetry will be observed. The stator asymmetry will also be observed higher for total pressure distortion than swirl distortion

The three hypotheses 1.1 - 1.3 delve into the flow physics of distortion and seek to understand each effect individually. If these hypotheses are correct, then it is

reasonable to expect that the design framework incorporating these effects will enable a design that demonstrates higher efficiency in the distorted flow field. Hypothesis 1 corresponding to research question 1 can be established based on the validity of hypotheses 1.1 - 1.3 and is stated as follows.

Hypothesis 1

If hypotheses 1.1 - 1.3 are true, then the fan stage design framework that incorporates the parametric variation of rotor blade angles, rotor unsteady response, and non-axisymmetric stators will be able to recover a significant portion of the losses in distortion that a fan designed for uniform flow experiences

3.4.2 Structural Analysis

The overarching research question was posed in terms of aerodynamic and structural effects. Now that we have looked at the aerodynamic effects, this section now examines the effect of structural analysis on the aerodynamically optimized design. Although some studies in the literature highlight structural concerns of rotor blades in a distorted flow application, the quantitative effects on fan stage design and the consequent trade-off on fan performance are lacking. Research question 2 is based on this gap and is stated formally below.

Research Question 2

How will the inclusion of structural analysis affect the design of the fan stage?

Observation 6 highlighted that the computational complexity of current fan transient structural analysis methods makes the exploration of a large design space infeasible. In order to answer research question 2, we will need to successfully analyze a design that is aerodynamically optimal. In case the design does not meet one or more criteria for structural safety, an optimization needs to be performed, and the structural

effects on the aerodynamic designs need to be analyzed in a parametric fashion. A lack of a computationally efficient yet accurate method for transient structural analysis of rotor blades used in the literature establishes the research question 2.1. In order to answer research question 2, a proper analysis method has to be modeled. Research question 2.1 formally poses that question.

Research Question 2.1

How can transient analysis of rotor blades be performed in a computationally efficient manner?

There are several ways to perform structural analysis. The following lists the available methods in the increasing order of fidelity (and thus, the computational cost).

- Strength of materials calculation [3, 105]
- Beam models [43, 158]
- Plate and shell models [53, 74]
- 3-D FEM [110]

Three-dimensional finite element models can provide good results; however, the computational cost associated with these tools makes them infeasible in the conceptual design phase. The nonlinearities associated with the transient analysis further exacerbate the issue of computational cost [**?**]. Plate methods can include detailed features and model material complexities but come with a computational burden compared with beam models. Beam models, however, cannot represent complex geometric features without making assumptions and come with inherent losses in accuracy.

To decrease the computational cost, another way to analyze is to reduce the complex structures to one-dimensional stick models. However, there are inherent trade-offs

associated with simplifications, and the result is a less accurate understanding of the developed stresses.

Hodges et al. [84] developed a set of non-linear equations for bending and twisting non-uniform beams with a motivation to develop a fast and accurate modeling environment using Variational Asymptotic Method (VAM). VAM has been developed and updated over decades and can be considered as a state of the art method for modeling complex beam-like structures. Using VAM, we can solve beam-like structures by formulating in a way that is free of assumptions. The process of VAM involves deriving the 3-D equations in terms of cross-sectional 2-D constitutive relations and a set of geometrically exact one dimensional beam equation [**?**]. The one dimensional beam equations are solved and the 1-D stresses and strains are recovered into 3-D fields using the recovery relations developed from 2-D analysis. A recent study by Gupta [**?**] showed that the results of the analysis by tools based on VAM were very close to FEM results and the computational cost associated was orders of magnitude lower than FEM model. For detailed background, theory, and calculations associated with VAM, Hodges [83] can be referred.

VAM has been successfully applied to helicopter rotor blades [164] as they are applicable to beam-like structures, such that $a << l$ and $a << R$, where a represents the cross-sectional characteristic dimension, l represents the deformation's wavelength, and R represents the radius of curvature [**?**]. The discussion that follows is the summary of VAM and have been compiled from Refs. [**?**, 71, 83, 163].

Fig. 43 shows the overall flowchart describing the beam modeling process using VAM. The process of VAM involves decoupling the three-dimensional problem. It is done by splitting the problem into 2-D cross-sectional analysis (linear) and 1-D beam analysis (non-linear). For the 2-D analysis, the cross-sectional geometry, elastic constants, and density are required. The loads and boundary conditions are supplied to the 1-D analysis. Initial twist and curvature must be supplied to both analyses.

The result of the 2-D analysis is the cross-sectional elastic and inertia constants used in the 1-D analysis. Besides, it also provides recovery relations on warping and strains to be later used. The 1-D beam analysis results in 1-D displacements, strains, and stresses. The recovery relations can then be used to recover the 3-D fields of interest.

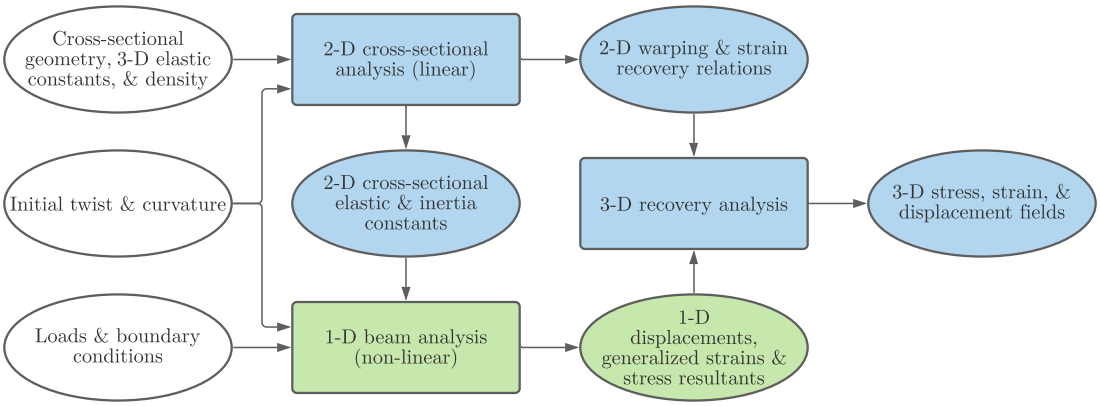

Figure 43: Beam analysis procedure using VAM, adapted from [83].

Stiffness matrix is extracted from the strain energy and recovery relations for stress-strain-displacement. The strain energy is asymptotically correct up to the second order. So, the warping expression should capture up to second-order terms. For dynamic analysis, the simulation time is divided into smaller time steps. The dynamic analysis uses information from previous time steps to compute the 3-D variables of interest at each time step. Fig. 44 shows a flowchart describing the steps used to compute 3-D stresses, strains, and displacements for dynamic analysis. Note that only the results of beam analysis at different time steps are used to recover stresses. This presents an opportunity to exploit parallel processing techniques for cross-sectional stress recovery.

Since a low hub-to-tip ratio fan can also be treated as a beam-like structure, we expect VAM to be able to model fan rotor blades as well, although this effort has not been pursued in the literature yet. Based on the discussion of different structural modeling techniques and VAM's general discussion, the following hypothesis is formed.

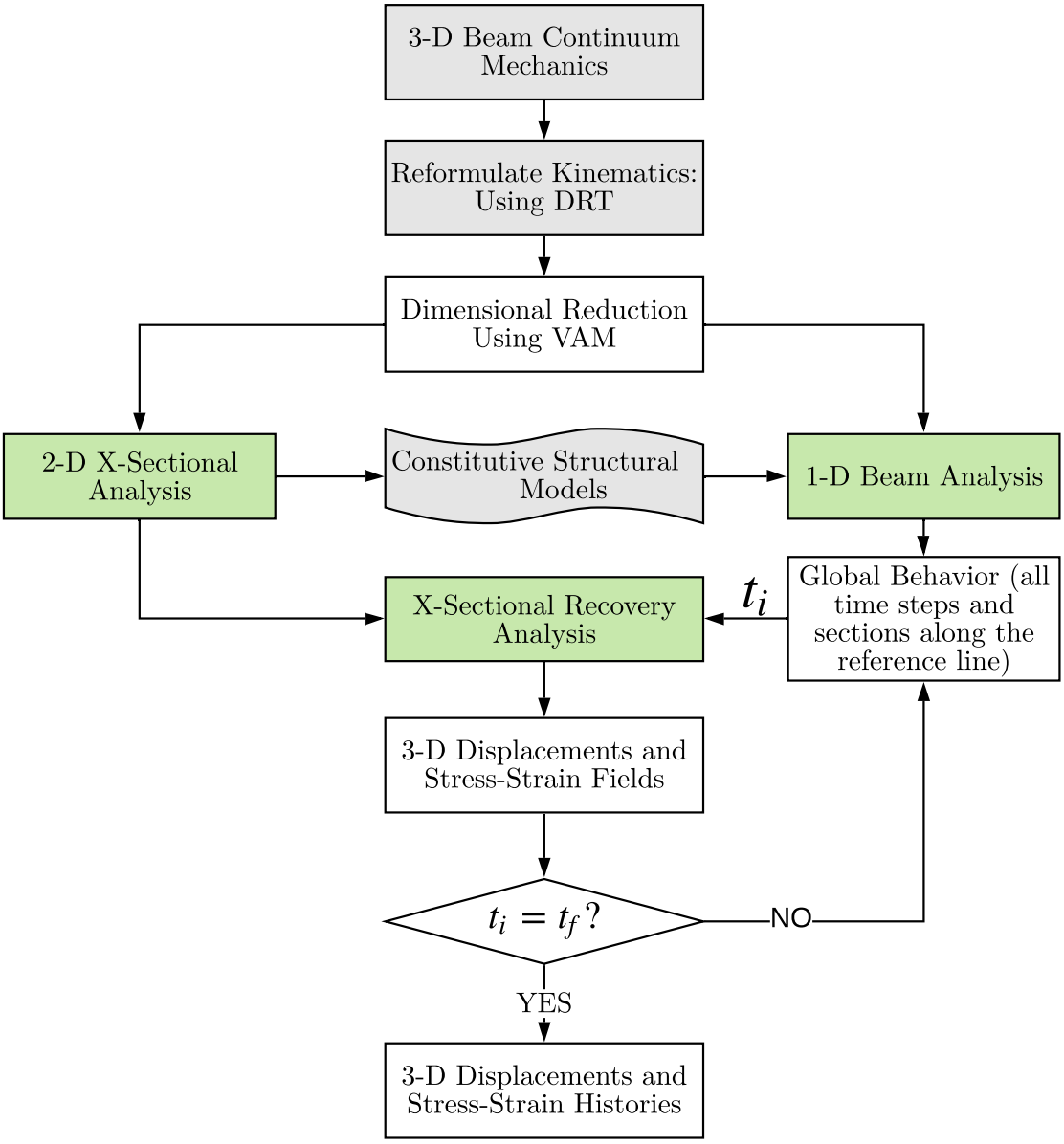

Figure 44: Flowchart representing the modeling approach for complete 3-D stress-strain-displacement history for dynamic analysis of beams.

Hypothesis 2.1

Variable Asymptotic Method (VAM) will be able to correctly predict the stresses and displacements acting on rotor blade like structures and can be used as a computationally efficient model for transient structural analysis of rotor blades

If hypothesis 2.1 is correct, then the structural evaluation of fan designs generated from the aerodynamic design framework will be computationally efficient. As evident in the literature, the designed rotor blade may likely demonstrate excessive vibratory stresses. It is also possible that the mode frequencies are in close contact with engine order frequencies that might exacerbate the structural issues. The presence of this computationally efficient method will enable rapid exploration and analysis of the design space. This capability will help evaluate the effect of varying different design parameters on the rotor blade. For each design, the effect on the structural integrity could be measured by its distance from the limit line in the Goodman diagram and the margins between the natural and engine order excitation frequencies. Thus, it is hypothesized that using we will be able to capture these effects and perform rapid analysis to identify a structurally sound design when operating in a distorted flow field. The hypothesis is formally stated as follows:

Hypothesis 2

Using VAM in the design framework will allow for rapid exploration of design space and generate a design that minimizes the amount of vibratory stresses with safe margins for operation represented in the Goodman and Campbell diagrams while also reducing the penalty in stage efficiency

Based on the understanding of research questions 1 and 2, qualitative knowledge regarding the overall aero-structural framework can be established. Suppose the aerodynamic effects mentioned in the research question 1 are accounted for in the design

process. In that case, it is expected that losses in the fan stage could be recovered to a larger degree. Based on the discussions in research question 2, it is opined that a blade with satisfactory aerodynamic and structural performance could be designed using VAM as the structural analysis tool. These arguments formally establish the hypothesis for the overarching research question formulated in this thesis. It is stated as follow:

Overarching Hypothesis

If the design framework ignores the impacts of the flow asymmetry, incidence swings, unsteady effects, and non-axisymmetric stator design, then the designed fan stage will demonstrate a reduction in isentropic efficiency. The impacts on stage isentropic efficiency become more pronounced with increasing distortion intensity. The framework that includes the aforementioned effects will help recover a large portion of these losses. The inclusion of transient analysis using VAM in the design framework will enable identification and mitigation of structural integrity concerns of the rotor blades

3.5 Design Framework for Experimental Analyses

The overarching hypothesis states that the conceptual design framework for distortion should include the effects of flow asymmetry, incidence swings, unsteady effects, and design non-axisymmetric stators. Besides, it claims that the inclusion of structural analysis in the design framework will constrain the design space. Validation of the overarching hypothesis is established by validating hypotheses corresponding to research questions 1 and 2 - hypotheses 1.1, 1.2, 1.3, 1, 2.1, and 2.

Hypothesis 1.1 claimed that a parametric variation of the rotor blade angles would lead to finding an optimal set of blade metal angles by minimizing losses. In order to test this hypothesis, an environment where a parametric variation of rotor blade angles can be implemented is required. Hypothesis 1.2 stated that rotor

unsteady response needs to be accounted for when measuring rotor pressures and forces at higher intensities of distortion. A method is needed that can compare the quasi-steady and unsteady flow behaviors. Similarly, hypothesis 1.3 asserted that a larger circumferential variation in stator blade angles is required for higher distortion intensities. As mentioned in the preceding sections, this asymmetry is generated by ensuring that the stator blade incidence is brought closer to its design value by changing the blade metal angles. Validating this hypothesis requires an environment where non-axisymmetric stators are designed for non-uniform flow. Finally, hypothesis 1 claimed that if the above hypotheses are true, the framework that includes all these effects will be able to design a more efficient fan stage. It was observed in Chapter 2 that currently, such methods do not exist in the literature. Naturally, before the experiments are carried out, it is necessary to develop such a framework.

Hypothesis 2.1 stated that VAM, a method that is generally used in the modeling of rotorcraft blades, can be used to perform structural analysis of fan blades. Establishing the validity of this statement requires creating an analysis framework for fan rotor blades using VAM. Finally, hypothesis 2 claimed that structural constraints would become active for some distortion conditions, and therefore, designs from the early stage should consider aero-structural optimization. This hypothesis can be validated if the aerodynamic framework designs violate the structural constraints when analyzed using VAM, assuming hypothesis 2.1 can be validated. Also, hypothesis 2 stated that designs that satisfy structural constraints could be created. It implies that the fan stage design framework needs to include optimization of some sort so that its validity can be tested.

From the discussions in the last two paragraphs, it is clear that a modeling environment is needed where aero-structural design and analysis of the fan stage can be performed that includes the aforementioned effects. Only then can the experiments relevant to each hypothesis can be conducted. In chapter 4, such a method is proposed

and discussed in detail. The aerodynamic design framework is built on the platform of Object-oriented Turbomachinery Analysis Code (OTAC) and is based on the NPSS language. Vartiational Asymptotic Beam Sectional Analysis (VABS) and Geometrically Exact Beam Theory (GEBT) are used as the structural analysis tools based on VAM. Modifications are made for the parametric analysis of the rotor geometry using the aerodynamic loads. The experiments related to each hypothesis are carried out in Chapter 5 and Chapter 6.

CHAPTER IV

A FRAMEWORK FOR FAN STAGE CONCEPTUAL DESIGN UNDER DISTORTION

4.1 Chapter Overview

This chapter provides a formal description of the proposed framework to satisfy the research objective and answer the research questions posed in chapter 3. Figure 45 presents the notional design structure matrix for the proposed framework. The design RPM, required pressure ratio, and the distortion profile feeds into the aerodynamic design block along with a set of fan stage design variables. The aerodynamic module is based on a semi-empirical approach. Therefore the result of this module is the generation of blade profiles at different radial segments. It also provides the unsteady loads acting on the rotor blades that are passed on to the structural analysis module consisting of VABS and GEBT - two tools based on the Variational Asymptotic Method. The following sections describe each block of the proposed framework.

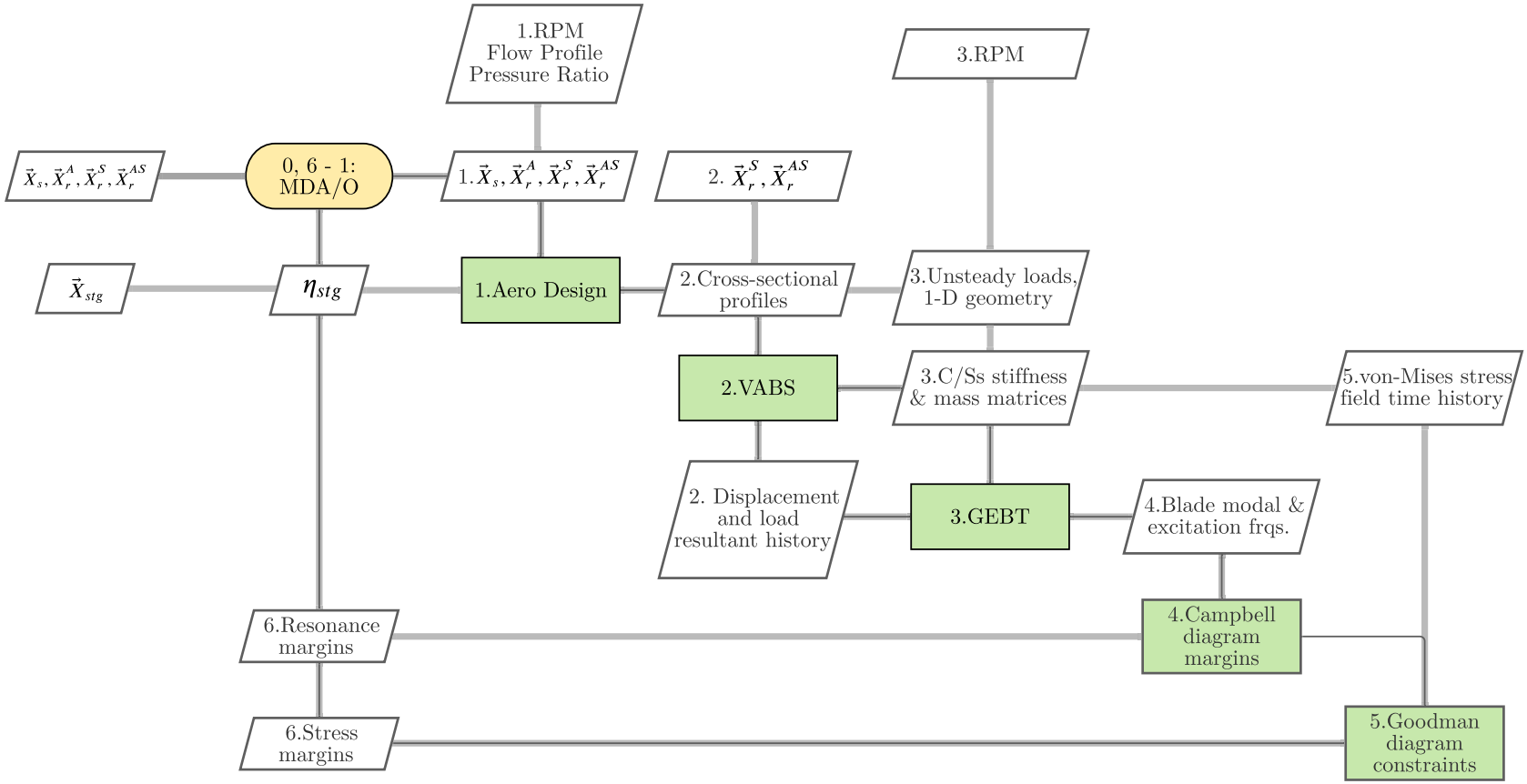

Figure 45: Extended design structure matrix of the framework.

4.2 Aerodynamic Design

The design of a fan stage can be split into several modeling elements. It is convenient to follow the flow through the fan stage to understand the modeling elements. The process comprises the following elements:

1. Rotor design considering asymmetric flow
2. Unsteady rotor response from quasi-steady response
3. Non-axisymmetric stator design
4. Convergence on target pressure rise

Below, a brief description of each step is provided. The details of the method is also presented in [125]. We assume that the flow profile information at the AIP is known. The discussed methodology is implemented on the platform of NASA's OTAC (Object Oriented Turbomachinery Analysis Code) tool [89] leveraging its already existing meanline modeling capabilities.

4.2.1 Rotor Design

The design phase starts with reading the AIP information. The description of flow properties at various spatial locations is provided. The losses in the rotor become more pronounced when operating in a distorted flow field. Therefore, it is important to come up with a design that can minimize the losses in the rotor. Designing the rotor for distortion purposes, therefore, means minimizing overall losses.

While the losses result from various 3-D effects of the flow, in conceptual design, empirical loss relations are added to describe and include the losses occurring in the compressor. Eq. 27 shows the form of loss coefficient, where 1 is the inlet, 2 is the

exit, and $'$ refers to an isentropic process.

$$\bar{\omega}_r = \frac{P_{t2',rel} - P_{t2,rel}}{P_{t1,rel} - P_{s1}} \tag{27}$$

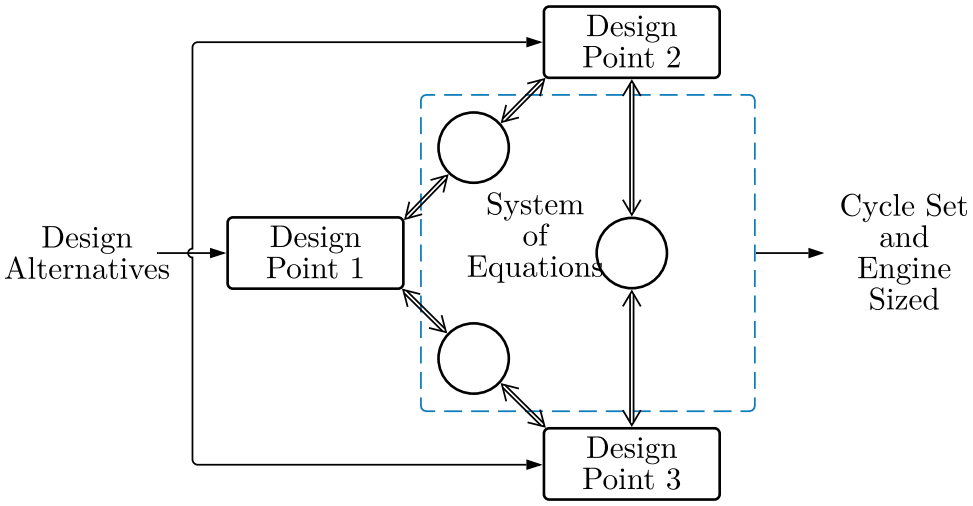

Figure 46: Concept description of multi-design point method, adapted from [139].

The modeling technique gets some inspiration from the Multi-Design Point (MDP) approach used in the engine modeling side. A concept description of the MDP approach is shown in Fig. 46. Traditionally, an engine is designed at a design point (usually cruise or sea level condition). When the engine has been optimized to work for cruise conditions, some off-design constraints are checked (for example, climb condition and sea-level thrust). When these constraints are met, the engine is considered optimal. However, an ideal condition would be to design an engine that provides optimal performance throughout the mission. Plus, it might be optimal to meet some equality constraints on off-design. That means a single design point is not necessarily the appropriate approach to design engines under these conditions. MDP method allows varying engine parameters in the design point such that the off-design constraints are automatically ensured. While not the same approach, the modeling technique employed here for rotor design is similar.

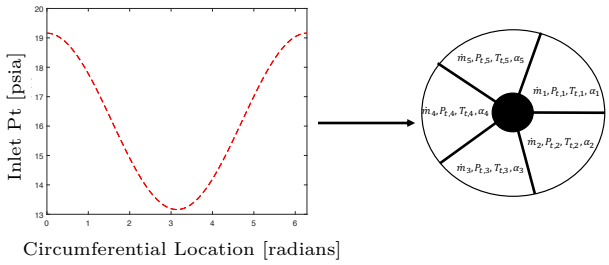

Figure 47: Representation of continuous flow profile via discrete uniform sectors.

Let us say, a non-uniform flow field at the AIP is given. A simplification is made here: the smooth non-uniformity in the flow field is discretized into circumferential sectors of uniform flow, as shown in Fig. 47. In the example shown, the smooth total pressure profile is used to locate five sectors. The goal is to design a rotor blade with an overall peak operating efficiency when operating in these discretized sectors.

First, a rotor modeling assembly (Fig. 48) is created that can operate in both "design" and "off-design" conditions. When run in the design mode, the blade angles are computed to ensure the enthalpy rise (or any other similar target parameter). The incidence and deviation are equal to the design values supplied. When run in the off-design mode, the saved geometry from the design mode will calculate the enthalpy rise and the rotor losses. A conventional multi-meanline modeling technique that uses some uniform flow condition is used to design the rotor. This designed rotor has to operate in the asymmetric flow field (the discretized sectors, as mentioned above).

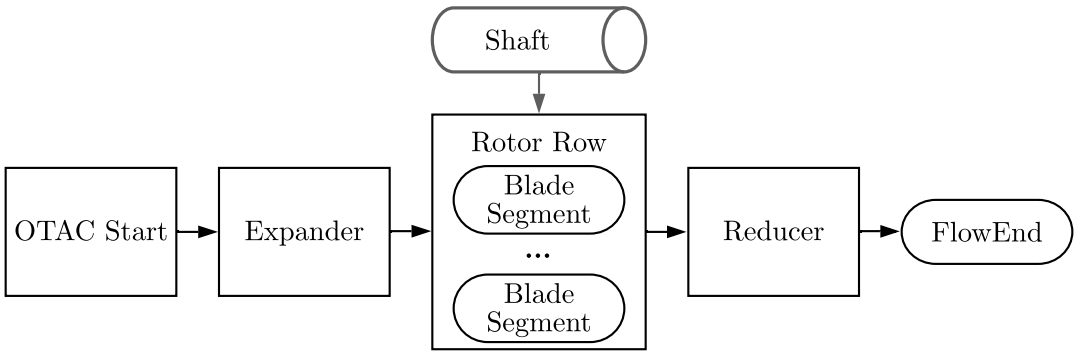

Figure 48: Schematic representing rotor design/analysis assembly.

For this proposed framework, the rotor is designed for some uniform flow. That

means the design point flow needs to account for the non-uniformities present in the true operating condition (like the one shown in Fig. 47). Understanding that the "design" point is not the true operating point allows us to produce a non-optimal rotor in the design point intentionally, but the one with minimal losses when operating in off-design points. This philosophy has been used in the framework shown in Fig. 49.

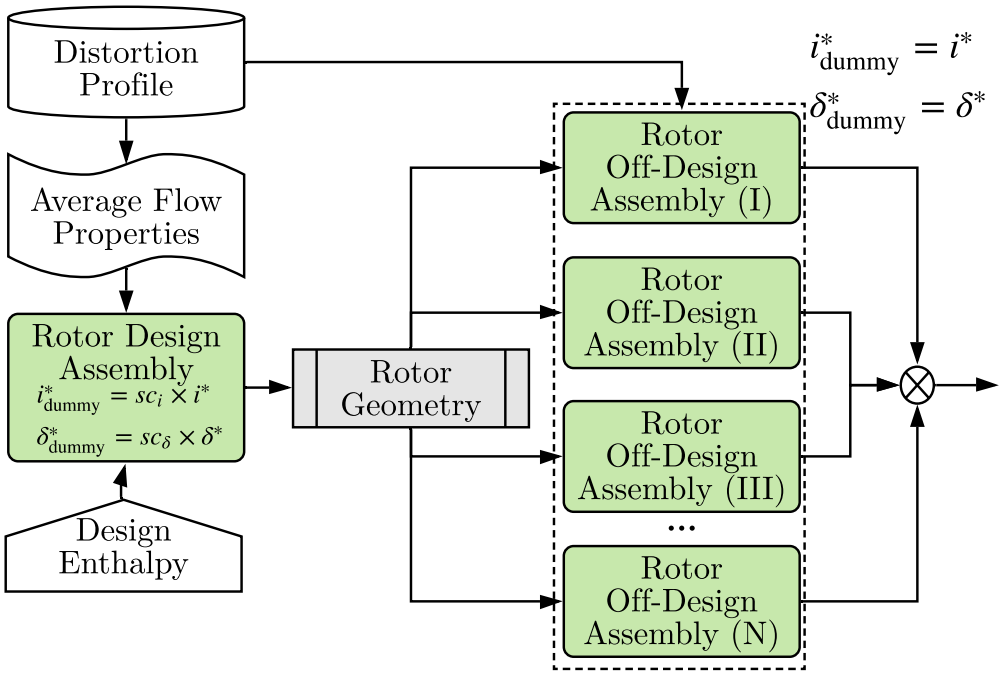

Figure 49: Rotor design framework.

First, a design point assembly of the rotor is used to design the rotor for mass-averaged flow. Each rotor design/off-design box includes a rotor assembly like the one shown in Fig. 48. The rotor is designed for a prescribed enthalpy rise. The saved geometry of that rotor is then used in off-design assemblies. Each off-design assembly has the inflow as defined from the sector averaging results, as shown in Fig. 47. The losses of these sectors are computed, and mass averaged to get the overall rotor loss. It is argued here that the rotor designed in this fashion does not necessarily lead to minimal losses, although it is intuitive to treat the design point as the average of the non-uniform flow field where the rotor operates.

Recalling that the design point is not a true operating point, two scalar parameters (sc_i and sc_δ) are introduced that modify the design incidence and deviation only in the design mode. Therefore, the loss it calculates in the design mode is not the correct form of the loss because its design incidence and deviation are not the correct ones. However, when operating in the off-design mode, sc_i and sc_δ will be set to unity, so the losses computed in the off-design mode are correct. The idea is to create the optimal blade angles when operating in off-design mode. These scalars, sc_i and sc_δ, can be varied until the minimum loss is achieved when operating in the asymmetric flow field.

4.2.2 Unsteady Rotor Response Model

The time-varying incidence angle on the fan blades as they rotate in the spatially non-uniform flow results in unsteadiness. The departure of the aerodynamic performance from quasi-steady performance depends on the per-rev distortion patterns, the extent of distortion, and the incidence variation rate.

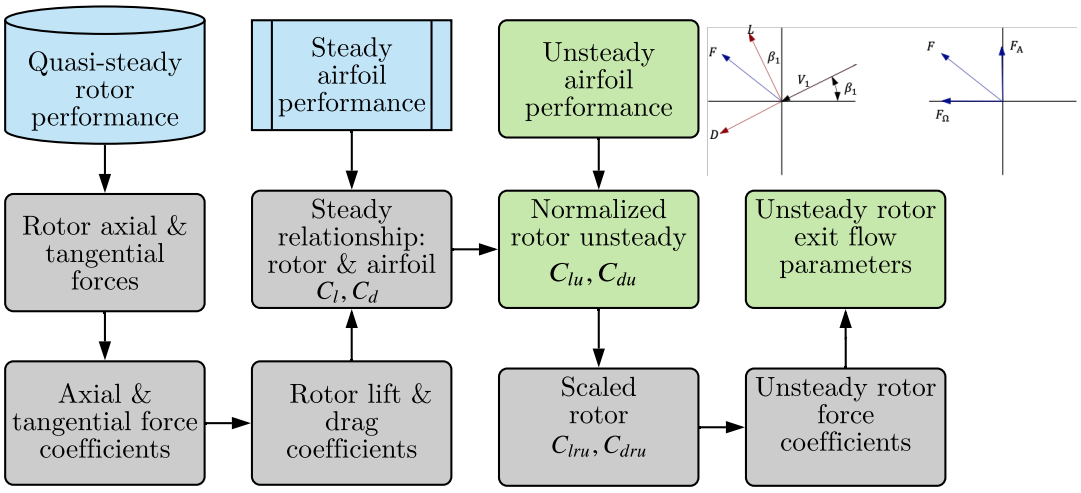

Figure 50: Unsteady approximation from quasisteady rotor performance.

We assumed that the distortion is steady-state and that the losses are accounted for by quasi-steady calculations. Herein, the work by Carta [20] is used. Although Carta's model was developed in the 1970s, the simple analytical equations used in

the unsteady formulation makes the modeling computationally elegant. This model also assumes that the quasi-steady response is already known. This assumption works very well with our modeling framework since the rotor exit performance calculated is a quasi-steady response. Using Carta's model, it becomes convenient to convert this quasi-steady response to the unsteady response. Fig. 50 summarizes the process. First, the quasi-steady performance of the rotor is computed. The flow properties at the rotor exit and inlet can be used to compute the axial and tangential forces. These forces can then be normalized and written in terms of coefficients of axial and tangential forces. The lift and drag coefficients can be obtained from force coefficients. The rotor lift and drag coefficients are compared with that of the airfoil, and a relationship is obtained. The airfoil unsteady lift and drag are computed, and the same relationship is used to obtain unsteady rotor lift and drag coefficients. The reverse calculation is performed to backtrack the unsteady force coefficients, forces, and finally, the unsteady flow parameters. Below, the description of all these steps is outlined.

Step 1: Quasi-steady rotor performance

The flow at the exit of Fig. 49 is the quasi-steady response of the rotor.

Step 2: Quasi-steady axial and tangential rotor forces

Consider a rotor rotating at an angular velocity, ω. The rotor is shown in Fig. 51 and is represented as a disk for simplicity. A fluid particle enters the rotor at a radius r_1 with absolute velocity V_1, and exits the rotor at radius r_2 with absolute velocity V_2. Here station 1 is the rotor inlet, and station 2 is the rotor exit.

The rotor's axial force is the sum of the force due to changes in axial momentum and static pressure across the rotor. Subscript A refers to the axial property. Eq. 28 gives the axial force, where F_{AH} refers to the axial force due to momentum change

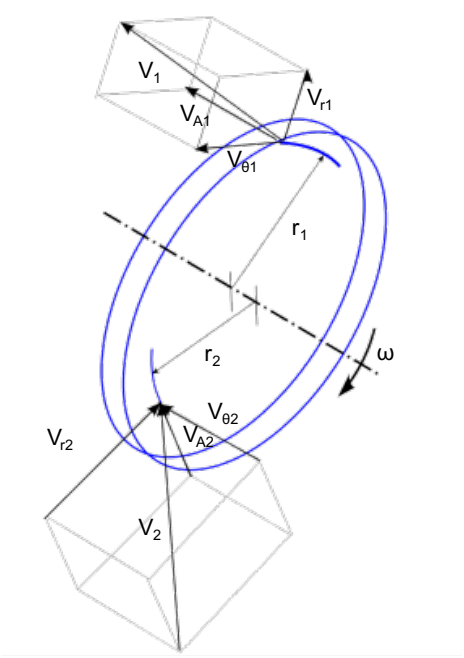

Figure 51: A rotor represented as a wheel.

and F_{AP} refers to the axial force due to pressure change.

$$F_A = F_{AH} + F_{AP} \tag{28}$$

Eq. 29 gives the axial force due to momentum change through a blade passage across a rotor, where $\Delta\dot{m}$ refers to the mass flow through the blade passage and $A_{passage}$ is the blade passage area.

$$F_{AH} = \Delta\dot{m}_2 V_{A1} - \Delta\dot{m}_1 V_{A2} = A_{\text{passage}}(\rho_1 V_{A2}^2 - \rho_2 V_{A1}^2) \tag{29}$$

Eq. 30 gives the axial force due to pressure difference.

$$F_{AP} = A_{\text{passage}}(p_2 - p_1) \tag{30}$$

From Eqns. 29 and 30, Eq. 28 can be written as:

$$F_A = A_{\text{passage}}(\rho_1 V_{A2}^2 - \rho_2 V_{A1}^2) + A_{\text{passage}}(p_2 - p_1) \tag{31}$$

Similarly, the tangential force is computed by the change in the flow's tangential momentum across the rotor, which is given by Eq. 32, where V_θ represents the swirl velocity.

$$F_\theta = \Delta\dot{m}V_{\theta 2} - \Delta\dot{m}V_{\theta 1} = A_{\text{passage}}V_A(\rho_1 V_{\theta 1} - \rho_2 V_{\theta 2}) \tag{32}$$

Step 3: Coefficients of axial and tangential forces

The axial and tangential forces computed in Step 2 can be written in terms of coefficients (Eqns. 33 and 34) by normalizing by the dynamic pressure at the rotor inlet and the reference area, which is taken as the product of blade span and the airfoil chord length.

$$C_{FA} = \frac{F_A}{\frac{1}{2}\rho V_1^2 A_{\text{passage}}} \tag{33}$$

$$C_{F\theta} = \frac{F_\theta}{\frac{1}{2}\rho V_1^2 A_{\text{passage}}} \tag{34}$$

Step 4: Conversion to lift and drag coefficients

The axial and tangential forces are represented in the vertical and horizontal axes on the right side of Fig. 52. The vectors (in red) on the left side represent lift and drag forces.

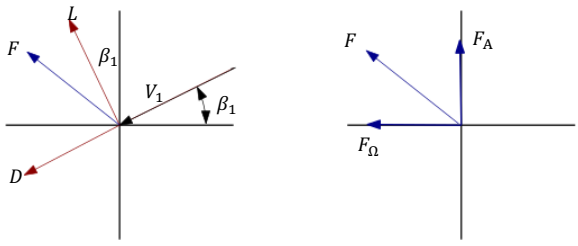

Figure 52: Relationship between axial-tangential forces and lift-drag forces.

Geometric relationships can be used to convert the axial and tangential forces to lift and drag forces in the forms shown in Eqns. 35 and 36.

$$L = F_A \cos\beta_1 + F_\theta \sin\beta_1 \tag{35}$$

$$D = -F_A \sin\beta_1 + F_\theta \cos\beta_1 \tag{36}$$

The same relationships can also be applied to the coefficients (shown in Eqns. 37 and 38)

$$C_L = C_{FA} \cos\beta_1 + C_{F\theta} \sin\beta_1 \tag{37}$$

$$C_D = -C_{FA} \sin\beta_1 + C_{F\theta} \cos\beta_1 \tag{38}$$

Step 5: Steady lift and drag of airfoil

Thin airfoil theory is utilized and is modified to account for camber and thickness to compute the steady lift characteristics. According to the thin airfoil theory, the lift slope is given by 2π. Experimentally, it has been observed that the lift curve slope is a function of thickness-to-chord (t/c) and is given by Eq. 39 [128].

$$\frac{dc_l}{d\alpha} = 2\pi \frac{[1 + (0.77t/c)]}{[1 + (0.77t/c)^2]} \tag{39}$$

According to the thin airfoil theory, zero-lift also occurs at zero degrees angle of attack. The zero-lift angle of attack ($\alpha_{L=0}$) is a function of airfoil camber as shown in Eq. 40.

$$\alpha_{L=0} = -2\theta_{\text{cam}} \tag{40}$$

From Eqns. 39 and 40, the lift at any angle of attack can be written as

$$c_l = \frac{dc_l}{d\alpha}(\alpha - \alpha_{L=0}) \tag{41}$$

A steady drag model can be assumed at this point since the purpose is to use the departure of unsteady characteristics from steady characteristics. To obtain the steady-state drag values, Carta [20] made some assumptions, and their model was in good agreement with the experimental results for drag coefficients. Since this work's focus is on the attached flow region, a constant value of c_d will be assumed.

Step 6: Scaling and relating rotor and airfoil lift and drag coefficients

From this point on, subscripts R and A will be used for rotor and airfoil, respectively. Scaling laws are introduced so that the rotor and normalized airfoil coefficients overlap in the lift curves' linear region. For the rotor, the linear region starts from the minimum loss point to the stall point. A normalized angle of attack scale for rotor can be written in the form of Eq. 42, where α_{RO} is the rotor minimum loss point, α_{RS} is the stall point, and α_R is the rotor angle of attack. The rotor angles can be computed by running the rotor in the off-design mode up to the stall point and computing these angles using the velocity triangles at that point.

$$\sigma_R = \frac{\alpha_R - \alpha_{Ro}}{\alpha_{Ro} - \alpha_{Ro}} \tag{42}$$

Similarly, Eq. 43 shows the scaling formula for the airfoil, where α_{AO} is the zero-lift angle of attack, α_{RS} is the stall point, and α_a is the airfoil angle of attack. Since potential flow theory is being used, the stall angle will be assumed.

$$\sigma_a = \frac{\alpha_a - \alpha_{ao}}{\alpha_{as} - \alpha_{ao}} \tag{43}$$

Next, the lift coefficients for both rotor and airfoil follow the same scaling laws

(Eqns. 44 and 45).

$$C^*_{LR} = \frac{C_{LR} - C_{LRo}}{C_{LRs} - C_{LRo}} \tag{44}$$

$$C^*_{La} = \frac{C_{La} - C_{Lao}}{C_{Las} - C_{Lao}} \tag{45}$$

The scaling laws above guarantee that the normalized steady lift coefficients of both rotor and airfoil coincide when plotted against the normalized angle of attack (σ). At stall point, both coefficients equal unity. So, the lift coefficients will likely not match after stall point (where $\sigma > 1$). Since we are only modeling the attached flow region, for our purposes, $\sigma < 1$. Based on this, a relationship can be constructed, as shown in Eq. 46.

$$C^*_{LR} = C^*_{La} \tag{46}$$

Normalization is not performed for the drag coefficients, but a relationship between rotor and airfoil drag coefficients is established. Nevertheless, these coefficients are plotted against the stall parameter (σ), and the relation, shown in Eq. 47, is established.

$$C_{DR} = C_{Da} + \delta_D \tag{47}$$

Step 7: Unsteady airfoil lift and drag coefficients

Experimental data for unsteady characteristics of any arbitrarily shaped airfoil is not readily available. So, to model the unsteady lift, the use of Theodorsen's theory is made to predict the unsteady behavior of the lift coefficient. At each circumferential location, the rotor inflow is given. The rotor angle of attack can be calculated in the off-design mode from the information of the blade geometry, the functional form of

which is shown in Eq. 48.

$$\alpha_R = f(\theta) \tag{48}$$

The rotor angle of attack can then be converted to the corresponding airfoil angle of attack using the relationship from Eqns. 42 and 43. The relationship is shown in Eq. 49. All the parameters except the airfoil angle of attack are known.

$$\frac{\alpha_R - \alpha_{Ro}}{\alpha_{Ro} - \alpha_{Ro}} = \frac{\alpha_a - \alpha_{ao}}{\alpha_{as} - \alpha_{ao}} \tag{49}$$

With the information of RPM, the airfoil angle of attack can be written as a function of time as follows:

$$\alpha_a = f(\theta, RPM) = f(t) \tag{50}$$

The formulation can be written in terms of a sinusoidal function of mean angle of attack (α_m), amplitude (α_{amp}), frequency (ω), and phase (ϕ) as shown in Eq. 51.

$$\alpha_a(t) = \alpha_m + \alpha_{\text{amp}}.\sin(\omega t + \phi) \tag{51}$$

It is now possible to compute the unsteady airfoil lift when pitching at some frequency. Theodorsen's theory can be used to compute the unsteady lift. This theory solves the equations on a frequency domain. Reduced frequency is used to compute the unsteady variation. The reduced frequency (k) is given by Eq. 52.

$$k = \frac{c/U}{2 \times \pi/\omega} \tag{52}$$

Theodorsen's function $C(k)$ is given by Eq. 53.

$$C(k) = \frac{\int_b^\infty \frac{\mu}{\sqrt{\mu^2-1}} e^{\iota k \mu} d\mu}{\int_b^\infty \sqrt{\frac{\mu+1}{\mu-1}} e^{\iota k \mu} d\mu} \tag{53}$$

This equation can be further written in terms of Hankel functions, as shown in Eq. 54. The phase is given by Eq. 55.

$$C(k) = \frac{H_1^{(2)}(k)}{H_1^{(2)}(k) + \iota H_0^{(2)}(k)} \tag{54}$$

$$\phi = |C(k)| \tag{55}$$

The resulting equation for unsteady lift coefficient is

$$c_{\text{lau}}(t) = -\frac{b}{U_\infty}[U_\infty \pi \dot{\alpha} - b\pi a\ddot{\alpha}] - \frac{2\pi}{U_\infty} C(k)[U_\infty \alpha(t) + b(\frac{1}{2} - a)\dot{\alpha}(t)] \tag{56}$$

Now that the unsteady hysteresis loop for the airfoil's lift coefficient is available, the unsteady drag is computed in a similar way the steady drag was calculated from the steady lift. The deviation of the unsteady drag from a baseline point will be assumed to be proportional to the lift deviation. When the unsteady lift is above the steady lift, the unsteady drag will be assumed to be below the steady drag, and when the unsteady lift is lower than the steady lift, the unsteady drag will be located above the steady drag value.

$$c_{\text{dau}}(t) = c_{\text{das}}(1 - \frac{c_{lau} - c_{las}}{c_{las}}) \tag{57}$$

Step 8: Normalized rotor coefficients from unsteady airfoil coefficients

The unsteady properties will also have a subscript u to differentiate it from its steady counterpart. First, the unsteady airfoil coefficients are normalized using the same scaling used in Eq. 45, which is re-written for the unsteady coefficient in Eq. 58.

$$C^*_{Lau} = \frac{C_{Lau} - C_{Lao}}{C_{Las} - C_{Lao}} \tag{58}$$

To convert the normalized unsteady airfoil coefficients into normalized rotor coefficients, an assumption here is that the relationship developed for a steady normalized

lift coefficient (Eq. 46) also holds for the unsteady relationship. With that, the normalized rotor lift coefficients can be extracted from Eq. 59.

$$C^*_{LRu} = C^*_{Lau} \tag{59}$$

Step 9: Rotor lift and drag coefficients

Eqns. 60 and 47 can be used to obtain the rotor lift and drag coefficients.

$$C_{LRu} = C^*_{LRu}(C_{LRs} - C_{LRo}) + C_{LRo} \tag{60}$$

The rotor lift coefficient computed above is a function of time. Once the unsteady coefficients are obtained as functions of time, they can be converted back to the circumferential location (θ) given the rotational speed.

Step 10: Unsteady axial and tangential rotor forces

The coefficients of unsteady lift and drag can be transformed into axial and tangential rotor force coefficients. These relationships can be obtained from the vector diagrams in Fig. 52 and represented in Eqns. 61 and 62.

$$C_{FAu} = C_{LRu}\cos\beta 1 - C_{DRu}\sin\beta 1 \tag{61}$$

$$C_{F\theta u} = C_{LRu}\sin\beta 1 + C_{DRu}\cos\beta 1 \tag{62}$$

The axial and tangential forces can be extracted from the coefficients, as shown in Eqns. 63 and 64.

$$F_{Au} = \frac{1}{2}\rho V_1^2 A_{\text{passage}} C_{FAu} \tag{63}$$

$$F_{\theta u} = \frac{1}{2}\rho V_1^2 A_{\text{passage}} C_{F\theta u} \tag{64}$$

Step 11: Unsteady rotor exit parameters

The axial force computed from the previous step can be split into axial force due to the momentum change and pressure change as given by Eq. 28. In order to conserve continuity, only the axial velocity is maintained constant. The force due to the change in momentum depends on axial velocity. That is why any change in axial force due to unsteadiness affects only the tangential force field. The change in static pressure can then be computed as shown in Eq. 65

$$p2 = p1 + \frac{F_{Au}}{A_{\text{passage}}} \tag{65}$$

The total pressure can be calculated using steady Bernoulli's equation (66).

$$P_{02} = p2 + \frac{1}{2}\rho_2 V_{02}^2 \tag{66}$$

The velocity triangle at the rotor exit yields the computation of absolute flow velocity at the rotor exit (Eq. 67).

$$V_{02}^2 = V_{A2}^2 + (U - V_{\theta 2})^2 \tag{67}$$

Re-arranging the Euler turbomachinery equation, the exit tangential velocity can be computed from Eq. 68.

$$V_{\theta 2} = V_{\theta 1} - \frac{F_{\theta U}}{\rho_1 A_{\text{passage}} V_{A1}} \tag{68}$$

Eq. 65 - Eq. 68 yield a final expression for the total pressure at rotor exit, which is shown in Eq. 69.

$$P_{02} = p2 + \frac{1}{2}\rho_2 \left[V_{A2}^2 + \left(U - V_{\theta 1} + \frac{F_{\theta U}}{\rho_1 A_{\text{passage}} V_{A1}} \right)^2 \right] \tag{69}$$

When the velocity and static and stagnation pressures are known, all other thermodynamic properties can be calculated from thermodynamic relationships. These

rotor exit flow properties are the inputs to the stator row.

4.2.3 Non-Axisymetric Stator Design

The unsteady flow parameters from the rotor exit are used to generate velocity triangles for stator quasi-steady performance calculations and corresponding design. The unsteady performance of the complete stage can then be calculated. Multi-point multi-meanline method is used for the design of stators. Multi-point refers to each circumferential location in the same way the rotor was treated, except in this case, the equations for design and not off-design are solved - the philosophy being that the stator has to match to the incoming flow from the rotor exit.

$$i - \delta = (\beta_1 - \beta_2) - (\kappa_1 - \kappa_2) \tag{70}$$

Eq. 70 shows the relationship between incidence (i), deviation(δ), flow angles (β), and blade metal angles (κ) at stator inlet (1) and exit (2). For symmetric stator, $(\kappa_1 - \kappa_2)$ is constant at all locations around the circumference. If the flow is symmetric, $(\beta_1 - \beta_2)$ is also uniform. Therefore, it is possible to bring the incidence and deviation towards their design values, where minimum losses occur at every location. However, if the flow is not symmetric, $(\beta_1 - \beta_2)$ is not uniform, so to bring the incidence and deviation to their design values along all circumferential locations, $(\kappa_1 - \kappa_2)$ need to be adjusted.

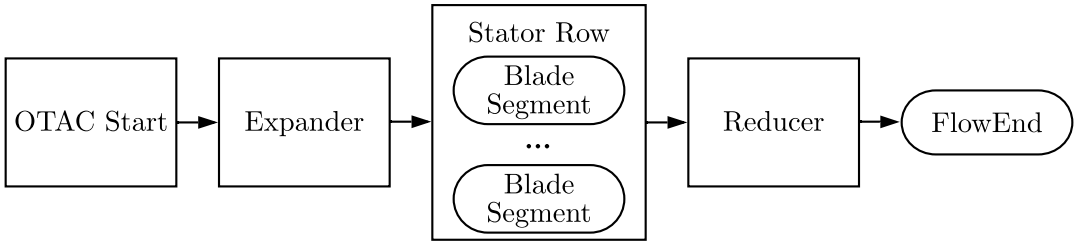

Figure 53: Schematic representing stator design assembly.

Fig. 53 shows the stator assembly for the design point in the stator design process. There are as many points as there are circumferential sectors at the AIP. The schematic diagram for the proposed approach is shown in Fig. 54. The inlet flow for the stator is the rotor exit flow field that is unsteady and non-uniform. The rationale is to design a stator for the incoming flow at each circumferential sector's location. Unlike the rotor, which was run in off-design mode, the stators are run in design mode since stators have to be designed to match the rotor's exit flow. The stator design assembly uses a multi-meanline design approach. As a boundary condition, the swirl angle at the stator exit is set to zero.

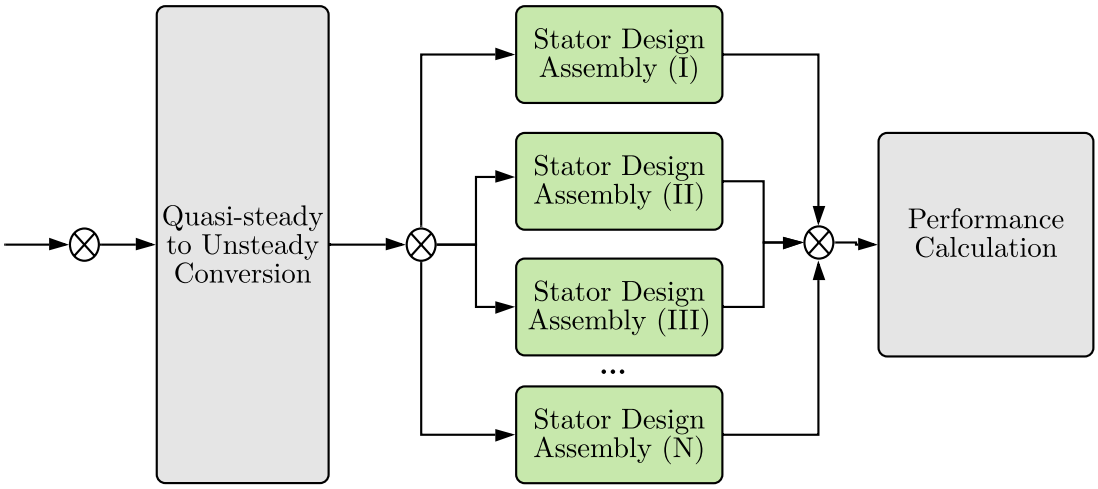

Figure 54: Stator design framework.

4.2.4 Convergence on target pressure rise

The determination of stator blade angles also provides stator exit flow information and, thus, the stage performance. In the first iteration, likely, the pressure rise across the stage does not match the pressure rise a designer might have wished to achieve in the first place. The rotor designed in Fig. 49 is designed for a certain prescribed enthalpy rise. This prescribed rise in enthalpy in the rotor design point does not

necessarily satisfy the pressure rise requirement across the stage. A Newton's solver is employed to vary that design enthalpy rise such that the actual stage pressure rise matches one that the designer wishes to achieve. The total pressure is computed using the ratio of mass averaged total pressure at the stator's exit to the mass averaged total pressure at the rotor's inlet. Fig. 55 summarizes the entire design framework. It combines all modeling elements discussed thus far and employs convergence of the overall stage pressure rise. It is important to note that the methodology outlined here does not consider any structural integrity analysis of the rotor blades operating in harsh conditions.

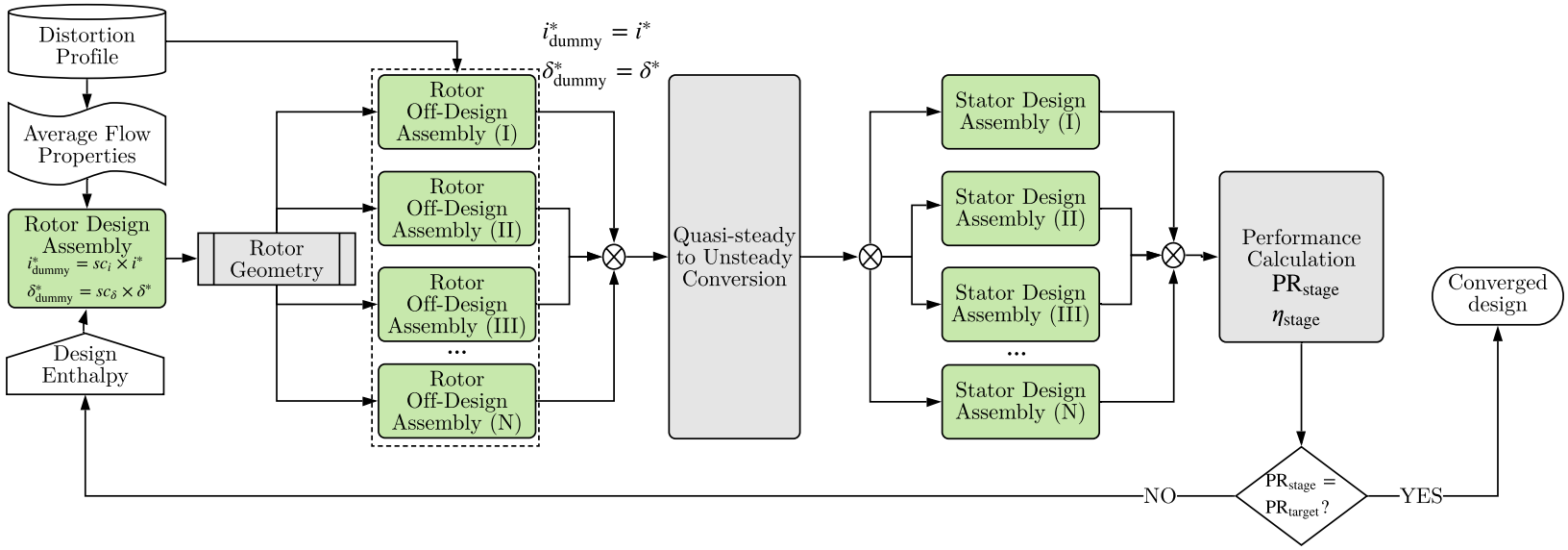

Figure 55: Fan stage design framework.

4.3 Structural Analysis

Referring to Fig. 45, after the fan stage's aerodynamic design, the next step is to perform a structural analysis of the fan rotor blades. This section describes the computation of aerodynamic loads, representation of the fan blade using the cross-sections generated from the aerodynamic design framework, followed by the discussions on the implementation of VAM and computing the structural constraints in the Goodman and Campbell diagrams.

4.3.1 Computation of Loads

The aerodynamic module provides the flow information at the rotor inlet and exit. These flow properties are responsible for exerting forces on the rotor, as explained in section 4.2.2. As seen in Fig. 45, the aerodynamic module's unsteady loads pass on to the structural module. The computation of aerodynamic loads from the flow parameters is described here.

The reader is reminded of the process of computing the quasi-steady forces in the rotor. The computation of loads is similar to the quasi-steady forces' determination, except the rotor exit flow is defined from the unsteady rotor performance module. Fig. 51 can be revisited to understand the concept. The equations are re-written below with subscript u for parameters representing unsteady rotor exit flow.

A fluid particle enters the rotor at a radius r_1 with absolute velocity V_1, and exits the rotor at radius $r_{2,u}$ with absolute velocity $V_{2,u}$. Here, stations 1 and 2 are the rotor inlet and exit, respectively.

The rotor's axial force is the sum of the force due to changes in axial momentum and static pressure across the rotor. Subscript A refers to the axial property. Eq. 71 gives the axial force, where $F_{AH,u}$ refers to the axial force due to momentum change

and $F_{AP,u}$ refers to the axial force due to pressure change.

$$F_{A,u} = F_{AH,u} + F_{AP,u} \tag{71}$$

Eq. 72 gives the axial force due to momentum change through a blade passage across a rotor, where $\Delta\dot{m}$ refers to the mass flow through the blade passage and $A_{passage}$ is the blade passage area.

$$F_{AH,u} = \Delta\dot{m}_1 V_{A1} - \Delta\dot{m}_2 V_{A2,u} = A_{\text{passage}}(\rho_1 V_{A1}^2 - \rho_{2,u} V_{A2,u}^2) \tag{72}$$

Eq. 73 gives the axial force due to pressure difference.

$$F_{AP,u} = A_{\text{passage}}(p_{2,u} - p_1) \tag{73}$$

From Eqns. 72 and 73, Eq. 71 can be written as:

$$F_{A,u} = A_{\text{passage}}(p_{2,u} - p_1) + A_{\text{passage}}(\rho_1 V_{A1}^2 - \rho_{2,u} V_{A2,u}^2) \tag{74}$$

Similarly, the tangential force is computed as the change in the flow's tangential momentum across the rotor, which is given by Eq. 75, where V_θ represents the swirl velocity.

$$F_{\theta,u} = \Delta\dot{m}_1 V_{\theta 1} - \Delta\dot{m}_2 V_{\theta 2,u} = A_{\text{passage}}(\rho_1 V_{A1} V_{\theta 1} - \rho_{2,u} V_{A2,u} V_{\theta 2,u}) \tag{75}$$

The centripetal force ($F_{r,u}$) acting along the span of the rotor can also be calculated from the angular velocity of the blades. Since the inlet and exit flow properties are different at various locations, these forces are functions of the circumferential location (θ).

$$F_{\theta,u}, , F_{A,u}, F_{r,u} = f(\theta, r) \tag{76}$$

Given Eq. 76 and angular frequency (ω), these forces can be converted to functions of time.

$$F_{\theta,u}, F_{A,u}, F_{r,u} = f(t) \tag{77}$$

As shown in Fig. 55, the loading behavior is different for every design since the rotor exit flow parameters are defined from work provided by the blades. In the following section, we discuss the fan blade's geometrical representation produced from the aerodynamic design block.

4.3.2 Geometrical Representation of the Fan Blade

The blade design is achieved by solving radial equilibrium equations, mass continuity, and energy conservation at each radial blade segment. The result is the determination of blade angles at the exit and the inlet, the stagger, and the stream's radial location. Fig. 56 shows the blade angles at the inlet and the exit. A double circular-arc airfoil is used to create the camber line, and the thickness to chord ratio defined from the aerodynamic module is used to draw the pressure and suction sides of the airfoil.

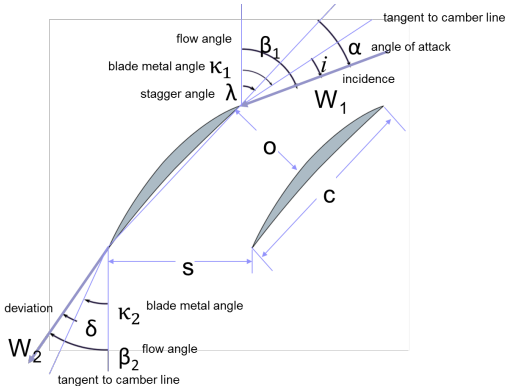

Figure 56: Cross-section definition from blade angles.

This process is repeated for each cross-section. There will be as many cross-sections as the number of radial segments used in the design process. The cross-sections can be stacked, and a 3-D skeleton of the blade geometry can be formed, as shown in Fig. 57.

We choose the centroidal axis as the default stacking option to balance the centripetal force acting due to the blade rotation.

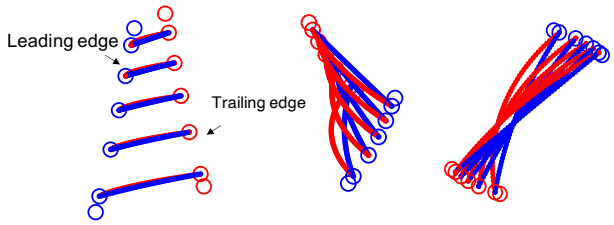

Figure 57: 3-D skeleton of the blade: hub to tip [left], obliqueness [center], twist [right].

Lofting these cross-sections, a full 3-D structure of the blade can be formed. An example is a blade shown in Fig. 58 that was lofted using the 3-D skeleton from Fig. 57 in 3-D CAD software.

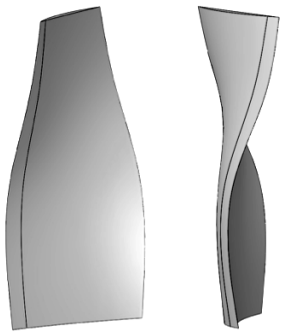

Figure 58: Lofted 3-D model of the fan blade.

A brief discussion on the required number of radial segments is warranted at this point. The representation of the blade geometry is made through the specification of the cross-section profiles. Since the fan blades have significant amount of twist, at least three segments are recommended to perform structural analysis. This ensures that a minimum level of blade twist and curvature is captured. In cases of design optimization, when several thousand cases are analyzed, it is also recommended that the final design is re-analyzed using higher number of segments (8 - 10) so as to remove any interpolation errors in the blade. This process also helps create a balance between the computational expense and accuracy.

4.3.3 Variational Asymptotic Method

Variational Asymptotic Method was developed by Hodges et al. to performn structural analysis in a computationally efficiency manner. Unlike many existing models, beam theories, and commercially available 3-D FEM tools for analyzing complex structures, the VAM's use is proposed [12]. It allows for a beam-like formulation that is free of ad-hoc assumptions. This approach is synergistic. The computationally inexpensive nature of beam modeling using the VAM is combined with modeling procedures using finite sectional elements to obtain reliable models for high-fidelity, multi-physics simulations. The process of VAM involves deriving the 3-D equations in terms of cross-sectional 2-D constitutive relations and a set of geometrically exact one-dimensional beam equation [70]. The one-dimensional beam equations are solved, and the 1-D stresses and strains are recovered into 3-D fields using the recovery relations developed from the 2-D analysis.

Rajagopal [130] have made some recent advancements to the cross-sectional analysis with regards to taper and cross-sectional obliqueness. Chen [22] presents a comprehensive validation study for a VAM-based beam analysis against 3-D FEM for rotor blade structures and thin-walled beams by Gupta et al. [68]. Gupta et al.'s further developments to expand the scope led to a framework for analyzing aperiodic and inhomogeneous beams [72, 73]. As far as developments in GEBT are concerned, Wang [152] has made substantial improvements, and Hodges et al. [135] have made contributions by using advanced rotation parameters and implementing the capability to understand the mechanical behavior of multi-functional materials, respectively. Similarly, Sarojini et al. [137] generalized the work of Gupta et al. [73] by formulation the stiffness matching problem as an optimization statement.

The discussion of VAM is incomplete without the mention of some of its limitations. There are various sources of errors that may arise during the computation of stresses and strains using VAM. The first error stems from the neglecting the higher order

terms in the expansion of the strain energy functional. The expansion up to the second order provides the Timoshenko solution, so the errors due to this should be negligible. The second source is due to the nature of the solutions. Since the 3-D solutions in VAM are obtained from 2-D and 1-D analyses respectively, these solutions lose some information due to the conversion of 2-D and 1-D to 3-D solutions and vice-versa. While other beam theory solutions neglect ad-hoc assumptions, VAM does not assume those. In addition, VAM also incorporates the solutions of warping variables. However, the boundary conditions are applied on the average condition. For example, if the boundary condition on the root of a cantilever beam is applied, the average displacement at the root is enforced to zero. Therefore, it is not advised to use VAM to predict the responses on the boundaries. Finally, another limitation could arise from the application of pinching loads. In case of the airfoils of blades, the loads act on both suction and pressure sides. However, during the analysis, the pinching loads are represented as net equivalent load. In cases when both loads are comparable in magnitude, the global deformation modes are negligible, but the stresses are not. Therefore, in such cases, the errors due to the pinching loads become significant. But, if the forces are significantly different, the global deformation modes are dominant and the pinching loads have inconsequential effects.

Fig. 59 shows the overall process of the set of equations to be solved using VAM. The overall analysis is divided into three parts. The first part deals with the 2-D cross-sectional analysis. This phase aims to determine the solution of the warping variable, stiffness matrix, and mass matrix for each cross-section under consideration. The warping variable is determined by minimizing the strain energy functional of the cross-section. Once the minimized strain energy is obtained using the warping variable solution, it is differentiated to obtain the stiffness matrix.

Similarly, the mass matrix can be obtained from the differentiation of kinetic energy. The second phase is the 1-D non-linear analysis phase. Here, the stiffness

and mass matrices computed from the cross-sectional analysis are used in conjunction with Hamilton's principle to solve for forces, moments, and momentum. The result of this phase is the 1-D displacement solutions. A transient analysis will provide the displacement at each time step. The final phase is the recovery of 3-D displacements, strains, and stresses. The 3-D displacements at each node of the cross-sections can be extracted using the 1-D displacements and warping solutions. The displacement solutions and the solutions of forces, moments, and momentum yield 2-D strains. The 3-D strains, and consequently, 3-D stresses, are obtained by transforming the 2-D strains to 3-D strains using warping variables. The recovery needs to be performed for the solution of each time step to obtain the evolution of stresses and strains.

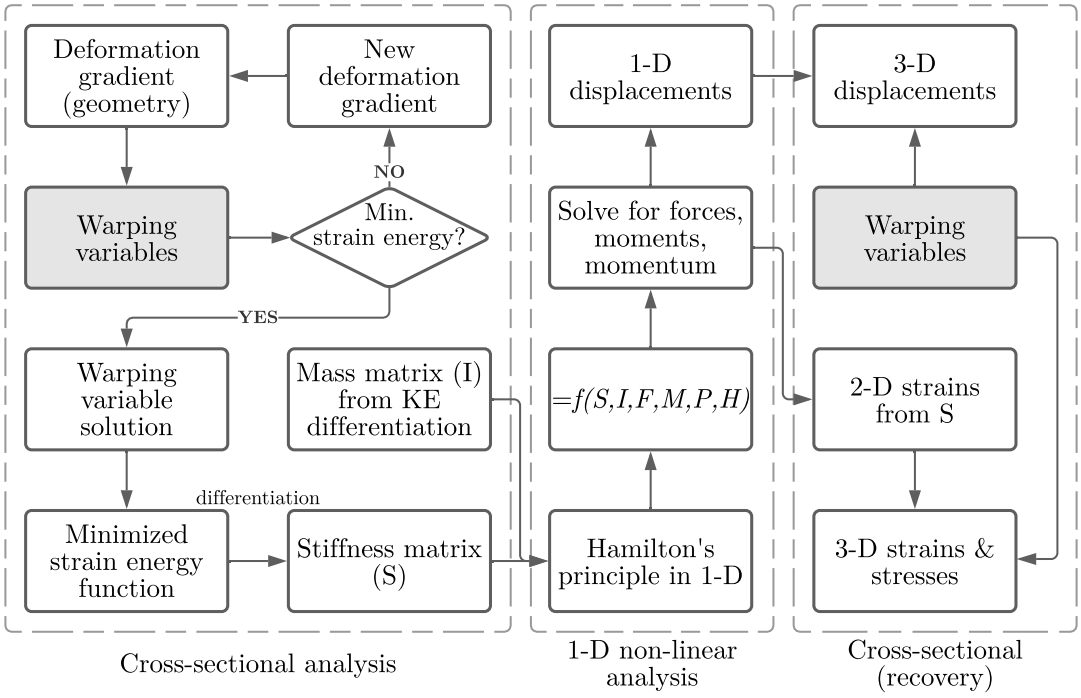

Figure 59: Process flowchart describing the sequence of calculations for VAM.

Variational Asymptotic Beam Section (VABS) [163] and Geometrically Exact Beam Theory (GEBT) [162] are two efficient tools for 2-D cross-sectional analysis and 1-D beam analysis, respectively. VAM employs asymptotic expansion of the energy

functional (instead of a system of differential equations [14, 15, 94]) in terms of the small parameters (a, l, R) and makes the modeling more compact and variationally consistent; i.e. all variables follow naturally from a minimization problem based on the variational principle.

In this thesis, the tools developed from equations presented in two references [163] and [162] Viz., VABS, and GEBT, respectively, are being used to solve the equivalent beam model or the intermediate beam problems generated during the formulation of the equivalence model. The entire 3-D analysis for any beam problem is split into a 2-D cross-sectional analysis and a 1-D beam analysis. In Fig. 59, VABS is used to perform the cross-sectional analysis and its recovery. GEBT is used to perform the 1-D non-linear analysis. Here, the two subsections below lay out an overview of VABS and GEBT.

4.3.4 Cross-sectional Analysis with VABS

Extended Hamilton's principle can be used to depict the beam behavior.

$$\int_{t_1}^{t_2} [\delta(\mathcal{K} - \mathcal{U}) + \overline{\delta\mathcal{W}}]dt = 0 \tag{78}$$

Here t_1 and t_2 represent two time stamps, $\mathcal{K}$ denotes kinetic energy, $\mathcal{U}$ denotes internal energy, δ represents Lagrangian variation, and $\overline{\delta\mathcal{W}}$ denotes the virtual work.

For a linearly elastic material, we write the strain energy and the material satisfies Hooke's law

$$\sigma = \mathcal{D}\Gamma \tag{79}$$

where Γ represents the three-dimensional strain tensor that is written as $\Gamma = \begin{bmatrix} \Gamma_{11} & 2\Gamma_{12} & 2\Gamma_{13} & \Gamma_{22} & 2\Gamma_{23} & \Gamma_{33} \end{bmatrix}^T$. x_i is the beam coordinate frame. x_1 is the span-wise direction and x_2, x_3 are orthogonal unit vectors on the cross-section. The warping functions are assumed to be of the order of strain. Therefore, neglecting higher-order

terms, the 3-D strain field can be written as

$$\Gamma = \Gamma_a w + \Gamma_\epsilon \bar{\epsilon} + \Gamma_R w + \Gamma_l w' \tag{80}$$

The symbols in Eq. 80 are further defined and derived in Ref. [83]. To make the dimensional reduction, one must rely on the inherent small parameters present in the structure [68]. If the initial radius of curvature is R, b/l and b/R are the small geometric parameters. We minimize the strain energy functional with respect to the warping function. Next, the warping solutions are perturbed to obtain asymptotically correct strain energy, depending on the order of approximation used. Using dimensional reduction, neglecting higher-order contributions, and transforming the energy into a beam model of the Generalized Timoshenko form, we can obtain the one-dimensional constitutive laws that relate the one-dimensional resultant forces to the one-dimensional strains.

$$\begin{Bmatrix} F_1 \\ F_2 \\ F_3 \\ M_1 \\ M_2 \\ M_3 \end{Bmatrix} = \underbrace{\begin{bmatrix} S_{11} & S_{12} & S_{13} & S_{14} & S_{15} & S_{16} \\ S_{21} & S_{22} & S_{23} & S_{24} & S_{25} & S_{26} \\ S_{31} & S_{32} & S_{33} & S_{34} & S_{35} & S_{36} \\ S_{41} & S_{42} & S_{43} & S_{44} & S_{45} & S_{46} \\ S_{51} & S_{52} & S_{53} & S_{54} & S_{55} & S_{56} \\ S_{61} & S_{62} & S_{63} & S_{64} & S_{65} & S_{66} \end{bmatrix}}_{S} \begin{Bmatrix} \gamma_{11} \\ 2\gamma_{12} \\ 2\gamma_{13} \\ \kappa_1 \\ \kappa_2 \\ \kappa_3 \end{Bmatrix} \tag{81}$$

This equation can be simplified as

$$\begin{Bmatrix} F \\ M \end{Bmatrix} = \begin{bmatrix} A & B \\ B^T & D \end{bmatrix} \begin{Bmatrix} \gamma \\ \kappa \end{Bmatrix} \tag{82}$$

where A, B and D are sub-matrices of the stiffness matrix each of size 3×3, $F = \begin{bmatrix} F_1 & F_2 & F_3 \end{bmatrix}^T$, $M = \begin{bmatrix} M_1 & M_2 & M_3 \end{bmatrix}^T$, $\gamma = \begin{bmatrix} \gamma_{11} & 2\gamma_{12} & 2\gamma_{13} \end{bmatrix}^T$ and $\kappa = \begin{bmatrix} \kappa_1 & \kappa_2 & \kappa_3 \end{bmatrix}^T$ as shown. Apart from this, one also obtains the 6×6 mass-matrix ($[I]$) from the cross-sectional analysis

as part of the Eq. 83 which is written as

$$\left\{ \begin{array}{c} P \\ H \end{array} \right\} = [I] \left\{ \begin{array}{c} V \\ \Omega \end{array} \right\} \tag{83}$$

4.3.5 1-D Beam Analysis with GEBT

For 1-D analysis, we use the GEBT, which is based on a mixed formulation. The variational statement in Eq. 78, after substituting values for $\mathcal{K}$, $\mathcal{U}$ and $\overline{\delta\mathcal{W}}$ from Ref. [162], is rewritten as a variational statement in the mixed formulation in Eq. 84.

$$\begin{aligned}
&\int_{t_1}^{t_2} \int_0^l \left\{ \left(\overline{\dot{\delta q}} + \widetilde{\Omega}\overline{\delta q} + \widetilde{V}\overline{\delta\psi} \right) P + \left(\overline{\dot{\delta\psi}} + \widetilde{\Omega}\overline{\delta\psi} \right) H - \left(\overline{\delta q}' + \widetilde{K}\overline{\delta q} + (\widetilde{e}_1 + \widetilde{\gamma})\overline{\delta\psi} \right) F \right. \\
&\left. - \left(\overline{\delta\psi}' + \widetilde{K}\overline{\delta\psi} \right) M + \overline{\delta q}^T f + \overline{\delta\psi}^T m \right\} dx_1 dt = \int_0^l \left(\overline{\delta q}^T \hat{P} + \overline{\delta\psi}^T \hat{H} \right) \Big|_{t_1}^{t_2} dx_1 \\
&- \int_{t_1}^{t_2} \left(\overline{\delta q}^T \hat{F} + \overline{\delta\psi}^T \hat{M} \right) \Big|_0^l dt
\end{aligned} \tag{84}$$

To proceed, the constitutive law from Eq. 82 and the momentum-velocity relations containing the mass-matrix from Eq. 83 are required. Further, to derive the mixed formulation, the kinematic differential relations in Eq. 85 are incorporated into the variational statement in Eq. 84 with the help of Lagrange multipliers and using the calculus of variations.

$$u' = C^{bB}(e_1 + \gamma) - e_1 - \tilde{k}u \tag{85a}$$

$$\dot{u} = C^{bB}V - v - \tilde{\omega}u \tag{85b}$$

$$c' = Q^{-1}(\kappa + k - C^{bB}k) \tag{85c}$$

$$\dot{c} = Q^{-1}(\Omega - C^{bB})\omega \tag{85d}$$

where Q is a set of Wiener-Milenković rotation parameters defined in Ref [152]. Following Wang [152], after identifying Lagrange multipliers associated with the

kinematic differential equations in 85, one obtains

$$\int_0^l \Big\{\delta u_a'^T F_a + \overline{\delta\psi}_a'^T M_a + \delta u_a^T(\dot{P}_a + \tilde{\omega}_a P_a) + \overline{\delta\psi}_a^T\Big[\dot{H}_a + \tilde{\omega}_a H_a + \tilde{V}_a P_a - C^{aB}(\tilde{e}_1 + \tilde{\gamma})F_B\Big]$$
$$- \overline{\delta F}_a^T\Big[C^{aB}(e_1 + \gamma) - C^{ab}e_1\Big] - \overline{\delta F}_a'^T u_a - \overline{\delta M}_a'^T c_a - \overline{\delta M}_a^T Q_a^{-1} C^{ab}\kappa$$
$$+ \overline{\delta P}_a^T(-\dot{u}_a + V_a - v_a - \tilde{\omega}_a u_a) + \overline{\delta H}_a^T(\Omega_B - \omega_B - C^{ba}Q_a\dot{c}_a) - \delta u_a^T f_a - \overline{\delta\psi}_a^T m_a\Big\}dx_1 =$$
$$\Big(\delta u_a^T \hat{F}_a + \overline{\delta\psi}_a^T \hat{M}_a - \overline{\delta F}_a^T \hat{u}_a - \overline{\delta M}_a^T \hat{c}_a\Big)\Big|_0^l \tag{86}$$

The variational statement in Eq. 86 is further treated using a suitable 1-D finite element discretization. Following Ref. [162], the system of equations, thus formed, is solved using the Newton-Raphson method along with a line search algorithm to ensure global convergence. Hence, solutions for the beam 1-D displacement variables are obtained.

4.3.6 Computation of Structural Constraints

Referring to Fig. 45, the structural analysis block receives the unsteady loads and the blade geometry and checks for structural integrity. The analysis will give a time history of stresses and strains experienced by the blade due to the loads. Stresses, both steady and vibratory, are analyzed. Besides, resonance margins are calculated to ensure that the blade vibrates without the potential of any resonance.

4.3.6.1 Stress constraint calculation

In this work, the blade is assumed to be made of an isotropic metal, and hence Von-Mises failure criteria can be applied to check for structural failure. The application of VAM provides a time-history of the six components of stress at each node in every cross-section along the span of the blade. The six components can be combined into the von-Mises stress using

$$\sigma_{VM} = \sqrt{\frac{1}{2}\left[(\sigma_{11} - \sigma_{11})^2 + (\sigma_{22} - \sigma_{33})^2 (\sigma_{33} - \sigma_{11})^2 + 6\,(\sigma_{12}^2 + \sigma_{23}^2 + \sigma_{31}^2)\right]} \tag{87}$$

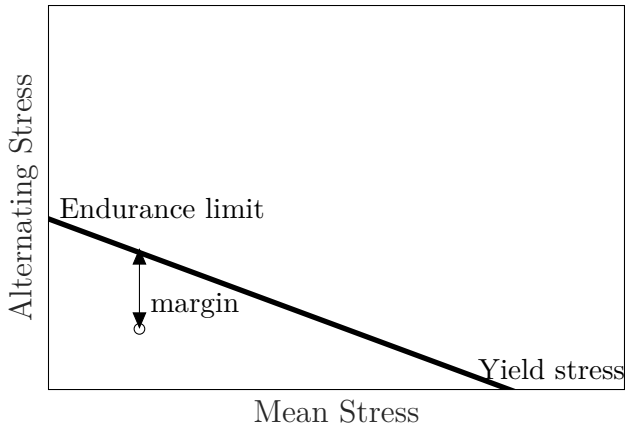

Figure 60: Notional Goodman diagram depicting margin for blade stresses.

Let us denote the von-Mises stress at time t and at node n_i on cross-section CS_j to be $CS_j n_i \sigma_{VM}^{(t)}$. The stresses on the blades will be oscillatory - with mean stress and some alternating stress. Fig. 60 shows a sketch of a Goodman diagram, where the horizontal axis represents the mean stress, and the vertical axis represents the alternating stress.

From the time-varying stresses contained in $CS_j n_i \sigma_{VM}^{(t)}$, mean and alternating stresses can be computed. Each node on the cross-sections of the blade can be plotted on the Goodman diagram. The vertical distance from the point to the limit line (in percentage) is the Goodman margin, also shown in Eq. 88. A Goodman margin of 60% is set as a requirement for the worst-case node of each cross-section to prevent producing a conservative design.

$$\text{margin} = \frac{\sigma_{\text{limit,alt}} - \sigma_{\text{VM,alt}}}{\sigma_{\text{limit,alt}}} \times 100 \tag{88}$$

4.3.6.2 Resonance margin computation

The excitation frequencies are generally engine order (EO) multiples. In the Campbell diagram shown in Fig. 61, the diagonal lines (possible excitation frequencies) are, therefore, functions of the speed of revolution. At any speed of rotation, not all engine order excitations are present. The excitation frequencies can be computed

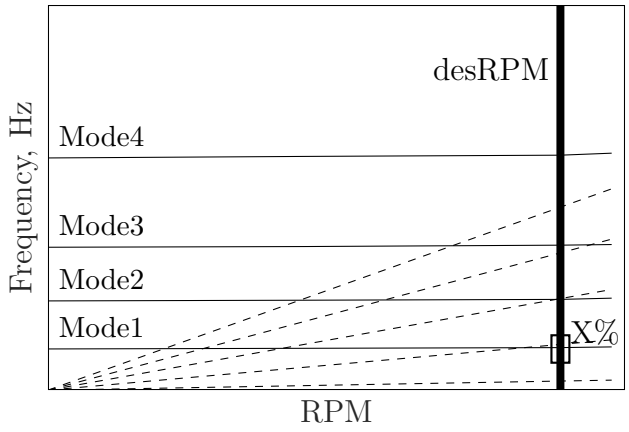

Figure 61: Notional Campbell diagram depicting margin at design speed.

via a Fourier Transform of the displacements. These frequencies are present in the Campbell diagram in the form of engine order excitations and are not dependent on the blades' geometry, but the amplitudes of these harmonics are. If these frequencies come in close contact with the natural frequencies, resonance is expected. In this present work, a 10% margin is set as a requirement for the first engine order frequency. A 5% margin is set for the other engine orders up to 4EO. The margin is calculated as the difference between the natural frequency and excitation frequency normalized by the natural frequency and represented in percentage. Eq. 89 shows the equation used to compute the margins, where subscripts *nat* and *ext* represent natural and excitation frequencies, respectively.

$$\text{margin} = \frac{\text{frq}_{\text{nat}} - \text{frq}_{\text{exc}}}{\text{frq}_{\text{nat}}} \times 100 \tag{89}$$

As defined in Section 4.3.3, GEBT can be used to obtain the time histories of displacement from unsteady loads. GEBT can also be used to run modal analysis and obtain the natural frequencies of the blade. Generally, crossings of concern are in the lower modes of vibration. Therefore natural frequencies of the first eight modes are evaluated.

4.4 Design Space: Exploration and Optimization

The successful linkage of all elements discussed above allows for rapid design space exploration of the fan stage. The goal is to identify the trade-offs between aerodynamic performance and choose a design that maximizes the fan's aerodynamic performance while respecting the structural constraints. Studies in the literature parameterize the stage design variables for each component (distribution of thickness, camber, chord, stacking axis, and flow path lines) [96, 98]. Variables that are chosen for the exploration include the hub to tip ratio of the blade, thickness to chord ratio, the radial distribution of thickness to chord ratio, loading type (hub loaded, uniformly loaded, or tip loaded), rotor area ratio, tip chord, chord distribution (or taper), and stator chord. The input variables are designed to change the behavior of flow profiles at the rotor exit, affecting the blade metal angles that define how the stresses act on them. For example, a varying hub to tip ratio for a fixed tip diameter affects the incoming Mach number (or velocity), thereby affecting the inlet's velocity triangles. Changing the loading type redistributed the amount of work imparted by various sections on the blade, thus redistributing the stresses.

Referring to Fig. 45, the information of the constraints and the objective function values enables the optimizer to choose a better set of design variables than the current iteration. At this point, it is relevant to discuss the tools used in the current study. The aerodynamic module is built on the Object-Oriented Turbomachinery Analysis Code (OTAC) [89] that outputs the information of blade geometry and loads. The structural analysis tools are wrapped in a MATLAB environment. The computation of constraints involves computing the Goodman margin for each cross-section and the resonance margin for each excitation frequency and natural frequency combination. Generating surrogate models for the responses and constraints can be computationally feasible, given the low computational time associated with the tools used in this framework.

A design of experiments is created. From the results of the design of experiments, the surrogate models of all responses are formed using neural networks. The presence of several discrete variables makes the polynomial fit more cumbersome. The optimization problem statement is expressed in Eq. 90 . The overall goal is to maximize the design point efficiency of the fan stage. Here, x_s and x_r refers to stator and rotor design variables respectively. Superscript A indicates the variables corresponding to the aerodynamic design only, and AS refers to the variables corresponding to both aerodynamic design and structural design. Aerodynamic and structural constraints are enforced. First, it is required that the stage pressure rise is the required pressure rise. At least a small positive value of reaction (≥ 0.05) is desired at the hub. Stall criterion is established by the use of the diffusion factor (DF). A DF of 0.6 is considered the threshold value. If a stricter stall margin criterion is desired to accommodate several types of transients (or for any other reason), it is recommended to lower the value of the threshold diffusion factor value. A 60% requirement on Goodman margin (GM) is set for each cross-section. A minimum of 10% margin is desired for the first excitation

frequency, and 5% margin is desired for other engine orders.

$$
\begin{aligned}
\min_{\vec{x}_s^A, \vec{x}_r^A, \vec{x}_r^{AS}} \quad & -\eta_{stg} \\
\text{s.t.} \quad & PR_{stg} - PR_{req} && = 0 \\
& -R_{hub} + 0.05 && \leq 0 \\
& DF - 0.6 && \leq 0 \\
& GM_k - 0.6 && \leq 0 \\
& -RM_{i,j} + 0.10 && \leq 0 (j = 1) \\
& -RM_{i,j} + 0.05 && \leq 0 (j > 1)
\end{aligned}
\tag{90}
$$

where

$i = 1, 2, 3, ...8$ (natural frequency mode)

$j = 1, 2, ...5$ (excitation frequency mode)

$k = 1, 2, 3$ (cross section index)

CHAPTER V

AERODYNAMIC DESIGN OF A FAN STAGE

5.1 Chapter Overview

In Chapter 4, the aero-structural framework for fan stage conceptual design was introduced. This chapter discusses the aerodynamic design of the framework and demonstrates the method's applicability in an example case for both clean and distorted flows. Following that, experiments using the framework are conducted to test the hypotheses corresponding to research question 1.

First, using the framework, a baseline design will be created. The baseline design will then be subjected to distorted flow, and results from the literature are compared to the proposed framework's results. Once confidence in the modeling framework is established, the framework will be used to conduct parametric experiments. Experiments 1.1, 1.2, 1.3, and 1.4 will be explained, and their results will help establish the conclusions related to hypotheses 1.1, 1.2, 1.3, and 1.

5.2 Verification of the Aerodynamic Framework

The framework introduced can design a blade for a prescribed distorted flow, and the quality of the design can be validated by running an experiment on that design. Due to the scope of this work, only numerical experiments are conducted. As a result, the verification of this framework will be done in the following way. First, a fan stage for a uniform flow is designed using the framework. The design flow properties of NASA Rotor 67 will be provided to the framework. The geometry of the rotor produced from this framework will be compared to the actual geometry of Rotor 67. Once this verification is complete, the geometry is subjected to an inlet distortion similar to the

Table 2: Design parameters for NASA Rotor 67.

Parameters	Value	Units
RPM	16043	-
FPR	1.63	-
AR	1.38	-
Number of blades	22	-
Tip clearance	0.039	in
Tip radius (LE)	10.11	in
Tip radius (TE)	9.547	in
Hub-to-tip ratio (LE)	0.375	-
Hub-to-tip ratio (TE)	0.478	-

Table 3: Flow parameters for NASA Rotor 67.

Flow Parameters	Value	Units
Design mass flow	73.304	lbm/s
Inlet Tt	288.15	K
Inlet Pt	14.69	psia

one performed using high fidelity numerical studies from the literature. A comparison is made between these two sets of results, and the confidence in the framework is established.

5.2.1 Baseline Fan Design: Uniform Flow

The baseline fan chosen for this study is NASA Rotor 67. NASA Rotor 67 is a commonly known rotor test case for many turbomachinery CFD codes, so it is easier to obtain experimental data for this blade. Fidalgo et al. [48] used a NASA Rotor 67 transonic fan stage with a 67A stator row. The version used here includes 22 multiple-circular-arc blades. The design fan pressure ratio is 1.63 at a design speed of 16043 RPM. Table 2 shows the design parameters of Rotor 67.

The design flow properties are shown in Table 3. The rotor inlet condition was specified, and the framework was used to predict the cross-sectional blade angles.

Fig. 62 shows the model predicted cross-sections when run in design mode for the Rotor 67 inputs defined by Table 2 and 2 for the hub, mid, and tip sections. It can be

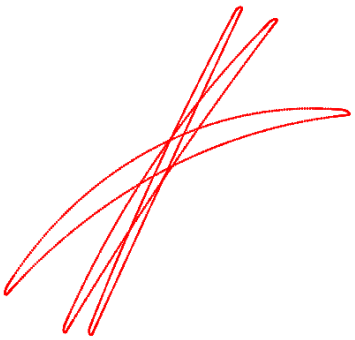

Figure 62: Rotor 67: predicted.

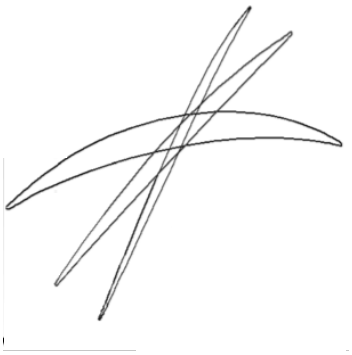

Figure 63: Rotor 67: actual.

Table 4: Performance parameters for NASA Rotor 67: predicted vs. actual.

Parameters (mid span)	**Predicted**	**Actual**
Diffusion Factor	0.51	0.5
Flow coefficient (ϕ)	0.65	0.55
Loading coefficient (ψ)	0.5	0.49
Efficiency (η)	0.879	0.9

seen that the method can produce twisting in the blade along the span. Fig. 63 shows the cross-sectional profiles of Rotor 67, reproduced from [48]. Note that in Fig. 62, the cross-sections at the exact root and tip are not available from the design framework, so the section at the root will be less twisted than the first section, and the section at the tip will be more twisted than the top section shown in the figure. A close match has been obtained between the leading and trailing edges blade metal angles. It is to be noted here that the airfoil shape has some differences. Rotor 67 uses multiple circular arc airfoils, whereas the developed model uses double circular-arc airfoils. The blade metal angles of the camber line were in close agreement with the ones specified in [145]. The predicted performance parameters at the design point compared to the actual Rotor 67 performance are listed in Table 4.

Some differences in performance parameters are expected. The diffusion factor and loading coefficient closely matched. A difference of 0.1 in flow coefficient was observed. A 2.1% difference in the design point efficiency was observed. This difference is very likely due to the loss models used for this work. These loss models have not been

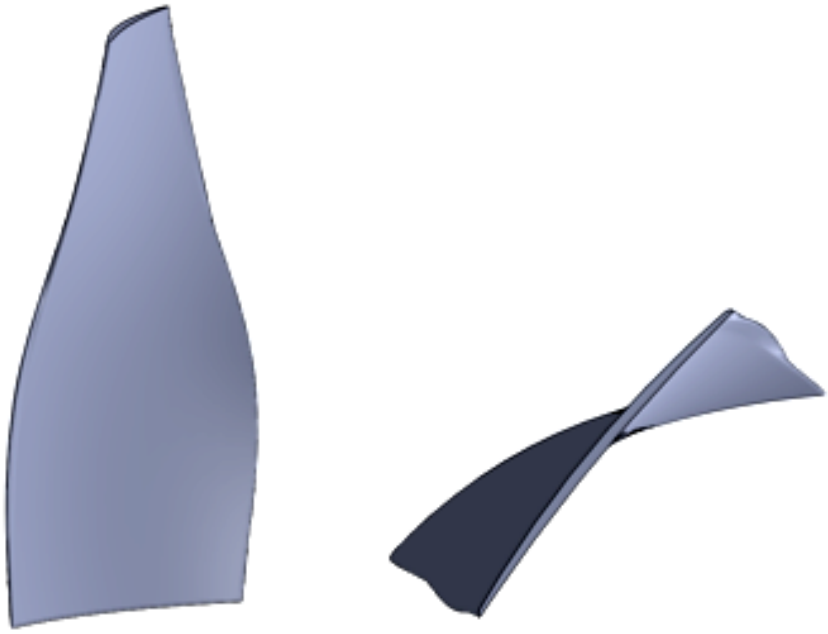

Figure 64: 3-D geometry of Rotor 67 generated by lofting the cross-sections.

calibrated to Rotor 67. Further, the loss models are based on a double circular-arc airfoil. It was verified that when lowering the design RPM, a blade with efficiency as high as 90% could be designed for the given input conditions. Since the goal was not to calibrate the loss models to Rotor 67, no calibration process was performed. While the efficiency numbers did not precisely match, the design was a match. Therefore, when comparing designs, instead of comparing efficiencies, the difference in the efficiency from the design point efficiency will be used. A 3-D view of the blade can be sketched using any 3-D modeling software from the cross-sections generated from the design method. Fig. 64 shows the side view and the top view of the blade drawn by lofting the sections in Fig. 62.

5.2.2 Baseline Fan Design: Non-Uniform Flow

The previous design provided a reasonable estimate of the Rotor 67 blade design. To understand how the methodology outlined in chapter 4 predicts the performance of the

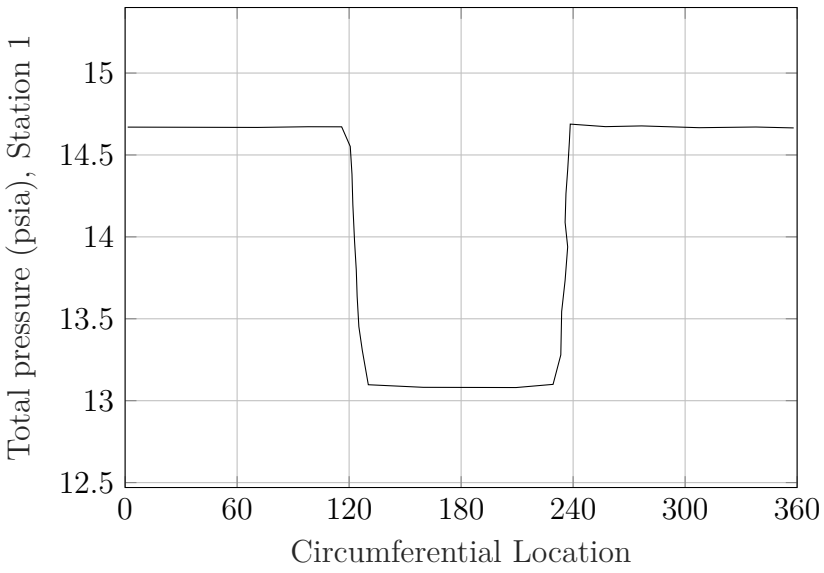

Figure 65: Variation of total pressure at Rotor 67 inlet, digitized from Fidalgo [48].

rotor behavior in a distorted flowfield, total pressure, and swirl distortion is applied. Results from the CFD analysis by Fidalgo et al. [48] is used to provide the flow inputs and rotor response. The CFD solver used in their work was the Roll-Royce's HYDRA that solves the Reynolds-Averaged Navier-Stokes (RANS) equations in compressible and unsteady flow using a finite volume approach on the unstructured grids. An explicit dual time-stepping procedure with a second order backward differencing method was implemented to expedite the computational speed. Similarly, for the convergence of subiterations, a four-stage Runge-Kutta scheme was used in the inner loop. Finally, the turbulence model used was the Spalart-Allmaras one-equation model.

In the study by Fidalgo, the distortion analysis was performed at 90% design speed and the total corrected mass flow of 70.54 lbm/sec based on the mass-averaged total conditions. This value corresponds to an uncorrected flow of approximately 66.0 lbm/sec for the mentioned operating conditions. Fig. 65 shows the total pressure distortion profile at the rotor inlet. The total pressure distortion intensity was approximately 0.055, with a circumferential extent of 120°.

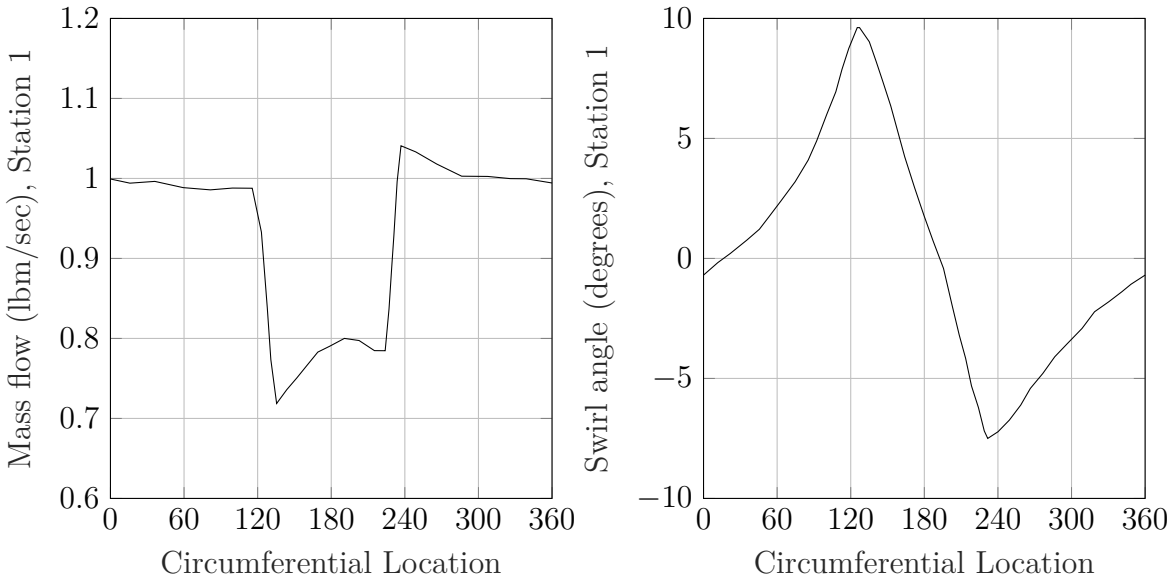

Figure 66: Variation of mass flow [left] and swirl angle [right] at the rotor inlet for Rotor 67, digitized from Fidalgo [48]

The upstream redistribution resulted in overall mass flow and swirl angle variation at the rotor inlet, as shown in Fig. 66. It can be seen that the mass flow was as low as 75% of the clean flow in the distorted sector at the rotor inlet. A co-swirl and counter-swirl varied from +10° to -10°. As the rotor moves from the clean to the distorted region (0° - 120°), the rotor experiences a positive swirl. The effect of positive swirl is the reduction in the incidence angles on the blades. In the low total pressure (120° - 240°), the swirl angle keeps on decreasing. This phenomenon is because of counteracting mass flow from either side of the annulus. In this sector, at ≈180°, it reaches a condition of no-swirl, after which the rotor begins to experience counter swirl as high as -8.5°. The effect of counter-swirl is the increase in the incidence angle for the rotor blades.

The inlet profile was then discretized into five circumferential sectors, and all properties were mass averaged for each sector. The flow at the rotor exit was then recorded, and the ratio of total pressure at the rotor exit to the clean total pressure was computed. The left side of Fig. 67 shows the ratio of total pressure at the rotor

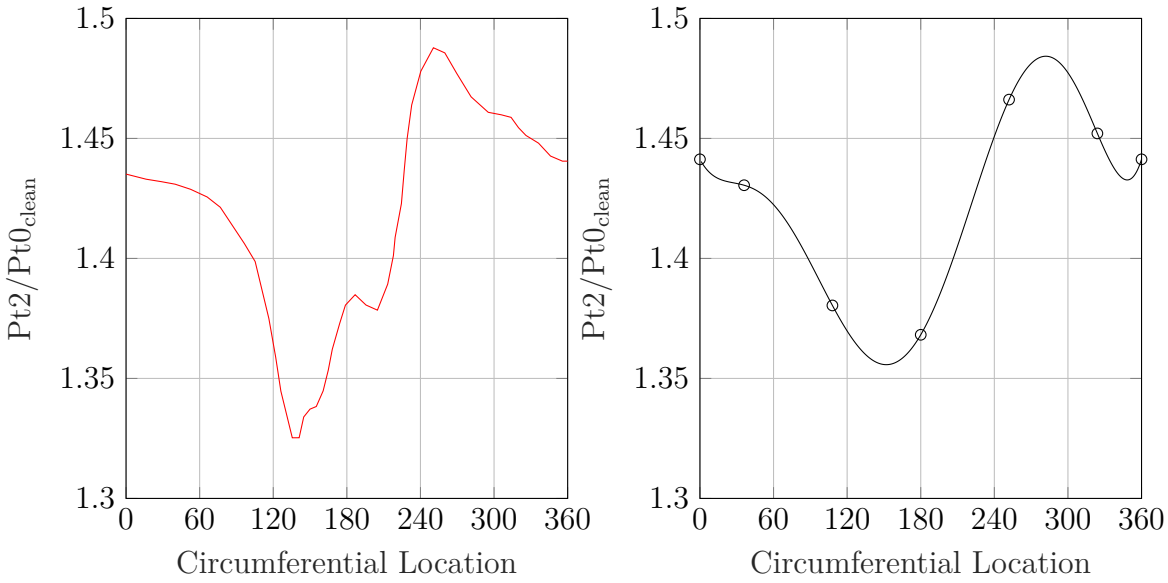

Figure 67: Variation of ratio total pressure at rotor exit to clean total pressure from unsteady CFD results of Rotor 67: continuous [left], discretized [right].

exit normalized by the clean total pressure at the inlet obtained from unsteady CFD solution for the mid-span. For an appropriate level of comparison, this continuous flow curve was also discretized into five areas, and a polynomial fit was used to create a smooth polynomial function from the discretized points. The polynomial fit obtained by discretized these sections are shown on the right side of Fig. 67.

The framework was run in the analysis mode in two separate scenarios using the baseline Rotor 67 design. First, a quasi-steady calculation was performed by switching off the unsteady module. Second, an unsteady calculation was performed by allowing the model to run and convert the quasi-steady to unsteady rotor response. Both quasi-steady and unsteady models averaged a total pressure rise of 1.46, matching the reference study results. It was observed that the distorted case experienced a 1.1% reduction in rotor efficiency compared to a 1.5% reduction obtained from the CFD analysis. Fig. 68 shows the difference between the results predicted by the model and the discretized CFD results. The dots represent the points extracted from the model, and the curves represent the polynomial fit obtained by using those points. It can be

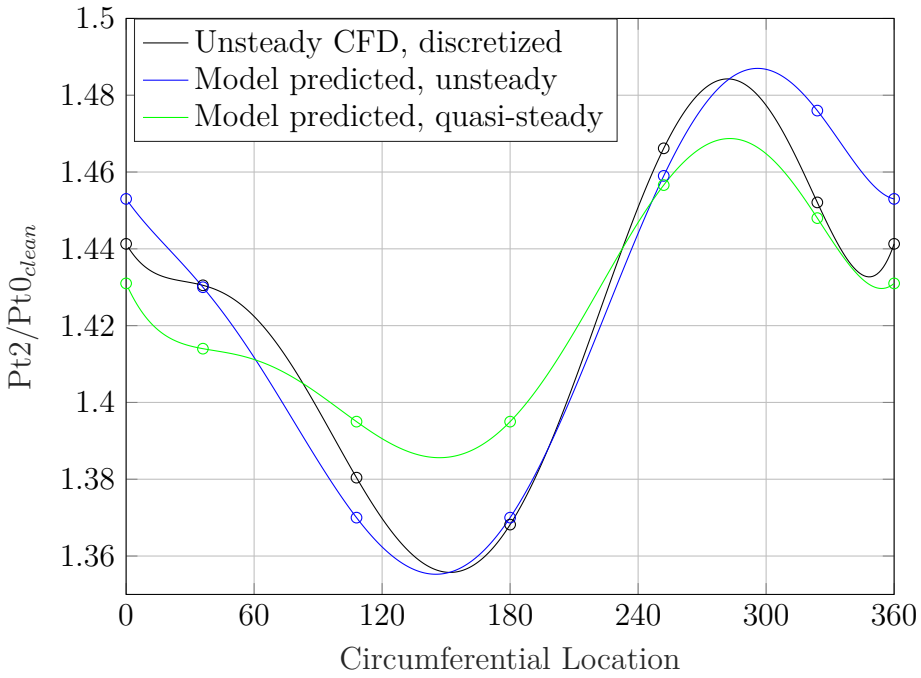

Figure 68: Comparison of Pt2/Pt0 between unsteady CFD and model predicted quasi-steady and unsteady results for Rotor 67.

seen that the model can correctly predict the variation of the total pressure at the rotor exit.

Fig. 68 also shows the comparison between the model predicted quasi-steady and unsteady versions. The results of the unsteady model seem to be in close agreement with the discretized CFD results. Although both quasi-steady and unsteady models result in the same average pressure ratio for this case, the amplitude of the total pressure at the rotor exit is correctly represented by the unsteady model. Some observations can be made when comparing the unsteady and the quasi-steady results. As the rotor rotates, the rotor is moving from the cleaner sector to the distorted sector. The rotor experiences a reduction in incidence angle, thus reduction in the total lift. Quasi-steady implementation accounts for this change instantly, while the unsteady version results in a lag. From approximately 70° to 150°, the mass flow is decreasing, and the swirl is increasing. The reducing mass flow tends to increase the incidence, and the increasing swirl tends to reduce the incidence. Both unsteady

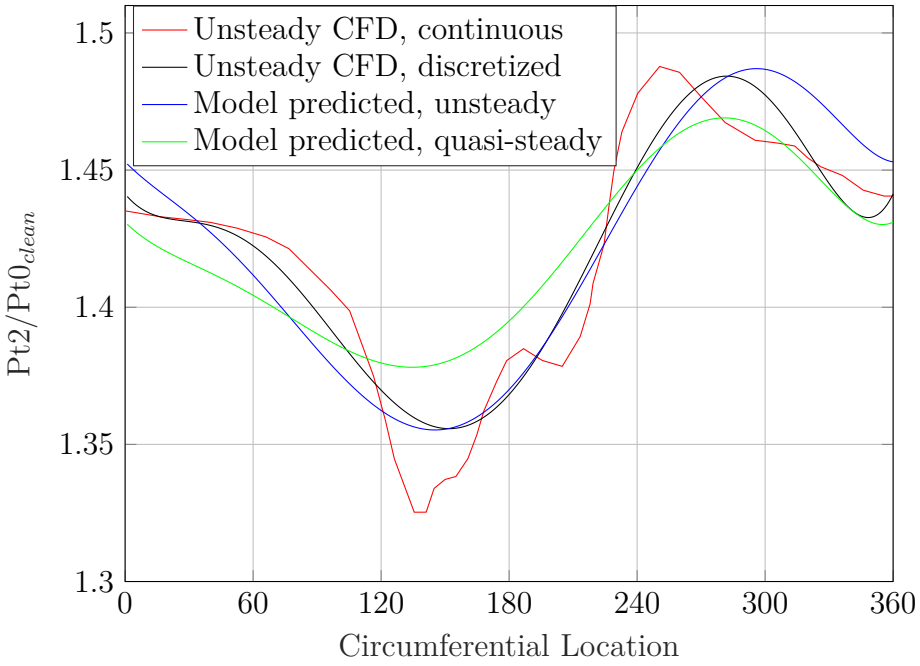

Figure 69: Overlaying Pt2/Pt0 values for various cases for rotor 67.

and quasi-steady models predict the lowest total pressure at around 150°, but the quasi-steady results lead the unsteady results by a few degrees. When rotating from the distorted sector to the clean sector, the incidence keeps on increasing. Here, the quasi-steady model predicts a change instantly, but the unsteady model considers the history of the flow around the annulus. While these results show a good match with the discretized CFD results, there is still a significant difference when compared with the continuous CFD results, as shown in Fig. 69. It makes sense because only five points were used to create inputs for the model used in this work. Given that these results were obtained in a few seconds, the model predicted quite reasonable results for quasi-steady and unsteady simulations.

It is also seen here that the unsteady loads are higher than quasi-steady loads. That means when performing structural analysis on the rotor blades, the loads should be calculated based on the unsteady model since they will likely induce more vibrations and increased stresses. Fig. 70 shows the variation of the swirl angle at the rotor exit. Although the results were not as close as the results for the total pressure, it

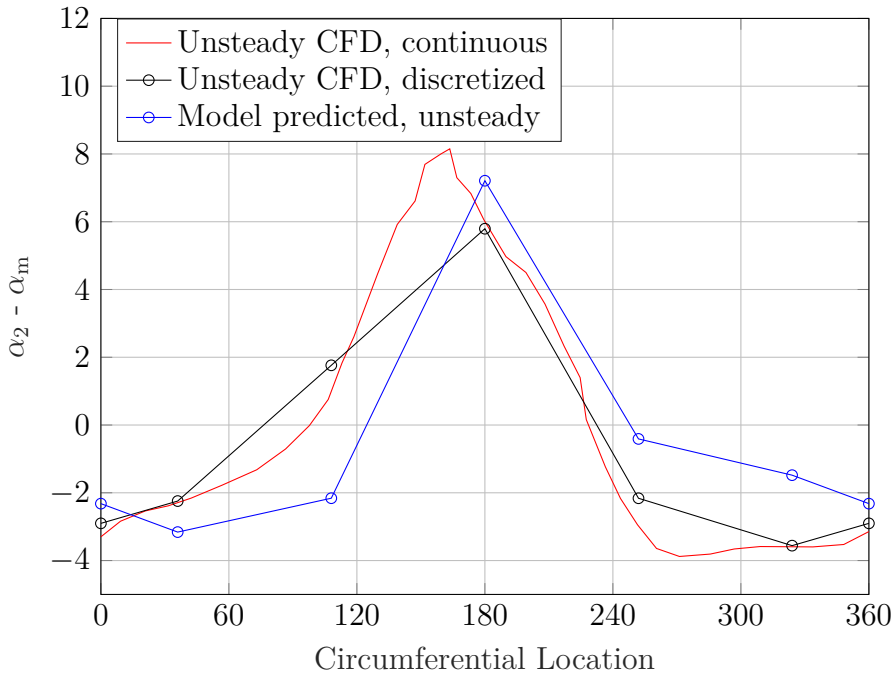

Figure 70: Variation of absolute swirl angle at rotor exit for rotor 67.

can be seen that the model can capture the relevant trends and the magnitudes of the swirl angle. It can also reproduce the attenuation of the swirl angle at the rotor exit compared to the inlet. Some of the discrepancies also arise from the fact that the Rotor 67 is a transonic fan. The presence of shock waves in the tip region is expected at the speed at which it operates. However, the modeling approach introduce here does not capture these additional shock formations - a possible reason for these differences. Generally, BLI fans operate at lower RPMs and shocks are unlikely for those cases. We see that the trends in almost all results are well-captured by the modeling process. The proposed method's ability to design a baseline fan and predict the rotor response in distorted flow conditions established confidence in the method outlined here to study, design, and optimize designs in a parametric fashion.

5.3 Experiment 1

Now that the aerodynamic design and analysis framework has been described and verified for a non-uniform flow application, it can be used to perform experiments

to test the hypotheses posed for research question 1 and its components. Before performing the experiments, the experimental setup is described here first. The general objective of experiment 1 is to verify whether the proposed aerodynamic framework described in chapter 4 can design the fan stage with higher efficiencies for distortion purposes.

5.3.1 Experiment Setup

Experimental steps have to be defined to test hypotheses 1.1 - 1.3 and, subsequently, hypothesis 1. The experimental setup consists of defining the types and intensities of inlet distortion, the exact set of cases to run, and the baseline blade geometry's definition to perform the test cases.

5.3.1.1 Flow profiles

Since the hypotheses make generic statements without defining a fixed distortion nature and intensity, the experiments' flow profiles should be generic. They should be in the range of operation for distorted inflows. In that regard, Fig. 71 shows the matrix of distortion types and the corresponding intensities that will be used. Two types of distortion will be considered: total pressure and swirl distortion. Total pressure distortion reflects the mass flow deficit arising from ingesting the boundary layer. Swirl distortion arises when the flow propagates from the inlet entrance to the fan face. For each distortion, four intensities are defined: no distortion, low distortion, mid distortion, and high distortion. The no distortion case represents a clean inflow condition that also serves as a baseline case for comparison. The low distortion and high distortion case represent the lower and upper bound of the distortion intensities typically experienced during the boundary layer's ingestion. The mid distortion case is a representative case of a typical distortion level. The dots in Fig. 71 represent the combination of total pressure and swirl distortion that will be used in the experiments. Three sets of flow conditions are used. The first one is the case where no swirl

distortion is considered. The second one is the case where no total pressure distortion is considered. While swirl and total pressure distortion typically present together, considering them separately allows for isolating the effects. The third set of cases will include a combination of both swirl and total pressure distortion. In reality, a low total pressure distortion will induce a low swirl distortion. So, this set will consist of similar intensities for both types of distortion.

The intensities are defined using total pressure distortion intensity (*dpcp*) given by Eq. 91, where PAV is the average total pressure on the annulus and PAVLOW is the average total pressure of the lower half of the total pressure profile.

$$dpcp = \frac{\Delta \mathrm{PC}}{\mathrm{P}} = \frac{\mathrm{PAV} - \mathrm{PAVLOW}}{\mathrm{PAV}} \tag{91}$$

A sinusoidal function is used to generate the flow profiles at the AIP. Total pressure intensities of 0, 0.035, 0.07, and 0.1 are used as distortion input profiles, and they will be referred to as no distortion, low distortion, mid distortion, and high distortion cases, respectively. The low and high distortion intensities are specified from the minimum and maximum intensities observed in the literature. The mid distortion is simply near the mean of these two extremes. For swirl distortion, co-swirl and counter-swirl are prescribed since swirl distortion generally occurs in pairs for distorted inflows. The maximum amplitude of 0°, 6°, 12°, and 20° in swirl variation is considered respectively for no, low, mid, and high distortion cases. These values are extracted from analyzing several distortion studies in the literature. Mid distortion is considered to be typical distortion levels, whereas low and high levels of distortion are set as the lower and upper bounds for distortion cases.

Figs. 72, 73, and 74 show the flow profiles (total pressure, mass flow, total temperature, and swirl angle) at the rotor inlet for the three sets of cases discussed above. Note that in all the cases, the temperature variation is not considered.

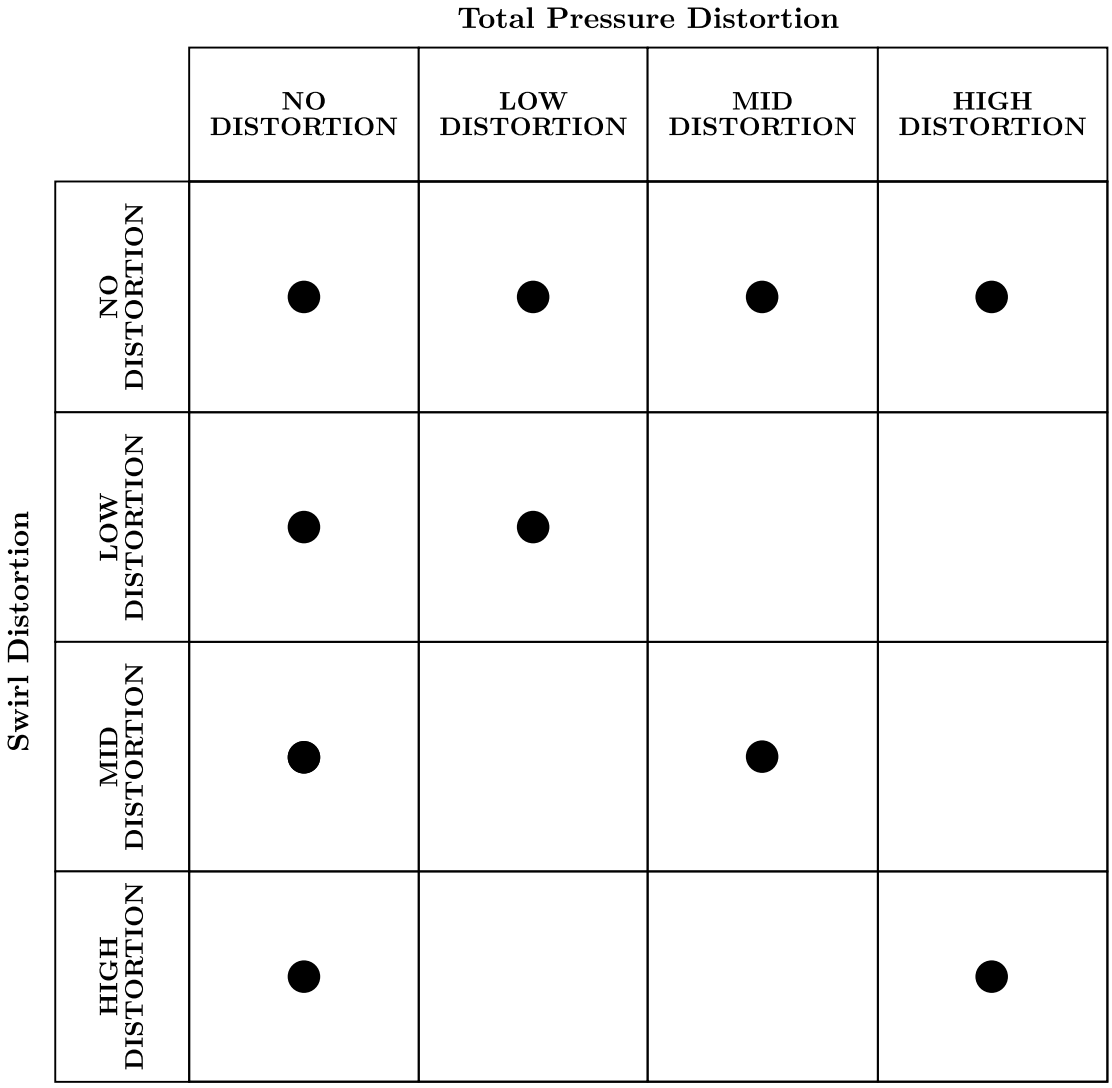

Figure 71: Experimental setup: Flow profiles at rotor inlet.

5.3.1.2 Reference fan stage design parameters

A reference blade is chosen to perform all the experiments on. Table 5 shows the parameters of the test blade that will be used to perform the experiments. The fan pressure ratio values, RPM, and tip radius were chosen to represent some of the concepts in the literature.

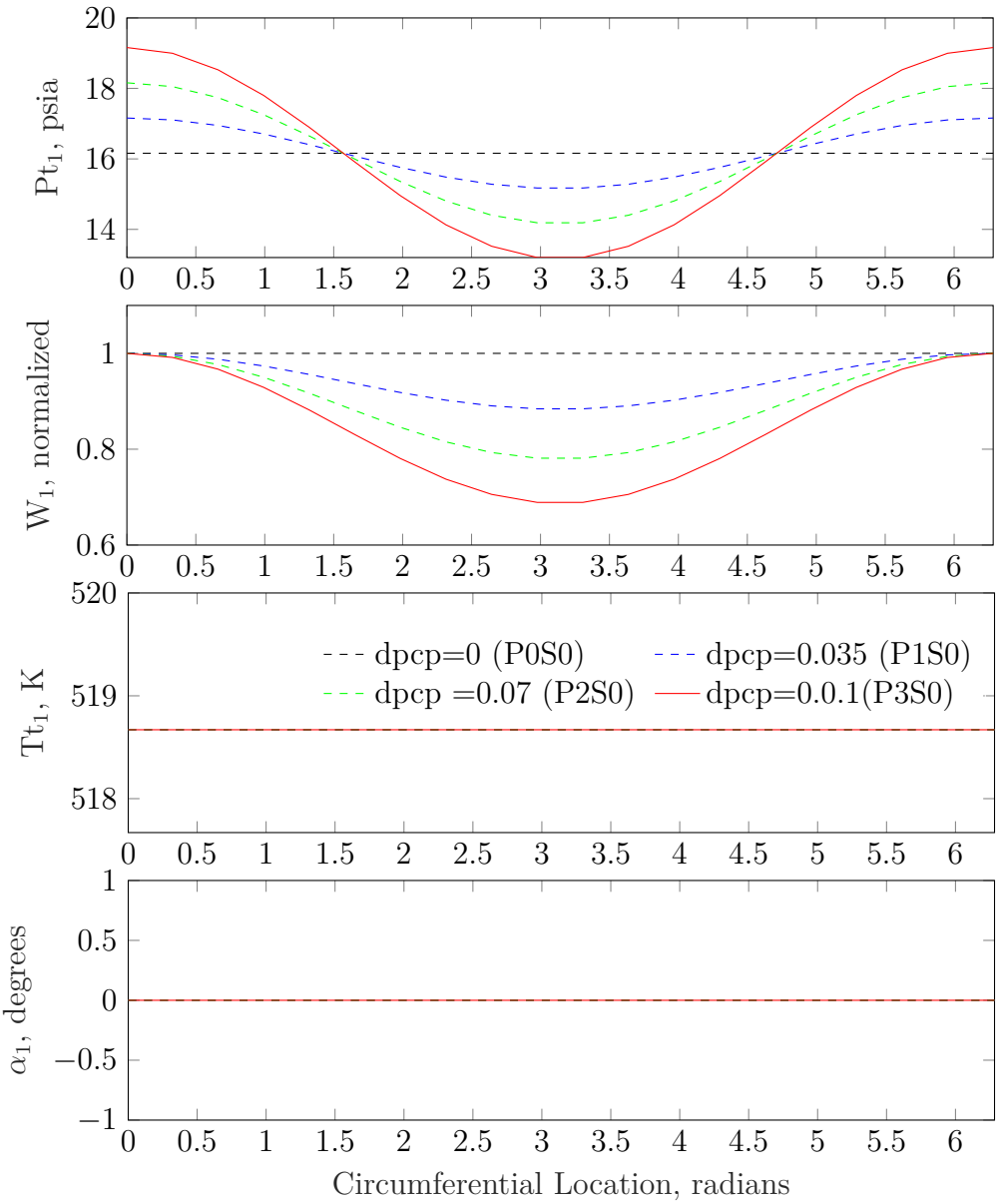

Figure 72: Flow profiles for pure total pressure distortion cases: P0S0, P1S0, P2S0, P3S0.

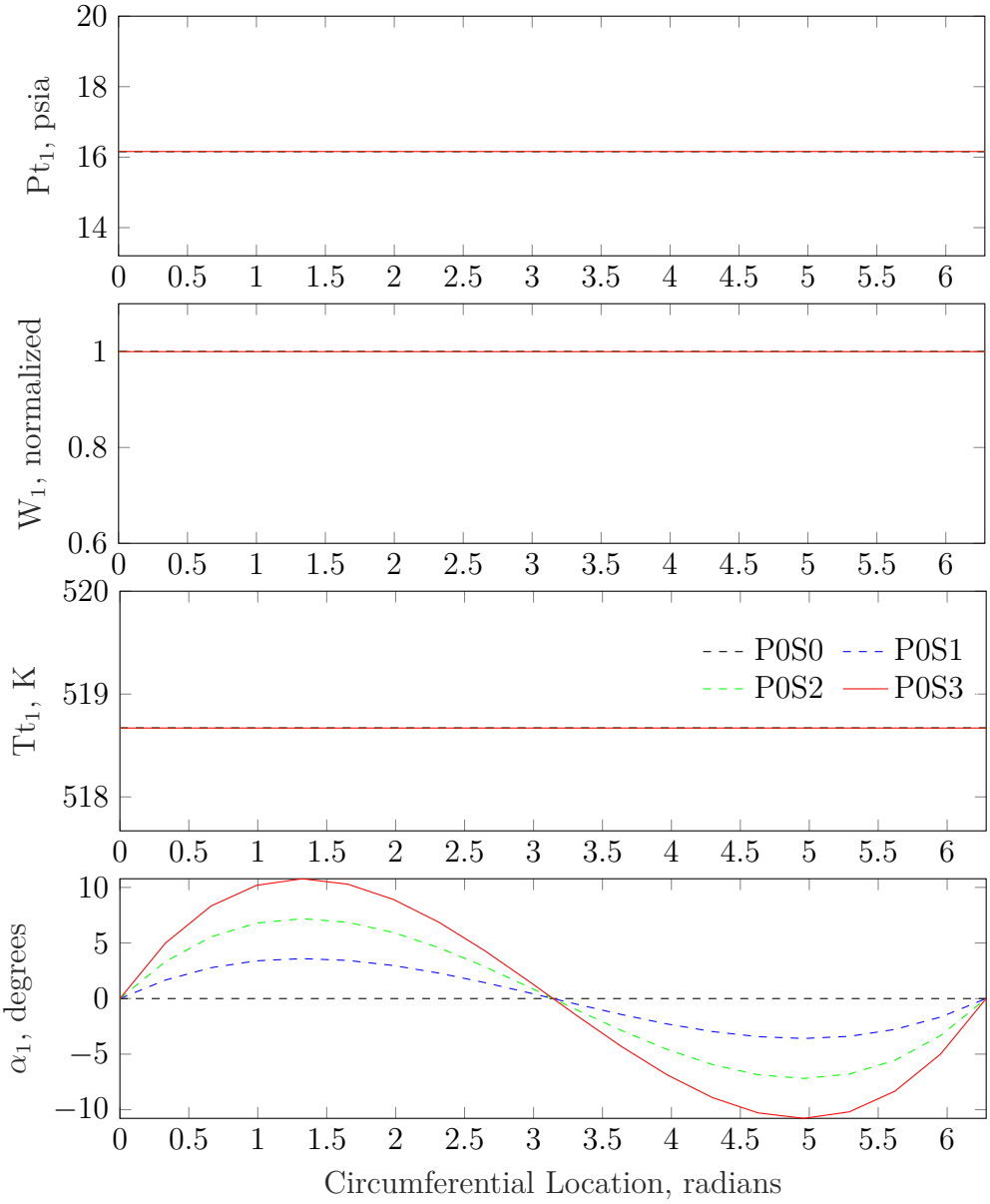

Figure 73: Flow profiles for pure swirl distortion cases: P0S0, P0S1, P0S2, P0S3.

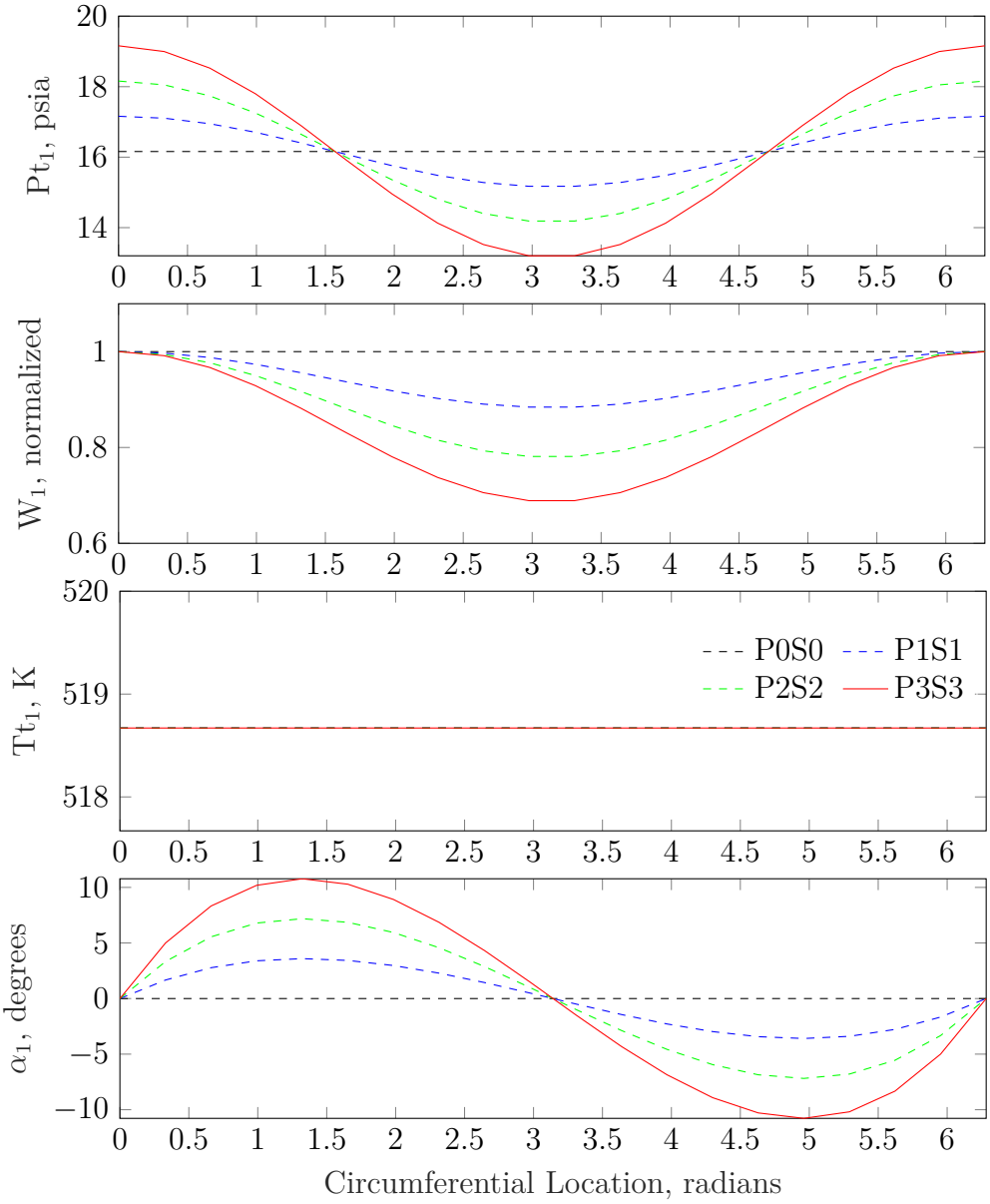

Figure 74: Flow profiles for mixed distortion cases: P0S0, P1S1, P2S2, P3S3.

Table 5: Fan design parameters for experiment 1.

Parameters	**Values**
Stage pressure rise requirement	1.25
RPM	4000
Tip radius	24"
Tip chord	8"
Taper type	No taper
Hub to tip ratio	0.25
Number of rotor blades	23
Number of stator blades	33
Stator chord	4.5"
Rotor airfoil type	Double circular arc
Machine type	Constant tip radius
Design type	Uniform loading

5.3.1.3 Summary of modeling scenarios

A summary of modeling scenarios is presented here, and a step by step discussion on the experimental procedure is provided in the respective experimental section. Research question 1 asked for the appropriate framework to create the aerodynamic designs of the fan blades. Three fan modeling elements were discussed as a part of research question 1: rotor losses, rotor response, and stator design. Hypothesis 1.1 stated that rotor losses could be minimized by optimizing the incidence angles. If designing for an averaged flow, the minimum loss incidence for uniform flow is different from the minimum loss incidence and deviation for non-uniform flow. Hypothesis 1.2 stated that the impact of rotor unsteady response would be essential to be considered with increasing distortion intensity. Both vibratory loads and rotor response will show non-negligible deviation from the quasi-steady response. Hypothesis 1.3 claimed that the required asymmetry for stators increases with increasing distortion intensity and that the effect of swirl distortion in stator asymmetry is less than total pressure distortion. Hypothesis 1 stated that if hypotheses 1.1 - 1.3 are correct, then the design framework that employs the physics mentioned above of the flow will help recover a

large portion of the stage losses when operating under distortion.

It was deemed necessary to create a framework that employs these aspects to test the hypotheses mentioned above. The absence of such a framework in the literature motivated to create such a framework described in Chapter 4. The aerodynamic design block of the framework, quite naturally, employed these three effects in a modular fashion. The rotor blades' incidence and deviation angles can either be set to design values or can be varied in a parametric fashion to find a better optimum if there exists one. The response of the rotor can be computed using quasi-steady analysis or unsteady analysis.

Similarly, stators can be designed to be symmetric or asymmetric in the circumferential direction. Fig. 75 shows the breakdown of the cases to run to test for the hypotheses corresponding to research question 1. Experiment 1.1 - 1.3 are designed to test hypotheses 1.1 - 1.3. Since the three hypotheses state the need for including the additional effects in the design process, the corresponding experiments are designed to compare the results when specific elements are turned on vs. when they are not. Experiment 1.1 compares the parametric variation of the rotor incidence with the case when the incidence is set to its design values. In this case, the rotor response is assumed as quasi-steady and stators as axisymmetric. Therefore the comparison is always made with the case when the design process follows the conventional design method. Experiment 1.2 compares the result of unsteady rotor analysis with quasi-steady analysis. Experiment 1.3 compares the performance difference between axisymmetric and non-axisymmetric stators for all levels and types of distortion. Once these experiments are conducted, Experiment 1.4 is intended to bring them together and test hypothesis 1. In this case, each modeling fidelity is added on a sequential basis as a part of the four-step process shown in Fig. 75 in the Experiment 1.4 section. This experiment will evaluate the effectiveness of the framework in recovering the losses.

	INCIDENCE & DEVIATION		ROTOR RESPONSE		STATOR DESIGN	
	Design	**Parametric**	**Quasi-steady**	**Unsteady**	**Symmetric**	**Asymmetric**
Experiment 1.1	✓		✓		✓	
		✓	✓		✓	
Experiment 1.2	✓		✓		✓	
	✓			✓	✓	
Experiment 1.3	✓		✓		✓	
	✓		✓			✓
Experiment 1.4	✓		✓		✓	
		✓	✓		✓	
		✓	✓			✓
		✓		✓		✓

Figure 75: Experimental setup: Modeling scenarios.

5.3.2 Experiment 1.1: Rotor Blade Angle Optimization

Hypothesis 1.1 claimed that if the fan is designed for an averaged flow, the minimum loss design incidence for non-uniform flow departs from its optimal value for uniform flow. In order to test this hypothesis, two conditions need to be satisfied. First, the rotor losses resulting from the case with parametric incidence variation must be lower than when the parametric variation is not performed. Second, the incidence angle in the former should be different from the case for the uniform flow. The procedure for performing experiment 1.1 is listed below:

- Step 1: Run the aerodynamic design framework on the fan variables in Table 5 by considering design incidence, quasi-steady rotor response, and symmetric stator design for each flow profile mentioned in Fig. 71
- Step 2: Record rotor loss coefficients and incidence angles for each case of Step 1
- Step 3: Run the aerodynamic design framework on the fan variables in Table 5 by considering parametric blade angle variation, quasi-steady response, and symmetric stator design for each flow profile mentioned in Fig. 71
- Step 4: Record loss coefficients and incidence angles for each case of Step 3
- Step 5: Compute the difference in the loss coefficient between Step 2 and Step 4
- Step 6: Validate hypothesis based on the observed discrepancy

The flowchart describing this process is also shown in Fig. 76. Each case's flow profile is analyzed separately in the discussions below, and a general commentary is provided. For each case, results on the relative flow angle (β_1), incidence angle (i_1), mean rotor loss coefficient (ω_p), and mean pressure ratio (PR) are provided.

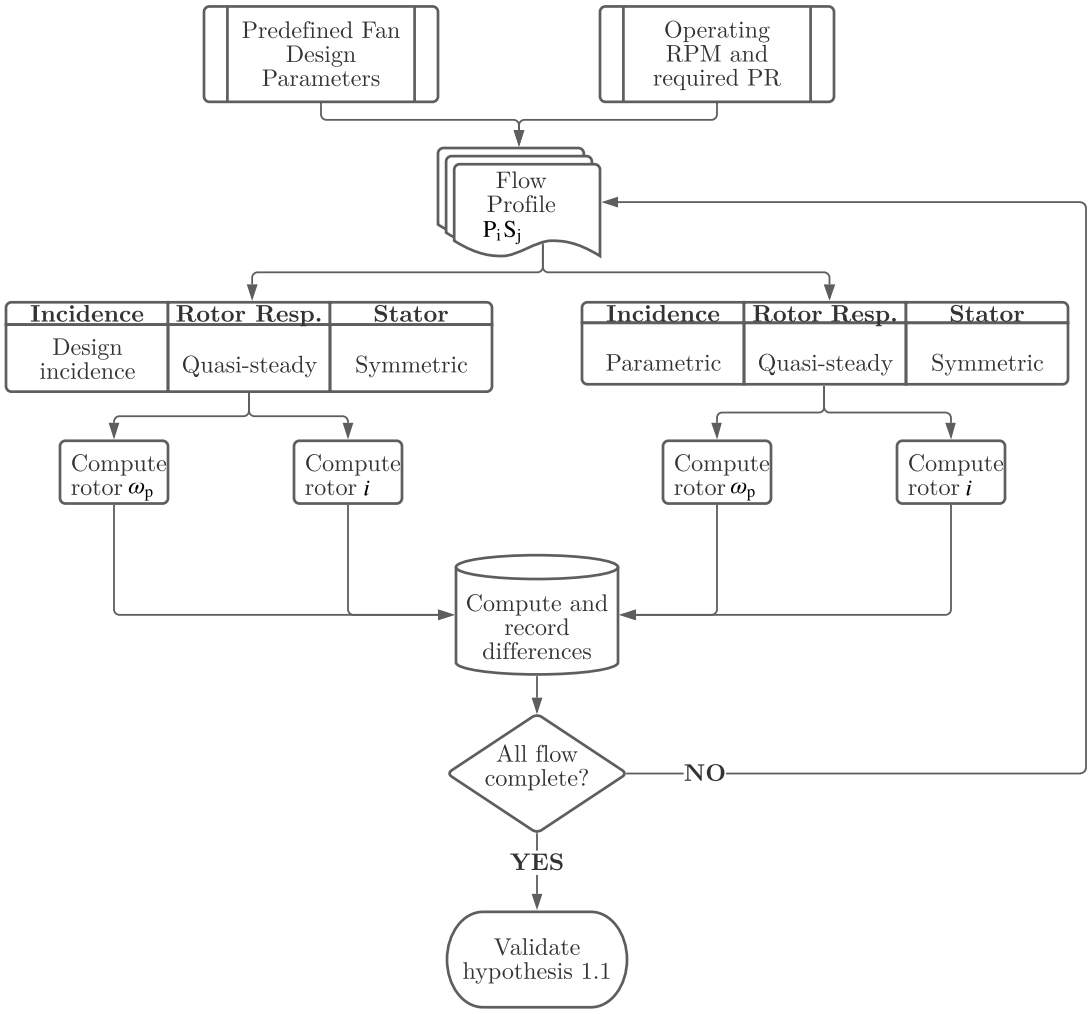

Figure 76: Flowchart describing the experimental setup for Experiment 1.1.

5.3.2.1 Flow Profile: P0S0

Fig. 77 shows the baseline case results for no distortion. Fig. 77(a) shows the overall relative flow angle variation. Since the inflow does not have any radial distortion, the absolute angles are the same for each case. The total conditions for the flow profile are the same along the span at the rotor inlet. Because of the differences in the blade speed at the hub and the tip, the relative conditions are different for these segments. The lower relative inflow angle at the hub, combined with a constant design incidence, forces the blade metal angles at the leading edge to be lower at the hub and higher at the tip. Fig. 77(b) shows the incidence angles at different locations. The design incidence value was set to 4° for all span-wise locations. The rotor loss coefficient, as shown in Eq. 21, is a function of not only the blade angles, but also of the flow velocities, blade angles, and solidity. It is seen that the mean coefficient is constant across the circumferential locations.

Similarly, the pressure rise is also constant at 1.25. The figure shows that both optimized and non-optimized results overlap, suggesting no changes were required. It makes sense since the uniform flow design should need no design changes. For other flow cases, variations relative to this case are discussed. Note that in both cases, the mean pressure rise is set to be constant. The reduction in rotor loss in the optimized case also leads to a reduced camber such that the overall pressure rise is constant in both cases.

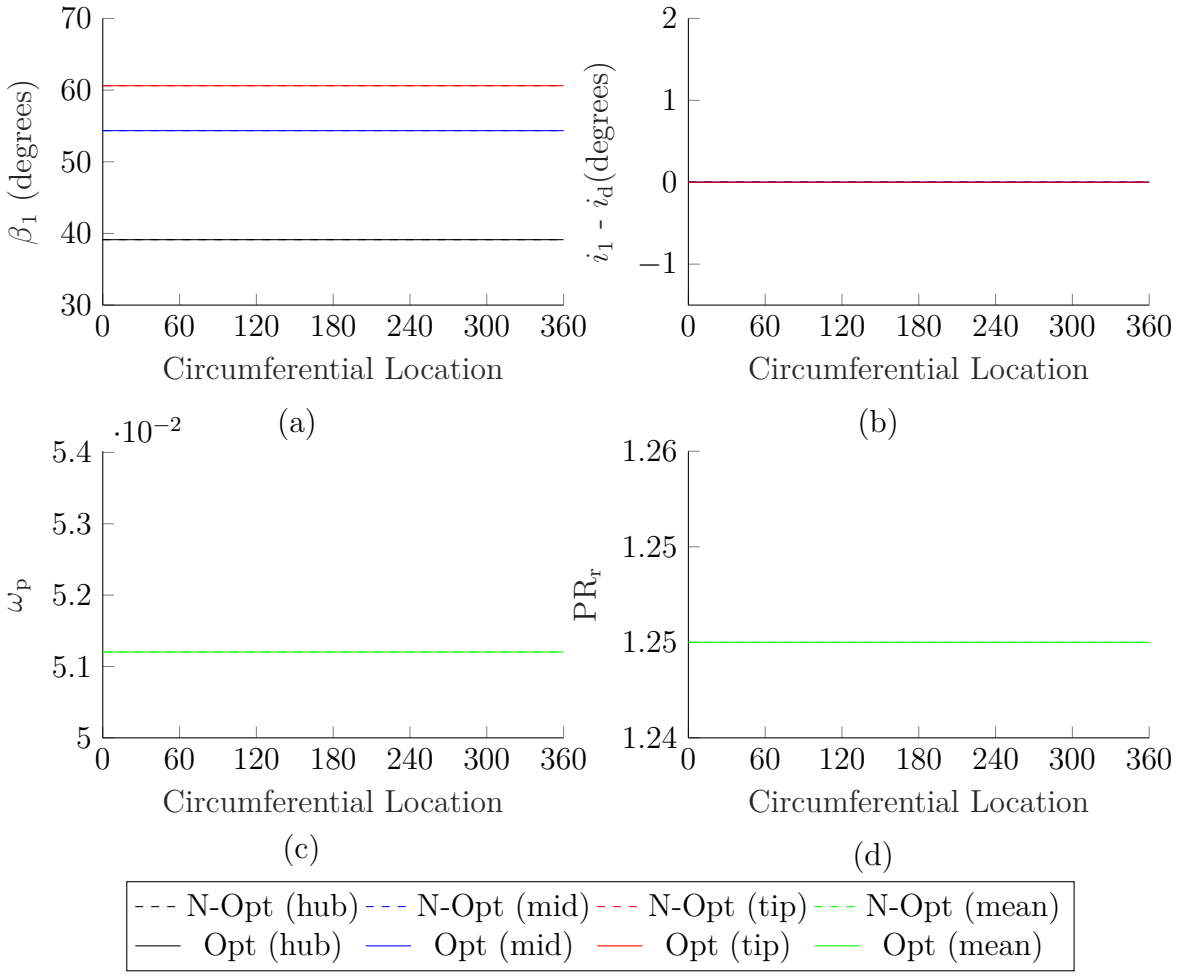

Figure 77: Variation of relative flow angle (a), incidence (b), rotor loss (c), and pressure ratio (d) for flow P0S0.

5.3.2.2 Flow Profile: P1S0

Fig. 78 shows the results for the case with no-swirl and low-intensity total pressure distortion. The dashed curves represent the results without blade angle changes, and the solid curves represent the case where parametric optimization on blade angles was performed. Fig. 78(a) shows the variation of relative flow angles at the rotor inlet. The presence of total pressure distortion, thus velocity distortion, causes the flow velocity to be lowest at 180° for all sections of the span. It also translates to reduced Mach number and reduced relative flow angle at the rotor inlet. For the non-optimized case,

the relative flow angle distortion causes an incidence variation of around 3°, as shown in Fig. 78(b) with the mean at 0°. The incidence variation follows the same nature as the flow angle variation.

The parametric variation of blade angles resulted in a reduced average incidence angle at the rotor inlet with a mean incidence higher than the design incidence by 0.3°. The effect of the change in incidence angles can be seen in Fig. 78(c), where rotor loss coefficients are shown. The distortion presence caused losses in the hub to reduce and other sections to increase in the distorted region. This phenomenon is likely because the losses are proportional to the diffusion factor. The hub diffusion factor is increasing from low values of 0.3 and up as it goes from 0°-180°, while the diffusion factor for the other sections was already in the 0.55s, so increasing it further exacerbates the loss. As a result, the overall pressure rise is also higher in the sections with low mass flow, as shown in Fig. 84(d). In the high mass flow regions, the hub's losses are maximum, and the contribution of these sectors to the mass averaged loss coefficients is also higher. It can be seen that the optimizer has the most considerable effect on the loss coefficients at the high mass flow regions (240°-120°). It comes at the expense of a slightly smaller increase in losses at the low mass flow region for the mid and the tip sections. The overall effect can be seen in the mean loss curves in Fig. 78(c) where the losses are reduced in the high mass flow regions and almost unchanged in the low mass flow regions. A comparatively smaller change in loss coefficients in the low mass flow regions are observed.

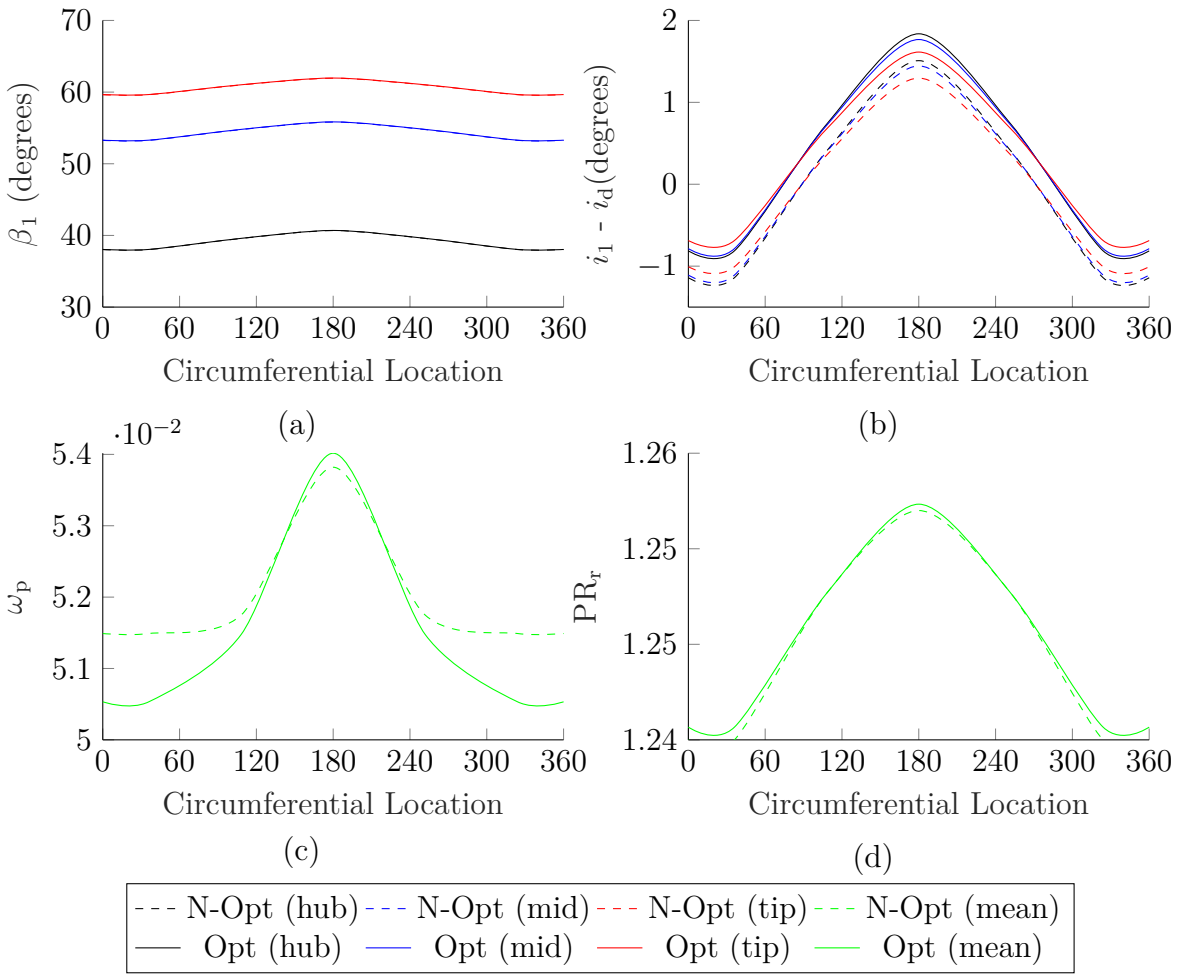

Figure 78: Variation of relative flow angle (a), incidence (b), rotor loss (c), and pressure ratio (d) for flow P1S0.

5.3.2.3 Flow Profile: P2S0

Fig. 78 shows the results of the case with no swirl distortion and mid-intensity total pressure distortion. This case shows a similar behavior as the results shown in Fig. 78 except that all changes are more pronounced. For example, the reduction in mean rotor losses is higher in this case than the case for P1S0.

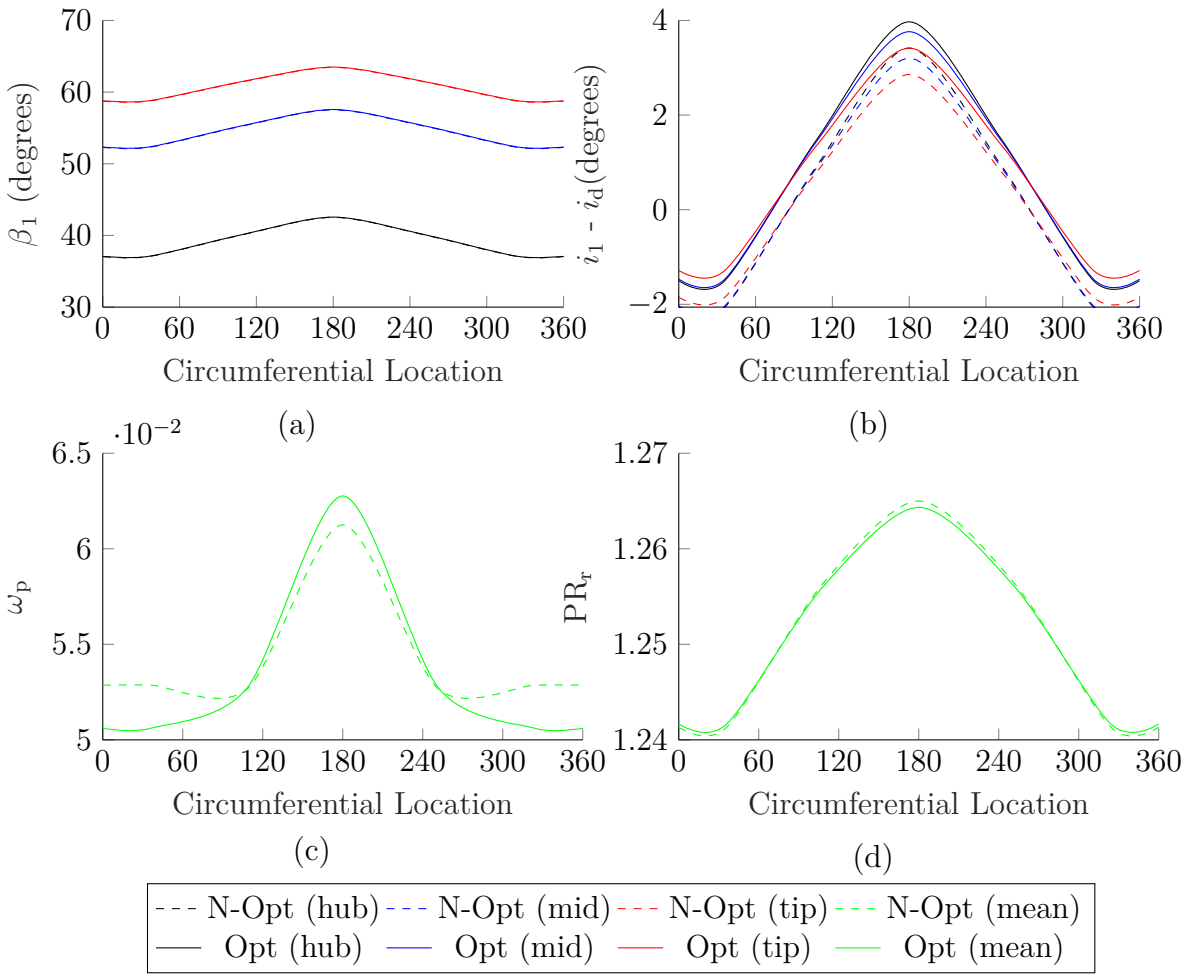

Figure 79: Variation of relative flow angle (a), incidence (b), rotor loss (c), and pressure ratio (d) for flow P2S0.

5.3.2.4 Flow Profile: P3S0

Similarly, Fig. 80 shows the results for the case with no swirl distortion and high-intensity total pressure distortion. The incidence variation is around 9° with the mean equal to the design incidence for the non-optimized case and 0.6° higher than design incidence for the optimized case. The losses in the low mass flow regions are reduced substantially in the optimized case, which resulted in slightly increased pressure rise in these regions. A 30% reduction in overall rotor losses is observed in this case. The pure total pressure distortion cases show that distortion causes increased losses in the

rotor, and optimizing blade incidence angles can help alleviate these losses.

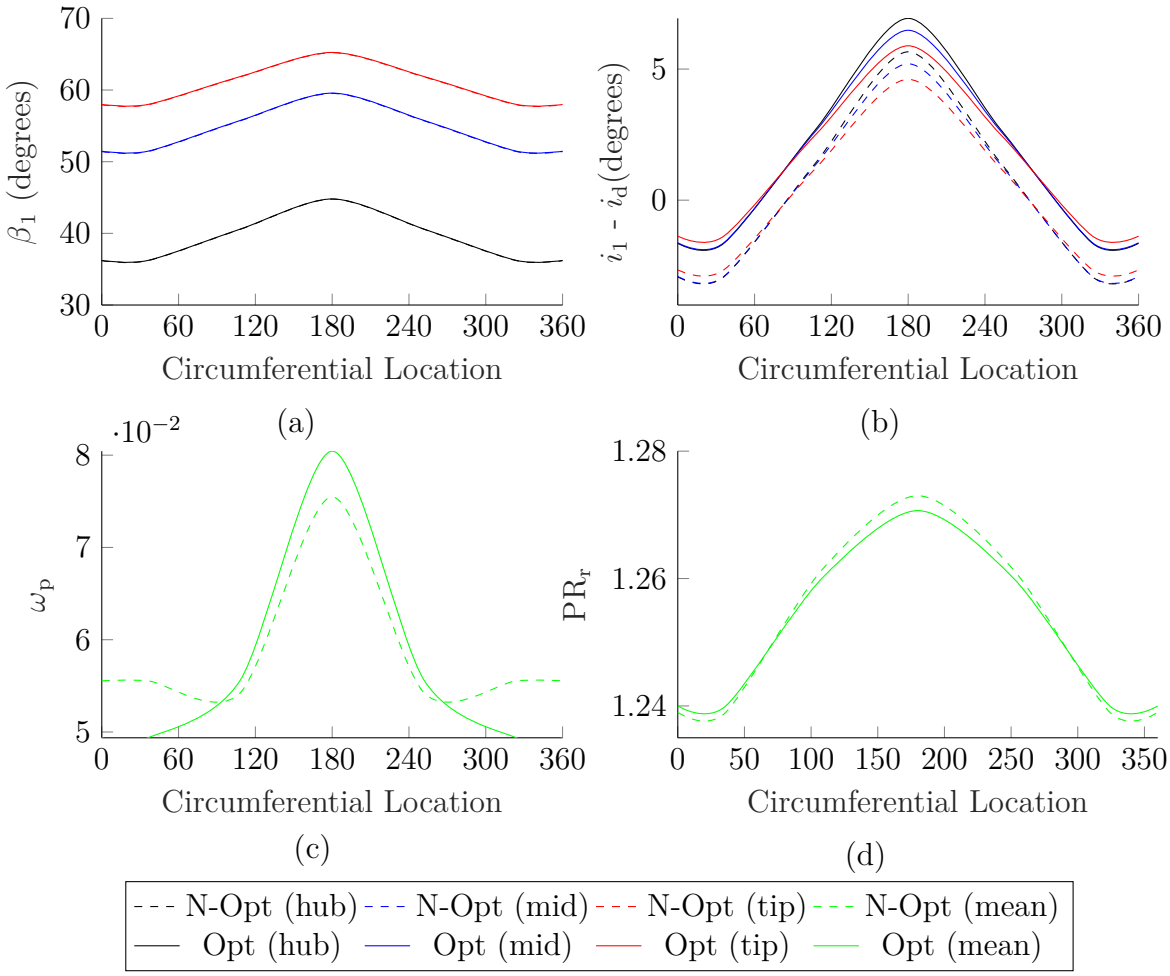

Figure 80: Variation of relative flow angle (a), incidence (b), rotor loss (c), and pressure ratio (d) for flow P3S0.

5.3.2.5 Flow Profile: P0S1

The next set of flow conditions are the cases with no total pressure distortion and pure swirl distortion. Fig. 81 shows the results for the case of low-intensity distortion. Fig. 81(a) shows the variation in relative flow angles at the rotor inlet, which shows a more prominent variation of swirl at the hub. It is caused by the implementation of free vortex condition in the span-wise direction. The free cortex condition ensures that rV_θ is constant along the span. The result is the largest tangential velocity at the

hub to satisfy the free vortex condition. Fig. 81(b) shows the incidence angle variation due to the swirl distortion. Incidence variation of 5° is present at the hub while the mid and the tip sections have a substantial swing in incidence. The positive swirl regions experience a negative reduction in incidence and vice-versa. The rotor losses were higher for the regions between 0° and 180° due to the presence of co-swirl. A larger efficiency was noted for these regions with the co-swirl present. The difference in the losses is not due to the effect of incidence directly, but rather the difference in the flow velocity that swirl generated. No noticeable change in incidence was resulted by the optimization process since the rotor losses could not be lowered further. As seen in Fig. 81(d), the pressure rise profile does not show any noticeable change.

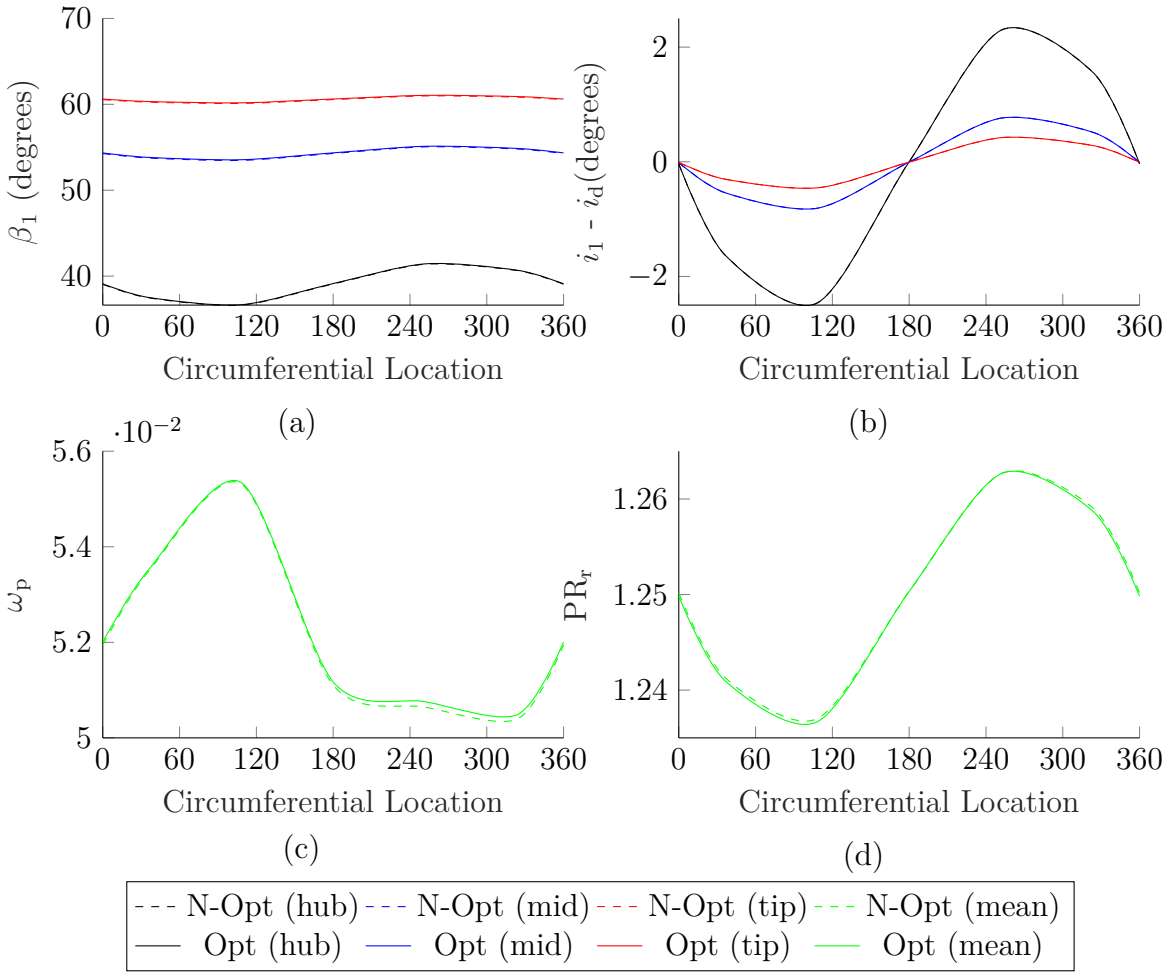

Figure 81: Variation of relative flow angle (a), incidence (b), rotor loss (c), and pressure ratio (d) for flow P0S1.

5.3.2.6 Flow Profile: P0S2

Fig. 82 shows the results for the case with no total pressure distortion and mid-intensity swirl distortion. Similar results as the low-intensity case for P0S1 are observed. The hub incidence swing resulted in a 10° variation. A small difference is observed in Fig. 82(c) in rotor loss coefficients. This difference is attributed to the optimizer's numerical convergence and difference in the initial guesses for both cases.

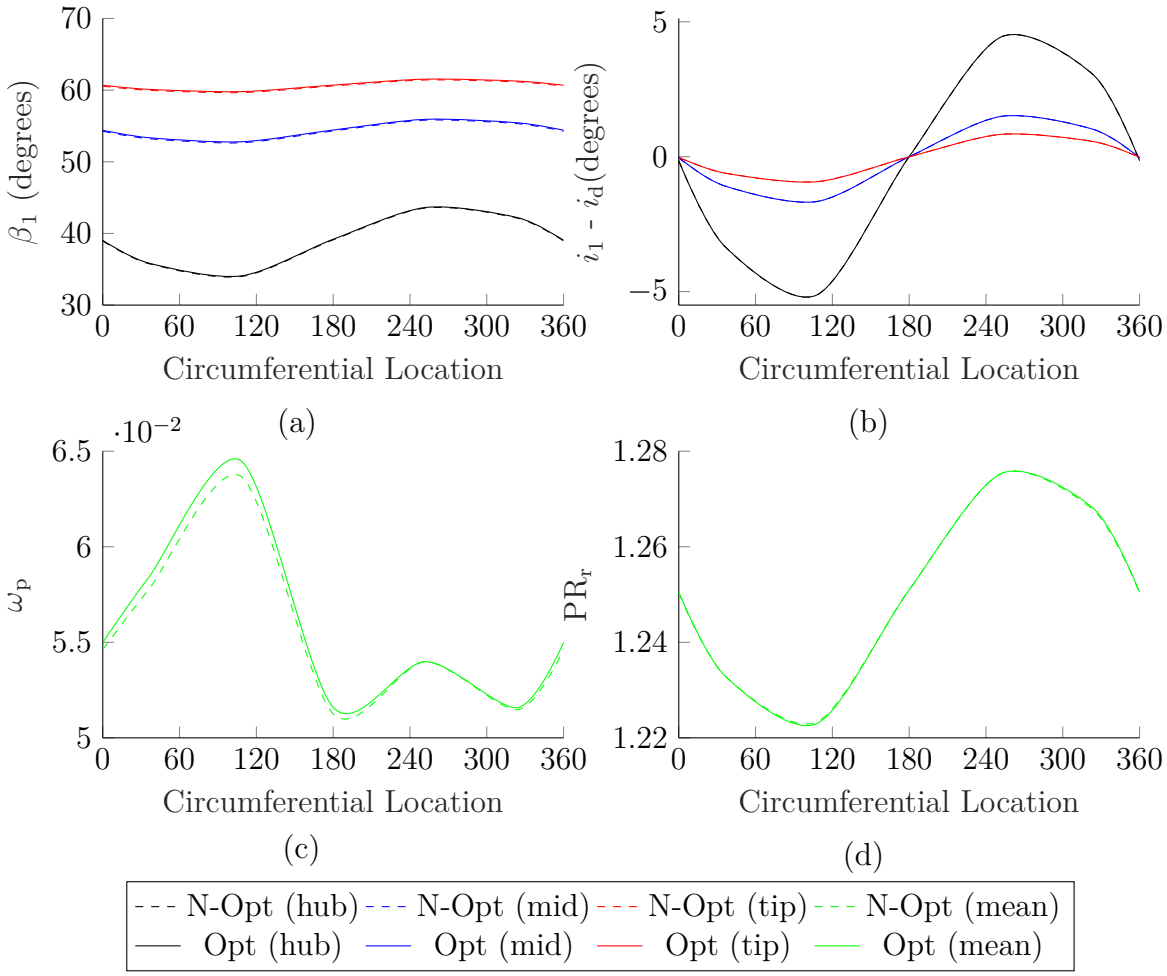

Figure 82: Variation of relative flow angle (a), incidence (b), rotor loss (c), and pressure ratio (d) for flow P0S2.

5.3.2.7 Flow Profile: P0S3

The results for no pressure distortion and high-intensity swirl distortion are shown in Fig. 83. Similar insights obtained from the other two cases of swirl distortion are obtained here. From Fig. 87, it can be seen that the losses recovered using blade incidence optimization were negligible for the cases of pure swirl distortion case. In Figs. 81 - 83, the presence of swirl led to an increased incidence in some regions and reduced incidence in others, so the blade angle optimization trades the losses in one part with the other. It can be said that the impact of blade angle optimization is less

useful for pure swirl distortion compared to pressure distortion.

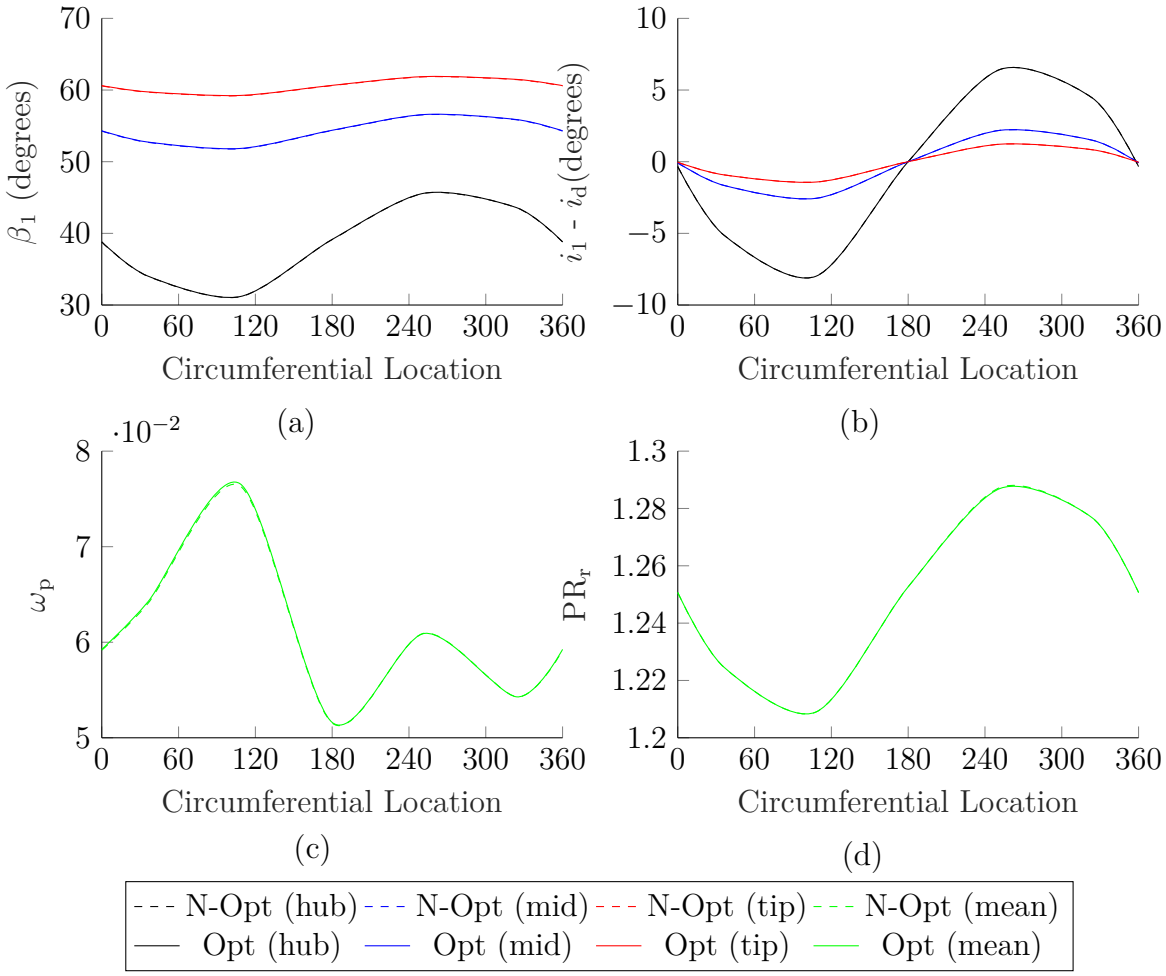

Figure 83: Variation of relative flow angle (a), incidence (b), rotor loss (c), and pressure ratio (d) for flow P0S3.

5.3.2.8 Flow Profile: P1S1

The next three sets of cases deal with a mixture of total pressure and total swirl distortion. Fig. 84 shows the results for the case of low-intensity total pressure and swirl distortion. Fig. 84(a) shows the relative flow angles at the rotor inlet. This flow can be thought of as the superposition of P1S0 and P0S1. It can be observed that combining Figs. 78(a) and 81(a) lead to Fig. 84(a). Fig. 84(b) shows the incidence variation of 5°. In the case of mid and tip regions, this variation is mostly due to total

pressure distortion. In the hub region, it is due to the combination of both. From 0° - 100°, swirl angle and mass flow, both are decreasing. A decrease in swirl results in decreased incidence whereas decreasing mass flow increases the incidence. The overall effect is dominated by swirl from 0° to 50°, after which the incidence increase due to mass flow is larger than incidence increase due to swirl. A similar argument can be made for the rest of the variation from 100° to 360°. Fig. 87 shows that the blade angle optimization reduced the loss coefficients by ≈15%. For P1S0, the more than 60% losses were reduced when optimizing blade angles, and for P0S1, the losses were almost the same. It implies that superposing inlet distortion profiles do not imply superposition in the rotor response. This can be seen in Fig. 84(c) where the losses are reduced in the high mass flow region in the co-swirl region.

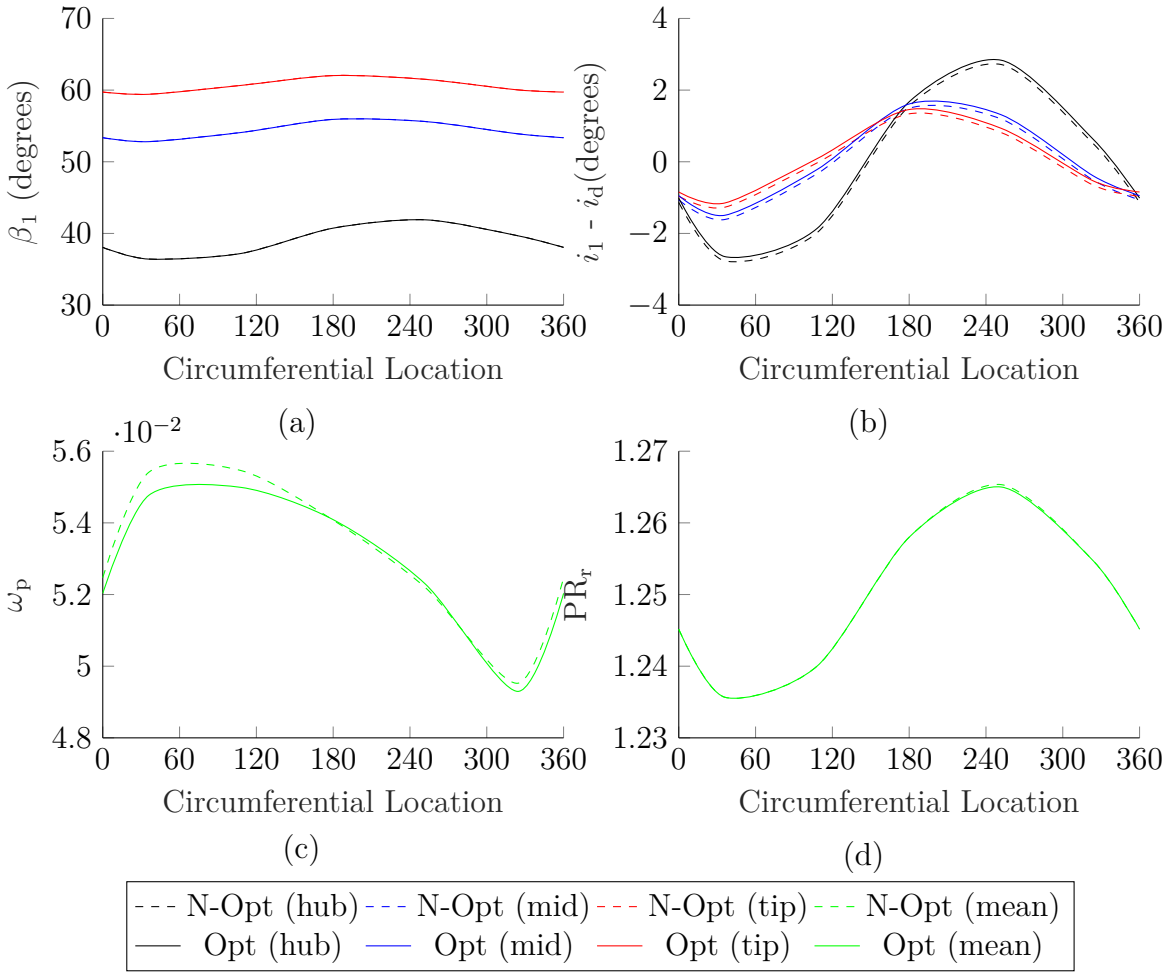

Figure 84: Variation of relative flow angle (a), incidence (b), rotor loss (c), and pressure ratio (d) for flow P1S1.

5.3.2.9 Flow Profile: P2S2

Fig. 85 shows the results for the case of mid-level total pressure and swirl distortion. The explanation of the general trends of the flow behavior is provided in the preceding case P1S1. For the case of P2S2, blade angle optimization was able to reduce the rotor losses substantially in the 0° to 120° by increasing the incidence angle by 1° compared to the non-optimized case. The overall effect is an overall recovery of around 15% of rotor losses. The trade-off was a comparatively lower increase in the losses between 180° to 300°. The net effect was a decrease in the averaged rotor loss.

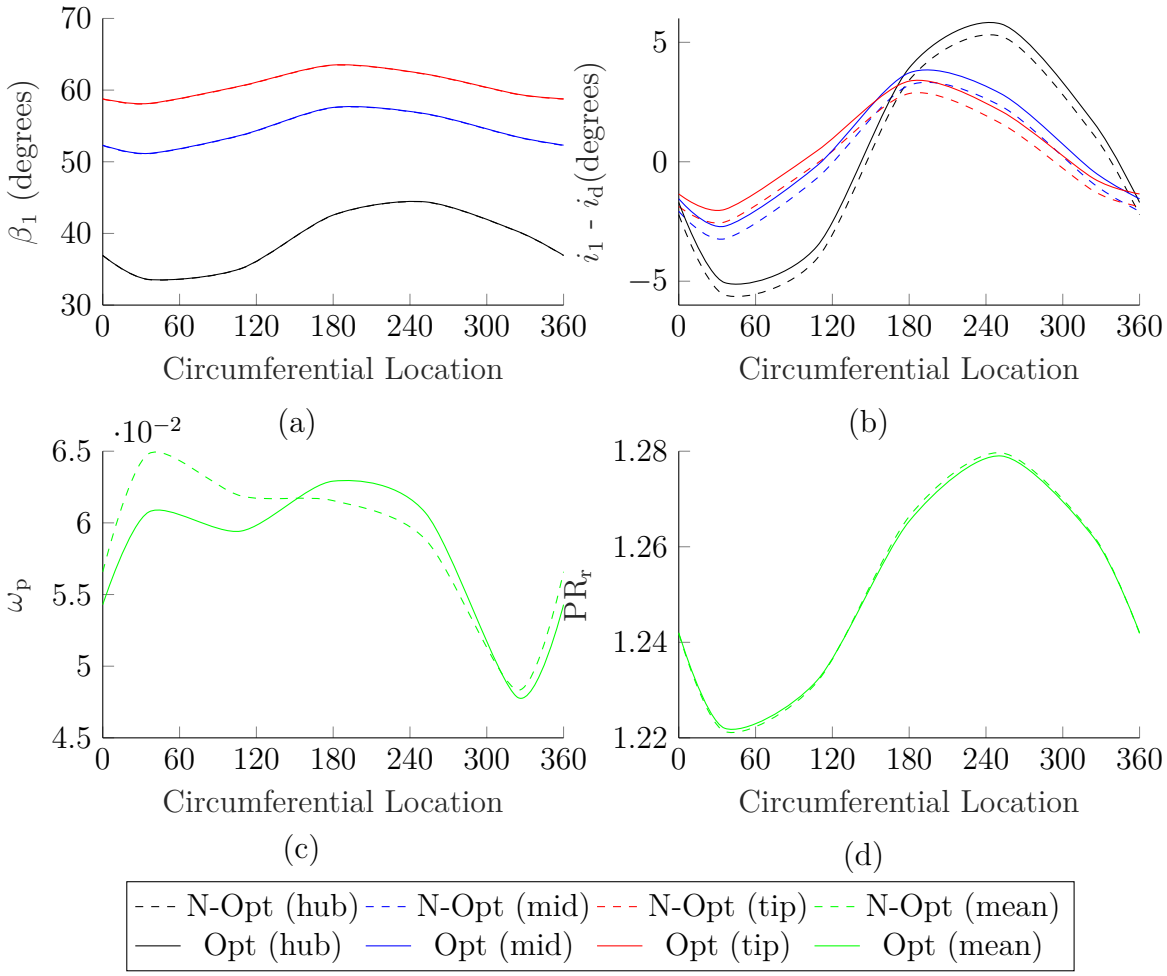

Figure 85: Variation of relative flow angle (a), incidence (b), rotor loss (c), and pressure ratio (d) for flow P2S2.

5.3.2.10 Flow Profile: P3S3

Fig. 86 shows the results for high-intensity total pressure and swirl distortion. The change in blade angles was able to recover 15% of the losses. The rotor loss profiles in Fig. 86(c) show similar trends as observed in P2S2, except the effects are more amplified.

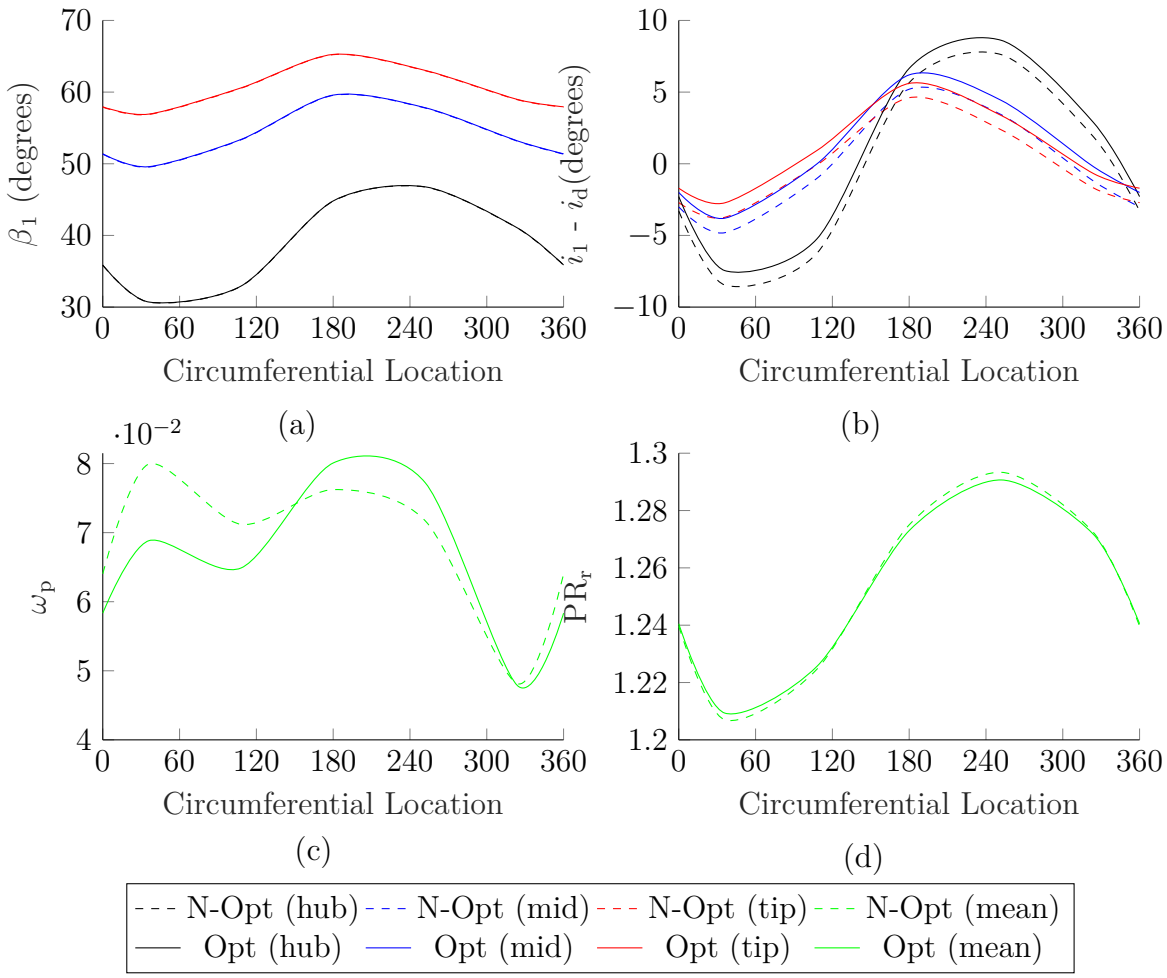

Figure 86: Variation of relative flow angle (a), incidence (b), rotor loss (c), and pressure ratio (d) for flow P3S3.

5.3.2.11 Change in rotor loss coefficients for all flow profiles

Fig. 87 shows the change in loss coefficients in the optimized design vs. the non-optimized design for various flow profiles. As evident, in the presence of no distortion (P0S0), the blade angles were already optimal, so no change was necessary. Cases with pure total pressure distortion (P1S0, P2S0, P3S0) observed a non-linear reduction in rotor loss coefficients with the linear increase in distortion intensity. Rotor losses reduced by 1% to 4% of the losses in the clean flow. In the cases of pure swirl distortion (P0S1, P0S2, P0S3), no change in rotor losses was observed. In the third set of cases

with both total pressure and swirl distortion (P1S1, P2S2, and P3S3), the reduction in losses ranged from 0.5% to 5% of the clean flow losses. It can be seen that the optimization of blade angles had more impact in the case of combined distortion.

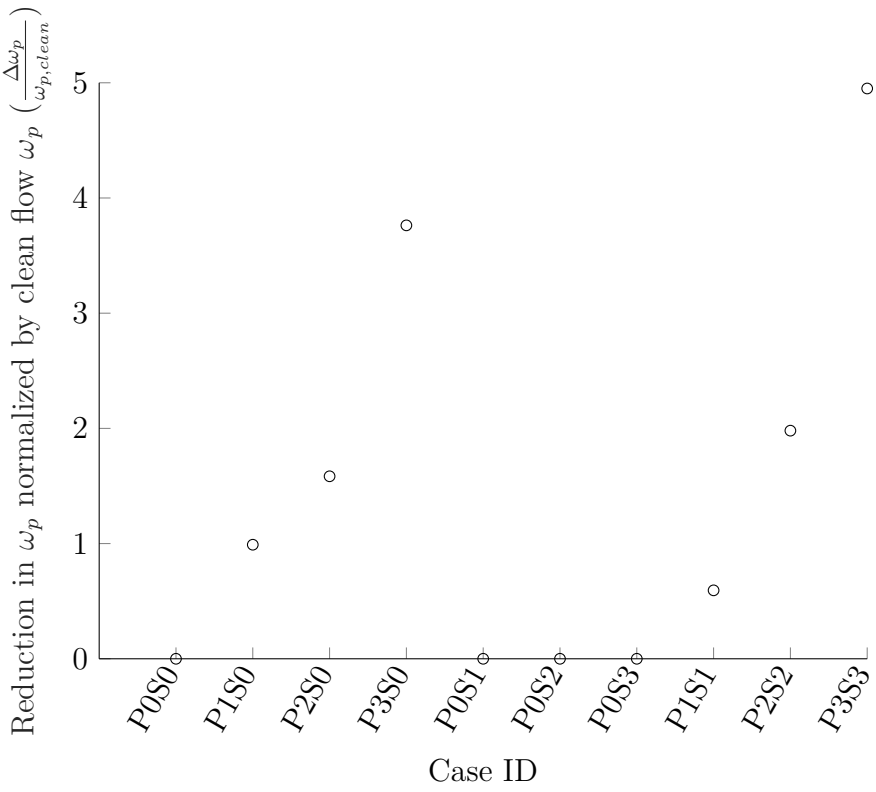

Figure 87: Change in rotor loss coefficient normalized by rotor loss in clean flow for various flow cases.

Fig. 87 alone does not provide a clear description of the importance of optimizing the rotor angles. It is important to understand how much of the losses were recovered compared to the clean operating condition. If the parametric variation of the rotor blade angles reduced the same absolute amount of losses in a low-intensity case and a high-intensity case, then the optimization was more effective in the low-intensity case. The overall loss when operating in the distorted condition is comparatively lower for this case than the high distortion case.

Fig. 88 shows the percentage of rotor losses recovered through the optimization

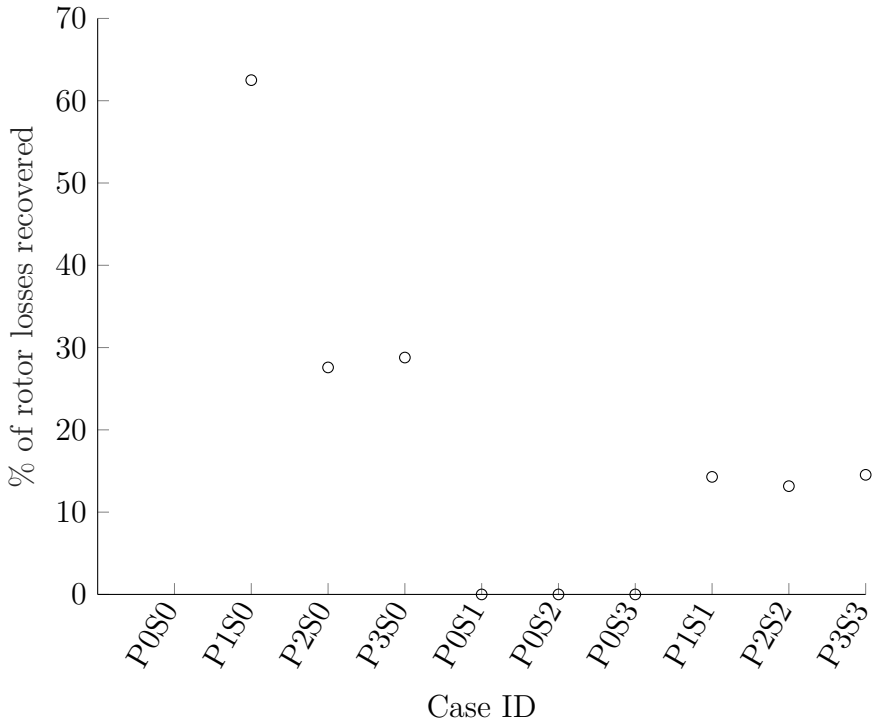

Figure 88: Percentage of the rotor losses recovered.

process. A slightly different message is conveyed here. Although the case with no swirl distortion and only total pressure distortion (P1S0) had a 1% reduction in the rotor loss coefficient compared to the clean case, this accounted for about 60% of the losses. In the case with pure total pressure distortion (P1S0, P2S0, and P3S0), no loss was recovered. In cases with combined distortion (P1S1 P2S2, P3S3), the losses recovered had a narrow range of around 15%. Therefore, in typical BLI distortion cases, a recovery in rotor losses of 15% can be expected using the blade angle optimization.

These results show that the parametric optimization of incidence angles is more effective for low distortion cases with pure total pressure distortion. The mass flow variation is present and is not effective for pure swirl distortion cases. The general discussions of why this is the case have been discussed in the detailed results for each flow case.

Fig. 89 shows the departure of the design incidence in the "uniform" design mode needed to reach these optimal losses in the "non-uniform" off-design mode. The vertical

axis shows the departure of the design incidence angles. Few general observations can be made. First, the case with no distortion (P0S0) observed no change in the design incidence angle. The same was the case with pure swirl distortion cases (P0S1, P0S2, P0S3). Second, all other cases observed minimum losses with increased design incidence angle. Third, the incidence variation ranged between 0° and 1.5°. The variation in design incidence is somewhat similar to the reduction in the rotor loss coefficient, as shown in Fig. 87. The change in design incidence angle affects the overall camber of the blades, which ultimately defines the blade row's off-design performance while operating in distorted inflow conditions. The behavior of the incidence angle is monotonic in terms of reducing overall rotor losses.

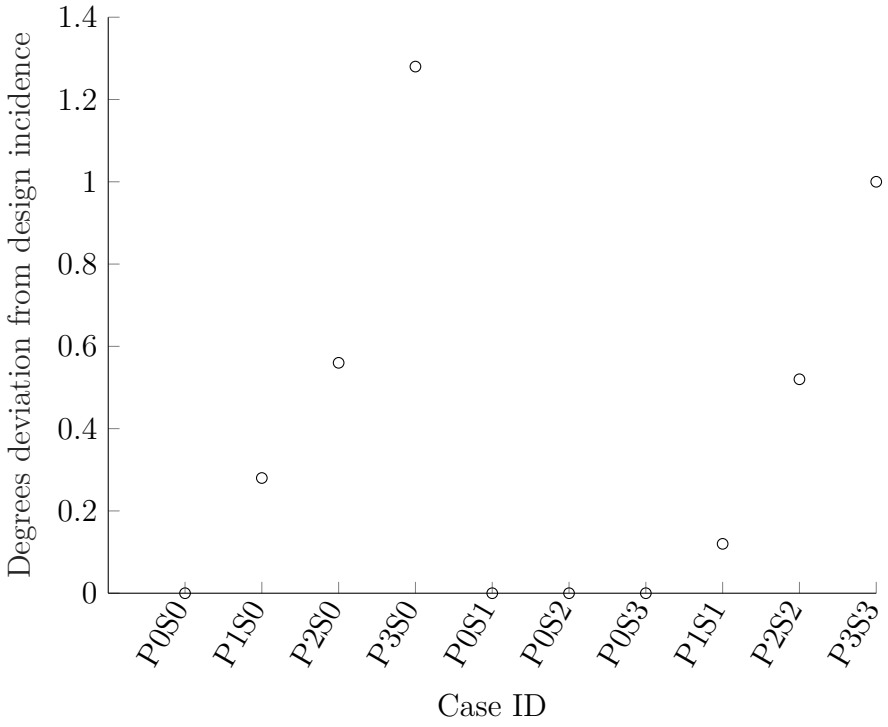

Figure 89: Optimization results: Deviation from design incidence.

One observation made in all the cases was that the hub rotor losses for the design test case were the highest. Therefore, the optimal search of incidence angle was dominated mainly by the hub region trends since the goal was to minimize the overall rotor loss. It highlights an opportunity to reduce the losses further. One scalar was

used to modify the design angles for the hub, mid, and the tip in all these cases. Instead, if each cross-section had a separate optimizer, then trade-offs in every cross-section could be seen. This process is not implemented in this thesis but is stated here to highlight the potential for further reduction in losses.

5.3.3 Experiment 1.2: Rotor Unsteady Response

The computation of unsteady rotor performance involves calculation of unsteady lift coefficient based on Theodorsen's theory. The results of the airfoil unsteady model is verified for a simple sinusoidal pitching condition ($\alpha = \alpha_0 + A_0 sin(\omega t)$) where $\alpha_0 = 0°$, $A_0 = 10°$, and $k = \frac{c}{U_\infty} / \frac{2\pi}{\omega}$. The time varying lift coefficients of the airfoil is observed in Fig. 90. The results shown here exactly match with the pitching results shown by Gulcat [64].

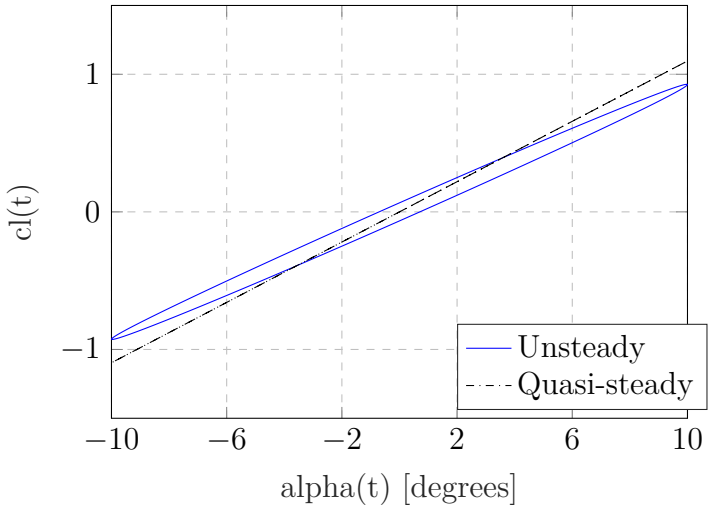

Figure 90: Quasi-steady and unsteady c_l of a thin airfoil pitching about 0°[amplitude = 10°, k = 0.1].

Hypothesis 1.2 claimed that unsteady rotor response measured in terms of blade forces and pressure rise deviate from the quasi-steady response. Experiments are carried out on two fronts to test this hypothesis. First, the baseline rotor design is subjected to the various distorted inflows, as described in Fig. 71. The deviation of

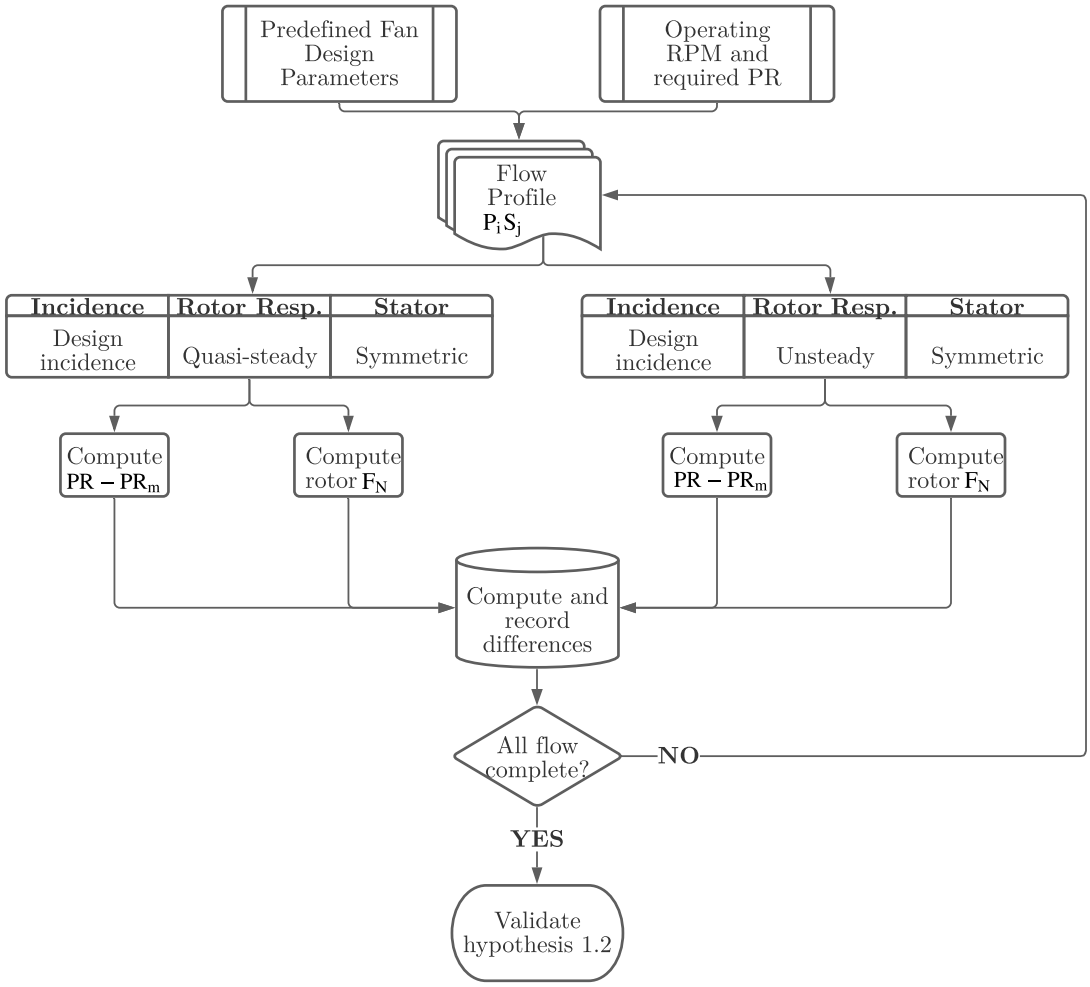

Figure 91: Flowchart describing the experimental setup for Experiment 1.2.

the pressure rise at each circumferential location from the mean pressure rise for both quasi-steady and unsteady response is analyzed. The difference in the normal forces predicted by the quasi-steady and unsteady forces are computed using the formula in Eq. 92.

$$\Delta F_{uns-qs}(\theta) = \frac{F_{uns} - F_{qs}}{F_{uns}} \times 100 \tag{92}$$

The procedure for performing experiment 1.2 is listed below. The flowchart describing the process is also shown in Fig. 91.

- Step 1: Run the aerodynamic design framework on the fan variables in Table 5 by considering design incidence, quasi-steady rotor response, and symmetric stator design for each flow profile mentioned in Fig. 71
- Step 2: Record rotor normal force and pressure rise variation along the circumference for each case of Step 1
- Step 3: Run the aerodynamic design framework on the fan variables in Table 5 by considering design incidence, unsteady rotor response, and symmetric stator design for each flow profile mentioned in Fig. 71
- Step 4: Record rotor normal force and pressure rise variation along the circumference for each case of Step 3
- Step 5: Compute the difference in normal force between Step 2 and Step 4
- Step 6: Compute the difference in the variation in pressure rise along the circumference between Step 2 and Step 4
- Step 7: Qualify hypothesis based on observed discrepancies from Step 5 and Step 6

5.3.3.1 Flow Profile: P0S0

Fig. 92 shows the results for the baseline flow profile. The mean blade forces and the pressure rise are constant throughout the annulus. No variation on either of these parameters is observed.

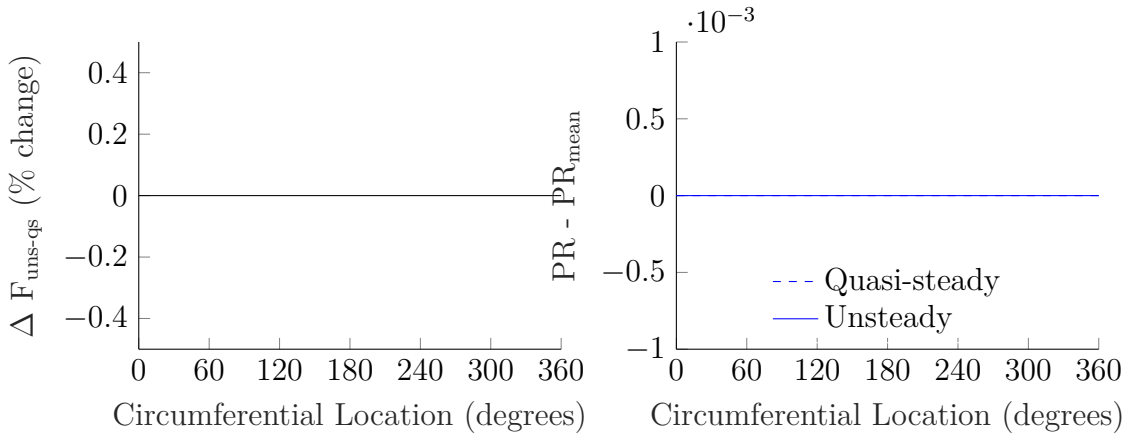

Figure 92: Circumferential variation of mean blade forces [left] and pressure rise [right] for flow P0S0.

5.3.3.2 Flow Profiles: P1S0, P2S0, P3S0

Figs. 93 - 95 show the results for the case of pure total pressure distortion for low, mid, and high intensities respectively. The vertical axes of all three figures are fixed to the same range. It was interesting to note that the mean pressure rise for the rotor was 1.26 for both quasi-steady and unsteady responses in all cases. For the case of P1S0, the quasi-steady behavior is only slightly different from the unsteady behavior. The quasi-steady response leads to the unsteady response by a few degrees. The variation in the normal force has an amplitude of less than 1%. For P2S0, the amplitude in the normal force difference is around 2%. The pressure ratio plots show a noticeable difference between the quasi-steady and unsteady responses. In locations where the unsteady pressure rise is lower than the quasi-steady pressure rise, the normal force change is a negative value and vice-versa. Although the incoming flow is symmetric around 180°, the variation in the normal force is not. This phenomenon is because when rotating from 0° - 180°, the rotor experiences an increase in the incidence angle. Therefore, the unsteady response is lower than the instantaneous quasi-steady response because when the unsteady response catches up with the quasi-steady response, the quasi-steady condition has already changed. An opposite trend

is found from around 180° - 360°. As the mass flow increases, the incidence angles decrease. The quasi-steady response at time $t + \delta t$ is smaller than the quasi-steady response at time t. When the unsteady response catches up with the quasi-steady response at time $t + \delta t$, the quasi-steady condition has already changed, and the unsteady response is comparatively higher. For the flow P3S0, a 4% amplitude in the force difference is observed. The pressure profile is also substantially different between the quasi-steady and unsteady responses. In all cases of P1S0, P2S0, and P3S0, regions of low mass flow correspond to a higher pressure rise, in qualitative agreement with the parallel compressor theory. Larger intensities resulted in deviation in the unsteady response, and that the normal force difference was proportional to the change in this deviation.

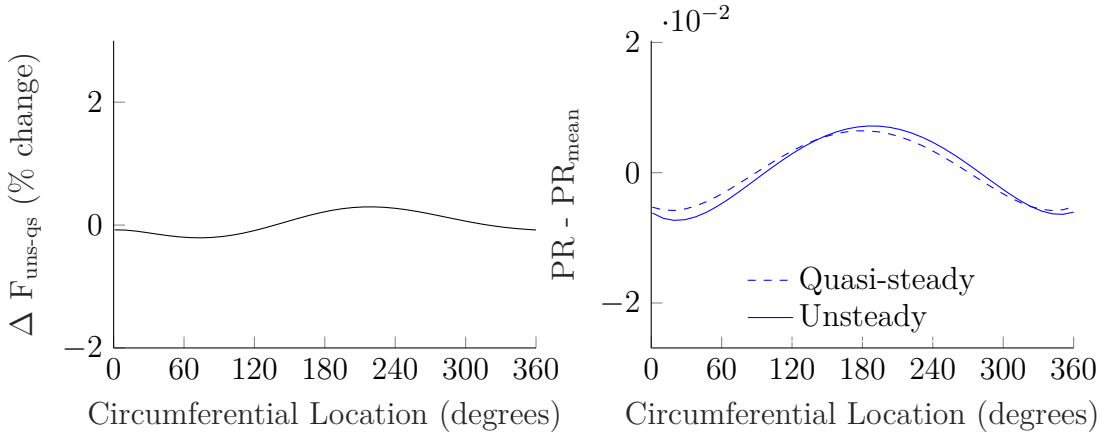

Figure 93: Circumferential variation of mean blade forces [left] and pressure rise [right] for flow P1S0.

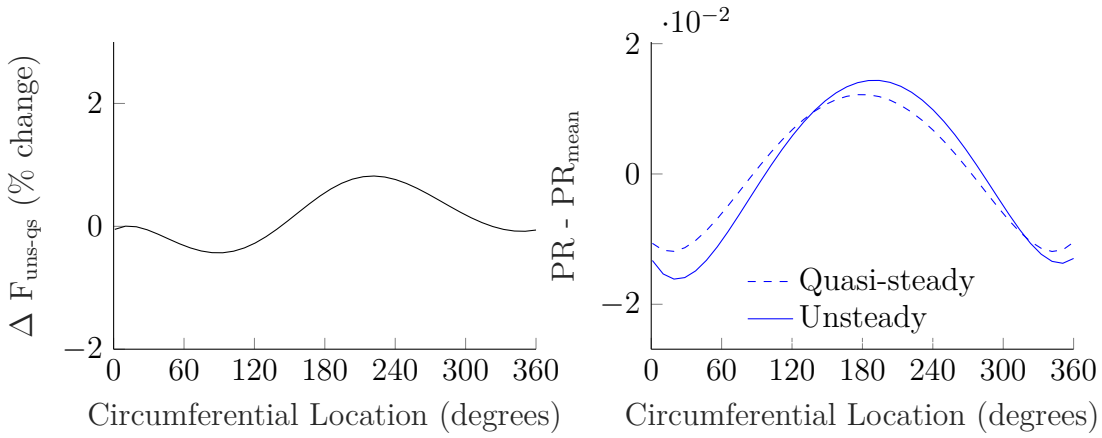

Figure 94: Circumferential variation of mean blade forces [left] and pressure rise [right] for flow P2S0.

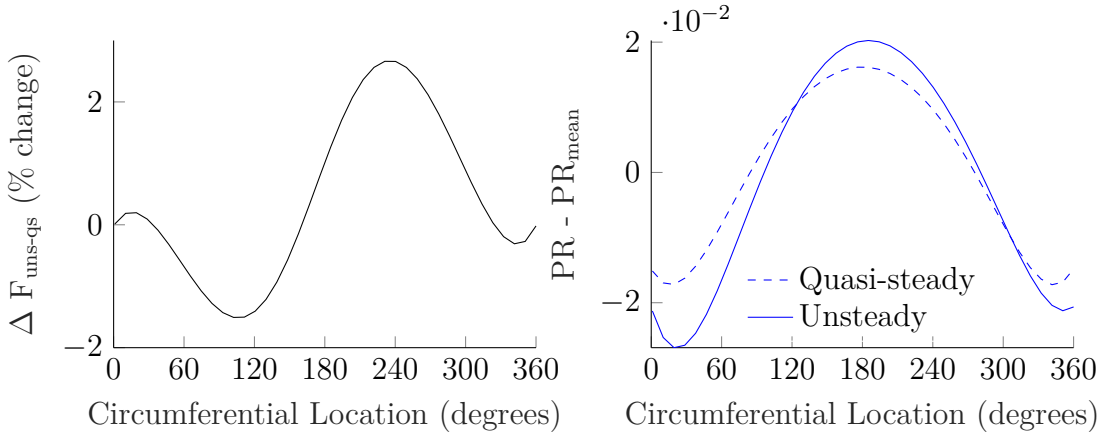

Figure 95: Circumferential variation of mean blade forces [left] and pressure rise [right] for flow P3S0.

5.3.3.3 Flow Profiles: P0S1, P0S2, P0S3

Figs. 96 - 98 show the results for the case of pure swirl distortion for low, mid, and high intensities respectively. All vertical axis have the same ranges. The first observation is that the normal force difference's amplitude is higher for these cases compared to the pure total pressure distortion cases. For these cases, the same can be said about the normal force difference amplitude that it increases with increasing intensity. The amplitude of the normal force difference ranges between 4% and 8%. Comparing

Fig. 95 and Fig. 96, it can be seen that in the case of P3S0, a pressure rise amplitude of 0.04 found a 4% amplitude in normal forces, whereas a pressure rise amplitude of 0.03 in the case of P0S1 resulted in a 3% amplitude in the normal force difference. The reason why swirl variation created a larger force variation is likely because the unsteady response is more sensitive to the tangential velocity difference. The presence of swirl distortion changes the tangential velocities at the rotor exit. For the three cases considered, the variation in pressure ratio profile increased with increasing distortion intensity.

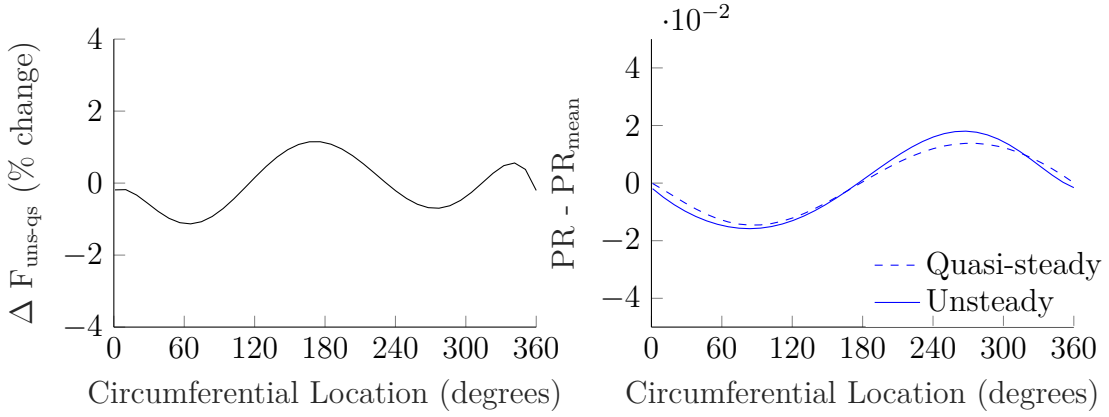

Figure 96: Circumferential variation of mean blade forces [left] and pressure rise [right] for flow P0S1.

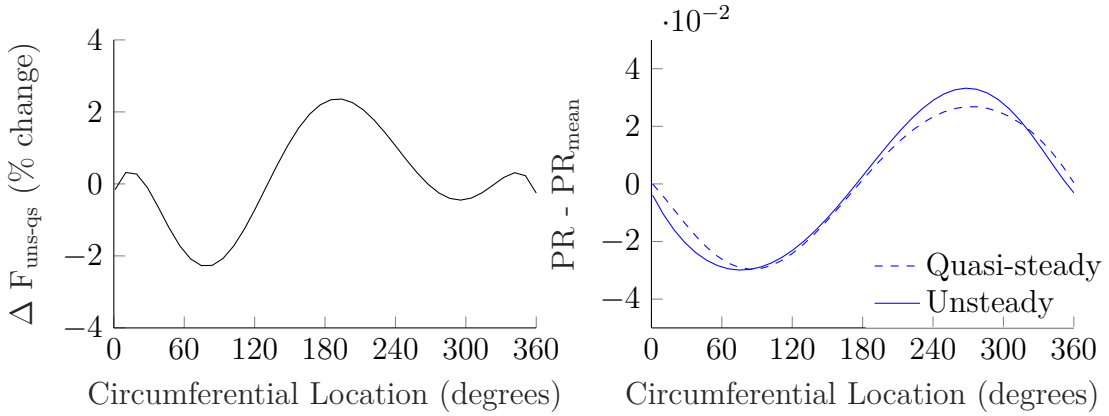

Figure 97: Circumferential variation of mean blade forces [left] and pressure rise [right] for flow P0S2.

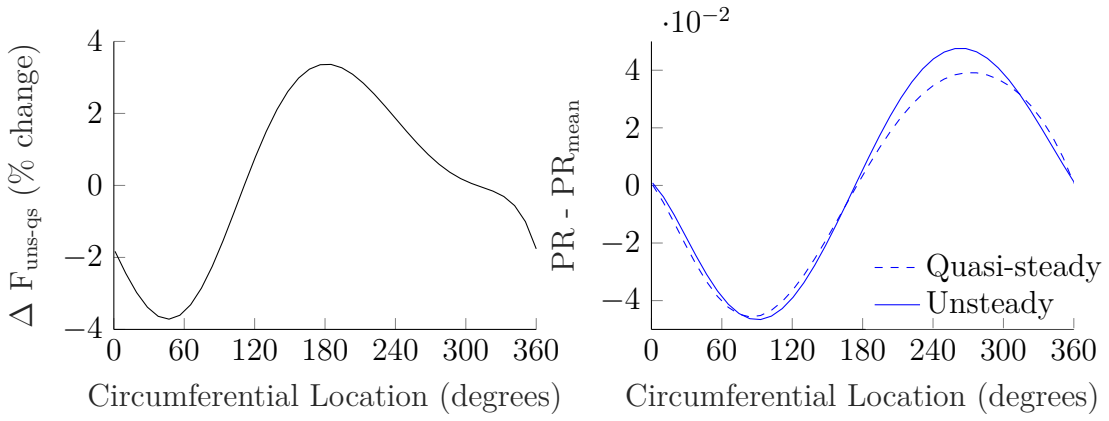

Figure 98: Circumferential variation of mean blade forces [left] and pressure rise [right] for flow P0S3.

5.3.3.4 Flow Profiles: P1S1, P2S2, P2S3

All cases with a combination of swirl and total pressure distortion with low, mid, and high intensities represented by flow profiles P1S1, P2S2, and P3S3 were considered in the third set of cases tested. Analyzing the results shown in Fig. 99 - 101, the amplitude in the normal force difference increases with increasing distortion. It also correlates to increasing differences in the pressure ratio curves between quasi-steady and unsteady responses. It is interesting to note that although higher unsteadiness was observed in the mixed distortion case, the case of pure swirl distortion showed a larger variation in the normal force compared to the corresponding case of the mixed intensities of distortion. It implies that the normal force amplitude can be used as an approximate parameter to measure the relative unsteadiness within a flow type. However, comparing the relative unsteadiness between two flow profiles using this parameter is not guaranteed to provide the relative unsteadiness's true information.

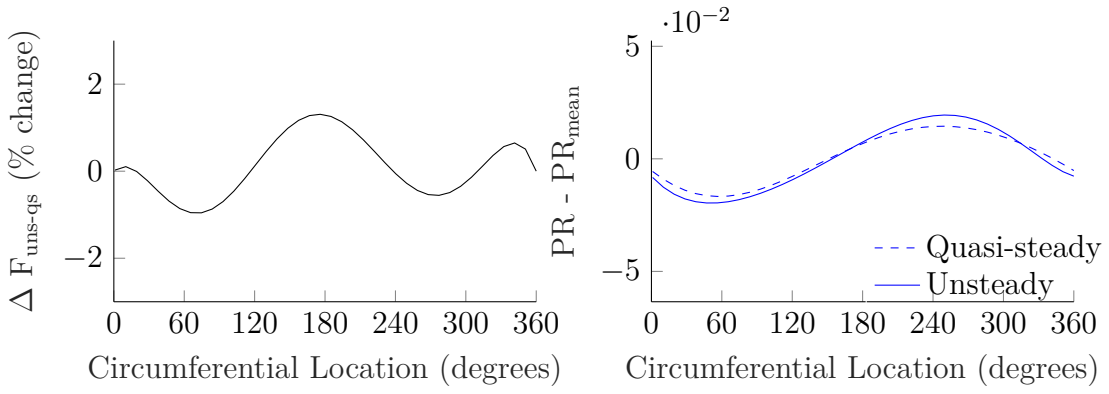

Figure 99: Circumferential variation of mean blade forces [left] and pressure rise [right] for flow P1S1.

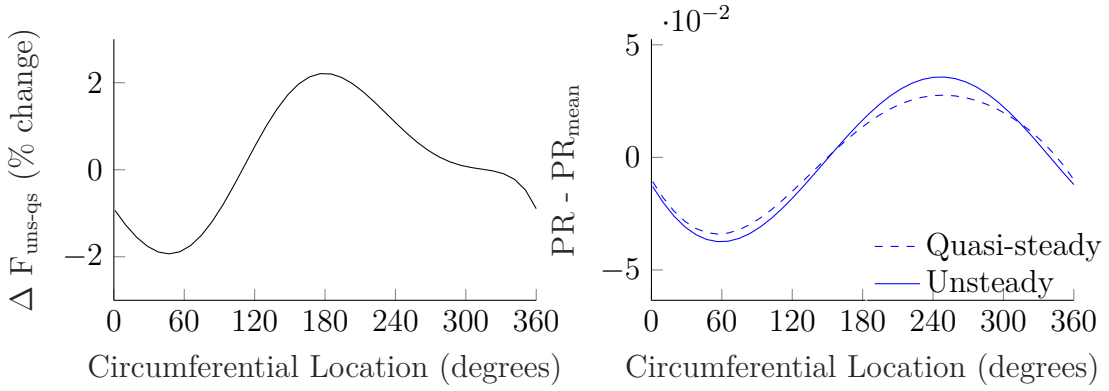

Figure 100: Circumferential variation of mean blade forces [left] and pressure rise [right] for flow P2S2.

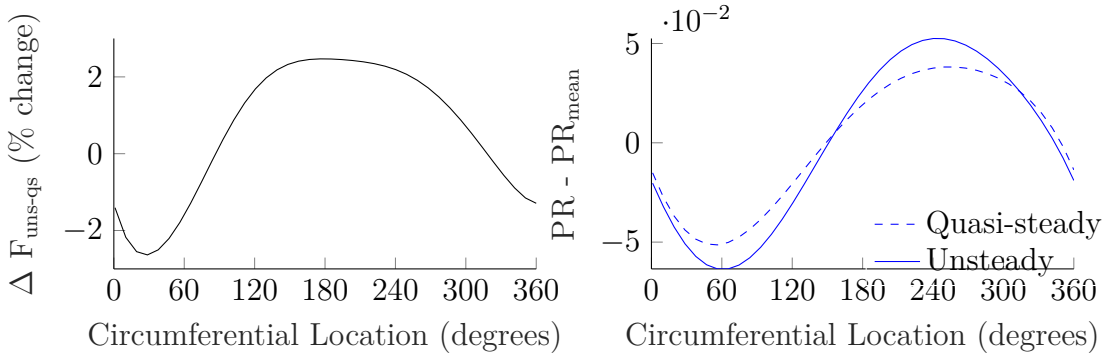

Figure 101: Circumferential variation of mean blade forces [left] and pressure rise [right] for flow P3S3.

5.3.4 Experiment 1.3: Non-Axisymmetric Stator Design

Hypothesis 1.3 claimed that the required degree of asymmetry in stators would increase with increasing distortion intensity and be observed less for swirl distortion than total pressure distortion. Experiment 1.3 is designed to test this hypothesis. For all flow cases, a rotor is designed for the averaged uniform flow. No rotor blade angle optimization is performed. The rotor exit flow computed from quasi-steady analysis is used as an inflow to the stator inlet angle design. The design incidence for stator blades is set to 0°. Zero swirl at the stator exit is prescribed as a boundary condition. The procedure for performing experiment 1.3 is listed below. The flowchart describing the process is also shown in Fig. 102.

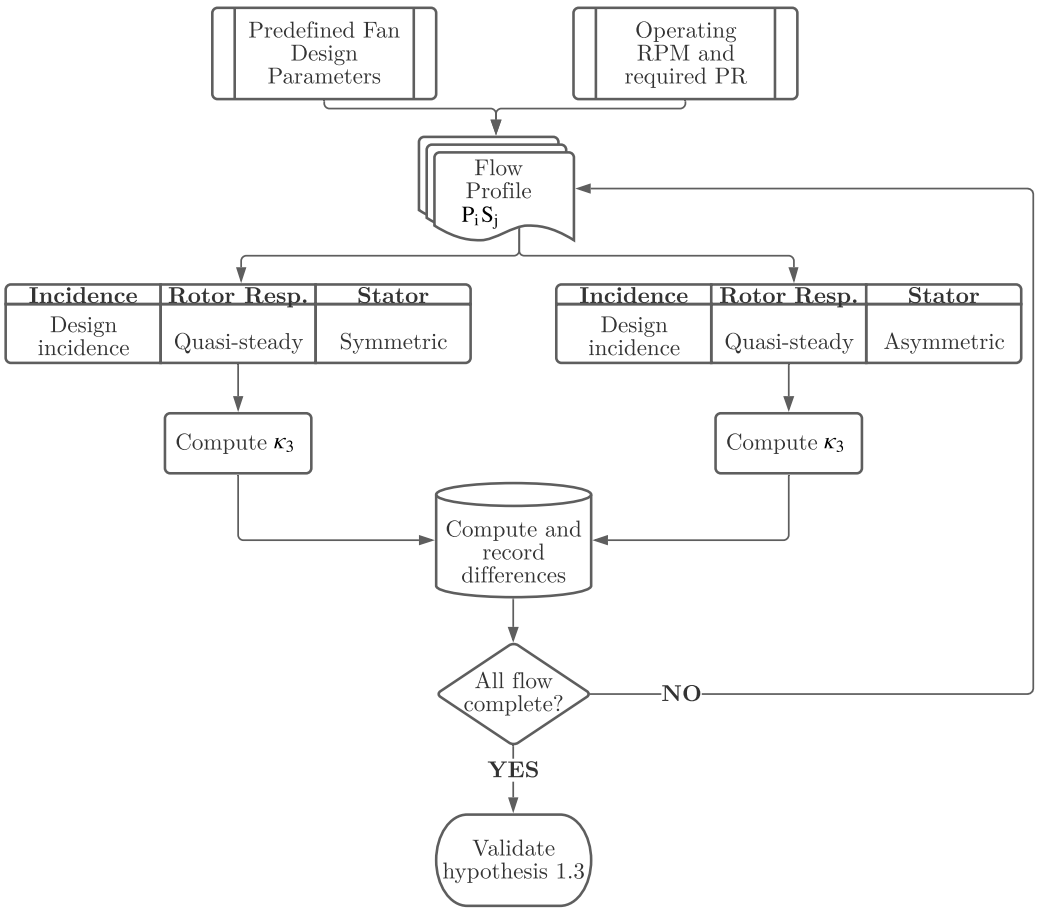

Figure 102: Flowchart describing the experimental setup for Experiment 1.3.

- Step 1: Run the aerodynamic design framework on the fan variables in Table 5 by considering design incidence, quasi-steady rotor response, and symmetric stator design for each flow profile mentioned in Fig. 71
- Step 2: Record stator blade angles at the inlet for each case of Step 1
- Step 3: Run the aerodynamic design framework on the fan variables in Table 5 by considering design incidence, quasi-steady response, and asymmetric stator design for each flow profile mentioned in Fig. 71
- Step 4: Record stator blade angles at the inlet for each case of Step 3
- Step 5: Compute the difference in the stator angles between Step 2 and Step 4
- Step 6: Compute the difference in stator blade angles between the pure swirl distortion and pure total pressure distortion cases in Step 4
- Step 7: Validate hypothesis based on observed discrepancies in Step 5 and 6

5.3.4.1 Flow Profiles: P0S0, P1S0, P2S0, P3S0

Fig. 103 shows the variation in the stator blade metal angles at the inlet for pure total pressure distortion cases. As expected, the stators are symmetric in the presence of no distortion. However, as the distortion level increases, the variation level seems to increase for both hub and casing. The vertical axis represents the deviation of the blade angle from the mean. The vertical limits of hub and casing variations are set equal.

The maximum amplitude of variation in the hub is around 7° for P3S0. The variation at the casing is, however, significant. This is a consequence of employing a free vortex design condition for the blade rows. In case a forced vortex condition is chosen, a different span-wise variation would be observed. Since this question's main aim is not to investigate the span-wise distribution, we resort to comparing the

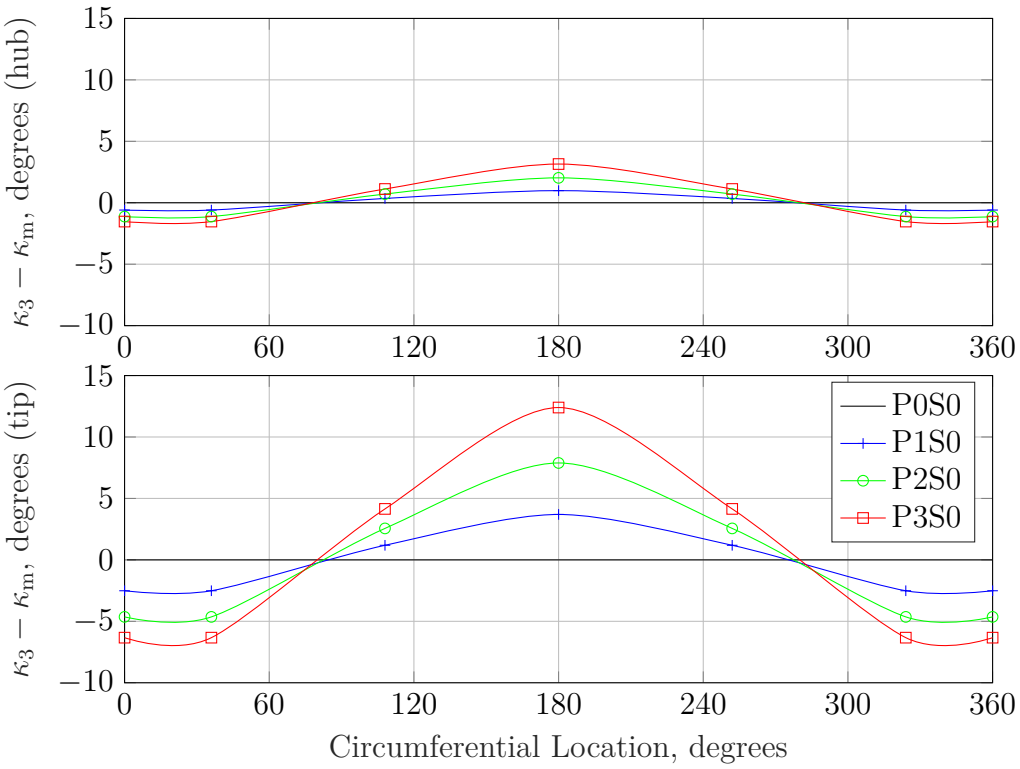

Figure 103: Circumferential variation of stator inlet blade angles [top: hub, bottom: casing] for pure total pressure distortion cases.

differences at specific span locations for various cases. The amplitude of variation at the ranges from around 6° for P1S0 to 19° for P3S0. The areas of high blade angles at the stator inlet correspond to the regions of low inlet mass flow and total pressure. Lower axial velocity increases the effective angle from the stator's perspective. It leads to higher angles for stators, so the effective incidence is lowered.

Using a multi-meanline technique at each circumferential sector can thus design stators with the degree of asymmetry established by the rotor exit flow.

5.3.4.2 *Flow Profiles: P0S0, P0S1, P0S2, P0S3*

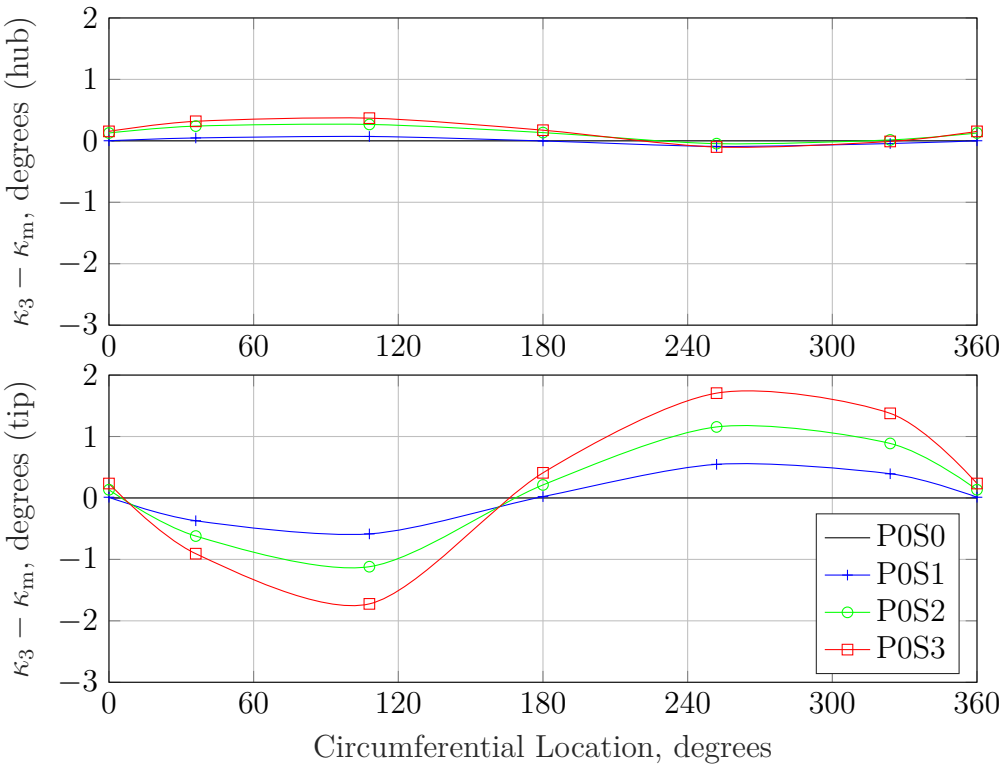

Figure 104: Circumferential variation of stator inlet blade angles [top: hub, bottom: casing] for pure swirl distortion cases.

Fig. 104 shows the variation in stator inlet angles for pure swirl distortion cases. Similar to pure total pressure distortion, the amplitude of the hub variation was minimal compared to the variation around the casing.

For pure swirl distortion, the variation of stator angles around the casing is much smaller than the variation for pure total pressure distortion. A maximum variation of 5° is observed for P0S3. The incidence variation due to swirl at the rotor inlet was larger than the swirl angle variation at the stator inlet. It implies that swirl distortion is attenuated through the rotor because the rotor exit flow will pass in the rotor deviation angle neighborhood. Since mass flow distortion is non-existent, the tangential velocity component is the only distortion present at the rotor exit. It is

also observed that the co-swirl areas lead to reduced blade metal angles, and areas of counter-swirl lead to increased blade metal angles.

5.3.4.3 Flow Profiles: P0S0, P1S1, P2S2, P3S3

Fig. 105 shows the effect of varying stator blade metal angles using multi-point multi meanline method for mixed distortion cases. Similar to the pure swirl and pure total pressure distortion observations, the hub variation is a little less than 1/4th the casing variation due to the free-vortex design condition.

The stator angles around the casing vary similarly to that of pure total pressure distortion case, but the variation is not symmetric about 180°. This asymmetry is due to the swirl component's contribution as swirl leads to asymmetric effects on the blade angles. From 0° - 100°, both swirl and total pressure distortion reduce the blade angles. Thus, the effect gets more pronounced in mixed distortion as the lowest point in the mixed distortion case for P3S3 is around 8°. From 100° - 180°, total pressure distortion tends to increase, and swirl tends to decrease the blade angles, with the fading effect of swirl and intensifying effect of total pressure distortion at larger angles. Thus, at around 110°, the metal angles are reduced but are the same at 180°, compared to the case of pure total pressure distortion. The trend reverses from 180° to 360°. Both swirl and the total pressure distortion increase the blade angles from the mean from 180° to 280°with the effect of total pressure fading away to 0 at 280°. Thus, the net effect is an increase in the blade angles at 250° compared to 110°. From 250° to 360°, the effect of swirl and total pressure are not in sync. The swirl's presence increases the metal angle while total pressure distortion decreases the metal angle; therefore, the blade angle at 325°, for example, is larger than the blade angle at 35°.

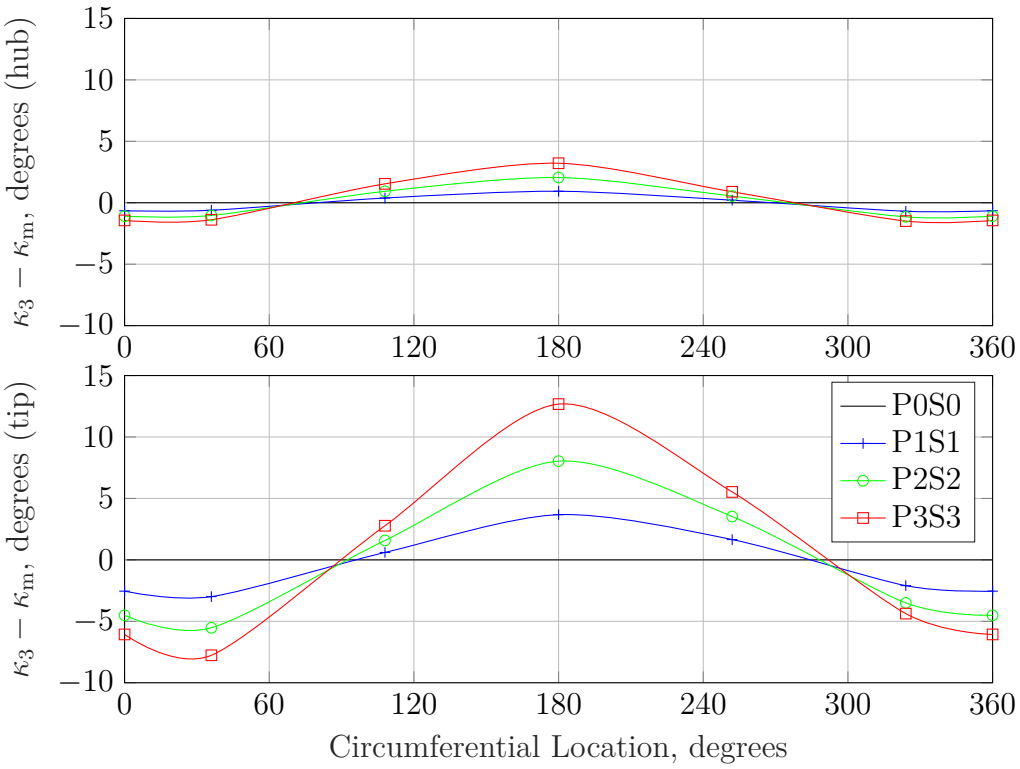

Figure 105: Circumferential variation of stator inlet blade angles [top: hub, bottom: casing] for mixed distortion cases.

5.3.5 Experiment 1.4: Evaluation of the Framework

Having performed experiments 1.1 - 1.3, we now aim to bring all the elements together to evaluate the framework's overall effectiveness. Hypothesis 1 claimed that if the fan stage is designed under distorted inflow using the framework proposed in this work that includes the optimization of blade incidence and deviation angles, designs non-axisymmetric stators, and incorporates the effects of unsteady rotor response, a significant portion of the losses can be mitigated. Experiment 1.4 is designed to test this hypothesis. A flowchart representing the set of steps to conduct this experiment is illustrated in Fig. 106. The basic idea is to isolate each modeling element's effect on the overall recovery of the stage losses. A brief explanation of these steps is given below.

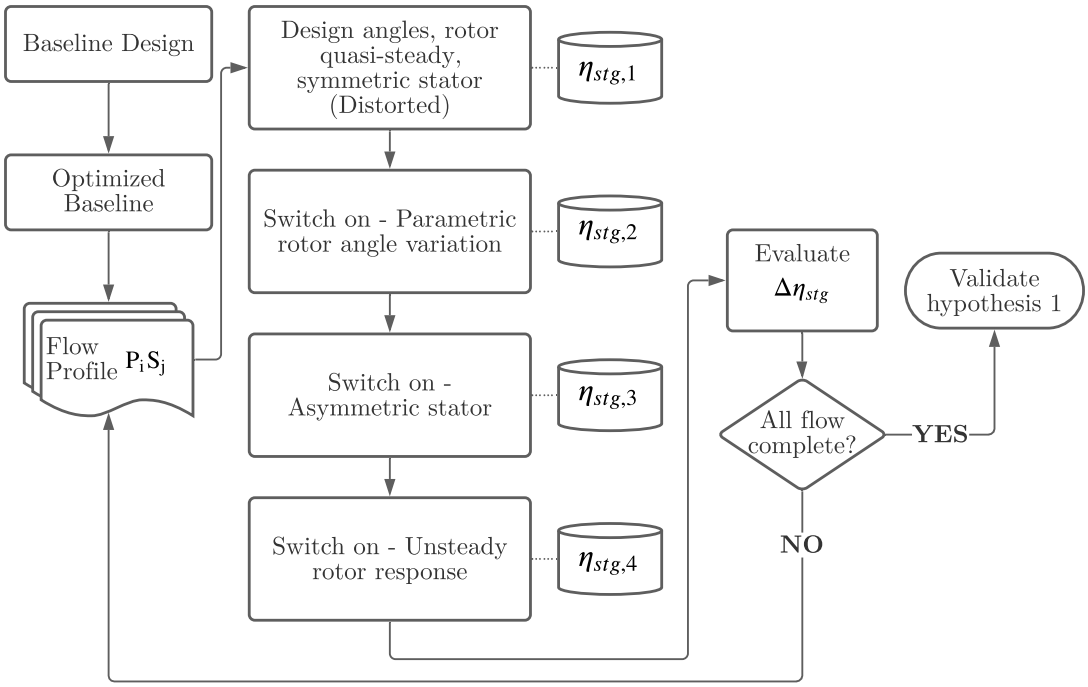

Figure 106: Flowchart describing the experimental setup for Experiment 1.4.

Step 1: All ten flow profiles consisting of no distortion (P0S0), pure total pressure distortion (P1S0, P2S0, P3S0), pure swirl distortion (P0S1, P0S2, P0S3), and mixed distortion (P1S1, P2S2, and P3S3) are averaged out to design a fan stage for uniform flow field. The averaging is performed in a mass-averaged sense. This is designated as the baseline design corresponding to each individual case. The baseline design parameters are described in Table 5.

Step 2: The baseline blade design parameters are not optimized for this flow scenario. Optimization of the baseline design is performed in order to make comparisons with the final case. The design space consisting of a subset of parameters listed in Table 5 are chosen for optimization. The optimization is performed for each flow case. The isentropic efficiency of the fan stage is recorded as a baseline. All designs are evaluated based on the changes in isentropic efficiency. Isentropic stage efficiency is given by

Eq. 93, where ht_{3s} is the specific enthalpy of the flow at the stator exit for an isentropic process, ht_1 and ht_3 are the actual specific enthalpies of the flow at the rotor inlet and the stator exit.

$$\eta_{\text{stg}} = \frac{ht_{3s} - ht_1}{ht_3 - ht_1} \tag{93}$$

Since specific enthalpies are extrinsic quantities, ht_1 and ht_3 are mass averaged. The isentropic enthalpy is calculated using the following process. First, the inlet's reference entropy is calculated using the mass averaged total temperature and mass averaged total pressure based on the 'GasTbl' thermodynamic package. For an isentropic process, the entropy at the stage exit is equal to the entropy at the rotor inlet. Finally, the exit enthalpy for an isentropic process is calculated using the entropy and the mass averaged total pressure at the rotor exit. The functional relationships are given by Eqns. 94 - 96.

$$s_1 = f(Tt_1, Pt_1) \tag{94}$$

$$s_2 = s_1 \tag{95}$$

$$ht_{2s} = f(s_2, Pt_2); \tag{96}$$

Step 3: The optimized stage designs from Step 2 are evaluated in this step, and drops in stage efficiency are computed. The additional losses in stage efficiency come from the combination of both rotor and stator losses. The stage efficiency computed in Step 2 is the predicted efficiency at the design RPM, given the flow is uniform. Computing the loss in efficiency at uniform flow can be done in multiple ways. One way to do this would be by running the rotor at the same RPM, and the drop in efficiency can be computed. A caveat of this approach is that the efficiency is measured at a different

stage pressure rise. Another way to measure the efficiency drop is by changing the rotor's RPM until the stage pressure rise in the distorted flow is equal to the design pressure rise in the uniform flow. Doing this would enable measurement at the same overall pressure rise. The losses computed in this step arise from including the effect of flow asymmetry through various circumferential sectors, unsteady rotor response, and asymmetry in the stators.

Step 4: Instead of turning all modeling elements in the proposed work simultaneously, a sequential approach is used here to evaluate the percentage of losses that can be recovered via the inclusion of each additional modeling element. However, it is not trivial to isolate the recovery from each modeling element. Stage efficiency is a function of rotor and stator losses. Optimizing blade angles may help contribute to an increase in stage efficiency. However, the blade angles cannot be considered fixed after blade angle optimization is performed since they should be free to change when non-axisymmetric stators are varied. In an attempt to isolate these effects, a design element turned on in one step will also be turned on in any following steps. Doing so helps provide optimized designs and ensure that the true efficiency gains via each modeling element are achieved. That means including unsteady response does not increase efficiency. It means that including the unsteady response correctly identified the rotor exit flow field and hence aided in the variation of blade angles that ultimately increased the stage performance. Step 4 comprises the addition of blade angle optimization while still designing symmetric stators and modeling quasi-steady response. The design generated using this way changes the blade incidence and deviation to minimize the overall rotor losses plus aligning the exit flow with the symmetric stator inlet so that the stage losses are minimal.

Step 5: In step 5, the non-axisymmetric stators are designed using the quasi-steady

rotor response. Both incidence and deviation angles are also allowed to vary in the design mode. In the off-design, the performance of this design is evaluated considering unsteady rotor response.

Step 6: The sixth step includes the addition of unsteady rotor response. The inclusion of unsteady rotor response affects the rotor blade angles optimization and the amount of turning required in the stators at various circumferential locations. The off-design and design stage efficiency are equal for this design.

Step 7: The final step involves a comparison of the framework using the percentage of losses recovered as a metric to evaluate the overall effectiveness of the proposed framework for each case. Hypothesis 1 will be validated based on the observed recovery in the cases.

5.3.5.1 Step 1: Baseline design

The baseline design resulting from the parameters listed in Table 5 yielded a stage efficiency of 90.32% for the uniform flow for all cases. All cases converged to the same design since the averaging resulted in the same flow for each case.

5.3.5.2 Step 2: Optimized baseline design

The optimization is performed by exploring the design space on the following parameters to control the parameters listed next to them. The bounds of variables for the design space exploration are listed in Table 6.

- Number of blades (rotor): controls the solidity
- Hub to tip ratio: controls the incoming flow velocity
- Rotor chord: controls the rotor diffusion
- Rotor exit area ratio: controls the velocity at the rotor exit

- Stator exit area ratio: controls the velocity at the stator exit
- Stator chord: controls the stator diffusion

Table 6: Bounds of variables for fan optimization for experiment 1.4.

Parameters	**Lower bound**	**Upper bound**
Discrete variables		
Number of blades	21	24
Continuous variables		
Hub to tip ratio	0.23	0.3
Rotor chord	6.5"	8.5"
Rotor exit area ratio	0.85	0.95
Stator exit area ratio	0.85	0.95
Stator chord	3.5"	5.0"

Three hundred experiments were designed using the Latin Hypercube Sampling technique. For each case, stage isentropic efficiency was recorded. A second-order polynomial function was used to create a model fit. The number of blades was considered as a continuous variable during the model fit with the eventual goal of choosing a discrete variable near the optimal design point. A second-order polynomial fit of stage isentropic efficiency was generated with R^2 of 0.98, RMSE of 0.0017, and a p-value of < 0.0001. Fig. 107 shows the actual vs. predicted stage efficiency for all 300 cases. The gray dots represent the training points (75%), and the red markers represent the validation points (25%).

The plot of residuals vs. predicted efficiency is shown in Fig. 108. The absence of a noticeable trend in the residual plot suggests that the model's variation in the errors is well captured.

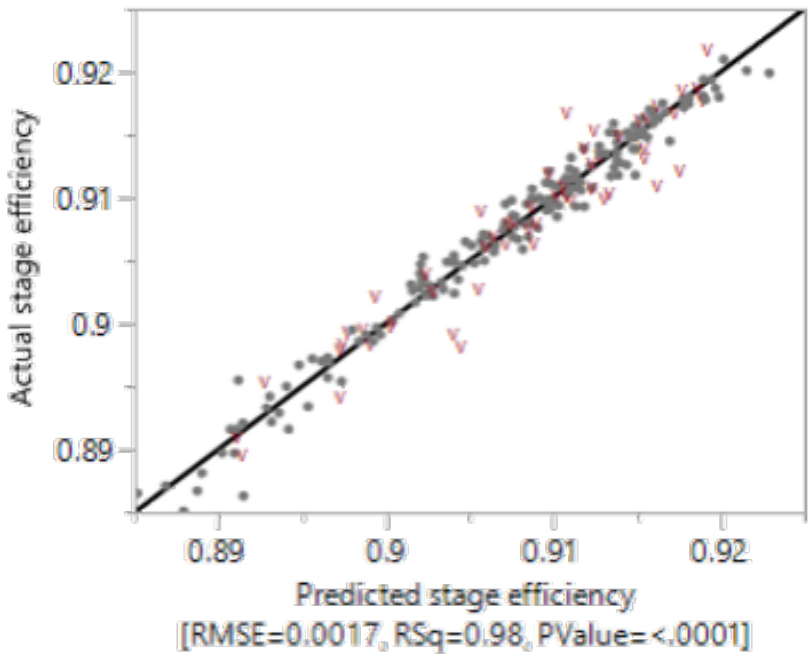

Figure 107: Uniform flow actual vs. predicted stage efficiency for various design parameters.

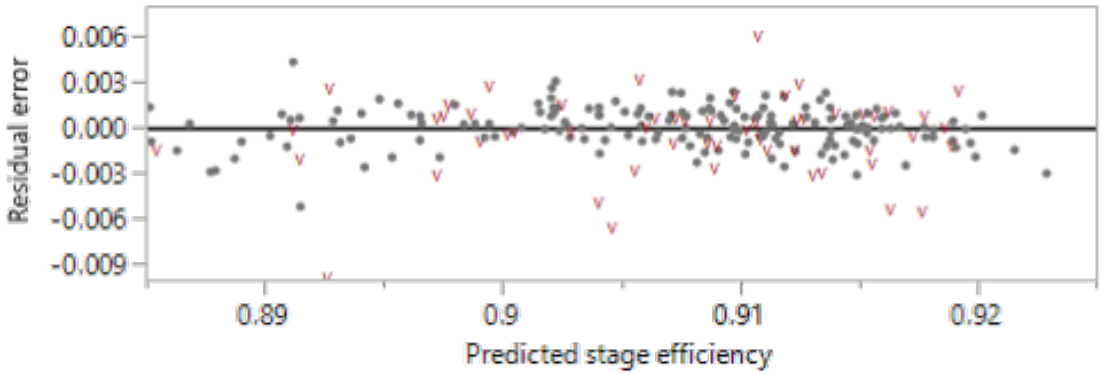

Figure 108: Uniform flow predicted vs. residual stage efficiency for various design parameters.

An optimization in the generated polynomial functional fit was performed, and the set of design parameters that generate maximum stage efficiency was computed. A design with a stage efficiency of 92.17% was achieved. The list of the optimized baseline parameters and other fixed parameters is presented in Table 7.

Table 7: Optimized baseline fan design parameters for experiment 1.4.

Parameters	**Values**
Stage pressure rise requirement	1.25
RPM	4000
Tip radius	24"
Tip chord	8.03"
Taper type	3
Hub to tip ratio	0.3
Number of rotor blades	24
Number of stator blades	33
Stator chord	3.94"
Rotor airfoil type	Double circular arc
Machine type	Free vortex

5.3.5.3 Step 3-7 for flow profiles: P0S0, P1S0, P2S0, P3S0

Fig. 109 shows the impact of the various elements of the proposed design framework for pure total pressure distortion cases. The vertical axis is the isentropic stage efficiency. The horizontal axis shows five-step changes. The first point is the predicted efficiency for the uniform flow case for the optimized baseline design (Step 2). The second point is the performance of that design in the distorted flow field. The next three points denote the optimal search of blade metal angles by varying incidence and deviation angles, design of non-axisymmetric stators, and modeling the unsteady rotor response.

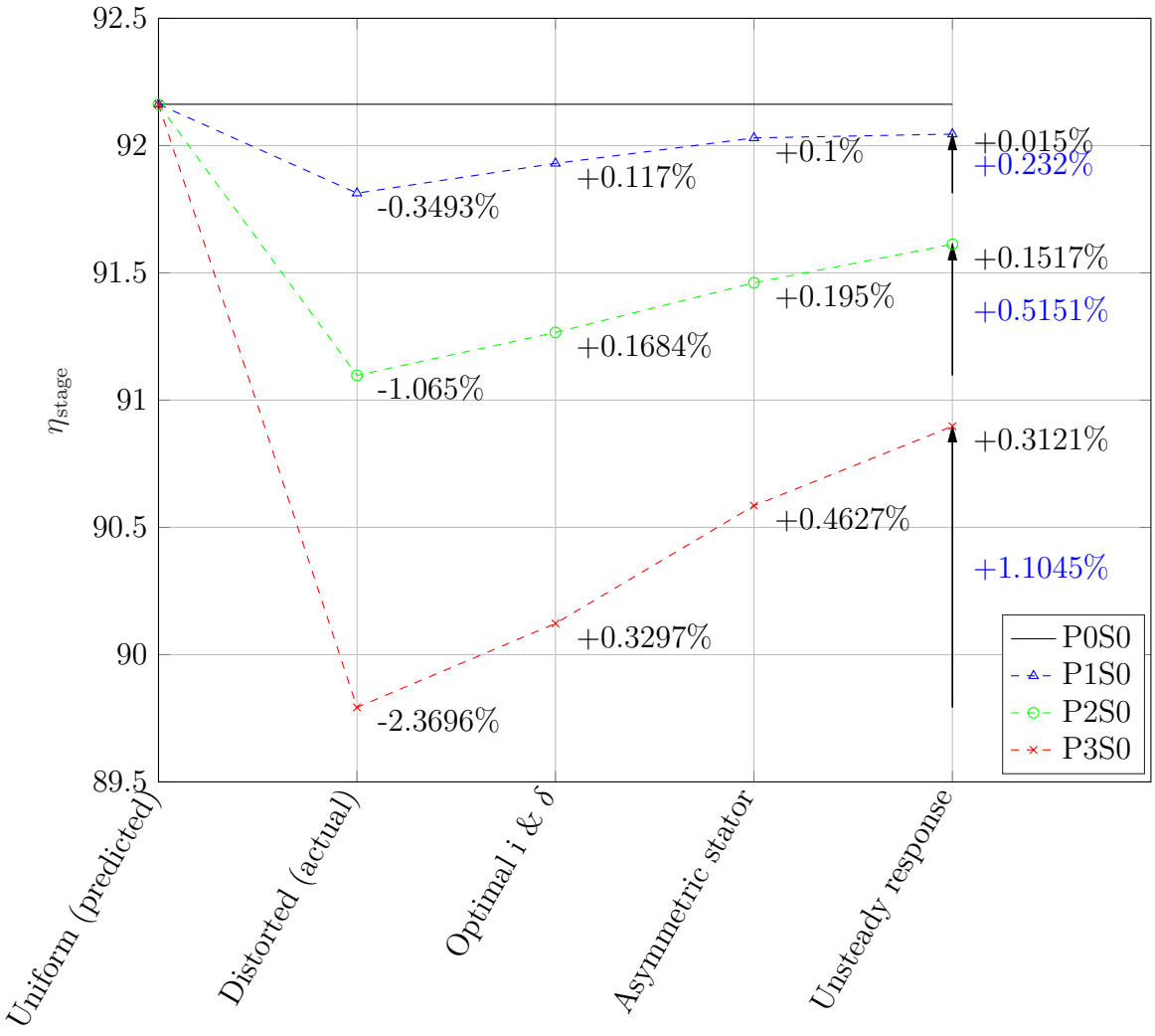

Figure 109: Impact of proposed design framework on stage efficiency for pure total pressure distortion cases.

All cases start with the same stage efficiency at the uniform flow's predicted efficiency. This design shows no change in the stage performance for P0S0, which should be the case since P0S0 is the clean case. With increasing distortion intensity, a larger drop in stage efficiency is observed in the distorted flow condition. The losses ranged from 0.35% for P1S0 to 2.37% for P3S0. A linear increase in distortion intensity did not equate to a proportional decrease in stage efficiency. The distortion intensity of P3S0 is equal to the sum of P1S0 and P2S0. However, the loss in P3S0 is

Table 8: Effect of flow distortion on rotor and stator efficiencies for pure total pressure distortion cases.

Case	$\eta_r(\%)$	$\eta_s(\%)$	$\eta_{stg}(\%)$	$\Delta\eta_r$	$\Delta\eta_s$	% Loss (r)	% Loss (s)
P0S0	94.86	97.16	92.16	-	-	-	-
P1S0	94.65	97.00	91.81	0.21	0.16	57.34	42.66
P2S0	94.12	96.79	91.10	0.74	0.37	67.20	32.80
P3S0	93.24	96.30	89.79	1.62	0.86	65.86	34.14

higher than the sum of the losses in the other two combined. This finding suggests that the losses cannot be scaled based on the distortion intensity. A linear increase in distortion intensity creates a linear change in the incidence angles. This is the case when comparing Figs. 78(b), 79(b), and 80(b). However, linear departure in incidence angles leads to a non-linear increase in rotor losses. Higher intensities of distortion also cause higher diffusion in the rotors. While the linear increase in mass flow translates to the rotor exit, the rotor exit flow profiles do not scale linearly. Besides, the losses in the stators also behave in a non-linear trend.

Table 8 shows the respective efficiencies of rotor and stator rows for each flow condition. It also provides a breakdown of the losses. For all cases, about 60-70% of the losses were due to the reduced rotor isentropic efficiency, and the rest was due to reduced stator efficiency. The findings agree with the study by Gunn [65], where the loss contributions of rotor and stator were within the ranges identified here.

Fig. 109 also shows the effect of optimizing rotor incidence and deviation angles (step 4). Recovery in the stage efficiency ranged from 0.12% for P1S0 to 0.33% for P3S0. This increase amounted to the loss of 33% for the low distortion case, 16% for the mid distortion case, and 14% for the high distortion case. The trend suggests that the impact of optimizing rotor angles decreases with increasing intensity. Regardless of the blade angle optimization, the incidence variation still exists. Therefore, the rotor optimization can only reduce a small percent of the losses due to incidence variation by changing the blade's average incidence angle. The other effect of the blade angle

optimization is by changing the rotor deviation angle. The blade angle optimization converges to a deviation angle that leads to optimal averaged incidence for the stator rows. Thus, it also helps increase stator efficiency as well.

The effect of designing asymmetric stators (step 5) leads to a monotonic increase in stage efficiency. The increase in stage efficiency ranged from 0.1% - 0.46%. This increase is equivalent to 29% of the losses for low distortion case, 18% of the losses for mid distortion case, and 20% of the losses for high distortion case. The final step (step 6) consisted of including the unsteady rotor response. The unsteady response's impact had a negligible effect for P1S0, therefore leading to almost no increase in stage efficiency. For the mid distortion case, it accounted for an additional 0.15% of the stage efficiency 0.31% for high distortion case. The arrows in Fig. 109 shows the amount of losses recovered by including all these modeling effects in the design process. The recovery in stage efficiency ranged from 0.23% to 1.1% using this process.

Table 9 shows the contribution of each design change on total loss recovered. Optimization of incidence and deviation angles has a relatively stronger effect on low distortion cases. The contribution seems to weaken with the increasing distortion intensity. It is because the optimizer attempts to find the optimal values of incidence and deviation angles for minimal losses. It cannot change the incidence fluctuations present on the fan face. Since the fluctuations are higher for higher intensities, only a relatively smaller fraction of those losses can be recovered by optimizing the angles. Non-axisymmetric stators help recover a large fraction of each case's losses as stator losses at each circumferential sector are minimized by varying the blade metal angles. Non-axisymmetric stator design changes are responsible for recovering 20-30% of lost efficiency. Increasing non-uniformities at the rotor inlet at higher intensities also equate to increasing non-uniformities at the rotor exit.

Similarly, the unsteady effects start becoming more pronounced for higher intensities. Unsteadiness could be ignored at low distortion cases. At high distortion cases,

Table 9: Contribution of various design changes on total loss recovered for pure total pressure distortion cases.

Case	Optimal i and δ	Asymmetric Stator	Unsteady Response	Loss Recovered
P1S0	33.50%	28.63%	4.29%	66.42%
P2S0	15.81%	18.31%	14.24%	48.37%
P3S0	13.91%	19.53%	13.17%	46.61%

however, the effect of including unsteadiness is similar in magnitude to the contribution of optimizing incidence and deviation. Therefore, the case for the inclusion of any modeling capability is justified depending on the type of distortion present. Including the unsteady response for P3S0 had a slightly lower contribution to the increase in stage efficiency compared to P2S0. This limitation is because of the increased turning required in the stator for higher distortion, leading to an increased diffusion factor. So, aligning stator blades completely with the flow could have a lesser impact because the increased diffusion offsets some of the gains.

5.3.5.4 Step 3-7 for flow profiles: P0S0, P0S1, P0S2, P0S3

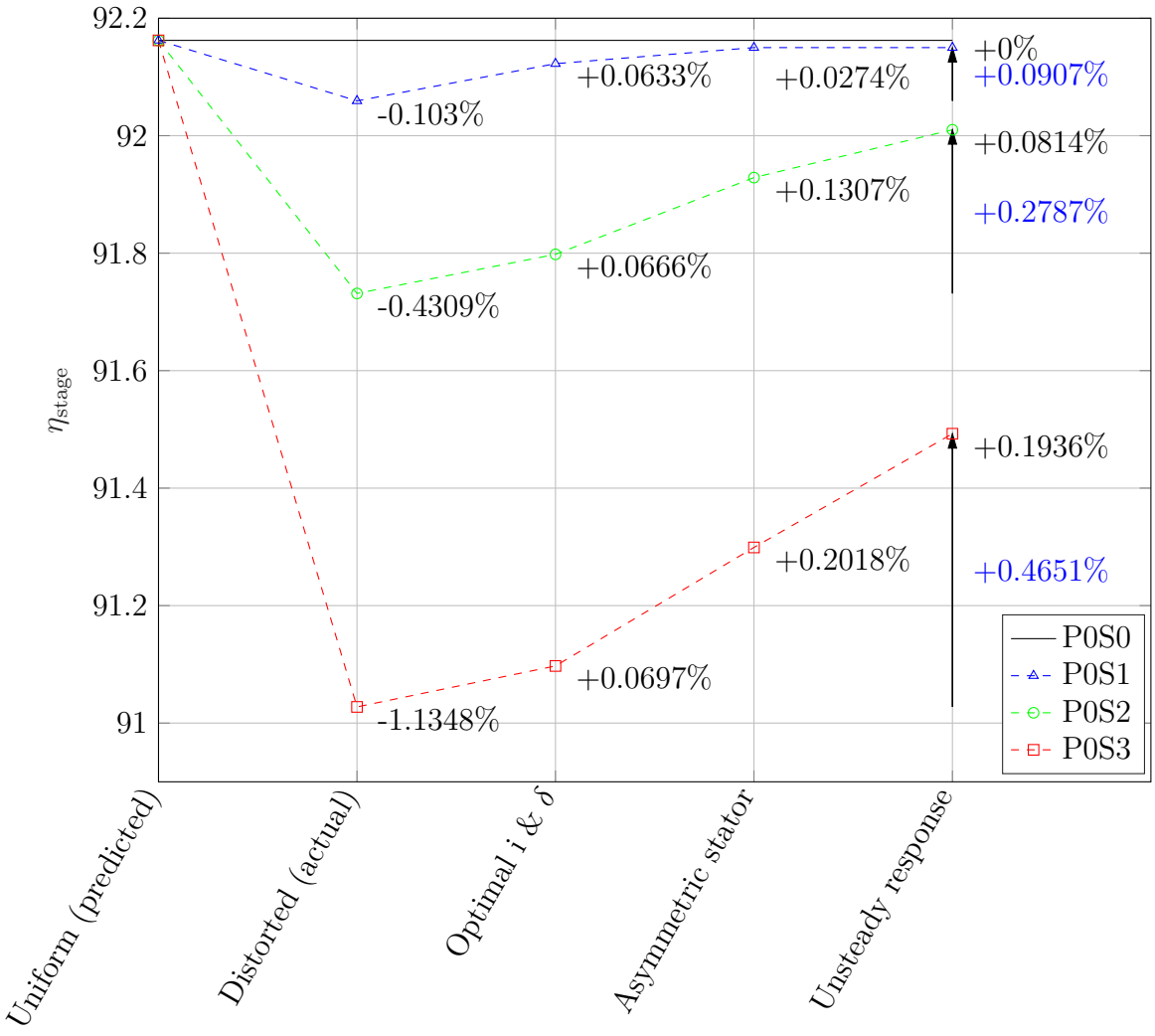

Figure 110: Impact of proposed design framework on stage efficiency for pure swirl distortion cases.

Fig. 110 shows the impact of the various elements of the proposed design framework for pure swirl distortion cases. For this set of cases, the reduction in stage efficiency was not as high as the pure total pressure distortion cases. The reduction in stage efficiency ranged from 0.1% - 1.13%. The only loss factors arise from the variation in swirl angles at the rotor inlet as the mass flow and total pressure distortion is non-existent. Similar to the case of pure total pressure distortion, the losses for pure

Table 10: Effect of flow distortion on rotor and stator efficiencies for pure swirl distortion cases.

Case	$\eta_r(\%)$	$\eta_s(\%)$	$\eta_{stg}(\%)$	$\Delta\eta_r$	$\Delta\eta_s$	% Loss (r)	% Loss (s)
P0S0	94.86	97.16	92.16	-	-	-	-
P0S1	94.76	97.15	92.06	0.10	0.01	91.11	8.89
P0S2	94.42	97.14	91.73	0.44	0.02	95.75	4.25
P0S3	93.74	97.10	91.03	1.12	0.05	95.83	4.17

swirl distortion cases increase non-linearly with increasing distortion. Table 10 shows the breakdown of the losses in terms of rotor and stator contributions. It is interesting to note that almost all of the reduction in stage losses arises from reducing rotor efficiency. The stator efficiency is almost invariant throughout all distortion intensities, decreasing only slightly. Mass flow distortion at the rotor inlet does not attenuate at the rotor exit, but swirl distortion does. Since the flow exiting the rotor is closer to the deviation angle, the non-uniform swirl at the rotor inlet is almost uniform at the rotor exit. Therefore, a symmetric stator row does not experience a significant level of distortion because of which the stator efficiency levels remain unchanged. Any change in the stator behavior is likely due to the incorrect representation of the rotor exit flow by the quasi-steady response. On the other hand, the rotor experiences the incidence swings, the variation of which increases with increasing intensity of distortion. Therefore, the losses in the stage is defined by the losses in the rotor.

The optimization of blade angles led to a constant increase in stage efficiency regardless of the distortion intensity. It is due to the presence of co-swirl on one side and counter swirl on the other. Optimizing the blade angles to reduce the losses for one type of swirl increases the other type's losses. Thus, any change in rotor efficiency is due to the difference in mass flow in different regions since the losses and efficiencies are computed from mass-averaged parameters. Asymmetric stators led to an increase in stage efficiency. It is interesting to note that the overall stator efficiency was higher than the case for no distortion. This phenomenon is because the blade optimization

Table 11: Contribution of various design changes on total loss recovered for pure swirl distortion cases.

Case	Optimal i and δ	Asymmetric Stator	Unsteady Response	Loss Recovered
P0S1	61.45%	26.61%	0.00%	88.06%
P0S2	15.45%	30.33%	18.89%	64.68%
P0S3	6.14%	17.78%	17.06%	40.98%

was also turned on during asymmetric stator design. Thus, it led to a reduction in design incidence and an increase in design deviation, resulting in a reduced diffusion in the stators and increased stator efficiency. During the non-axisymmetric stator design, the rotor efficiency also increased as the rotor efficiency increase was not offset by any losses in the stator. The effect of asymmetric stators was an increase of 0.02% to 0.20% in stage efficiency. Finally, the inclusion of unsteady effects resulted in no change for P0S1 but a 0.08% and 0.19% increase in stage efficiency for P0S2 and P0S3 respectively.

Table 11 shows the amount of loss recovered using various elements of the modeling framework. Similar to the case of pure total pressure distortion, the effect of optimizing incidence and deviation reduced with increasing distortion intensity. Asymmetric stators consistently accounted for a significant portion of the recovered losses. The effect of unsteadiness was also similar to the case of total pressure distortion such that its inclusion contributed to around 15-20% of the losses for mid to high-level distortions. Overall, almost all losses were recovered for low distortion case. This does not provide any significant effect since the loss was only 0.1%. For P0S2 and P0S3, the recovery amounted to 65% and 41%, respectively. It is seen that the rate of improvement of the stage efficiency declines non-linearly with increasing distortion intensity. Thus, a higher benefit can be realized for lower levels of distortion.

5.3.5.5 *Step 3-7 for flow profiles: P0S0, P1S1, P2S2, P3S3*

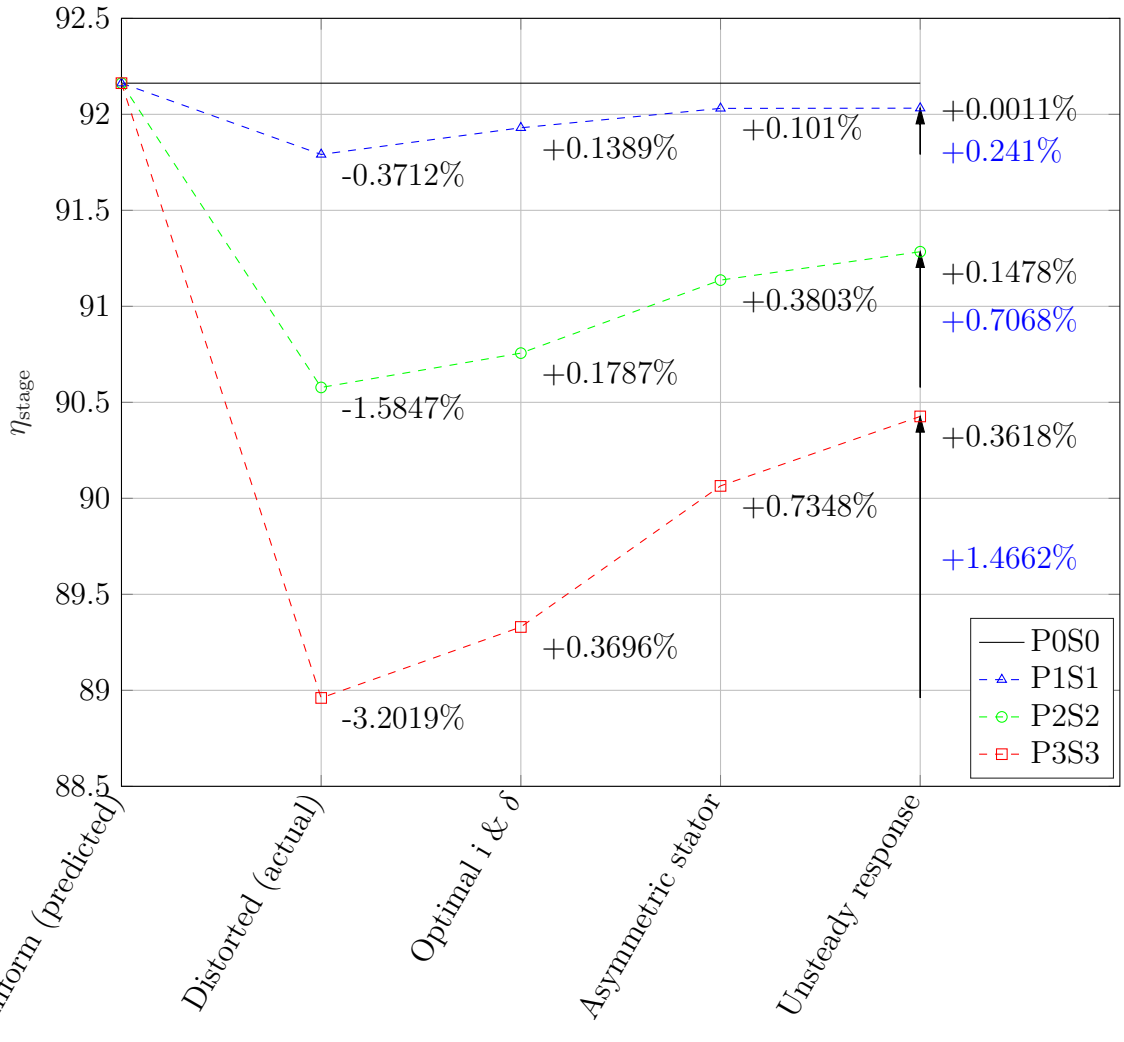

Figure 111: Impact of proposed design framework on stage efficiency for mixed distortion cases.

Fig. 111 shows the impact of the various elements of the proposed design framework for mixed distortion cases. The losses range from 0.37% for P1S1 to 3.20% for P3S3. Similar to the trends observed in pure swirl and total pressure distortion, the reduction in stage efficiency is non-linear with higher values for larger intensities. The losses for mixed distortion cases are not equal to the sum of the respective case for pure total pressure and swirl distortion. For example, the P2S2 flow profile can be considered as

Table 12: Effect of flow distortion on rotor and stator efficiencies for mixed distortion cases.

Case	$\eta_r(\%)$	$\eta_s(\%)$	$\eta_{stg}(\%)$	$\Delta\eta_r$	$\Delta\eta_s$	% Loss (r)	% Loss (s)
P0S0	94.86	97.16	92.16	-	-	-	-
P1S1	95.54	97.10	91.79	0.32	0.06	84.52	15.48
P2S2	93.61	96.76	90.58	1.25	0.40	76.19	23.81
P3S3	92.45	96.23	88.96	2.41	0.92	72.85	27.15

a superposition of P2S0 and P0S2. The respective efficiency drops were 1.07% and 0.43%. For the case of P2S2, the reduction in stage efficiency was 1.58%, slightly higher than the sum of the two individual cases combined. On the other hand, the stage efficiency drop of P3S3 is 3.2%, lower than the sum of the efficiency drops in P2S0 and P0S2. Thus, the superposition of individual distortion responses does not lead to the response for combined distortion. No conclusive evidence is found regarding the magnitude of losses between the individual and the superposed flow fields.

Table 12 breaks down the stage efficiency drops into rotor and stator effects. In general, 1/4th of the losses arise in stators and 3/4th in the rotors. Comparing Table 8, Table 10, and Table 12, it is seen that the fraction of the losses in rotor increases when swirl distortion is present. This observation is likely because most of the losses in swirl distortion occur in rotors. Therefore, additional losses in stators due to distortion range anywhere between 1/5th to 2/5th of the overall stage losses.

The optimization of rotor incidence and deviation angles led to an increase of 0.14% to 0.37% in stage efficiency with larger increases corresponding to higher intensities. The recovery in stage efficiency due to non-axisymmetric stator design ranged from 0.1% to 0.73%. Including the effect of unsteady rotor response resulted in an additional increase of 0.15% for P2S2 and 0.36% for P3S3. Comparing Figs. 109, 110, and 111, it is observed that the superposition of flow do not lead to superposed responses. Therefore, the recovery from different modeling elements also does not lead to a summation effect for the combination of flow profiles.

Table 13: Contribution of various design changes on total loss recovered for mixed distortion cases.

Case	Optimal i and δ	Asymmetric Stator	Unsteady Response	Loss Recovered
P1S1	36.63%	26.64%	0.30%	63.55%
P2S2	11.28%	24.00%	9.33%	44.60%
P3S3	11.54%	22.95%	17.06%	45.78%

Table 13 lists the contribution of each design change on total loss recovered for mixed distortion cases. The effect of optimizing rotor incidence and deviation angles contributes to the recovery of a large portion of losses for P1S1 (≈37%), but only a smaller amount at larger distortions. This observation is in agreement with the findings of the other two sets of cases. Asymmetric stators helped recover approximately 25% of losses in all cases. It is to be noted here that the design of asymmetric stators or the optimization of incidence and deviation does not only affect stator or rotor losses. For example, stator losses in P1S1 contributed to 15% of overall losses, but the design of asymmetric stators contributed to the recovery of 26% losses. It implies that asymmetric stators also allowed rotor incidence and deviation to further optimize and further lower losses. Similarly, the effect of unsteadiness is higher in P3S3 and helps contribute to the recovery of 17% loss by accounting for the flow field correctly.

5.3.6 Summary of Experiment 1

Experiment 1 was conducted to answer research question 1 that inquired about the fan stage framework for conceptual designs for distorted flow that maximized the stage efficiency. Research question 1 is restated as follows.

Research Question 1

What is an appropriate design framework to maximize the stage efficiency of a fan in presence of flow asymmetry?

A design framework was proposed in the preceding chapter 4 that included all the

elements proposed in hypothesis 1. Experiments 1.1 - 1.4 were conducted to validate various statements made regarding the research question 1. A summary of experiments 1.1 - 1.4 and discussion on the validation of hypotheses 1.1, 1.2, 1.3, and subsequently, hypothesis 1 is provided here. Hypothesis 1.1 stated that rotor minimum loss design incidence is different for uniform and non-uniform flow.

Hypothesis 1.1

If the fan is designed for an averaged flow, the minimum loss design incidence for non-uniform flow departs from its optimal value for uniform flow

From the results of experiment 1.1, it was observed that up to 1.4 degrees increase in design incidence was able to recover up to 65% of the losses for various distortion cases. However, it was observed that no increase was obtained for pure swirl distortion cases, and it was only the case for either pure total pressure distortion and mixed distortion cases. The reason as to why this occurs was discussed earlier. While the results are in agreement with the hypothesis, the more specific statement could be stated as follows:

Validated Hypothesis 1.1

If the fan is designed for an averaged flow, the minimum loss design incidence for non-uniform flow, with total pressure distortion present, departs from its optimal value for uniform flow

It was also observed for the specific fan design parameters in experiment 1.1 that the hub losses dominated the rotor losses. Three radial streams were analyzed for each case, and one scalar was used to modify the design incidence for all three streams at once. Therefore, some areas showed an increase in mid and tip losses because that increase was less than the decrease in the hub losses. An extended hypothesis, which is not tested here, but is stated as a natural extension of the results seen here can be

established and is stated as follows:

Extended Hypothesis 1.1

If the fan is designed for an averaged flow, the minimum loss design incidence for non-uniform flow, with total pressure distortion present, departs from its optimal value for uniform flow. In addition, the minimum loss design incidence for different radial segments are not necessarily equal to each other

Hypothesis 1.2 stated that a larger deviation in rotor response in terms of blade normal force and pressure rise will be observed between quasi-steady and unsteady analyses and was stated as follows:

Hypothesis 1.2

The necessity of including unsteady rotor response will be dependent on the intensity of distortion. At high distortion intensities, the effect of unsteady response on pressure rise and the blade normal force will be non-negligible

From the results of experiment 1.2, it was observed that the change in rotor normal force was 1% to 4% for pure total pressure distortion cases, 3% to 8% for pure swirl distortion cases, and 3% to 6% for mixed distortion cases. Similarly, the difference at peak pressure rise location and value varied with increasing intensity of distortion. The results of experiment 1.4 also substantiate this hypothesis, where the level of contribution of unsteady modeling helped recover a higher percentage of losses in all cases of distortion. It was observed that for the low-intensity case, the contribution was negligible. However, it was deemed necessary to include these effects for mid and high-intensity distortion for all flow profiles. Therefore, experiment 1.2 qualified the hypothesis, and the results of experiment 1.4 further validated it.

Hypothesis 1.3 claimed two points: (i) the required degree of asymmetry in stators will increase with increasing intensity of distortion, and (ii) the level of asymmetry for

swirl distortion is lower than that for total pressure distortion.

Hypothesis 1.3

If the distortion intensity is higher, a larger increase in the level of required stator asymmetry will be observed. The stator asymmetry will also be observed higher for total pressure distortion than swirl distortion

Experiment 1.3 was designed to test this hypothesis. For pure total pressure distortion, the amplitude of circumferential variation in the tip blade angles ranged from 4° to 20°, with increasing amplitude for higher distortion levels. For the case of swirl distortion, the maximum amplitude was less than 4° for the highest distortion case (lower than the amplitude of variation for the lowest intensity of total pressure distortion). Similarly, for mixed distortion cases, the observed variation ranged from 4° to 22°. These results validated the statements posed in hypothesis 1.3.

Hypothesis 1 claimed that the inclusion of rotor blade angle optimization, unsteady rotor response, and non-axisymmetric stator design would help recover a large portion of distortion losses. It was formally stated as follows:

Hypothesis 1

If hypotheses 1.1-1.3 are true, then the fan stage design framework that incorporates the parametric variation of rotor blade angles, rotor unsteady response, and non-axisymmetric stators will be able to recover a significant portion of the losses in distortion that a fan designed for uniform flow experiences

Experiments 1.1 - 1.3 were performed to qualify the statements made in hypotheses 1.1 - 1.3. Experiment 1.4 was an attempt to bring all elements together. The results of experiment 1.4 showed that around 45% - 65% of losses could be recovered by the implementation of the proposed framework for pure total pressure distortion cases. For swirl distortion cases, this ranged from 40% to 88%, and for mixed distortion cases,

the recovery ranged from 45% to 65%. In general, it was observed that higher recovery was achieved for lower intensities of distortion. Another observation was that the rotor blade angle optimization was more beneficial at lower intensities. The parametric variation of deviation angle also helped increase the stage efficiency by creating a favorable flow direction at the stator inlet. It was also seen that at higher intensities of distortion, a larger improvement in stage efficiencies was not obtained by asymmetric stators due to the increase in diffusion factor caused by higher turning. It suggests that stator chords could also be varied circumferentially to control the amount of diffusion through the stator blade passages. Finally, as mentioned earlier, the unsteady modeling provided no substantial benefit at lower intensities but contributed significantly to the recovery at mid and high distortion levels. The observations from the results of experiment 1.4 thus validate hypothesis 1.

CHAPTER VI

APPLICATION OF VARIATIONAL ASYMPTOTIC METHOD FOR STRUCTURAL ANALYSIS OF ROTOR BLADES

6.1 Chapter Overview

Chapter 5 detailed all experimental efforts dedicated to testing hypotheses corresponding to research question 1 on the aerodynamic design of the fan stage. This chapter focuses on the experimental efforts targeted towards answering research questions 2 and 2.1. These questions relate to the structural analysis of rotor blades.

Research question 2 inquired about the effects on the fan stage design due to the inclusion of the rotor blades' structural analysis. A lack of a computationally efficient parametric modeling method for transient rotor analysis led to the formulation of research question 2.1 that inquired about the appropriate modeling technique for transient analysis of rotor blades. Hypothesis 2.1 was formulated regarding VAM's applicability as a computationally efficient model for transient structural analysis of rotor blades. Hypothesis 2 claimed the following: (i) an aerodynamically optimized design might not satisfy the structural constraints and (ii) using the aero-structural framework will enable a design that can satisfy the structural constraints with a minimal penalty on stage efficiency.

Two sets of experiments are carried out to test this hypothesis. Experiments 2.1a - 2.1d are dedicated to establishing VAM's validity for transient analysis of fan rotor blades. Experiment 2.2 is carried out on two fronts. Experiment 2.2a is used to demonstrate whether aerodynamically optimized designs can satisfy structural constraints. If the aerodynamically optimized design does not satisfy the structural

constraints, then Experiment 2.2b is used to create an optimized design using the framework detailed in chapter 4.

6.2 Experiment 2.1: Validation of Variational Asymptotic Method

The purpose of this section is to establish the relevance of beam theory tools based on VAM, such as VABS (2-D sectional analysis), followed by the use of GEBT to simulate the structural behavior of a fan blade undergoing rotation in a BLI flow field. A fan blade experiences dynamic loads that result from non-uniform work imparted by the blades in a distorted flow field. Hence, the rotor blades would structurally demonstrate a non-linear transient behavior analyzed using GEBT while the blade's cross-sectional properties are evaluated using VABS. With the discussions provided in subsequent sections, the goal is to demonstrate that the beam-theory-based tools can properly simulate unsteady loads on a fan blade.

6.2.1 Experiment Setup

To test hypothesis 2.1, i.e., validating VAM's applicability for transient structural analysis of fan rotor blades, a set of tested scenarios needs to be defined first. It consists of defining the experimental procedure, geometry, loads, and modeling environments. The goal is to compare the results for a non-linear transient analysis obtained from the proposed technique to those obtained from 3-D FEM for a couple of simple dynamic loading scenarios considering the computational effort needed to solve 3-D FEM problems. We will perform analyses on loads acting on the tip of the blade for both rotating and non-rotating cases to benchmark our studies. The results from VABS and GEBT will be verified with that of COMSOL - the 3-D FEM tool used in this work. Once this verification is complete, the analyses are repeated for distributed loads applied on a fan blade, and relevant 3-D displacements and 3-D stress resultants from the proposed use of VAM based tools are obtained and compared with 3-D FEM

results.

Fig. 112 shows the flowchart describing the general process for experimenting. Two sets of loads and two sets of motion are tested. The first loading type is a pure sinusoidal load. This load will be applied at the tip to simulate a simple dynamic loading condition. The other set of loads is distributed loads. These loads are computed using the inlet and the exit flow profiles of the rotor. For both loading conditions, the blades are first simulated as if they are non-rotating. After that, the rotating case is simulated. The presence of rotation will likely induce some harmonics that might not be present in the non-rotating case. The comparisons will be made with the results from 3-D FEM software, and the results will be used to validate the hypothesis. The general process for conducting experiment 2.1 is illustrated in Fig. 112. Note that the analysis is performed by constraining the root, and the attachment is not modeled. A subset of the results shown in this section is also presented in [69].

For each case, the procedure for performing the experiments are as follows:

- Step 1: Select a baseline rotor geometry
- Step 2: Select loads acting on the blades
- Step 4: Define the modeling environment
- Step 5: Use VAM to compute stresses and displacements for each case
- Step 6: Use a 3-D FEM tool to compute stresses and displacements for each case
- Step 7: Compute the differences in stresses, displacements, and computational time obtained from step 5 and step 6
- Step 8: Use GEBT to compute the natural frequencies for the first eight modes
- Step 9: Use 3-D FEM tool to compute the natural frequencies for the first eight modes

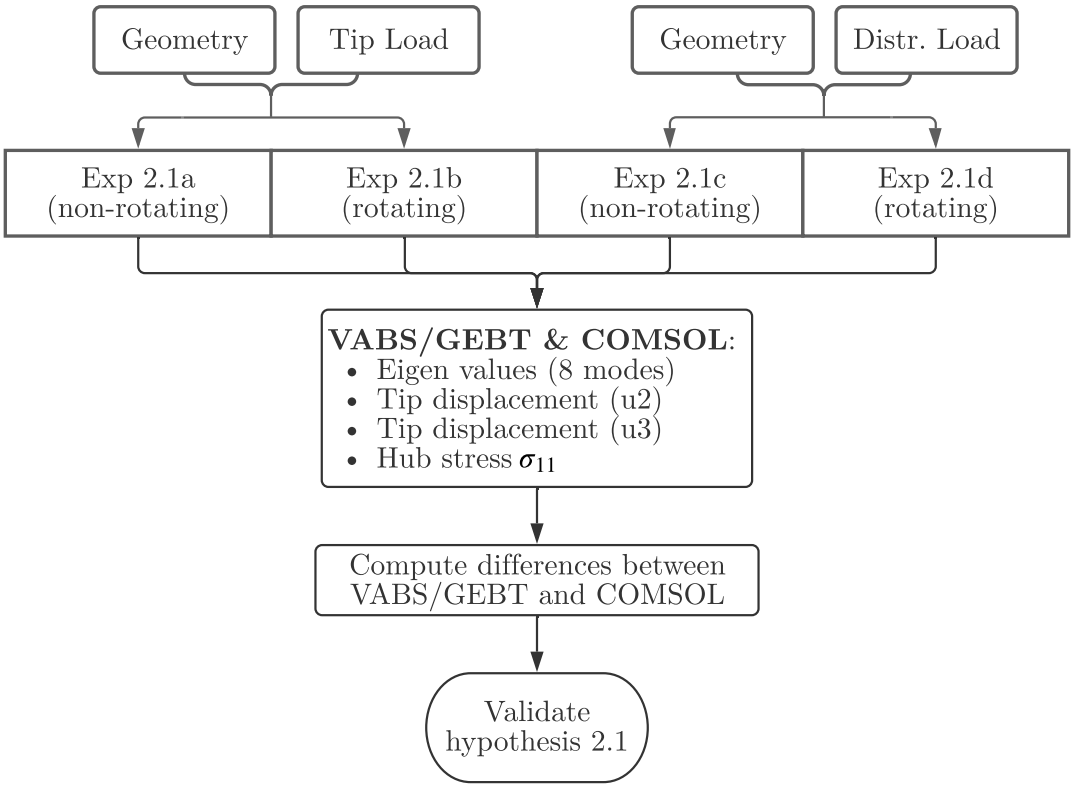

Figure 112: Flowchart describing the elements of Experiment 2.1.

- Step 10: Compute the differences in eigenvalues between step 8 and step 9
- Step 11: Validate hypothesis based on observed discrepancies in Step 7 and 10

6.2.1.1 Notes on the modeling environments

The solution of VABS results in the two-dimensional sectional elastic and inertia constants as stiffness and mass matrices. These matrices are 6×6 if a Generalized Timoshenko model analysis is used. The output of VABS also includes the warping variable solutions. These solutions help recover 3-D stresses and strains once 1-D solutions are obtained from GEBT. We can also use these information to compute and visualize the evolution of stresses and strains on the cross-section. The 1-D analysis is performed on the locus on the point defined by the centroids of the cross-sections. Further, with the computation of the 3-D recovery variables using VABS, the stress

distribution is obtained corresponding to a given time step at a specific cross-section. Upon repeating this for all sections, the 3-D variables for entire geometry can be obtained.

COMSOL multiphysics is used here as the 3-D FEM modeling tool because of its availability to the author. The blade is meshed using a physics-controlled fine mesh using tetrahedral elements. The smaller regions, such as the leading and trailing edges, have higher mesh density than the bulk region of the blade. We use solid mechanics module to obtain the eigenvalues and the results for different time steps in a time-dependent analysis. For non-linear transient analysis and cases that include rpm application on the rotor blade, we need to include geometrical non-linearities to obtain correct results. Besides, VABS and GEBT perform non-linear analysis, so a proper comparison can only be with the inclusion of non-linearities. The rotation is applied on the blade in specific cases using a rotating frame by including the centrifugal acceleration, Euler acceleration, and the spin softening. Consideration has been made to make sure that we are testing the cases in 3-D FEA, which are analogous to the cases being analyzed using VAM. To enable this, we apply the loads over the entire cross-section area with the equipotent resultant at the centroid of the cross-section when compared with the analysis in VAM.

6.2.2 Experiment 2.1a: Sinusoidal Tip Load (Non-Rotating)

Experiment 2.1a includes analyzing and comparing the displacements, stresses, and natural frequencies obtained from COMSOL and VABS/GEBT for the non-rotating blade with sinusoidal tip loading.

6.2.2.1 Baseline geometry

Fig. 113 provides a snapshot of the 3-D fan blade model. The blade geometry used in this study was obtained using a model built on the platform of Object-Oriented Turbomachinery Analysis Code (OTAC) [89]. This approach was described in detail

in Chapter 4. The blade is formed by identifying three distinct cross-sections from OTAC. Once these sections are obtained based on an efficient flow condition, we use a variable section sweep to join the sections smoothly and create the blade's baseline geometry for structural analysis.

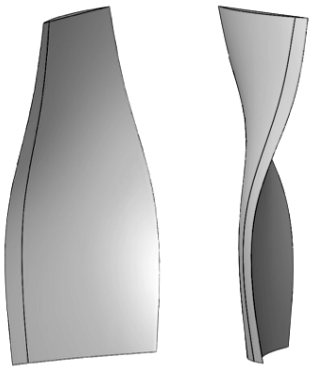

Figure 113: 3-D model of the fan blade used for analysis for Experiment 2.1a.

It is to be noted that the blade has a large twist and sharp edges that make it a complex component for dynamic structural analysis. Also, this blade has not undergone any structural analysis, so the blade is not optimized for structural integrity. However, in reality, it is important to design a structurally strong blade to withstand desired loads. Since this experiment's objective is to establish the relevance of the use of VAM-based tools for structural analysis, we will only focus on the mechanical response and characteristics of the stresses obtained between VABS and GEBT and compare it to that obtained from the 3-D FEA. The optimization of the structural aspects of the blade is carried out later. The geometric, material, and design parameters of the blade are listed in Tables 14, 15, and 16 respectively.

Table 14: Geometric properties of the fan blade for experiment 2.1a.

Geometric Parameters	**Value**	**Unit**
Blade span	15.75	in
Hub radius	6.6	in
Tip radius	22	in
Blade chord	8	in
Airfoil type	DCA	-
Hub stagger	2.5	deg.
Tip stagger	34.22	deg.

Table 15: Material properties of the fan blade.

Material Properties	**Value**	**Unit**
Material	Titanium	-
Young's Modulus	116E09	Pa
Poisson's ratio	0.32	-
Density	4506	kg/m^3
Yield stress	9.6E08	N/m^2
Endurance limit	5.17E08	N/m^2

Table 16: Design parameters of the fan blade for experiment 2.1a.

Design Parameters	**Value**	**Unit**
Design avg. mass flow	414	lbm/s
Design PR	1.35	-
Design RPM	2500	-

6.2.2.2 Meshing

Fig. 114 shows three cross-sections of the blade obtained from the calculations in OTAC and discretized using a very fine mesh to accommodate the intricate geometric features of the blades. The meshing was obtained using triangular grid elements. Significant changes in the blade inlet and exit metal angles and twist can be observed. These three cross-sections are analyzed in VABS because these are the characteristic cross-sections that define the overall blade geometry. The required input parameters such as the initial twist, curvatures, and obliqueness, etc. for the cross-section (2-D) as well as for the beam reference line (1-D) are defined in VABS and GEBT, respectively, for a correct representation of the geometry. Similarly, Fig. 115 represents the rotor blade model considered for structural analysis in COMSOL. The blade is meshed using a physics-controlled mesh using tetrahedral elements.

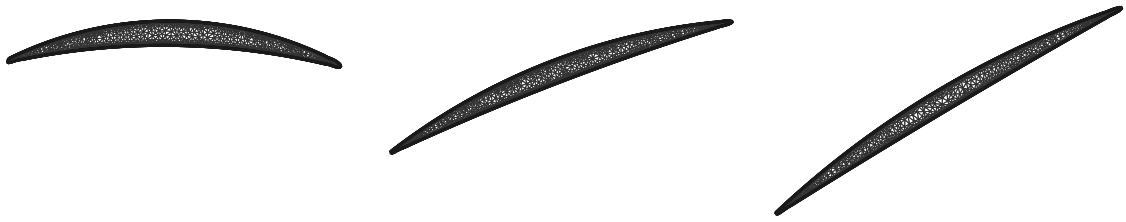

Figure 114: Triangular mesh grid of cross-sections: left (hub), center (mid), right (tip)

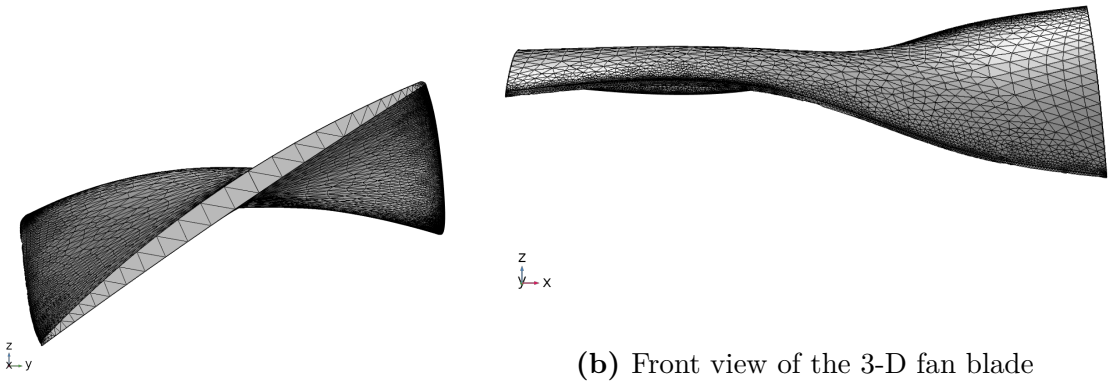

(a) cross-sectional view of the entire blade

(b) Front view of the 3-D fan blade

Figure 115: Representation of the meshing of the 3-D rotor blade in COMSOL

6.2.2.3 Loads

Since tangential loads are more dominating for the rotor blade, a sinusoidal tip transverse load is applied. Fig. 116 shows the variation of this load in [0,1] seconds. The amplitude is 10,000 N with a period of $0.5s$.

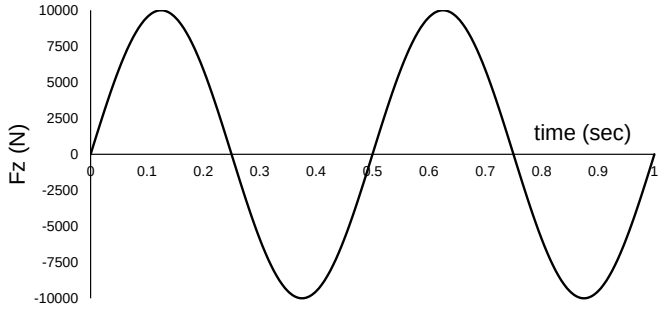

Figure 116: Sinusoidal tip loading behavior.

6.2.2.4 Results: Eigen analysis

For any structure undergoing dynamic loading, it is essential to look at the natural frequencies of the system undergoing free vibrations. Table 17 provides a comparison of the frequencies obtained from VABS/GEBT and 3-D FEA. Mode shapes corresponding to the first 10 natural frequencies are also provided for better understanding. Due to the blade's complex geometry, there is a strong coupling between various modes, such as bending in-plane and out-of-plane with torsion. It is also evident that the modes that predominantly contain torsion contributions have eigenvalues from GEBT with significant deviation from the 3-D FEA. However, most of the eigenvalues calculated using GEBT have good agreement ($< 5\%$) with the 3-D FEA with errors mentioned in the table alongside the frequencies.

6.2.2.5 Results: Tip displacements

Fig. 117 shows the tip displacements obtained from both VABS/GEBT and COMSOL for the sinusoidal tip load described in Sec. 6.2.2.3. The dominant displacements on the cross-section at the tip in chord-wise ($u2$) and flap-wise ($u3$) directions are plotted since the blade in the span-wise direction ($u1$) does not undergo any significant longitudinal displacement as compared to the out-of-plane and in-plane transverse displacements. Based on the frequency of the load applied (frequency of the applied load is much smaller than the fundamental frequency), the peak displacements for a cantilever beam at a given time step would be at the tip.

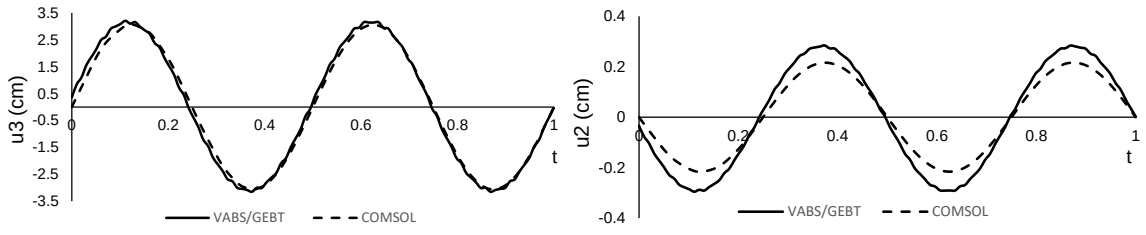

(a) u3 **(b)** u1

Figure 117: Displacement at the tip (non-rotating): VABS/GEBT vs. COMSOL

Table 17: Natural frequencies (non-rotating): VABS/GEBT vs. COMSOL.

ID	Natural Frequencies (Hz)		% Difference	Mode Shape
	VABS/GEBT	COMSOL		
1	103	106	-2.83%	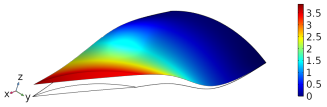
2	316	361	-12.47%	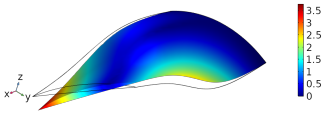
3	512	507	0.99%	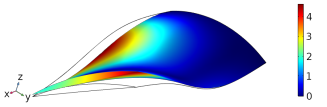
4	771	745	3.49%	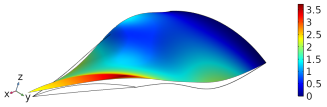
5	1171	1197	-2.17%	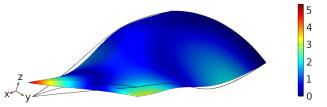
6	1654	1443	14.62%	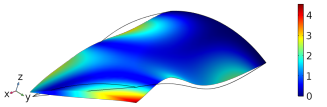
7	1927	1872	2.94%	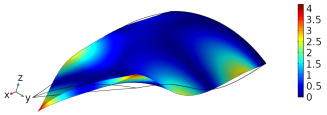
8	2370	2272	4.31%	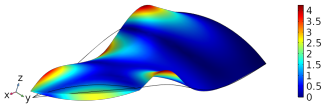
9	2579	2726	-5.39%	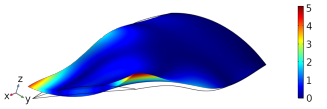
10	3076	2887	6.55%	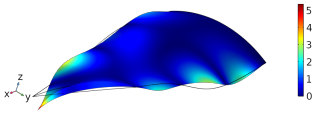

When the time-varying sinusoidal tip load is applied, the average displacement in u_3-the direction from COMSOL is 3.15 cm, and that from VABS and GEBT is 3.07 cm (≈2.5% difference). It is interesting to note that the results from COMSOL show a small phase lead in the first load cycle. However, the phase difference disappears in the second load cycle (0.5 s - 1 s). This phenomenon could be observed because of a difference in the numerical damping of the two solvers considered. In the u_2-direction, the displacements from the two analyses do not overlap. Further investigation was not warranted since the displacements in u_2 direction are small compared to the u_3 direction. These differences are likely attributed to the same reason that explains the differences in the natural frequencies in the torsion mode in Table 17.

6.2.2.6 Results: Stress analysis

Fig. 118 shows precisely how the dominant stress component σ_{11} evolve at the section present at 0.195 m in the blade along with the timestamps when the span ranges from 0.16 m to 0.6 m, keeping in mind that the corresponding load values over the duration of the applied load as shown in Fig. 116. Similar graphs can be obtained for the rest of the stress components σ_{12}, σ_{13}, σ_{22}, σ_{23} and σ_{33}. However, for the sake of simplicity in understanding, we resort to plotting the histories of only σ_{11} at the cross-section located at a distance of 8% of the span from the root. The periodic fluctuations on the blade stresses are easily visible when looking at Fig. 118. The maximum stress is located either at the tips or the suction side of the cross-section.

Fig. 119 shows the comparison of the maximum values of σ_{11} at the desired cross-section, against the results from 3-D FEA (COMSOL). Although the peak displacements match strictly between COMSOL and VABS and GEBT, the σ_{11} does not follow the same trend. The difference in peak σ_{11} obtained from VABS and GEBT and COMSOl is approximately 12%, with COMSOL predicting a lower value. We observe that the error percentage goes smaller as the time proceeds forward. The

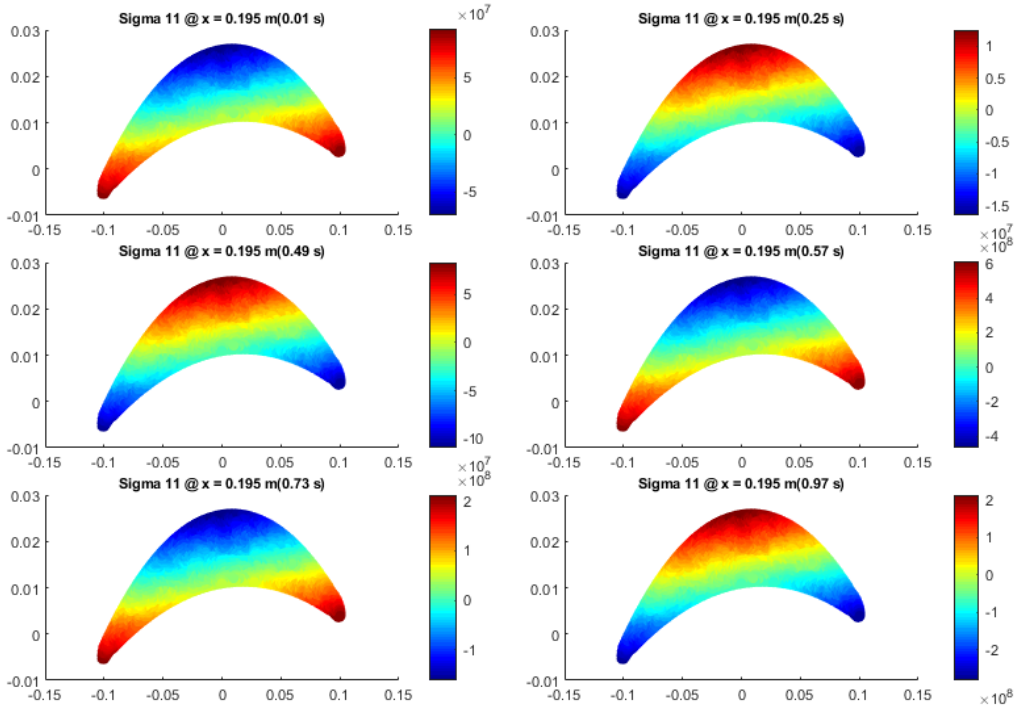

Figure 118: Snapshots of evolution of σ_{11} (N/m^2)at $x = 0.195m$ (non-rotating)

maximum stress locations predicted by VABS matches exactly with the ones obtained from COMSOL, and this is an essential feature when designing any new component.

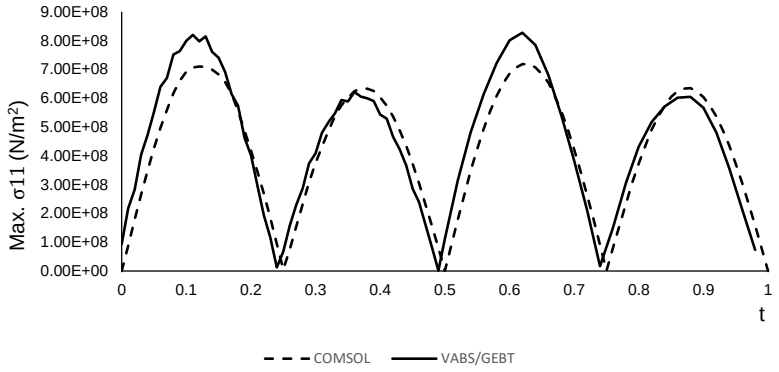

Figure 119: Max σ_{11} at $x = 0.195m$ (non-rotating): COMSOL vs. VABS/GEBT

Similar plots for the 3-D strain variables can also be obtained through this method. Another important observation is that even though the input force is sinusoidal, the output stress has a certain number of sub-peaks apart from the prominent peaks.

These subpeaks are due to the inclusion of inertia effects. It is basically due to the inclusion of a higher-order harmonic, which will not be present if a quasi-static analysis is performed.

6.2.2.7 Results: Computational effort

Table 18 shows the comparison of the computational variables for VABS/GEBT and 3-D FEA (COMSOL). VABS/GEBT provides high fidelity solutions free of any assumptions as is also much faster. A number of significant parameters can be extracted using the data stored. These parameters include exact location of maximum and minimum stress over time, maximum displacement, forces, and moments at all time steps. Simulating the 3-D FEM solution on COMSOL took a total of 21.5 hours when non-linearities were included for a very fine mesh. The analysis via VABS/GEBT took only 4 minutes with parallel processing implemented during the recovery of stresses on the cross-sections. Another benefit of using VABS/GEBT is the lower storage requirements afforded by VABS/GEBT that makes the storage, extraction, and processing of data convenient and efficient.

Table 18: Comparison of computation variables (VABS vs 3-D FEM)

Parameter	VABS + GEBT	3-D FEM (COMSOL)
Duration of Analysis	1 s	1 s
Time-Steps	100	100
Number of Elements	1000 (2-D); 150 (1-D)	1000 tet. elements/section
Memory (RAM) used	2 GB; 1-core	16 GB, 2-cores
Computation Time (Solver)	30 s (VABS) , 1 min(GEBT), 2.5 mins (VABS recovery with parallel processing) 4 mins (Total)	21.5 hrs
Storage Requirements	$\sim$ 50 MB	$\sim$ 6 GB

6.2.3 Experiment 2.1b: Sinusoidal Tip Load (Rotating)

In this case, the external loads and geometry are the same as in Experiment 2.1a with an additional rotational force. The rotor is simulated at a RPM of 2500.

6.2.3.1 Results: Tip displacement

Fig. 120 shows the displacement in the u_3-direction for the tip of the blade when the sinusoidal load is applied as the blade is rotating (2500 RPM). As seen in the case without rotation, the displacement results from VABS and GEBT and COMSOL seem to overlap. The overlapping is not as perfect as in the case without rotation. This small discrepancy is mainly attributed to the fact that the results from COMSOL and VABS and GEBT were plotted for different time steps. Another observation is that the peak displacement in the $+u_3$-direction is higher (approx. +3.0 cm) than the peak displacement in the $-u_3$-direction (approx. -2.5 cm). This difference arises due to rotation. A constant rotation introduces a constant centrifugal force that offsets the non-rotating displacement curve. The third observation is the wavy nature of displacements. Upon close observation, the waviness frequency is almost the same in the results from both COMSOL and VABS and GEBT. This behavior is because of the inclusion of higher-order harmonics in the response due to rotation.

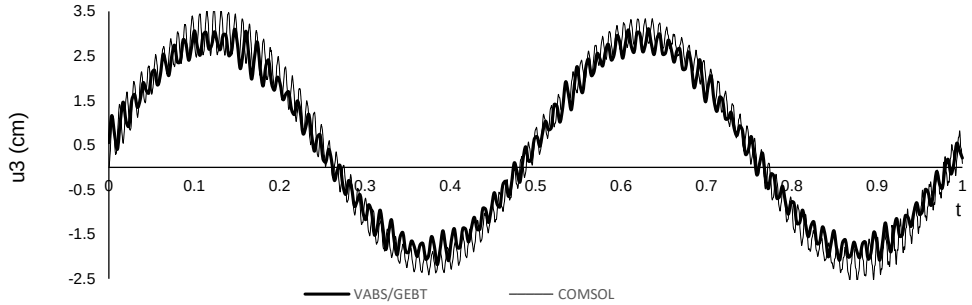

Figure 120: Displacement at the tip (RPM - 2500): VABS/GEBT v. COMSOL

6.2.3.2 Results: Stress analysis

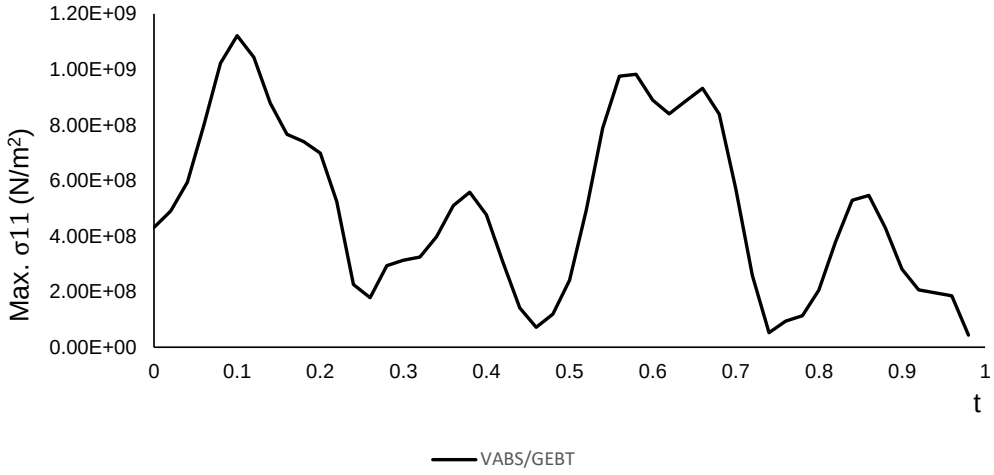

Figure 121: Max σ_{11} at $x = 0.195m$ (RPM - 2500)

Fig. 121 shows the variation of maximum σ_{11} at $x = 0.195$ m at various time steps. We observed that the displacements for this case were almost close between COMSOL and VABS/GEBT. However, the solution for this case did not converge in COMSOL, and displacement results were obtained by placing probes on the solver. That is why the values of maximum σ_{11} from COMSOL are unavailable, and only the stresses from VABS/GEBT is presented here. The plot shows two full cycles of the load being applied. Unlike the case without rotation, we do not observe similar peaks every half cycle. This observation is mainly again because of the rotation. As

mentioned earlier, the centrifugal force's presence causes an initial displacement in the u_3-direction. Thus, the stress values also show higher magnitudes in the first half cycle because of larger strains from rotation. It is also important to note that solutions from any 3-D FEA tool are highly dependent on the ability to mesh the geometry appropriately. If the geometry has sharp edges, tools such as COMSOL can not mesh the geometry appropriately, affecting the overall convergence of the solution. An important observation we made during the analysis is that the 3-D FEA, with geometric non-linearities, consume significantly more time and computational power to provide results when there are sharp edges involved. At times, it does not converge to a meaningful result at all.

Fig. 122 shows exactly how the dominant stress component σ_{11} evolves at the section present at 0.195 m in the blade during rotation along with the timestamps. The corresponding load values over the applied load duration, as shown in Fig. 116.

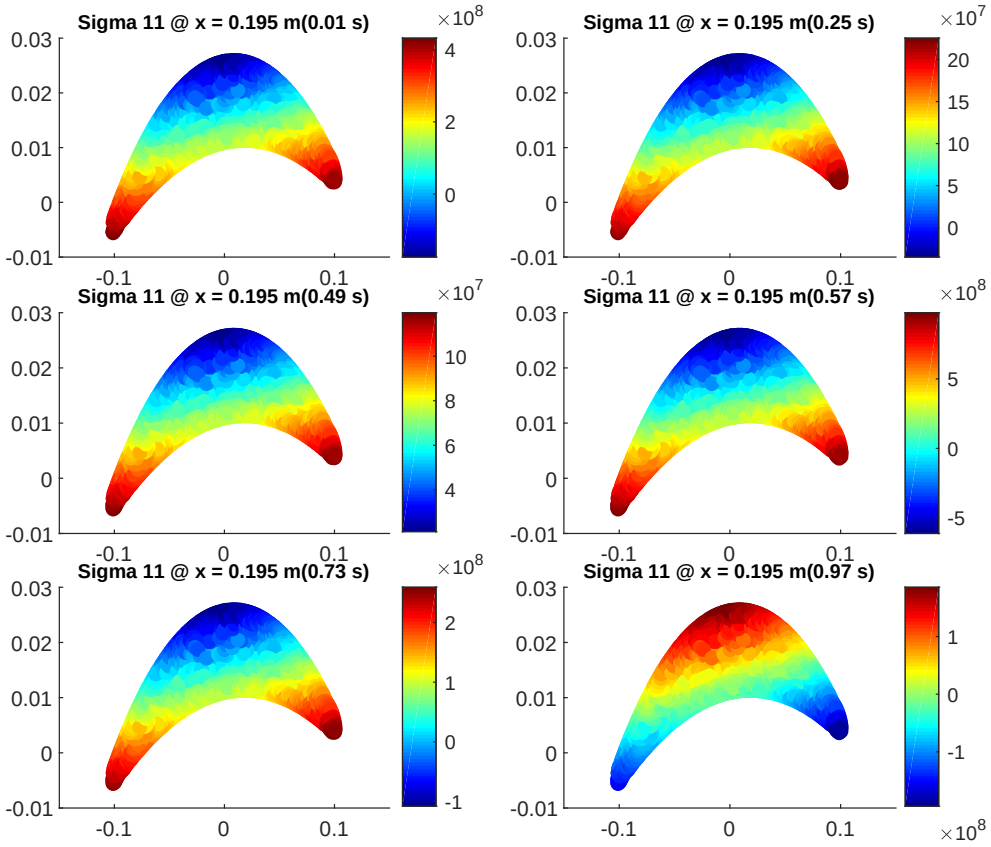

Figure 122: Snapshots of evolution of σ_{11} (N/m^2)at $x = 0.195m$(RPM - 2500)

6.2.4 Experiment 2.1c: Distributed Loads (Non-Rotating)

In the third set of cases, we will examine the applicability of VABS/GEBT in the presence of distributed loads.

6.2.4.1 Geometry

The geometry used for the case of distributed loads is similar to the one used for the case of tip load in Fig. 113, except that the one used here is slightly smaller in the span. It was chosen intentionally to perform the analysis on a shorter blade. This blade shows a significant amount of twist from the hub to the tip. Notice that the stagger at the hub is minimal, but a larger stagger at the mid and tip sections results in a high twist. The detailed geometric properties of the blade are provided in Table 19.

The 3-D sections stacked along the centroidal axis are shown in Fig. 123. Fig. 124 shows the 3-D model obtained by lofting these cross-sections.

Table 19: Geometric properties of the fan blade for experiment 2.1c.

Geometric Parameters	**Value**	**Unit**
Blade span	15.4	in
Hub radius	6.6	in
Tip radius	22	in
Blade chord	8	in
Airfoil type	DCA	-
Hub stagger	2.5	deg.
Tip stagger	34.22	deg.

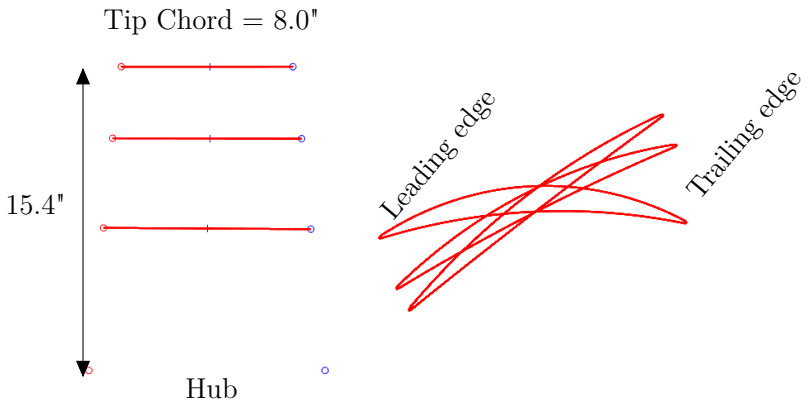

Figure 123: 3-D skeleton of the fan blade used for the application of distributed loads.

6.2.4.2 Loads

In this case, the analyses will be carried under the presence of distributed loads. These loads are obtained from manipulating the rotor flow parameters for the case P3S0 from chapter 5. As can be seen, the tangential loads are comparatively larger because

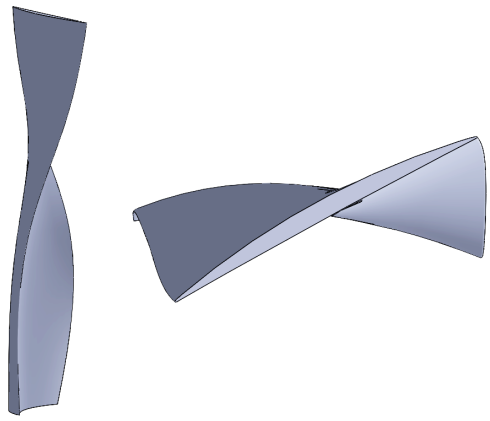

Figure 124: 3-D model of the fan blade used for the analysis of distributed loads.

of the larger turning force required. The variation in axial loads is also smaller as the axial loads are strong functions of static pressure change with relatively lesser variation along the circumference.

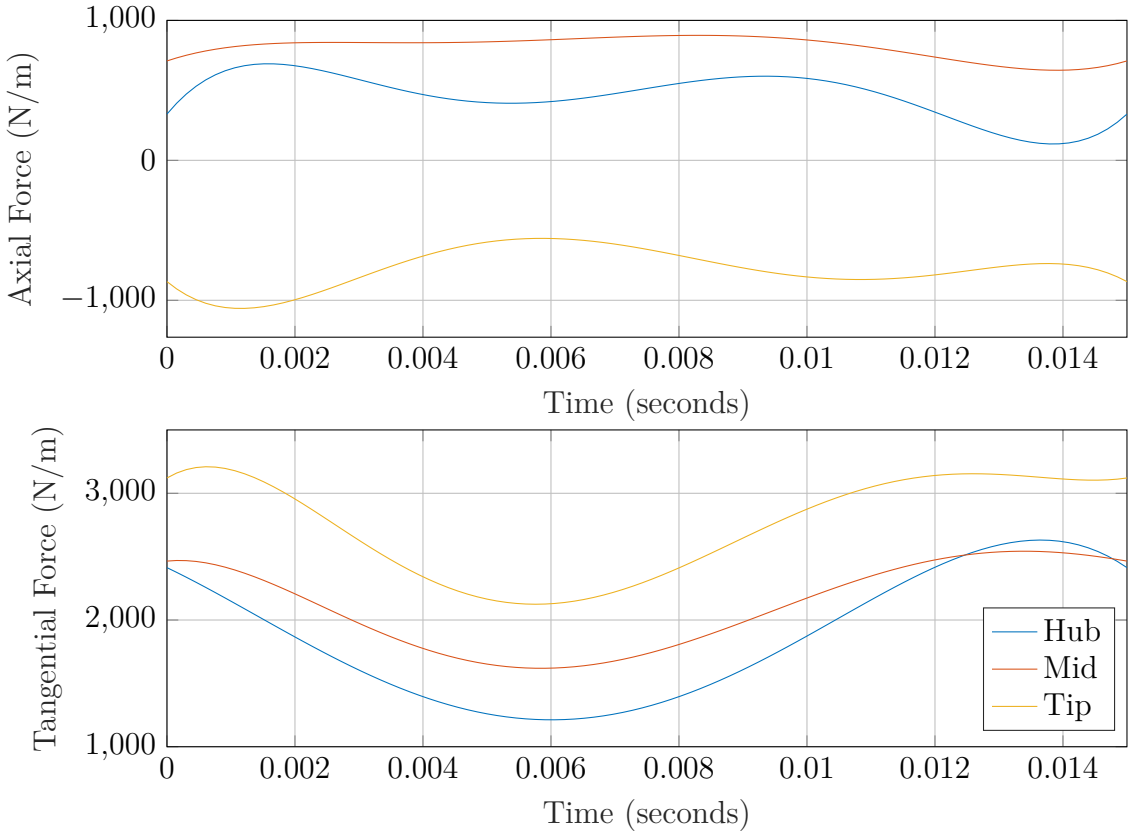

Figure 125: Variation of axial and tangential forces for Experiment 2.1c.

6.2.4.3 Meshing

Fig. 126 shows the triangular grid meshing of the hub, mid, and the tip cross-sections in VABS. The leading and trailing edges have finer grids to capture any stress concentration present in those regions. The mesh generated in COMSOL for the P3S3 design is shown in Fig. 127.

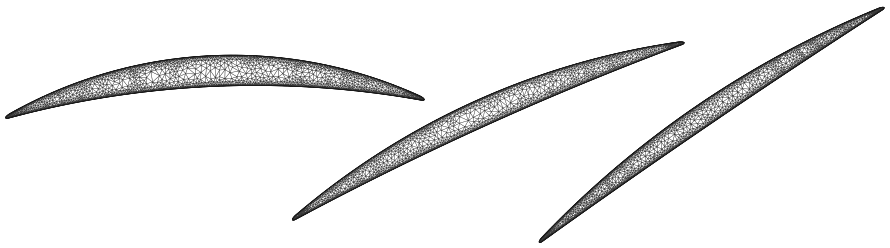

Figure 126: Triangular meshing of cross-sections for the P3S3 design in VABS.

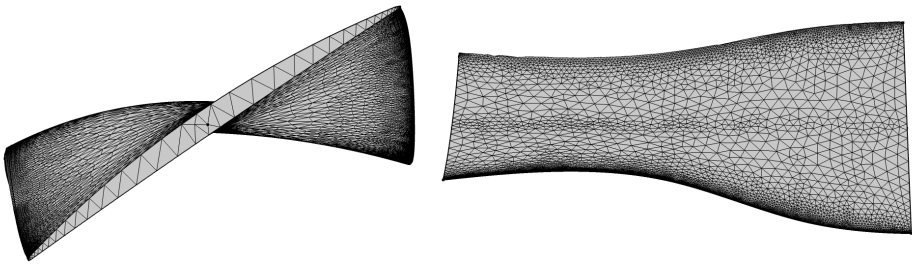

Figure 127: Meshing of the P3S3 design in COMSOL.

6.2.4.4 Results: Eigen analysis

Eigenvalue analysis was performed to compute the natural frequencies of the first eight modes. Table 20 shows the differences in the natural frequencies of the first eight modes between VABS/GEBT and COMSOL. It is observed that the natural frequencies for all modes computed by VABS/GEBT, except the second, are within 1% - 6% of the natural frequencies computed by COMSOL. The second mode (torsional mode) has a 15.33% difference between these two modeling methods. A similar difference in the second mode natural frequency was also observed in Table 17 for a different geometry.

The current author is unable to pinpoint a reason for the discrepancy observed in this mode. Further analysis is warranted before a valid argument is established.

Table 20: Natural frequencies (non-rotating): VABS/GEBT vs. COMSOL

ID	Natural Frequencies (Hz)		% Difference	Mode Shape
	VABS/GEBT	COMSOL		
1	106	109	-2.75%	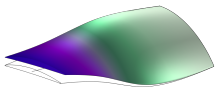
2	310	367	-15.53%	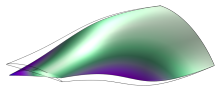
3	518	510	1.57%	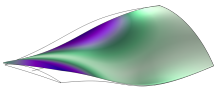
4	782	740	5.68%	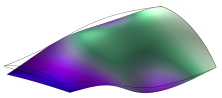
5	1170	1235	-5.26%	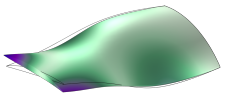
6	1917	1888	1.54%	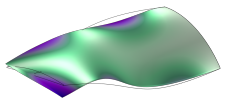
7	2320	2197	5.60%	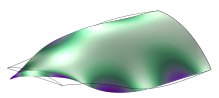
8	2542	2697	-5.75%	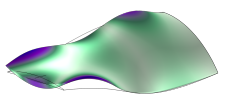

6.2.4.5 Results: Tip displacements

Fig. 128 shows the comparison of the tip displacement in the flap-wise (u3) direction between COMSOL and VABS/GEBT. Note that the results are likely to differ because VABS/GEBT performs analysis with non-linearities included, and the results from COMSOL are without the application of any non-linearities. It was observed that a very fine mesh with non-linearities included did not converge in COMSOL. That is why the results for COMSOL shown here do not include the presence of non-linearities. A close match has been observed between these results in the u3 direction. A maximum tip deflection of 0.275 cm is observed in both COMSOL and VABS/GEBT. The overlap between the results is much closer in the first half cycle than the second half.

Fig. 129 shows the tip displacement comparison in the chord-wise (u2) direction. Similar to the displacement for the tip load, the u2 displacement is slightly larger in the results from VABS/GEBT. The maximum tip deflection in the chord-wise direction is -0.019 cm by VABS/GEBT and -0.011 cm by COMSOL. The results from both COMSOL and VABS/GEBT follow the same trend with the peak displacements co-occurring. The key differences in the peak amplitudes in displacements are likely due to the absence of linearities in COMSOL analysis.

6.2.4.6 Results: Stress analysis

Comparisons on maximum and minimum stresses at the hub are made. Fig. 130 compares the maximum tensile principal stress (σ_{11}) at the hub cross-section. Similar to displacements, the results obtained from COMSOL do not include non-linearities, whereas VABS/GEBT includes them. The first observation is that the maximum stress variation is similar for both VABS/GEBT. It is due to the similarity in the displacement nature predicted by both these modeling tools. The maximum stress predicted by VABS/GEBT is also higher than that predicted by COMSOL. The same trend can also be observed for the minimum stress, as shown in Fig. 131. However,

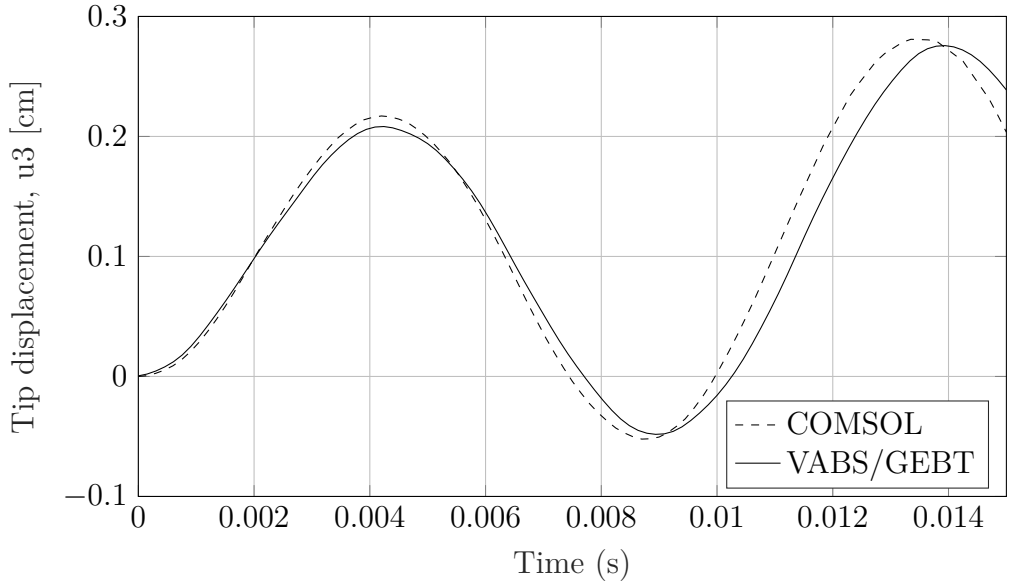

Figure 128: Comparison of tip displacement (u3) between COMSOL (linearities) and VABS/GEBT (non-linearities).

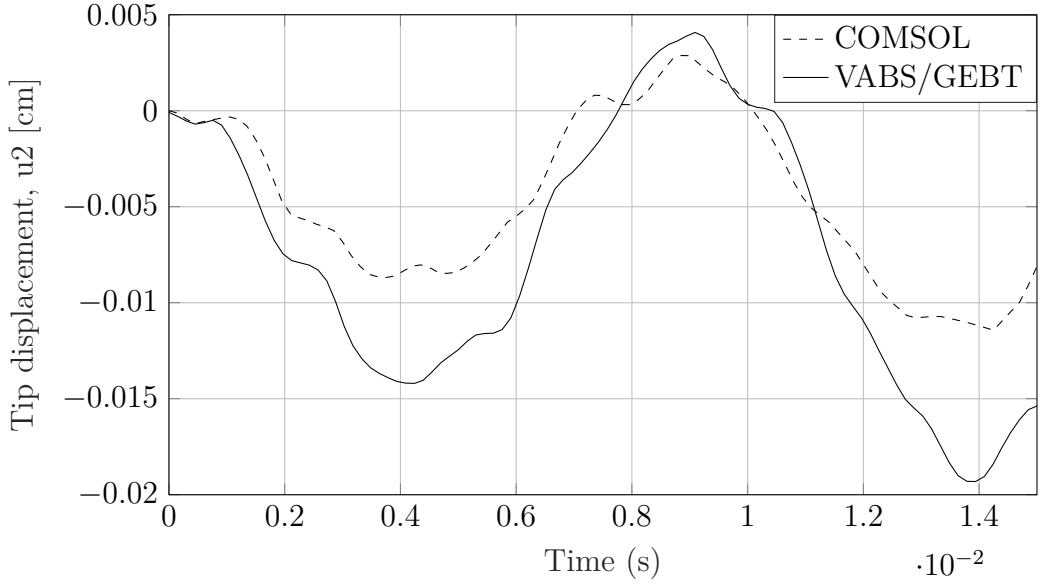

Figure 129: Comparison of tip displacement (u2) between COMSOL (linearities) and VABS/GEBT (non-linearities).

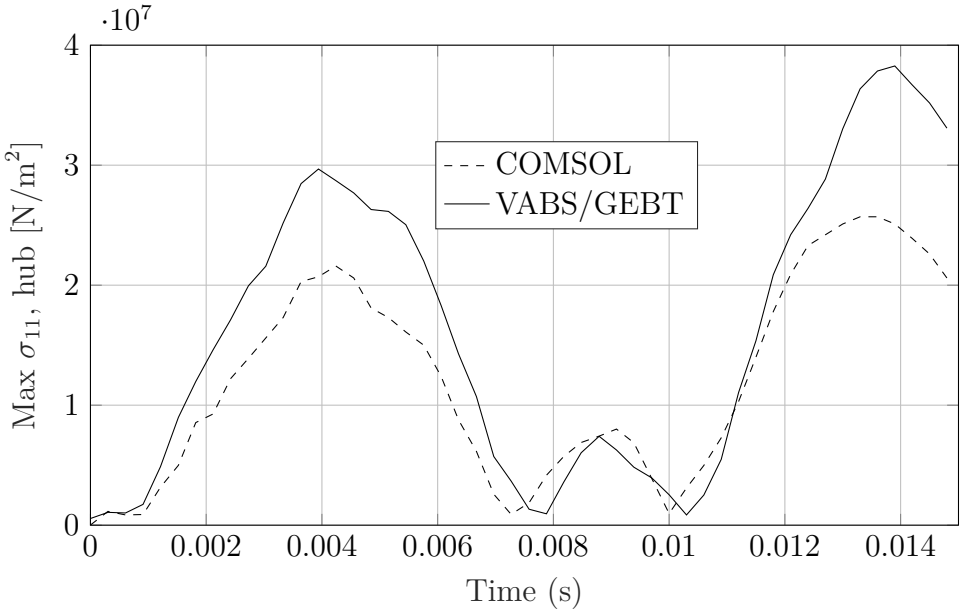

Figure 130: Comparison of maximum hub stress (σ_{11}) between COMSOL (linearities)and VABS/GEBT (non-linearities).

the magnitude of the minimum stresses predicted by COMSOL is higher.

Fig. 132 shows the overlay of minimum, maximum, and average stresses and their variation with time. A consequence of VABS/GEBT predicting larger magnitude maximum stress and COMSOL predicting a larger magnitude minimum stress is a close match in the average stresses. In determining the feasibility of any structure, the overall amplitude of the stress variation is an important parameter because that provides the information on the vibratory nature of the blades. The maximum amplitude of the stresses predicted by COMSOL and VABS/GEBT is 30 MPa and 33.5 MPa, respectively.

While multiple efforts dedicated to converging the simulation with non-linearities with a fine mesh grid failed in COMSOL, convergence was achieved for a coarser mesh with the inclusion of non-linearities. Fig. 133 shows the comparison of maximum and minimum hub stresses (σ_{11}). Note that with the inclusion of non-linearities, the results from COMSOL are in close agreement with that of VABS/GEBT, further highlighting the robustness of VABS/GEBT in performing analysis with the inclusion

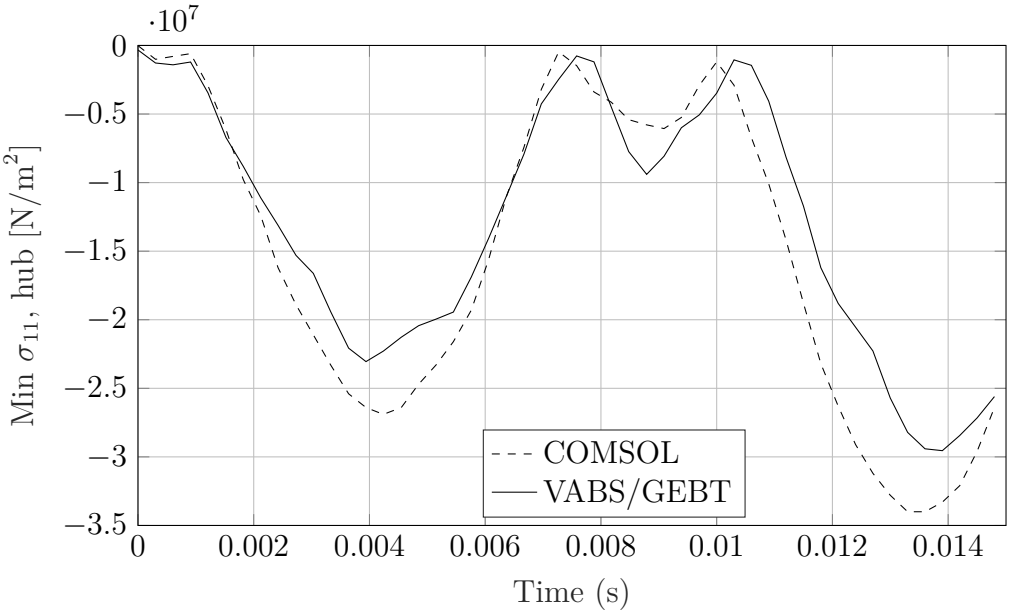

Figure 131: Comparison of minimum hub stress (σ_{11}) between COMSOL (linearities)and VABS/GEBT (non-linearities).

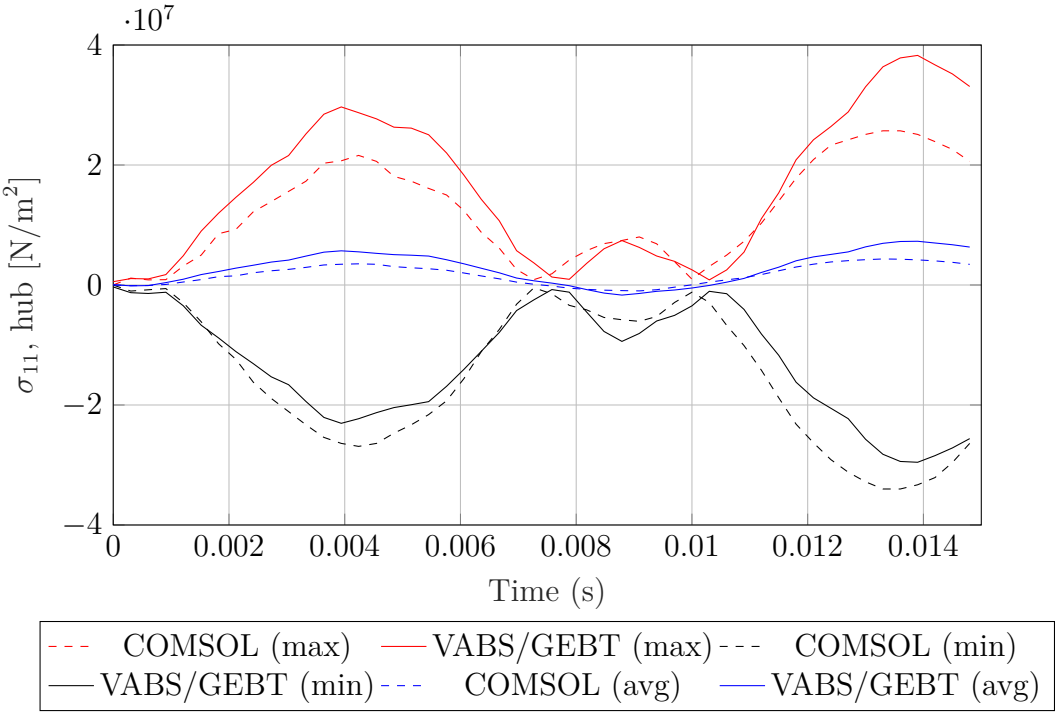

Figure 132: Comparison of maximum, minimum, and average hub stresses (σ_{11}) between COMSOL (linearities)and VABS/GEBT (non-linearities).

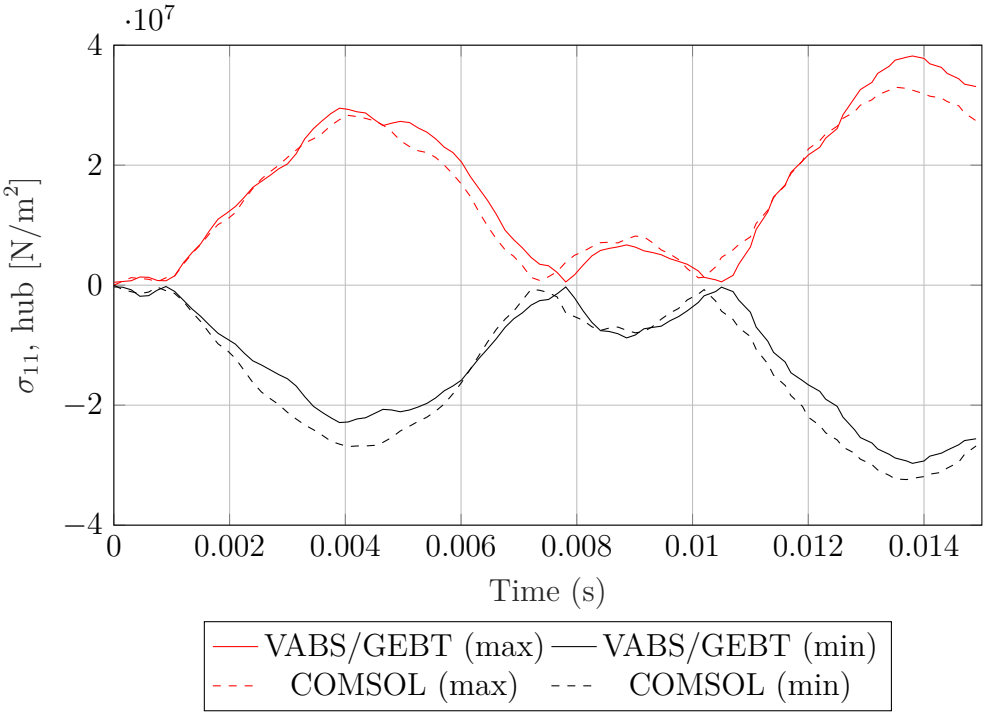

Figure 133: Comparison of maximum and minimum hub stresses (σ_{11}) between COMSOL (non-linearities - coarser mesh) and VABS/GEBT (non-linearities).

of non-linearities. A 16% difference in the maximum peak stress and an 8% difference in the peak minimum stress is observed between the two results. Note than in this case, the average stresses are not shown. Because of the coarser mesh in COMSOL, stresses in many nodes, where stresses were available in VABS/GEBT, were unavailable. So the average stresses would not render any meaningful comparison. An induction is made at this point. Based on how the results varied in COMSOL due to the inclusion of non-linearities, it is likely that a finer mesh in COMSOL will close any differences in the computed stresses between the results of COMSOL and VABS/GEBT. This effort could not be materialized into this document due to the non-convergence issues with the finer mesh.

6.2.5 Experiment 2.1d: Distributed Loads (Rotating)

The last case is when the distributed loads are applied on a rotating blade at 4000 RPM. For the rotating case in COMSOL, centrifugal acceleration, Euler acceleration,

and spin-softening components were included in the analysis.

6.2.5.1 Results: Eigen analysis

Table 21 shows the differences in the natural frequencies of the first eight modes between VABS/GEBT and COMSOL for the case when the blade is rotating at 4000 RPM. We observe that the first mode frequency is almost equal in both. The second mode has the largest difference of 16%. As observed in other cases, the second mode, dominated by torsion, seems to have a significant discrepancy in the results. The results of all other modes were approximately within a 5% difference. It is also seen that most of the modes have significant contributions from both torsion and in-plane bending. Overall, the natural frequency results from VABS/GEBT and COMSOL are in good agreement.

Table 21: Natural frequencies (rotating): VABS/GEBT vs. COMSOL.

ID	Natural Frequencies (Hz)		% Difference	Mode Shape
	VABS/GEBT	COMSOL		
1	109	110	-0.91%	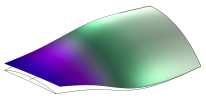
2	308	367	-16.08%	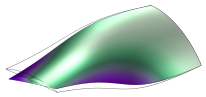
3	532	511	4.11%	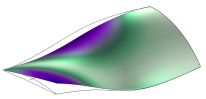
4	792	741	6.88%	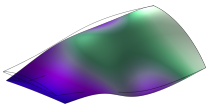
5	1185	1237	-4.20%	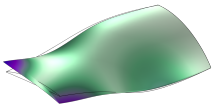
6	1936	1887	2.60%	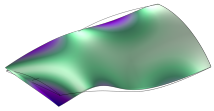
7	2322	2197	5.69%	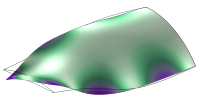
8	2551	2699	-5.48%	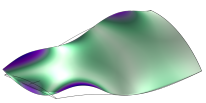

6.2.5.2 Results: Tip displacements and stress analysis

After multiple efforts to converge a fine mesh grid with the inclusion of non-linearities failed in COMSOL, we decided to lower the RPM for the sake of validation. Even at 200 rad/s (1909 RPM), only coarser mesh converged with the inclusion of non-linearities. Therefore, a strong basis for comparison is unavailable for rotating case with distributed loads. Given that the cases representing rotation and distributed loads were a good match between the two modeling software, confidence in the results provided by VABS/GEBT has been established already. Nevertheless, tip displacements and maximum stresses between COMSOL and VABS/GEBT are presented here. No comparison of these values' magnitude is made because of the significant differences in meshing, and only trends in the results are discussed.

Fig. 134 shows the comparison of the u3 displacement. Both COMSOL and VABS/GEBT predict the peak displacement at approximately the same time. In addition, small subpeaks can be observed, a consequence of including non-linearities in both modeling environment.

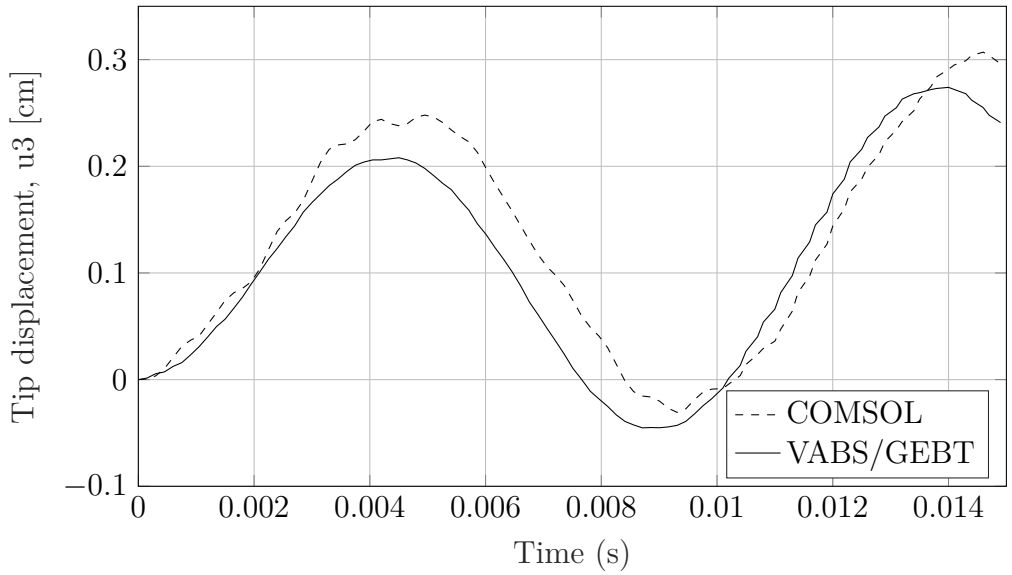

Figure 134: Comparison of tip displacement (u3) between COMSOL (coarser mesh) and VABS/GEBT (non-linearities) at 1909 rpm.

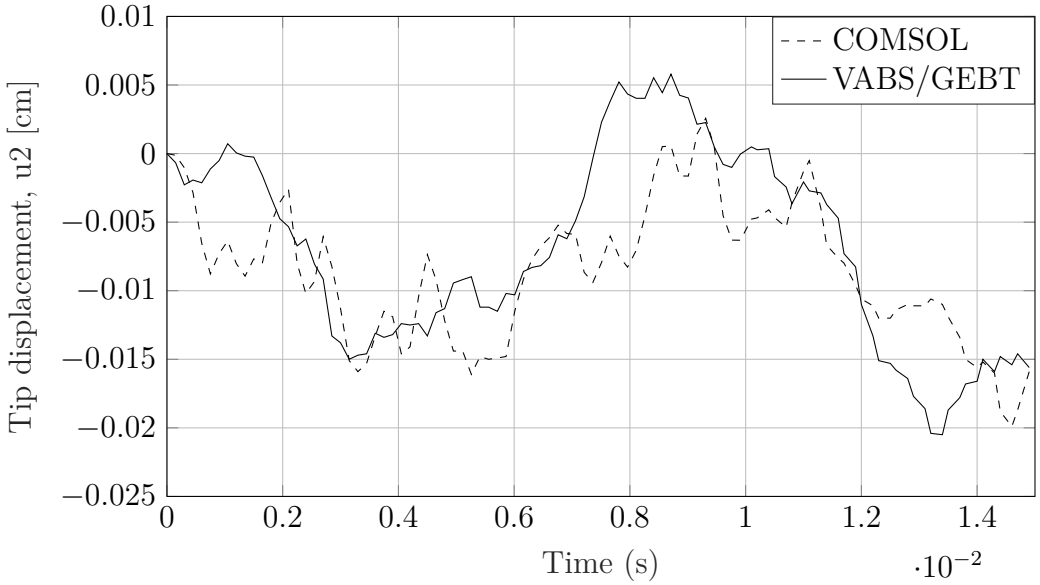

Figure 135: Comparison of tip displacement (u2) between COMSOL (coarser mesh) and VABS/GEBT (non-linearities) at 1909 rpm.

The comparison in the u2 displacement is shown in Fig. 135. A larger dip in the displacement curve is initially seen in the results from COMSOL. Both curves demonstrate a waviness in the response. The waviness can be attributed to the higher-order harmonics introduced by the transient effect of rotation.

Similarly, Fig. 136 shows the comparison of the maximum tensile stress (σ_{11}) at the hub section. Like the u2 displacement, the presence of rotation induces several harmonics in the hub's stresses. Both results estimate the peak stress at the same time step. We observe regions of high variation in max stresses in the first half of the cycle. The maximum stress stays approximately constant for a brief period and increases rapidly after that. On closer observation, the dominating frequencies for both the plots are also similar. Given that the nature of the stresses and displacements align between these two results and the ability of VABS/GEBT to reproduce stresses and displacements properly for the other three cases, it is reasonable to state that a finer mesh density in COMSOL would be able to match the stresses computed by VABS/GEBT.

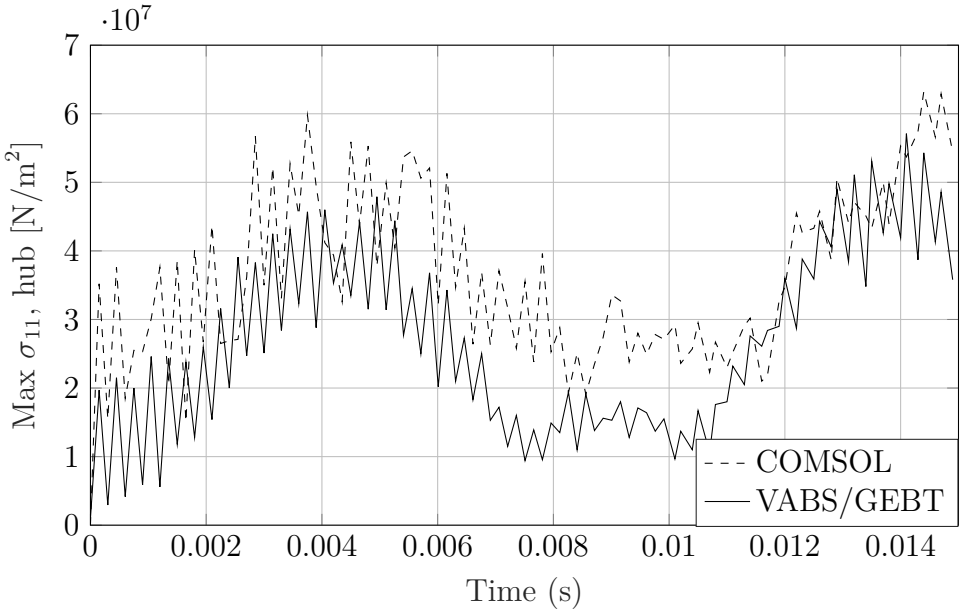

Figure 136: Comparison of maximum hub stress (σ_{11}) between COMSOL (coarser mesh) and VABS/GEBT (non-linearities).

Further analysis of the hub stresses can be seen in Fig. 137. It shows exactly how the dominant stress component σ_{11} evolves at the section present at the hub in the blade along with the timestamps. The periodic fluctuations on the blade stresses are easily visible when looking at Fig. 137. The maximum stress is located either at the tips or the suction side of the cross-section.

6.2.6 Summary of Experiment 2.1

Hypothesis 2.1 claimed that VAM could be used as a computationally efficient method for transient structural analysis of fan rotor blades. From the results of experiment 2.1a and 2.1b, it was observed that for both rotating and non-rotating cases, the tip displacement in the dominant direction was an exact match. For the stresses, a maximum of 12% difference in peak stress was observed. The location of peak stress and the time at which it occurs also matched. The eigenvalue analysis suggested that the difference in various eigenmodes were less than 5%, except in a couple of modes, where the error was up to 14%. The most crucial difference between VAM

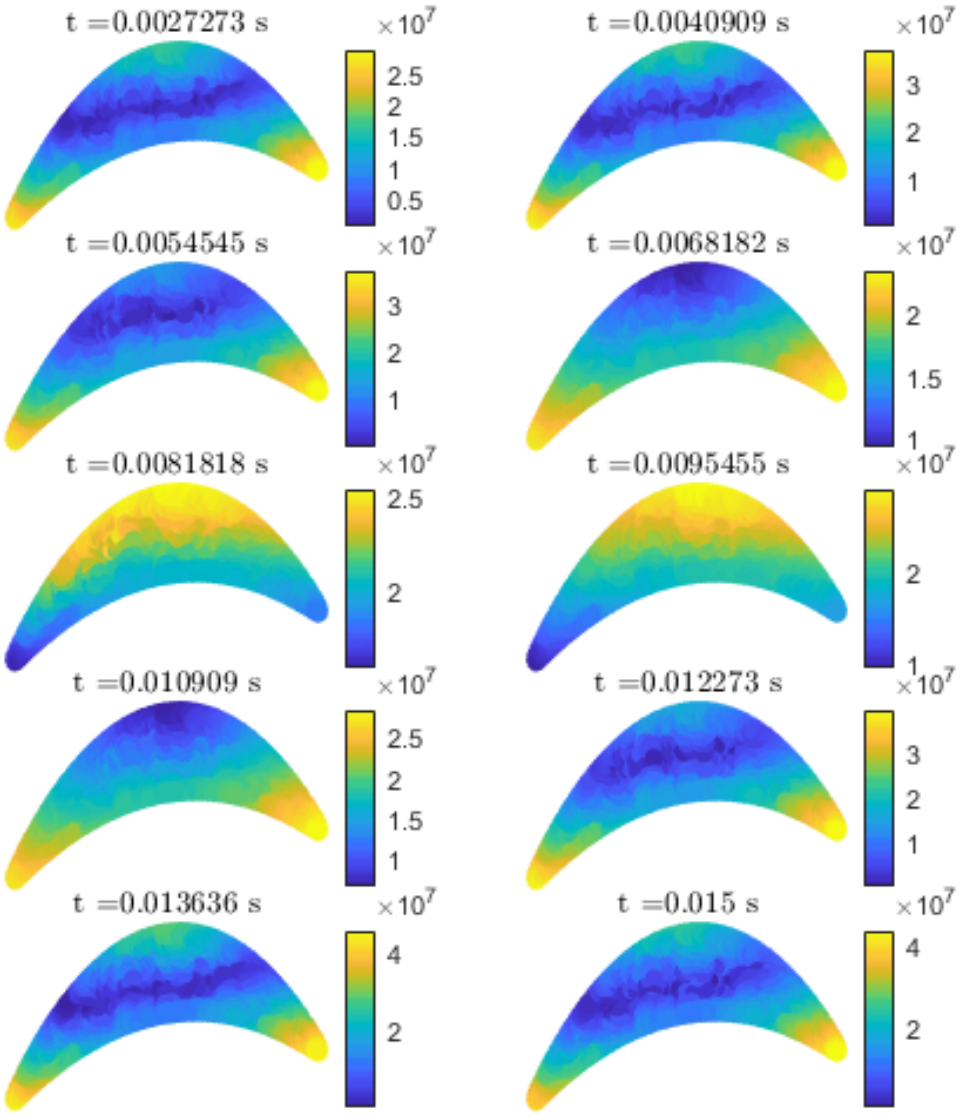

Figure 137: Snapshots of evolution of σ_{11} (N/m^2) at the hub cross-section (rotating: 1909 RPM with distributed loads).

and 3-D FEM was the difference in computational time and storage requirements. 3-D FEM analysis using COMSOL required, for the non-rotating, approximately 6

GB of storage requirement and 21.5 hours of computational time. On the other hand, using VABS and GEBT took 4 minutes with parallel processing for the VABS recovery phase with less than 50 MB storage requirements. Similarly, experiments 2.1c and 2.1d were conducted for the case of distributed loads. Since VABS/GEBT performs analysis, including geometric non-linearities, a valid comparison can be made only with these parameters included in COMSOL. The results of experiment 2.1c showed that the tip displacement in the dominant direction was an exact match. Similarly, the maximum and minimum stresses showed close similarity between VABS/GEBT and COMSOL. The natural frequencies were within a 5% difference except for the second torsional mode. Finally, experiment 2.1d could not converge in a standard PC with non-linearities included at 4000 rpm. At 1909 rpm, the results did not converge for fine mesh, and a coarser mesh was not adequate to make the quantitative comparisons with rotational motion. The results of experiment 2.2d suggest similarity in the trends of the results between VABS/GEBT and COMSOL. Overall, these observations from the results of experiment 2.1 suggest that VAM is an extremely efficient tool for analysis of rotor blades along with reasonable accuracy compared to 3-D FEM results for conceptual level design and analysis. Thus, hypothesis 2.1 is validated.

6.3 Experiment 2.2: Feasibility Analysis and Design Space Exploration

Now that we have recognized the applicability of VABS for the transient structural analysis of rotor blades, the focus is on using it to analyze practical designs. Experiment 2.2 is designed to test hypothesis 2, i.e., to analyze the structural feasibility of aerodynamically optimized design and perform optimization to obtain a design that meets all constraints. By virtue of the hypothesis, it is convenient to divide this experiment into two parts - 2.2a and 2.2b. In experiment 2.2a, we analyze an aerodynamically optimized design to evaluate its feasibility. It will be observed that the example case used in this experiment does not satisfy the structural constraints.

Experiment 2.2b is designed to perform design space exploration to meet the structural constraints and find an optimal design. In the discussions to follow, we will begin with the explanation of the experimental setup, where all the steps necessary to guide the experiments will be detailed. Following this description, detailed results of experiments 2.2a and 2.2b are provided.

6.3.1 Experiment Setup

This experiment aims to demonstrate that an aerodynamically optimized design may not necessarily satisfy structural constraints. Also, if deemed unsatisfactory, the goal is also to change the design to meet these constraints. Therefore, we choose a more likely design to violate these constraints, which makes the optimization challenging. In that regard, the results from one of the cases from chapter 5, P3S3, is used to demonstrate the feasibility assessment. Flow P3S3 is chosen as the example case since it combines both total pressure and swirl distortion and represents a high distortion case.

As mentioned earlier, experiment 2.2a is conducted to test the first part of hypothesis 2. A flowchart describing the experimental process to evaluate the design's feasibility is shown in Fig. 138. We first evaluate the time-varying loads from the aerodynamic design using the process described in chapter 4. With the geometry and loads defined, the VABS/GEBT setup is used to perform the structural analysis. The natural frequencies are evaluated by running GEBT at different RPMs to compute the resonance margins in the Campbell diagram. The excitation frequencies are evaluated by looking at the excited frequencies using fast Fourier Transformation of displacements and stresses. The margins between natural and excitation frequencies are used to define the resonance margin. Similarly, to evaluate the high cycle fatigue safety, 2-D cross-sectional analysis in VABS is followed by performing 1-D non-linear analysis in GEBT. One important consideration here is isolating the effects of transients present

due to the time-varying loads only. To account for this, GEBT is first run for the mean static load. The blade's deformed state under mean static load is defined as the initial condition of the blade when performing transient analysis. Therefore, any variation in stresses can be attributed to only the variation in loads due to inlet distortion. The results not accounting for the isolation of transient effects are presented in [126]. A five-step summary of the procedure for conducting experiment 2.2a is listed below.

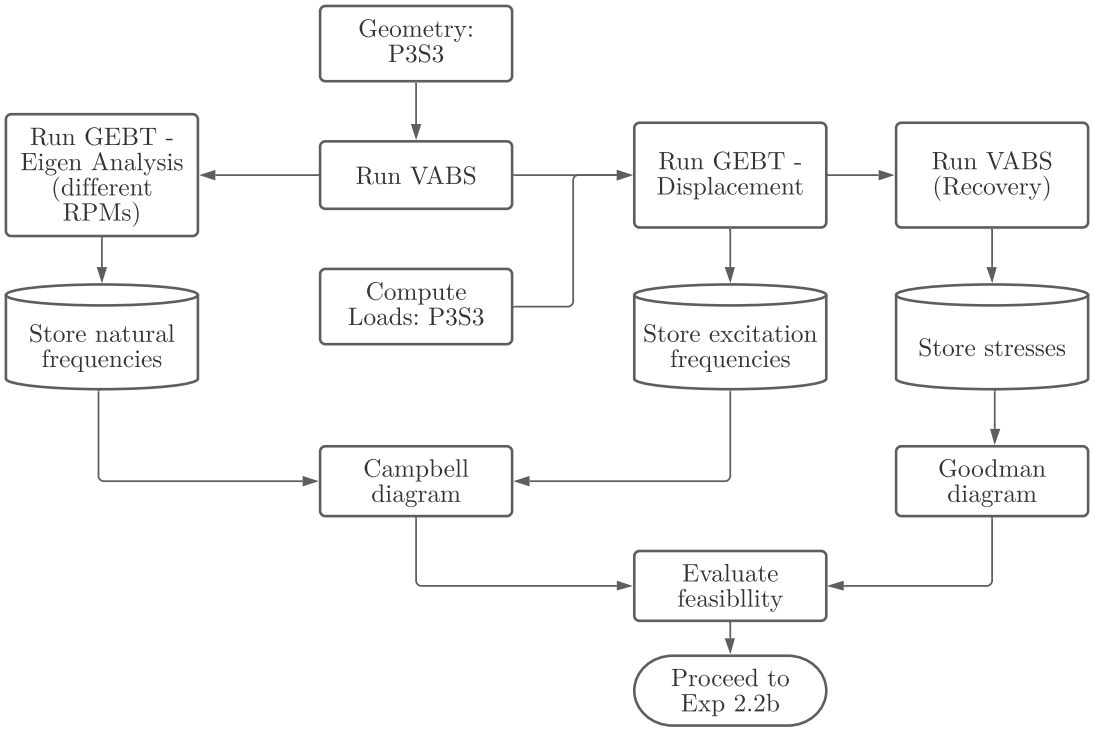

Figure 138: Process flow diagram for conducting Experiment 2.2a.

- Step 1: Evaluate the axial, tangential, and rotational forces for the aerodynamically optimized design P3S3
- Step 2: Evaluate the deformed geometry under the mean load following a quasi-static analysis. Use this position as the initial condition for Step 3
- Step 3: Calculate the mean and alternating stresses for all cross-sections and plot them on a Goodman diagram and compute Goodman margins

- Step 4: Determine the excitation frequencies by taking Fourier Transform of the tip displacements in flap-wise and chord-wise directions and von-Mises stresses at three cross-sections
- Step 5: Compute the natural frequencies of the first eight modes and calculate the margins between natural frequencies and excitation frequencies from step 3
- Step 6: Using the margins from step 2 and step 4, comment on the feasibility of the designs

The results of experiment 2.2a will demand design changes. Experiment 2.2b is hence conducted to test the second part of hypothesis 2 i.e., to optimize the design by satisfying these constraints. Fig. 139 shows the flowchart describing the process for conducting experiment 2.2b. Given the computational efficiency of both aerodynamic and structural modules used in this work, it is manageable to run a large number of cases. For that reason, we will perform optimization by generating surrogate models based on the exploration of the design space. First, we will identify the set of high-level design variables that will be allowed to vary to explore the design space. After identifying these variables, a space-filling design will be created to generate a sample of 1000 cases. Each set of variables will be used to design the fan stage. Each case's corresponding designs are then evaluated in the VABS/GEBT framework to compute the frequency margins and the mean and alternating stress pairs. A surrogate model will be developed to aid in rapid optimization when all aerodynamic and structural responses are obtained. The optimal set of values obtained from the optimization will be re-run in the aerodynamic/structural framework to calculate the true performance. The seven-step procedure for conducting experiment 2.2b is listed below.

- Step 1: Create a space-filling design of experiments (1000 cases) using lower and upper bounds of design variables

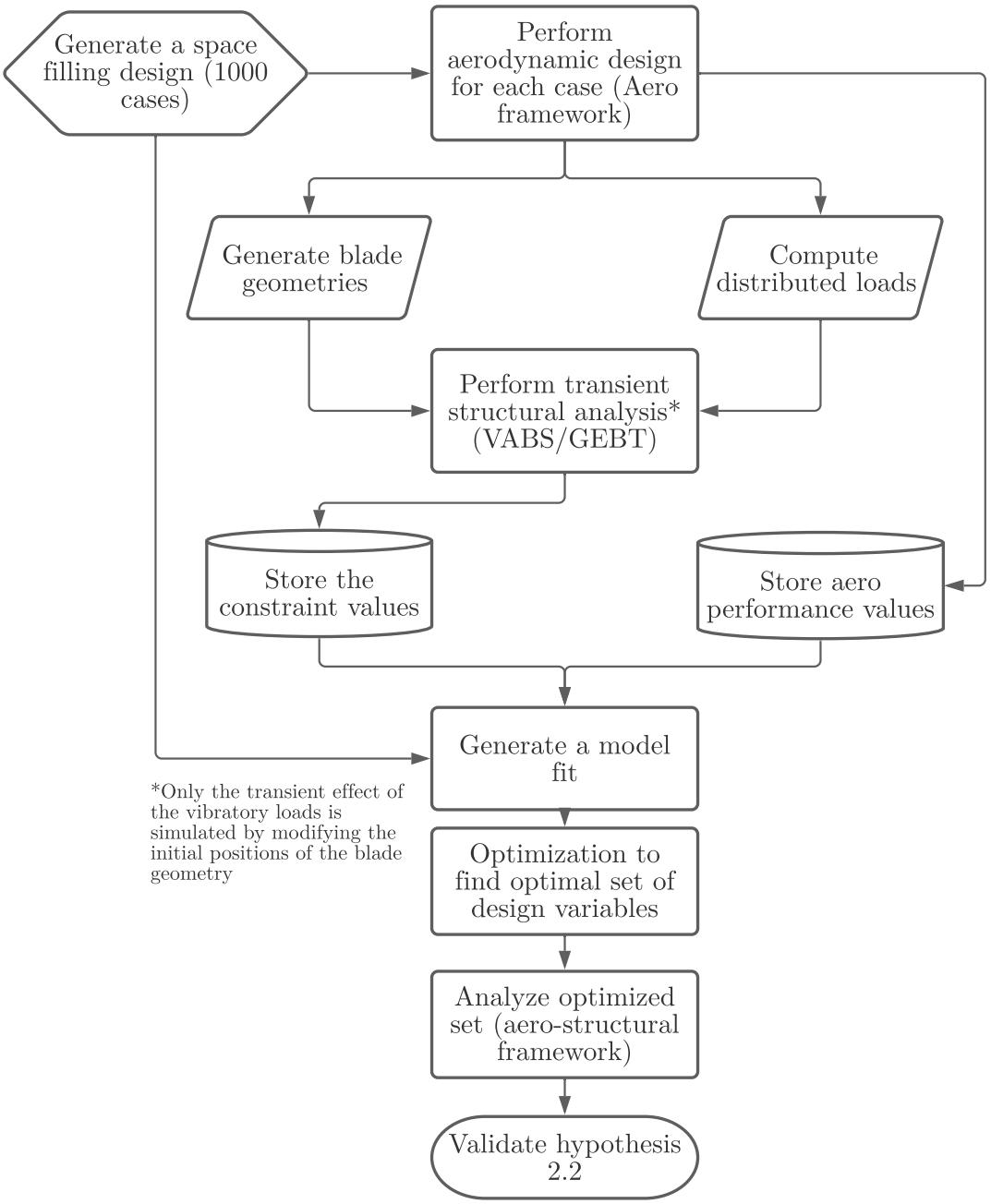

Figure 139: Process flow diagram for conducting Experiment 2.2b.

- Step 2: Evaluate structural constraints for all 1000 generated designs
- Step 3: Create a model fit of the structural constraints and aerodynamic responses as functions of the design variables

- Step 4: Perform optimization on the generated model to find an optimal solution that meets the structural constraints
- Step 5: Use the design variables generated from Step 5 in the aerodynamic design module, obtain the design and loads, and compute the constraints with the structural analysis framework
- Step 6: Evaluate the differences in design and performance between Step 2 and Step 6

6.3.2 Experiment 2.2a: Using VAM to Evaluate the Feasibility of the Aerodynamically Optimized Design

The results of Experiment 2.2a are shown here. First, descriptions of loads, geometry, and meshing are provided. Following that, plots of stresses, displacements, and constraints are defined in the form of Goodman and Campbell diagrams.

Loads

The tangential and axial loads for one revolution generated from the final design of the P3S3 case is shown in Fig. 140. It can be seen that the blade forces have a variation along the circumference. The magnitude of the tangential force is higher than the axial force as the force due to turning is more dominant. The axial force on the tip shows the strongest variation, likely because of the strongest static pressure rise towards the tip regions. Since this design is a tip loaded design, the tangential forces also have higher magnitudes towards the tip compared to the hub. A constant influence of centrifugal force is also present due to the influence of rotation.

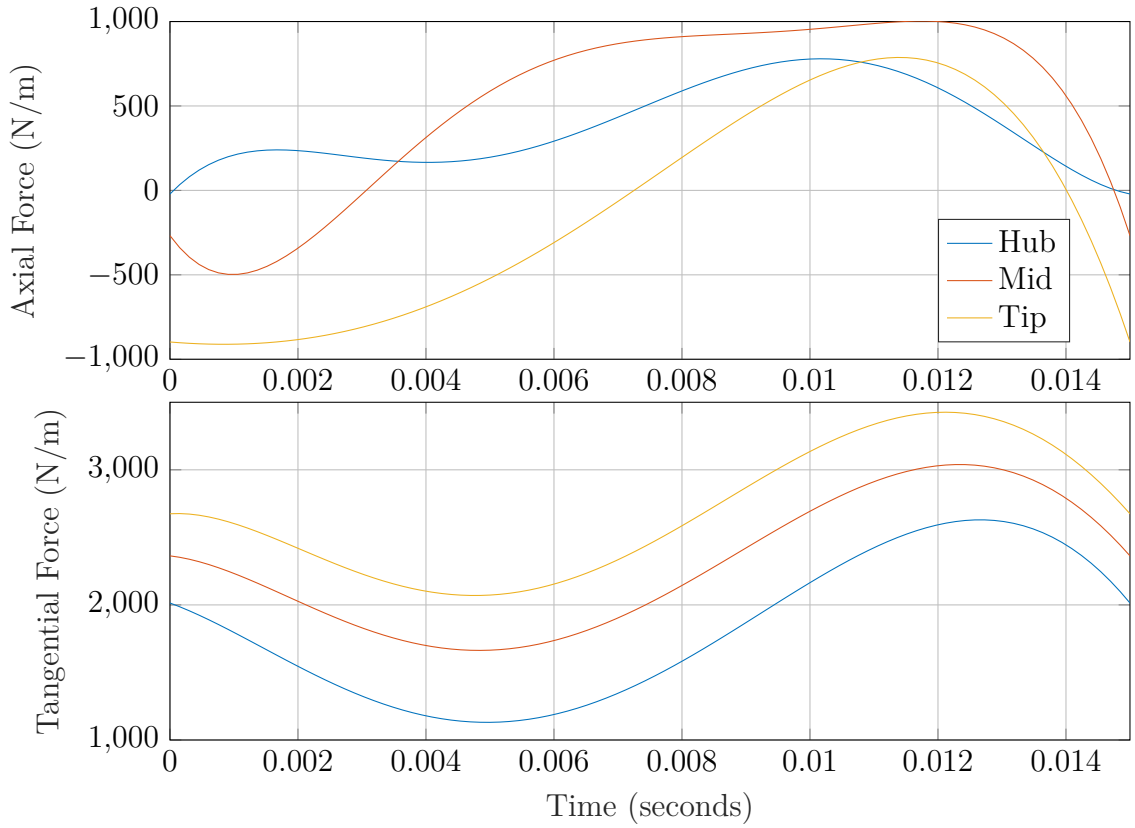

Figure 140: Variation of axial and tangential forces for P3S3 design.

Geometry

Following the process in chapter 3, the 3-D representation of the blade was created. Area centroid was chosen as the radial stacking axis since this axis is generally the first stacking choice to balance the centrifugal stresses. The span-wise and cross-sectional views of the blade are shown in Fig. 141. The blade is 16.8" long with a tip chord of 8.03". The cross-sections' stagger at the hub, mid, and tip sections were 10.6°, 34.5°, and 43.5° , respectively. Similarly, the inlet and exit angle pairs for these cross-sections were [36°, 15°], [51°, 20.1°], and [55°, 33.6°] respectively. Note that we perform interpolation on the cross-sections to create a continuous variation in the blade geometry. Since cross-section information at the very root is unavailable, it is assumed to be the same as the available cross-section closest to the root.

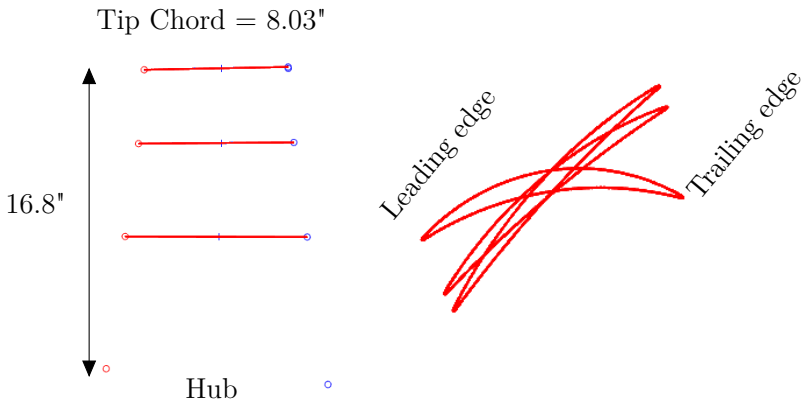

Figure 141: 3-D skeleton of the fan blade for P3S3.

Cross-sectional Mesh

Triangular mesh grids were used to mesh the three cross-sections that formed the blade stacking. A denser grid was formed around the leading and the trailing edges to capture any stress concentration that may be present around these edges. Fig. 142 shows the grids used for each cross-section.

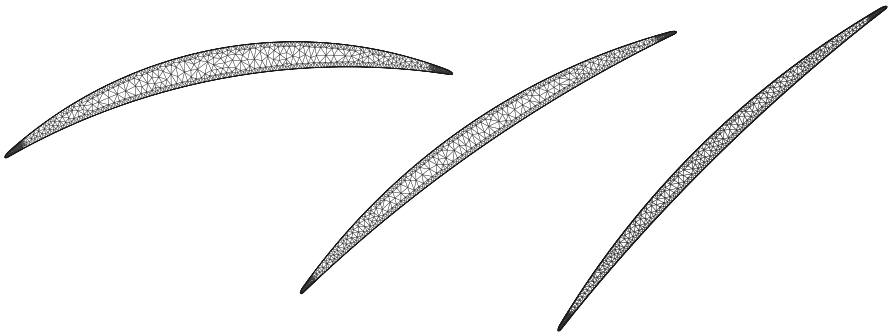

Figure 142: Triangular meshing of cross-sections in VABS for P3S3 design.

Goodman diagram

With aerodynamic loads and baseline geometry available, the structural analysis of the blade was performed. Stresses along the blade at every node of each cross-section were computed. Fig. 143 shows the evolution of von-Mises stress acting at the most

constraining node at the hub, mid, and tip regions. In Fig. 141, these cross-sections refer to the one at the root (not shown in the figure) and the two sections closest to the root. The analysis was performed for six cycles. Analyzing Fig. 143, few observations can be made. First, in all sections, we see the presence of significant stress vibrations. The magnitude of stresses is maximum in the mid-section. As highlighted earlier, this is due to the sudden twist present from the 1st to the 2nd section and a relatively lower thickness to chord ratio. The stresses in the tip section also seem to contain higher-order harmonics compared to the other two.

From the stress plots, the mean and alternating stresses are calculated to plot on the Goodman diagram. The alternating stress is defined by the average of the maximum and minimum stress. The material assumed for this blade was Ti-6Al-4V. While the material properties are proprietary information, an effort was made to recreate the 10^9 cycles Goodman limit from Fig. 13 from [129] that also used Ti-6Al-4V as the material for the blade. With the vibratory amplitude available and assuming that the x-intercept of the limit curve is the yield stress of the material, the curve was digitized. The y-intercept in the vibratory axis was identified as 2.55×10^8 N/m^2, and the x-intercept in the steady stress axis was 9.6×10^8 N/m^2. While these numbers are subject to change based on the material property and the desired life, it serves as a good baseline to proceed with our analysis in absence of any quantitative information.

Fig. 144 shows the Goodman diagram for the P3S3 design. The limit curve represents the 100% margin. The stresses acting on the three cross-sections are plotted (only the worst node of each cross-section is shown). It can be seen that mid-section operates outside the envelope of safe operation by 18%. The hub section had a 56.4% margin, while the tip section was safe with a 10.6% margin. This result suggests that the fan is likely to suffer from fatigue before the end of its desired life.

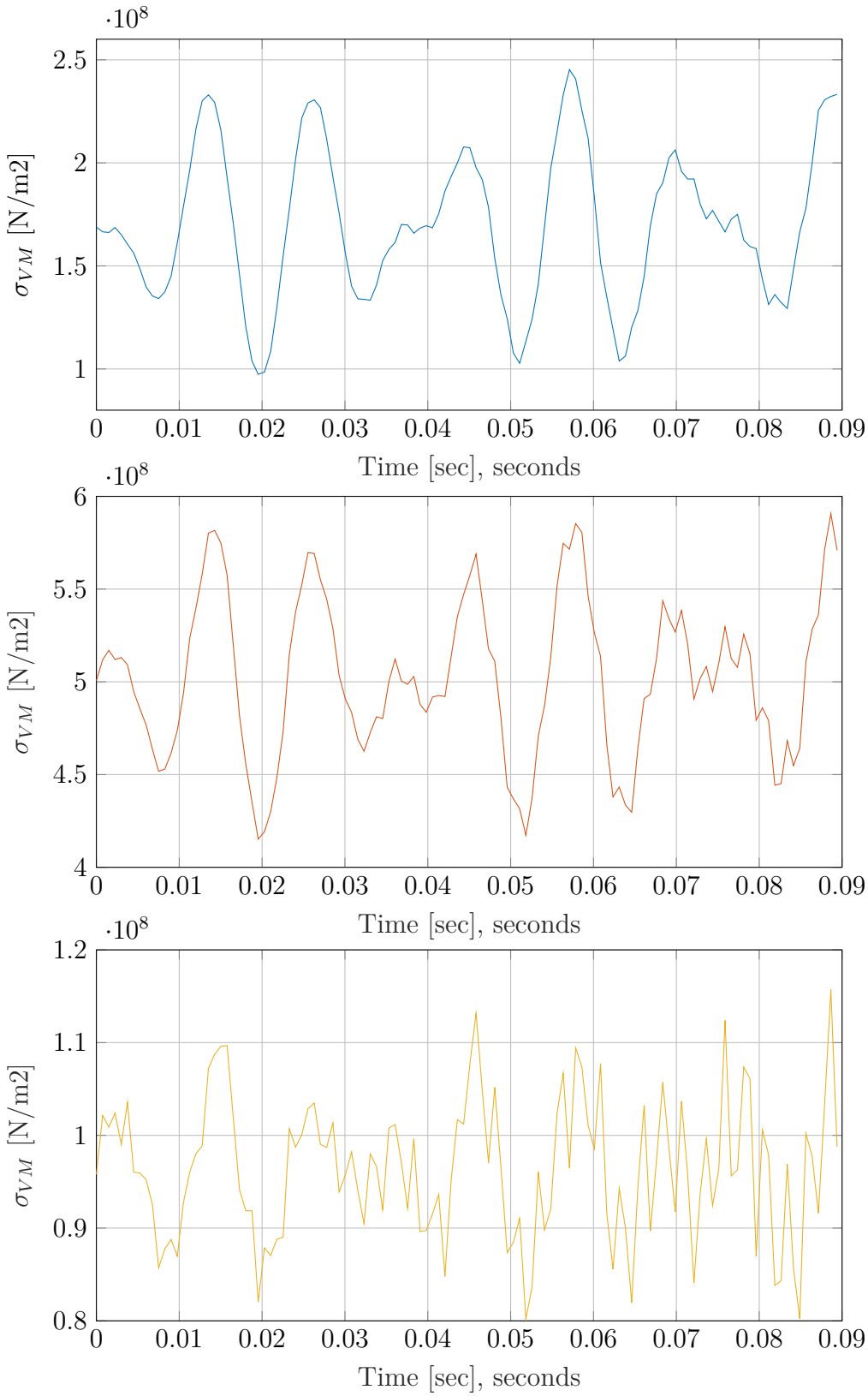

Figure 143: Evolution of von-Mises stresses over time: hub, mid, and tip sections [top to bottom] for P3S3 design.

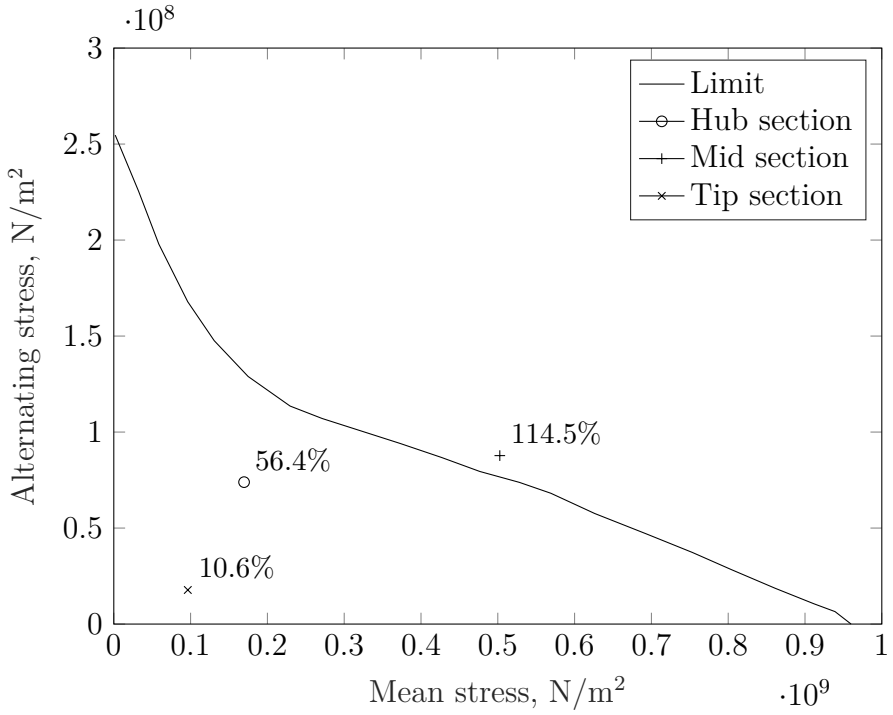

Figure 144: Goodman diagram for P3S3 design.

Campbell diagram

Next, we analyze the margins between the excitation and natural frequencies. First, the dominant frequencies responsible for the harmonics are plotted. The dominant frequencies are determined by analyzing each cross-section's stresses and the tip displacements in the chord-wise and flap-wise directions. Fig. 145 shows the Fast Fourier Transformation of the stresses that highlight the dominant frequencies present. In the first two sections, two frequencies are dominant: 1EO and M1 and M3/6EO have relatively smaller contributions. The first flapping mode is excited. Through the analysis of the third section, contributions from higher modes become apparent. Except for the M3/6EO contribution, the amplitudes of other peaks were relatively smaller.

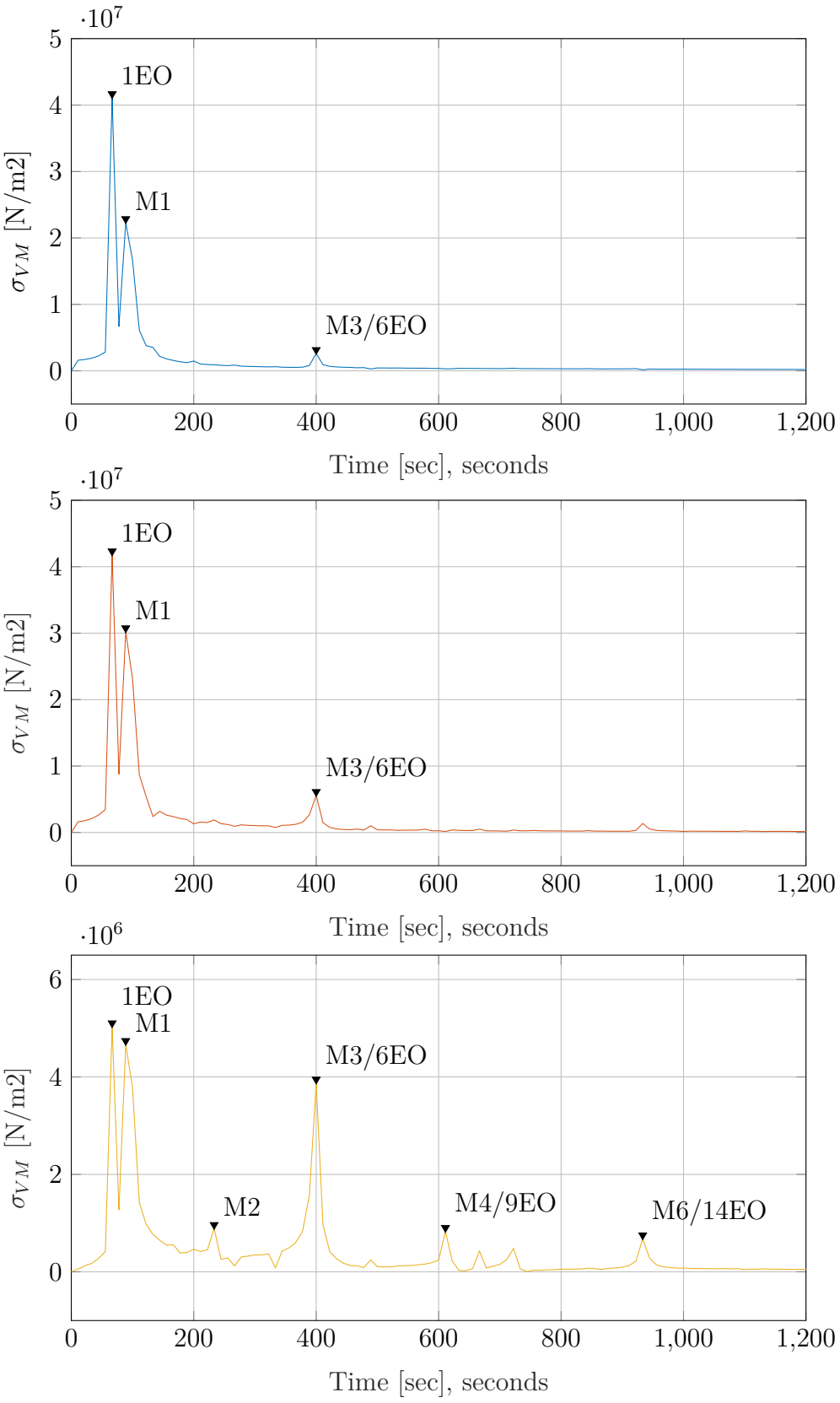

Figure 145: FFT of von-Mises stresses at hub, mid, and tip sections [top to bottom] for P3S3 design.

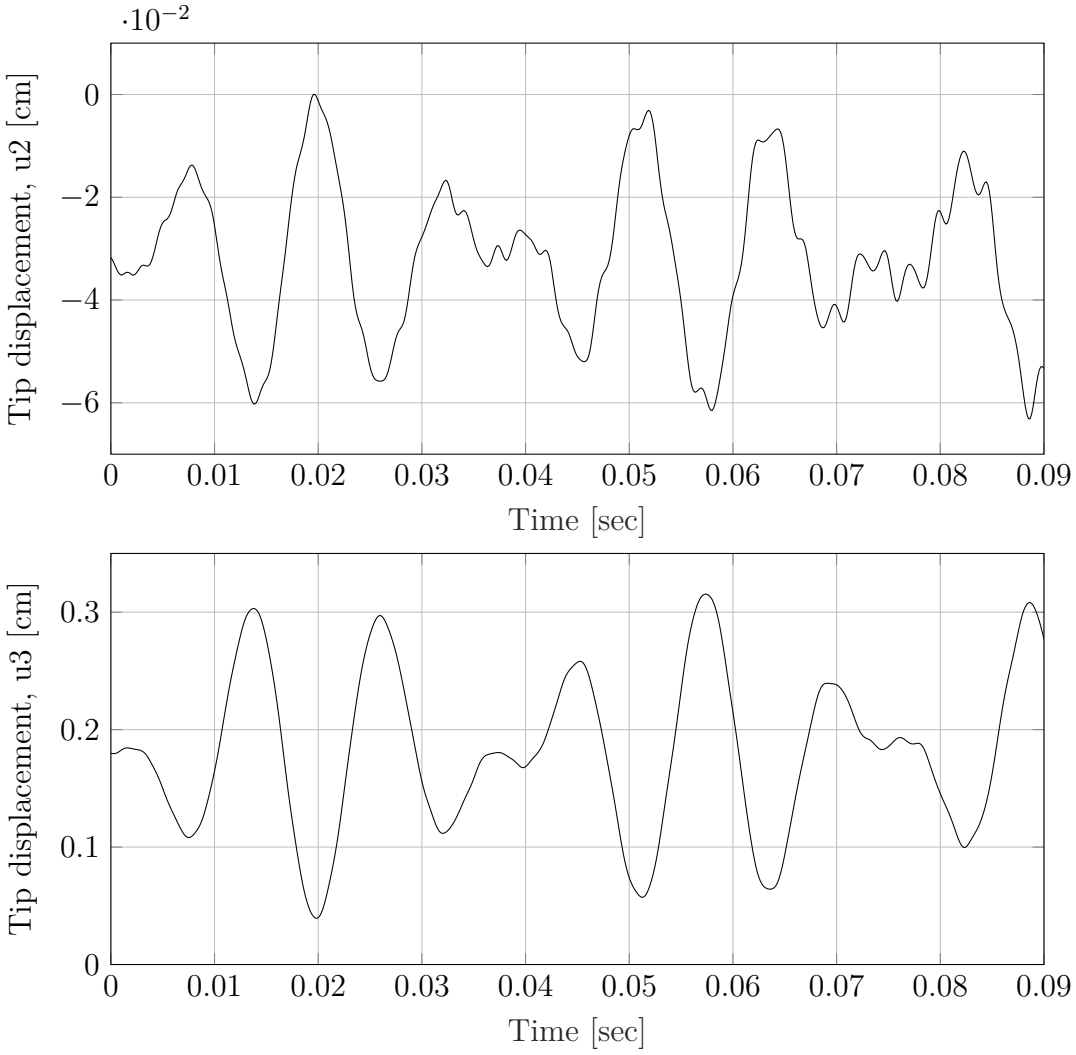

Figure 146: Tip displacements in the chord-wise (u2) and flap-wise (u3) directions for P3S3 design.

Fig. 146 shows the displacement of the tip region. The maximum tip displacement in the dominant direction is 0.32 cm. In the u2 direction, the displacements are smaller in magnitude, and higher-order harmonics are present in the response.

Fig. 147 shows the results of the FFT of the tip displacements in chord-wise (u2) and flap-wise (u3) directions. Similar to the stress analysis, the first engine order is observed to be a dominant harmonic in the response in both directions. Mode 1 is also excited. Displacement in the span-wise (u1) direction is not shown because the root is assumed to be fixed and has virtually no displacement in that direction. In

the u2 direction, the M3/6EO contribution is also present, albeit small. This crossing is likely the reason why the stresses in the tip showed similar excitation.

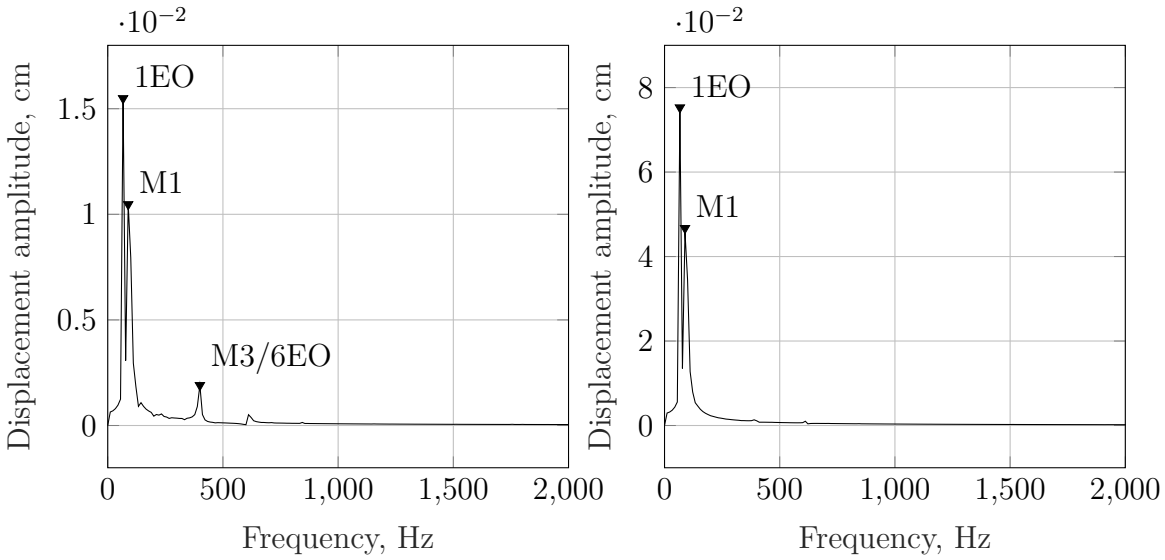

Figure 147: FFT of tip displacements for P3Se design - u3 [left] and u2 [right].

Natural frequencies for the first eight modes were computed by repeating the eigenanalysis at various RPMs to establish the mode lines and plotted on a Campbell diagram to evaluate the crossings of concern, as shown in Fig. 148. Only some engine order lines are shown for the sake of clarity. Crossings of concern were avoided at the lower engine order frequencies. The first natural frequency was observed between the first and second excitation frequency with a reasonable safety margin. M1/1EO and M1/2EO had 29% and 42% margins, respectively. 12.6% margin was present between Mode 2 and 4EO. We saw the 6EO response to be excited. It is likely because the Mode 3 and 6EO frequency at the design speed was the same. While the 6EO contribution is not too high, we desire at least a 5% margin at this frequency for higher engine orders.

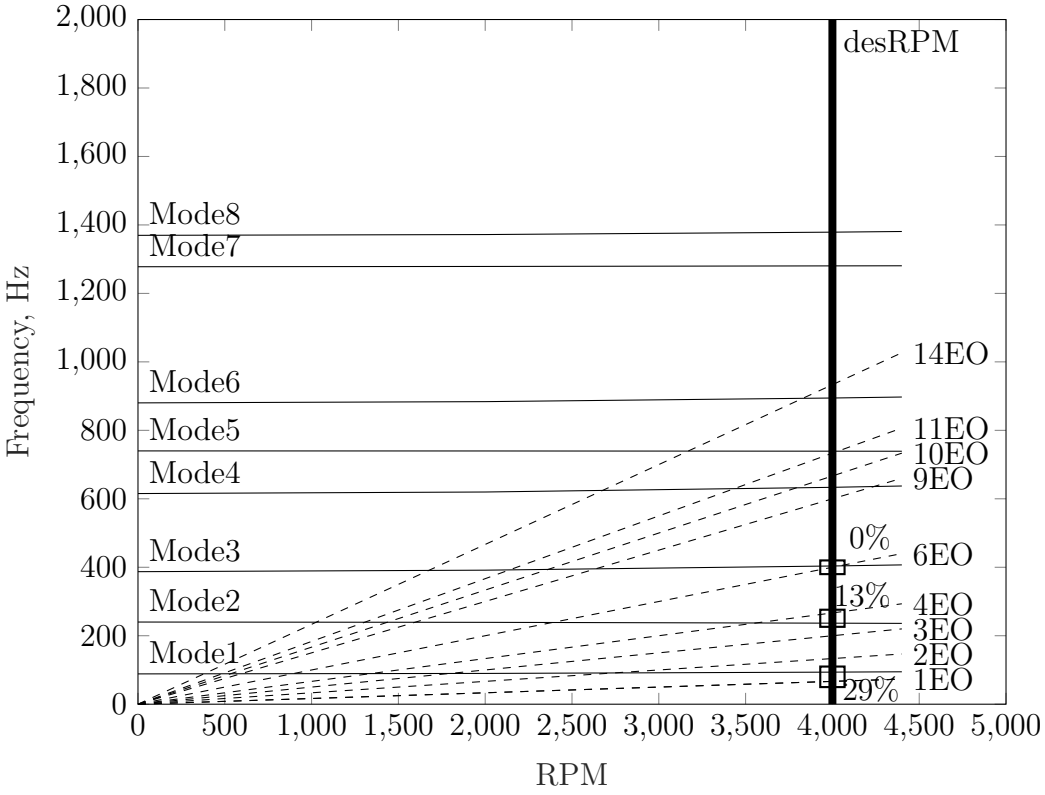

Figure 148: Campbell diagram for P3S3 design.

Feasibility Analysis

While the fan design's aerodynamic characteristic was desirable, it failed to meet the structural constraints defined by the Goodman and Campbell diagrams. Therefore, this design is not deemed as a feasible design. When optimizing the design for stresses and reducing margins at other crossings, a small design change may change the 1st natural frequency and bring the M1 frequency closer to the 1st or the 2nd EO frequency. Therefore, care should be taken to establish the margin between these two frequencies as well.

6.3.3 Experiment 2.2b: Using VAM to Explore the Design Space for a Feasible Solution

Experiment 2.2a showed that the aerodynamically optimized design was not structurally feasible. Experiment 2.2b is conducted to explore the design space defined by

various design parameters. The process for conducting this experiment is shown in Fig. 139.

6.3.3.1 Defining the variable space

Nine design variables that conceptually influence the aerodynamic, structural, or both performances are chosen to explore the design space. The list of variables along with the rationale for selecting them are provided below:

- Number of blades (rotor): controls the solidity and loading per blade
- Hub to tip ratio: controls the incoming flow velocity, the distributed load value, and natural frequencies
- Rotor chord: controls the rotor diffusion, total force, and natural frequencies
- Rotor exit area ratio: controls the velocity at the rotor exit, axial force, and influences natural frequencies
- Stator exit area ratio: controls the velocity at the stator exit
- Stator chord: controls the stator diffusion
- Thickness to chord variation: controls the stress distribution and natural frequencies
- Taper type: controls natural frequencies and stress distribution
- Loading type: controls the variation of distributed loads and consequently influences the blade camber and twist

The bounds of design variables were created to explore the design space to search for an optimal set of design variables. Table 22 lists the variables described above and their corresponding baseline, and lower and upper bounds. The design variables are in the form of categorical and continuous variables. Design type, taper, thickness distribution, and number of blades constitute categorical variables. Since blades

Table 22: Bounds of variables for design space exploration for aero-structural optimization.

Categorical Variables			
Parameters	**Baseline**	**Levels**	
Loading type	1	-1, 0, +1	
Taper type	0	-1, 0, +1	
Thickness distribution	1	1, 2, 3	
# of blades	22	21, 22, 23, 24, 25	
Continuous Variables			
Parameters	**Baseline**	**Lower Bound**	**Upper bound**
Hub to tip ratio	0.3	0.23	0.3
Rotor tip chord	8.03"	6.5"	8.5"
Rotor exit area ratio	0.90	0.87	0.95
Stator exit area ratio	0.95	0.90	0.97
Stator chord	3.935"	3.5"	5"

can only be integer-valued, it is intuitive to consider it as a categorical variable. Design type, taper, and thickness distribution are naturally continuous variables. This experiment's main goal was to understand how these parameters influence the overall performance; therefore, the discrete variable types were used for parameters and analyzed as three separate levels. A brief explanation of these variables is provided here.

Three loading types are considered: hub loaded (-1), uniformly loaded (0), and tip loaded (+1). The loading input is prescribed by the enthalpy rise distribution along the rotor span. Fig. 149 shows the span-wise distribution of the enthalpy rise across the rotor for the three cases described. Similarly, Fig. 150 shows the thickness to chord distribution chosen for the design space exploration. Note that the thickness to chord ratios at the hub and tip are fixed, and only the distribution between them is changed. This distribution was specified intentionally to investigate if we could satisfy the constraints without exceeding the maximum thickness to chord ratio. It was observed that the hub was only slightly above the 50% Goodman margin limit, and the mid section suffered the most stresses. So, the distribution was assigned to

have a higher variation towards the mid section. The taper distribution follows a similar rationale, wherein 0 indicates no taper, -1 indicates a shorter hub, and +1 indicates a shorter tip. A linear distribution in taper is specified. The variation of other parameters - the hub to tip ratio, rotor tip chord, rotor area ratio, stator area ratio, and stator chord follows the same bounds as defined in Table 22. Based on the bounds of variables shown in Table 22, a total of 1000 designs were created using the Latin Hypercube Sampling technique.

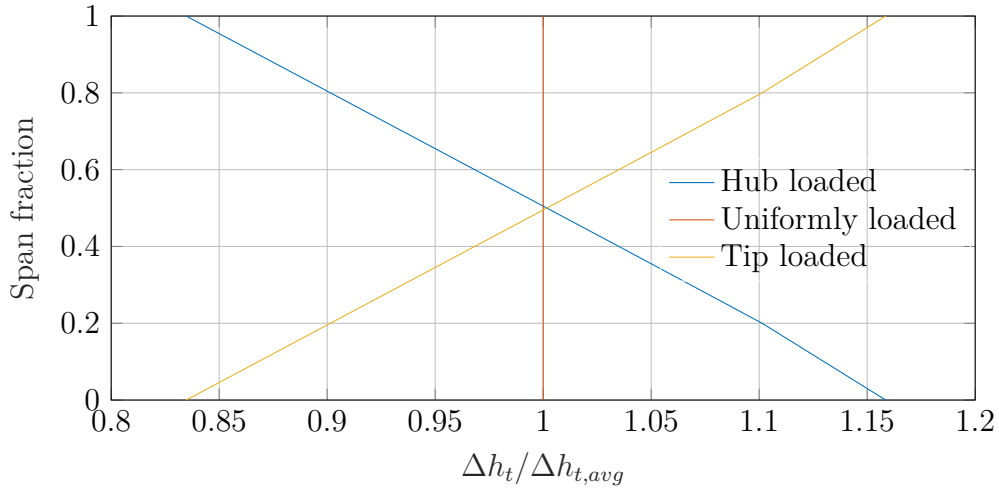

Figure 149: Span-wise loading distribution for design space exploration.

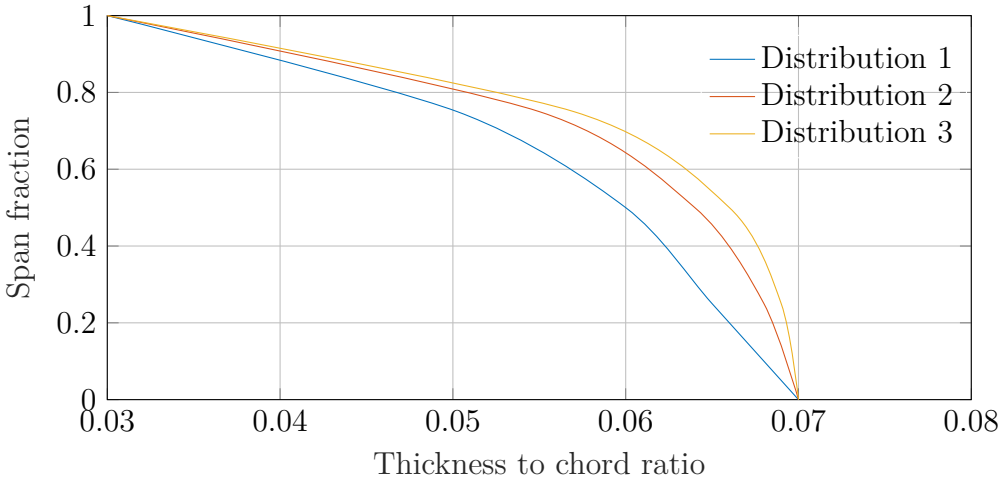

Figure 150: Span-wise thickness to chord distribution for design space exploration.

6.3.3.2 Design space exploration

All 1000 generated cases were run in the aerodynamic design framework with their aerodynamic performances recorded along with the geometry and loads. These geometries were then subjected to the respective loads, and the structural analysis was performed. The following responses were tracked:

- **Isentropic stage efficiency:** The stage efficiency is the primary aerodynamic performance parameter we seek to maximize. It will be denoted as η_{stg}.
- **Hub reaction:** The reaction of the hub is recorded to ensure that the hub reaction is positive and that the hub is contributing to the overall increase in the pressure rise. It will be denoted as R_h.
- **Number of stall cells:** During the fan stage's aerodynamic design, the diffusion factor at each radial segment is recorded. Diffusion factor (DF) > 0.59 is considered as a surrogate for the stall. The number of locations where DF exceeds this limit is recorded and counted as the number of stall cells. For example, if three radial segments are defined and five circumferential sectors exist, 15 DF values are computed. If segment 2 had a diffusion factor $>$ 0.59 in two circumferential sectors, then the number of stall cells recorded is two. Recording the stall criteria this way eliminates the need to track all stall conditions. Eventually, we seek to attain a design where the number of stall cells at the design point in 0. It will be denoted as N_{st}.
- **Goodman margins:** It was observed in the cross-sectional analysis that the hub and the mid sections are the most constraining sections while the tip section was relatively safe in terms of the vibratory stress margin. In that regard, we will only seek to satisfy these margins. They will be denoted as GM_{hub} and GM_{mid}.

- **Frequency margins:** Observation of the Campbell diagram in Fig. 148 showed that only certain frequency crossings were of concern. In that regard, we focus only on those margins. Crossings of evaluation include M1/1EO, M1/2EO, M2/3EO, M2/4EO, M3/6EO, and M3/7EO. These margins will be discussed in absolute percentages.

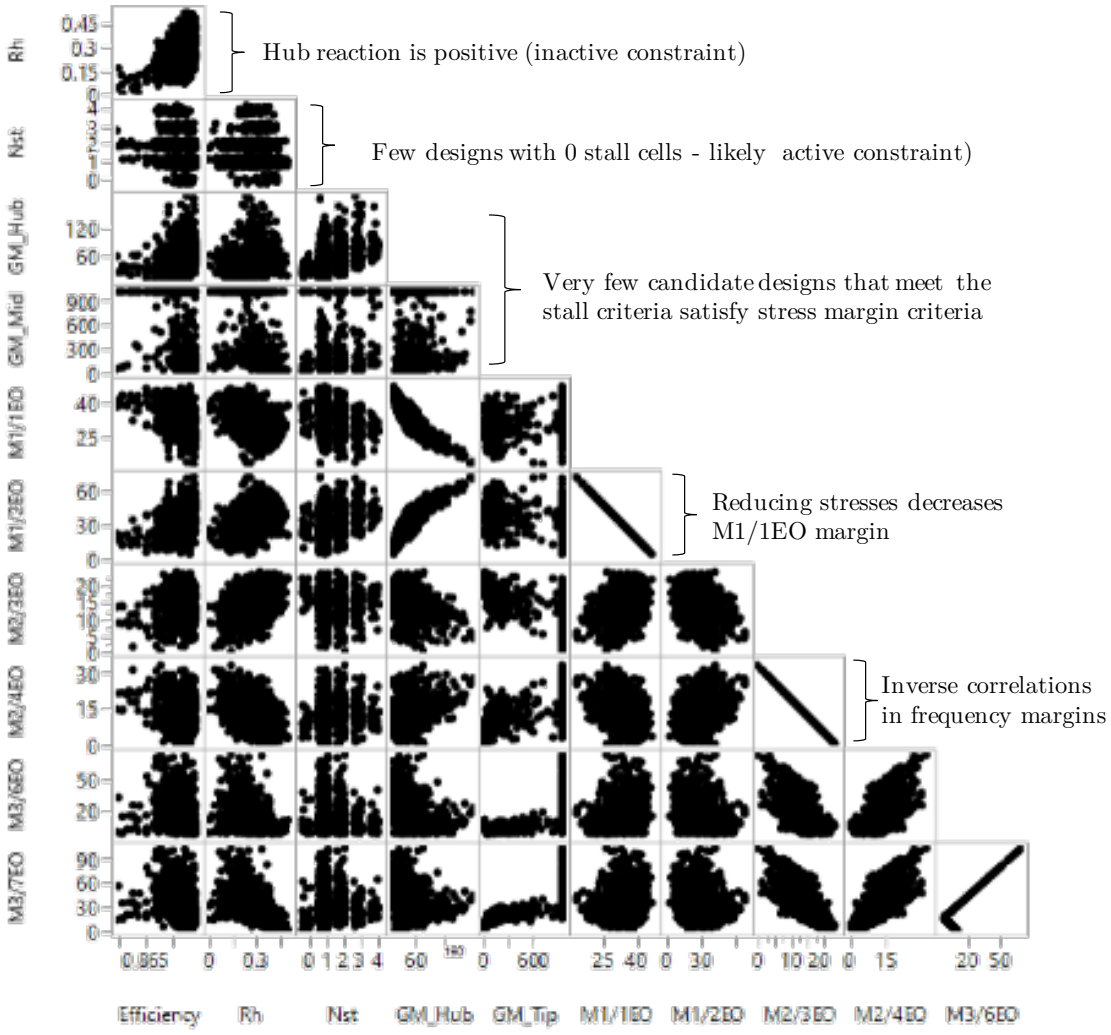

Figure 151: Scatter plot matrix of responses.

From the outcomes of the analysis, the responses as mentioned above were tracked. Fig. 151 shows the scatter plot matrix of these responses. Each plot in Fig. 151 contains all points from the analyses. The scatter plot matrix is a good way of visualizing the correlation between the two responses. Few insights can be gained

from these responses. The stage efficiency is mostly greater than 87.5%. For any given set of input design parameters, the aerodynamic design framework tries to achieve the best efficiency possible by modifying the blade angles accordingly. Hub reaction is positive for all cases considered, so it should not be an active constraint moving forward. The stall indicator shows that anywhere from 0 to 4 cells have stalled based on the stalling criteria defined earlier. In most cases, the number of stall cells is greater than 0, suggesting that the stalling criteria would be an important constraint moving forward. Similarly, the Goodman margin for the hub section is spread everywhere, with the majority of the points below 80%. However, the Goodman margin for the mid section has a lot of cases where significantly high vibratory stresses are present. Here, a band of vertical points is also observed. These points are a condensed way of representing the cases where even the mean stress was outside the limit, suggesting a higher thickness to chord ratio at the mid section. As mentioned earlier, our goal is first to check whether we can achieve satisfactory performance without increasing the peak thickness to chord values. Frequency margins for M1/1EO and M1/2EO are distributed throughout the ranges. The matrix of plots representing the relation between M1/1EO and M1/2EO has a slope of -1. As the natural frequency of Mode 1 gets closer to 1EO, it gets farther away from 2EO. The negative correlations are also observed in other margins M2/3EO and M2/4EO. Interesting to note is the positive correlation and then the negative correlation between M3/6EO and M3/7EO. This kink highlights a point where the M3 frequency is higher than 7EO and then the margin increases for both. Some trade-offs are also apparent here. An example is a relationship between Goodman margin for the second cross-section and M1/2EO margin. A reduction in the Goodman margin brings the first natural frequency closer to second engine order excitation frequency. While that does not mean an optimal solution cannot be achieved, it highlights how even the structural constraints have opposing trends. An ability to explore the entire design space provides designers with

clues on the critical aspects to analyze after design changes are made.

6.3.3.3 Surrogate model generation and optimization

After obtaining the analyses' responses, surrogate models were generated to fit the aero-mechanical responses as functions of the design variables listed in Table 22. Especially given that the responses contain natural frequencies, a neural network method was used to fit these responses, given its applicability in generating good models based on some prior studies [6, 9]. Other methods based on neural network type deep architectures leveraging Gaussian processes may also be used for similar engineering functions [132, 133]. A good model fit was obtained for all the responses using three activation functions (hyperbolic tangent, linear, and Gaussian). Appendix A shows the model fit results for all the responses. Table 23 summarizes the number of layers, nodes for each activation function, and the training and test R^2 values for all responses. Except for the margins for GM_{mid}, the R^2 values for all responses are satisfactory. The fit for GM_{mid} could not be made better since there were less than 400 cases where the mean stress was below the yield limit. In that regard, we proceed with the model obtained above, and the results are verified with the actual analysis. Discussion on the N_{st} parameter is warranted at this point. The number of stall cells is a categorical response variable. A probabilistic approach is implemented to approximate the model for predicting this number. For each case, we define the likelihood of each number (0 - 4) to stall. The one with the highest probability is, therefore, the most likely number of cells to stall. Since the goal is to ensure that our final design does not have any stall cell, $P(N_{st} > 0)$ computes the probability of the design not meeting the required criteria. The target design ensures that this probability is less than 0.01.

Fig. 152 shows a snapshot of the profiler of the response variables obtained using the models built using neural networks. The horizontal axis parameters are the design parameters listed in Table 22, and the vertical axis lists the responses tracked. The plot

Table 23: Neural network fit of aero-mechanical responses.

Parameter	Layers	Nodes			R^2 (training)	R^2 (test)
		HTan	Linear	Gaussian	N = 591	N = 198
η_{stage}	1	4	0	0	0.997	0.994
R_{hub}	1	3	0	0	0.996	0.995
P (N_{st} >0)	1	4	1	0	0.965	0.913
GM_{hub}	1	5	2	2	0.998	0.997
GM_{mid}	1	12	0	4	0.957	0.800
M1/1EO	1	5	2	2	0.998	0.997
M1/2EO	1	5	2	2	0.998	0.997
M2/3EO	1	5	2	2	0.997	0.992
M2/4EO	1	5	2	2	0.997	0.992
M3/6EO	1	7	3	3	0.982	0.974
M3/7EO	1	7	3	3	0.995	0.992

corresponding to i^{th} parameter on the x-axis and j^{th} response on the y-axis represents the sensitivity of the input i on response j, given all other design parameters are constant at the values represented by dashed red lines. While the sensitivity of a given design parameter on a particular response cannot be described solely based on this chart since the argument only applies when other variables are fixed, we can identify some important design characteristics. Hub to tip ratio, thickness to chord ratio, tip chord, taper type, and rotor area ratio strongly influence the mid section's stress margin. Tip chord and loading type strongly influence the margin on the hub cross-section. Hub to tip ratio is the most constraining factor for the mid-section's stress margin. While the stress margin is lowered at a high hub to tip ratio, we also observe the reduction in M2/4EO with that increase. Therefore, the optimizer will likely select a slightly lower than a hub to tip ratio of 0.3. A lower hub to tip ratio implies a longer blade, which increases the bending moment and, consequently, the stresses. Similarly, we can observe a negative correlation in the stress margins between the two sections and the loading type. Changing the loading type alters the distribution of stresses along the span. A hub loaded design will induce most of the stresses in the mid section, and shifting the distribution changes the stress distribution

accordingly. The probability of stall criteria' satisfaction increases with an increasing hub to tip ratio and tip chord. So, some trade-offs in aerodynamic performance are likely, based on the observations from Fig. 152.

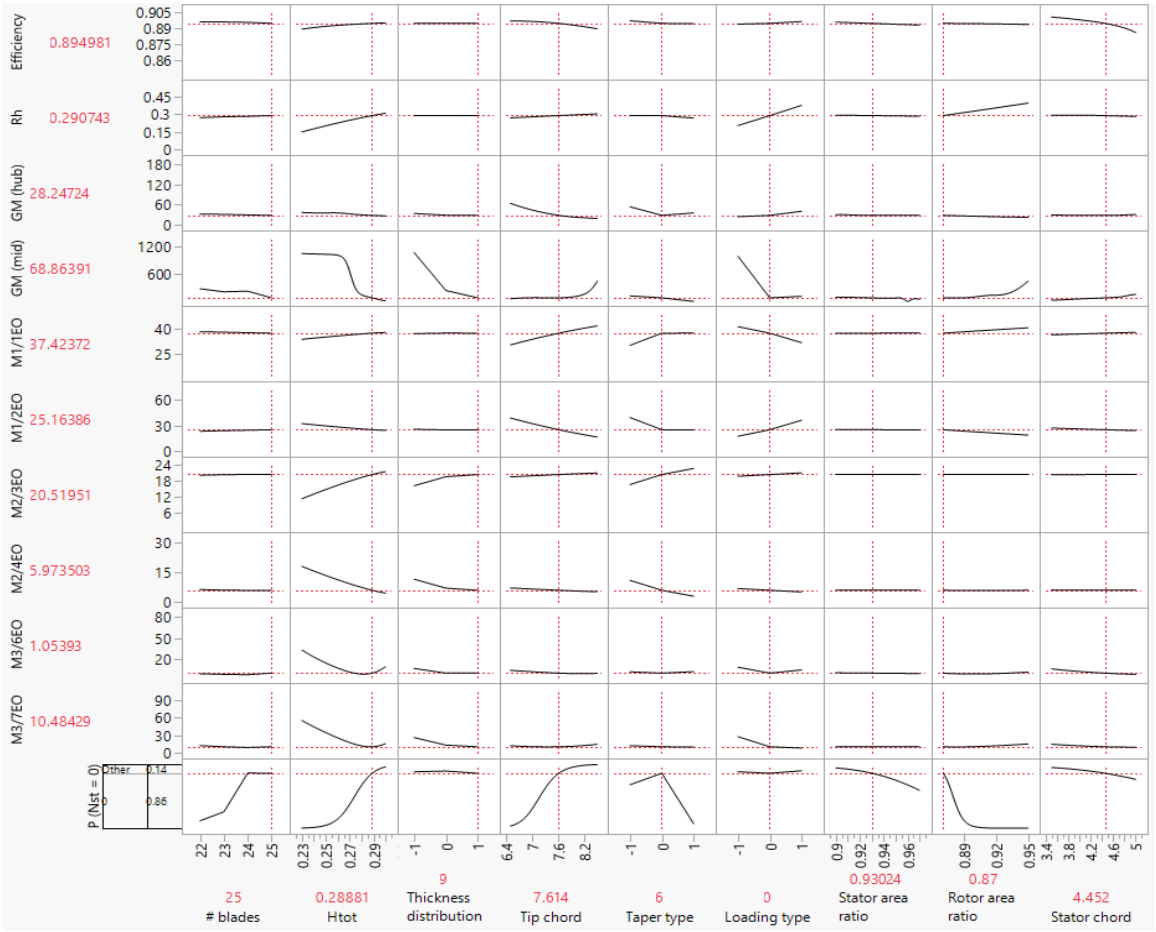

Figure 152: Profiler plots for aero-mechanical responses.

The surrogate models developed were used to solve the optimization problem outlined in Eq. 90. A solution that satisfied the optimization criteria was achieved. The optimal set of design variables was then used to evaluate the true aerodynamic performance and true structural constraints. Table 24 lists the variables and parameters for the optimized design. Note that the blade metal angles and twist are defined in the aerodynamic design module. Therefore those variables also change as a result of the optimization.

Table 24: Final blade parameters: optimized design.

Variables	Optimized Value
Loading type	Uniformly Loaded
Taper type	+1
Thickness distribution	+1
# of blades	25
Hub to tip ratio	0.292
Rotor tip chord	7.676"
Rotor exit area ratio	0.87
Stator exit area ratio	0.946
Stator chord	3.501

6.3.3.4 Analysis of the optimized design

The optimal set of design variables obtained from optimization was used to design the aerodynamic module's blade. The calculated isentropic stage efficiency was 90.2%, 0.22% reduction from its previous maximum.

Geometry changes

Compared to the design in Fig. 141, the optimized design underwent a few changes. Due to the changes in design parameters in Table 24, the blade stagger, and metal angles also changed. Table 25 lists the cross-sectional changes in the hub, mid, and tip sections. The stagger in the hub and mid sections reduced and in the tip section increased. Similarly, an increase in loading toward the hub than the initial design resulted in higher turning in the hub region. These changes should determine the loading variation, as well.

Loads

The time-varying axial and tangential loading distribution for the optimized design is shown in Fig. 153. We can observe that the peak tangential load value has reduced in this case compared to the initial design by ≈15%. While the axial load has a

Table 25: Blade angle changes in the optimized design.

Rotor Parameter	Initial value	Optimized value	Unit
Stagger (hub)	10.6	7.0	deg.
Inlet angle (hub)	36.0	36.0	deg.
Exit angle (hub)	15.0	22.45	deg.
Stagger (mid)	34.5	33.0	deg.
Inlet angle (mid)	51.0	49.7	deg.
Exit angle (mid)	20.1	18.03	deg.
Stagger (tip)	43.5	44.7	deg.
Inlet angle (tip)	55.0	55.7	deg.
Exit angle (tip)	33.6	34.2	deg.

similar variation with time, the amplitude of the variation has lowered compared to the initial design, as shown in Fig. 140. The tangential forces show lesser variation in the span-wise direction compared to the initial design. The amplitudes for these loads were also reduced with the design changes. The reduction of the loading amplitudes shall likely translate to a decrease in the stress variation as well.

Goodman diagram

We plot the evolution of von-Mises stresses on the three cross-sections for the optimized design. Fig. 154 shows the von-Mises stress variation for six cycles on these cross-sections. Given the similarity in the average loads and the shape of the loading variation, the stress plots' shape looks similar. The most concerning parameter was the mid section's vibratory stresses. It is evident from the figure that both mean and vibratory stresses in the mid-section reduced due to the design changes. Higher thickness to chord ratio and changes in loading distribution and twist are most likely responsible for reducing both mean stress and vibratory stresses in the mid section. The same can be implied about the tip section, while the reduction is not as prominent as the mid-section.

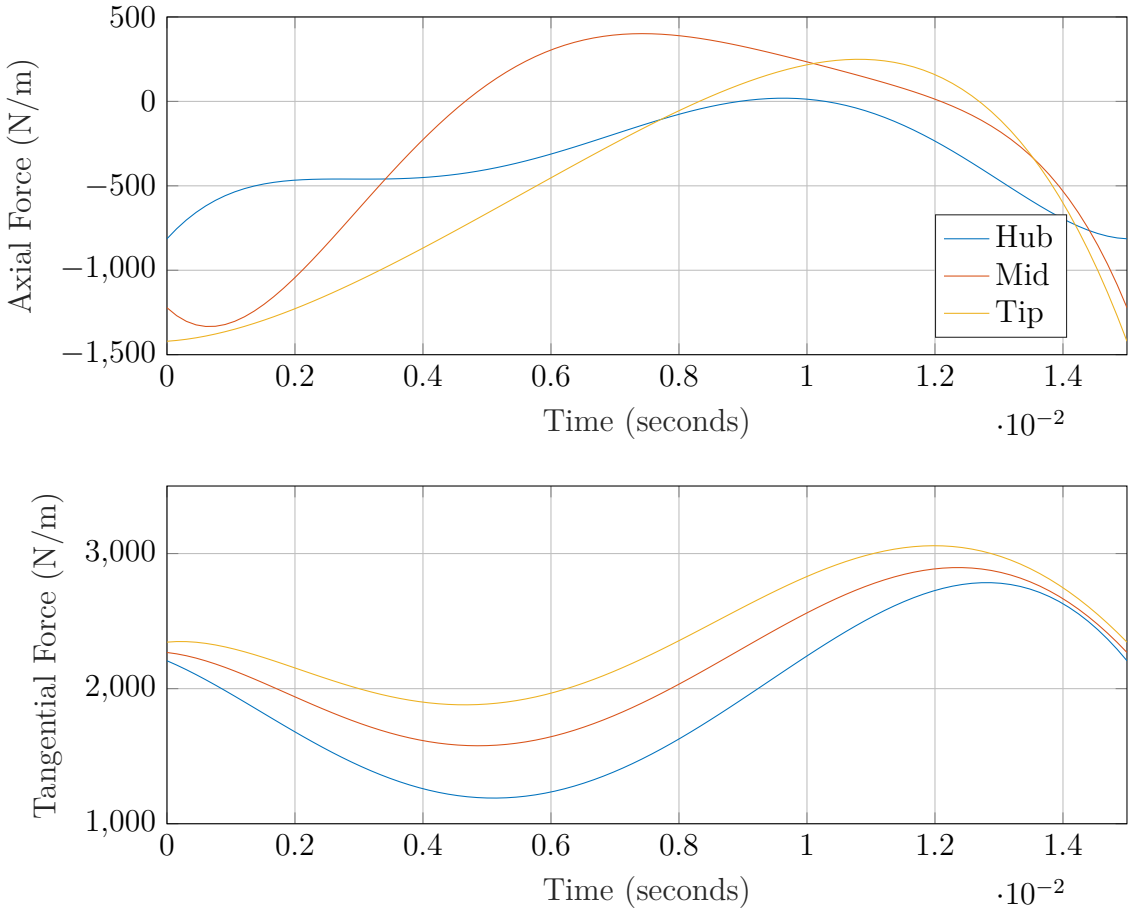

Figure 153: Variation of axial and tangential forces for optimized P3S3.

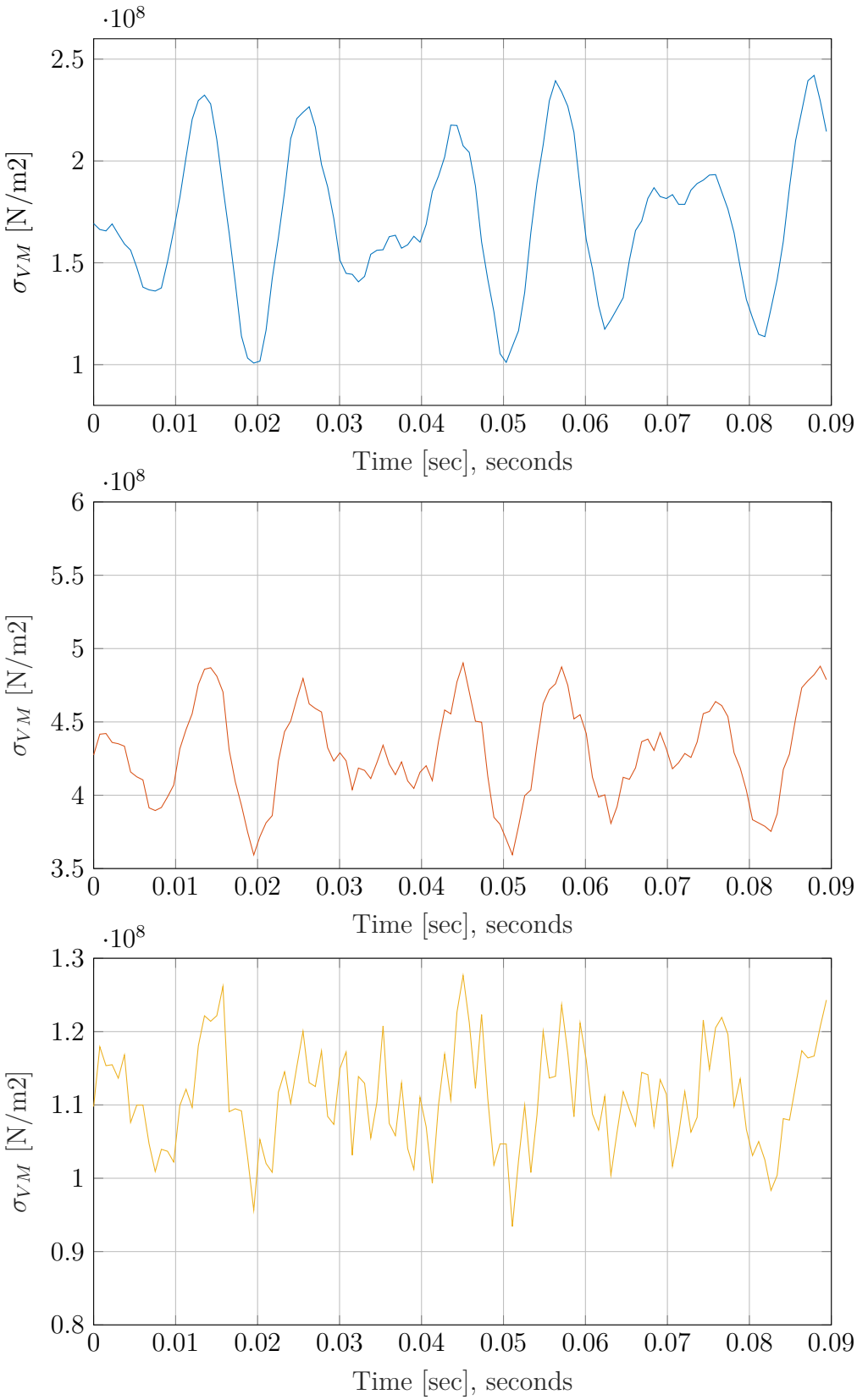

Figure 154: Evolution of von-Mises stresses over time: hub, mid, and tip sections [top to bottom] of optimized P3S3 design.

From Fig. 154, the mean and alternating stresses were computed and plotted on the Goodman diagram. Fig. 155 shows the Goodman diagram for the optimized design. The stresses for all cross-sections meet the safety criteria for 10^9 cycles defined earlier. While a design could achieve much lower vibratory stresses, an inequality constraint was set on the Goodman margin, so the optimizer chose a design very close to the optimal solution. From the perspective of these criteria, the optimized design is deemed satisfactory.

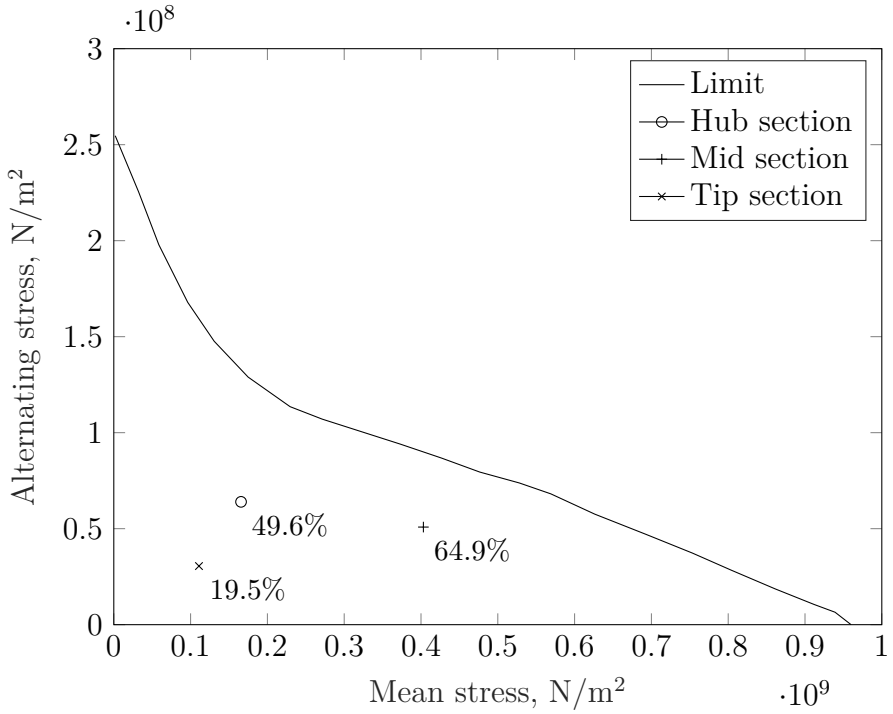

Figure 155: Goodman diagram of optimized P3S3 design.

Campbell diagram

Next, we evaluate both natural frequencies of the blade and the excitation frequencies using Fast Fourier Transformation of the tip displacements and stresses. Natural frequencies of different modes at various speeds are computed by running GEBT in eigenanalysis mode. Fig. 156 shows the frequency analysis of the stresses. The contribution of 1EO and M1 in the mid-section is significantly reduced from the initial

design, as shown in Fig. 145. The frequencies that are excited are similar in both designs.

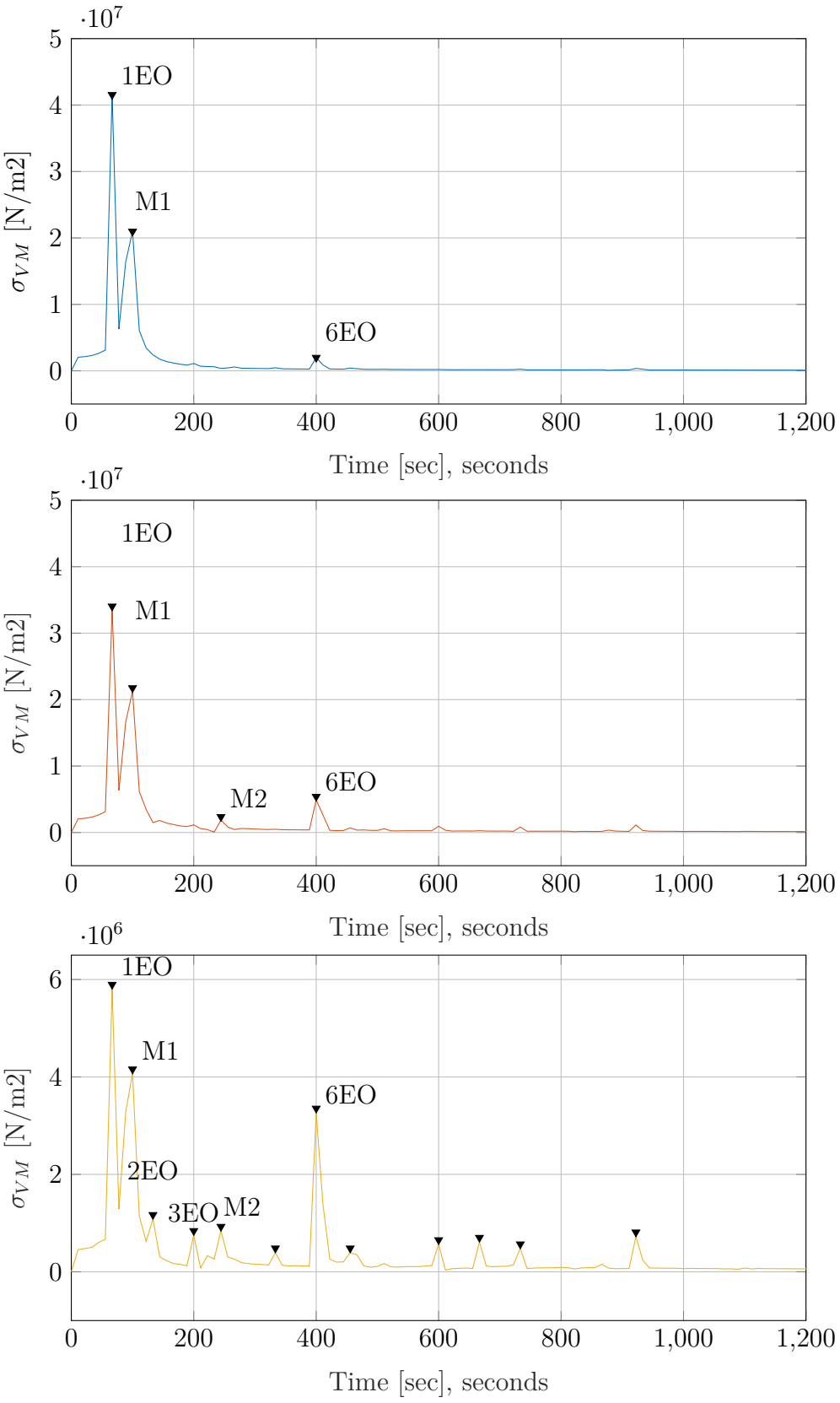

Figure 156: FFT of von-Mises stresses over time: hub, mid, and tip sections [top to bottom] for structurally optimized P3S3 design.

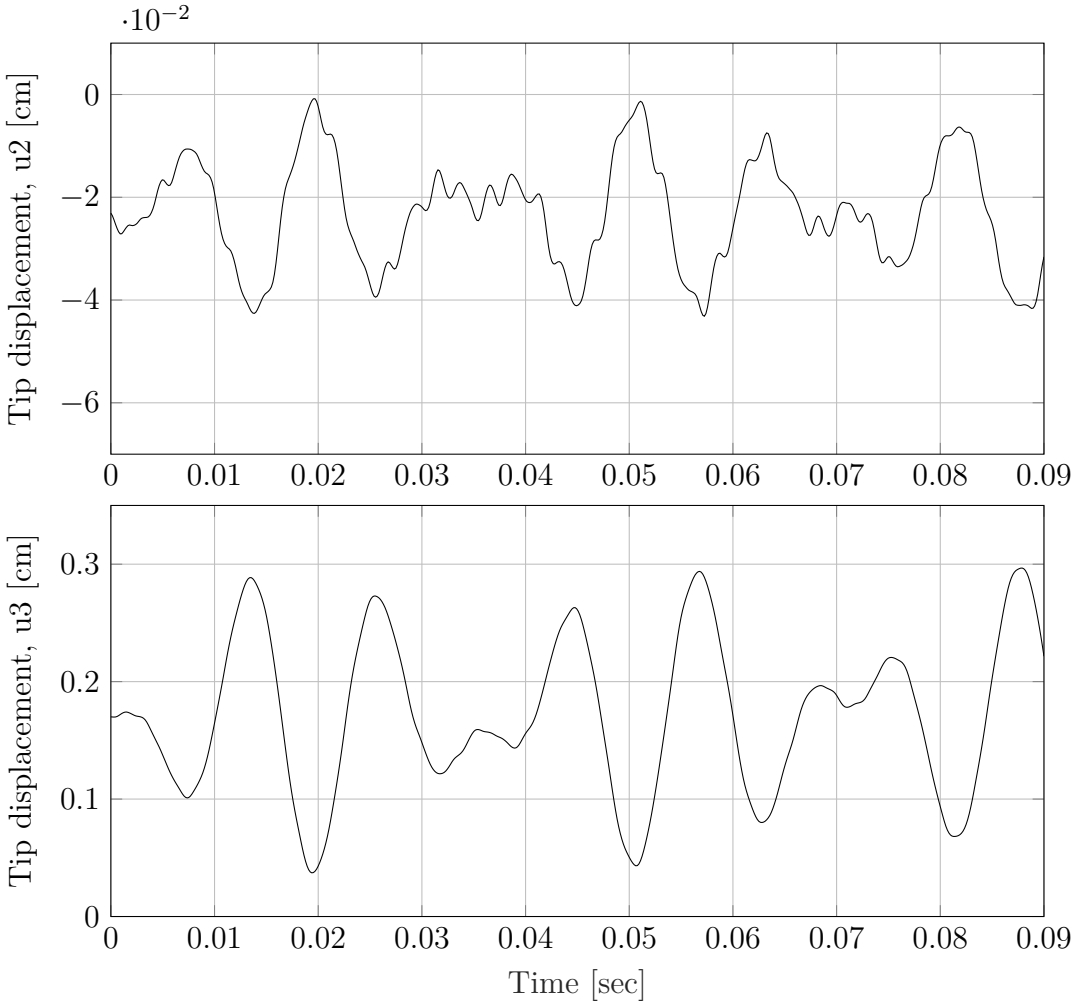

Figure 157: Tip displacements in the chord-wise (u2) and flap-wise (u3) directions of optimized P3S3 design.

Fig. 157 shows the tip displacements in the u2 and u3 directions. The amplitude of the displacement in the u2 direction lowered from 0.06 cm to 0.04 cm. Similarly, the peak tip displacement in the transverse direction also reduced slightly. The frequency analysis of the tip displacements is shown in Fig. 158. The excitation frequencies are the same, and only the amplitudes of each frequency are reduced.

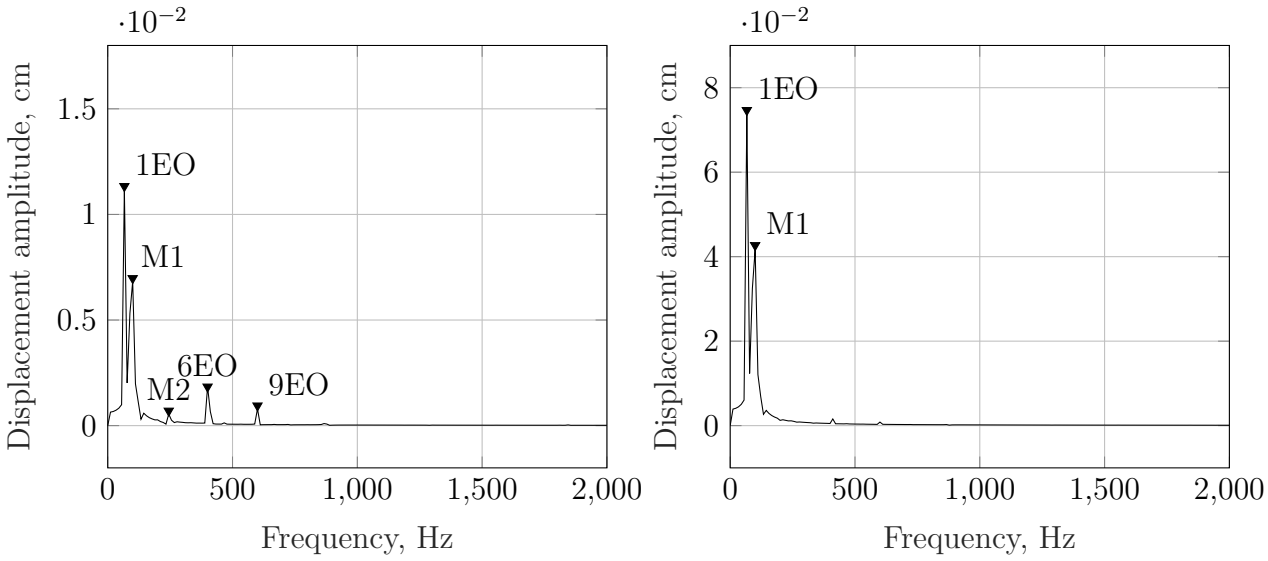

Figure 158: FFT of tip displacements of optimized P3S3 design - u3 [left] and u2 [right].

The previous discussions desired to have at least a 5% margin with engine orders greater than 2EO and at least 10% margin on 1EO and 2EO. The natural frequencies and the engine order excitation frequencies were plotted on a Campbell diagram, and it can be seen that a significant margin is present between M1 and 1EO and 2EO. Similarly, compared to the initial design, we can see a safe margin of 6.9% for M3 and 6E0. The margin between M2 and 4EO is also 5.5%, higher than the desired 5%.

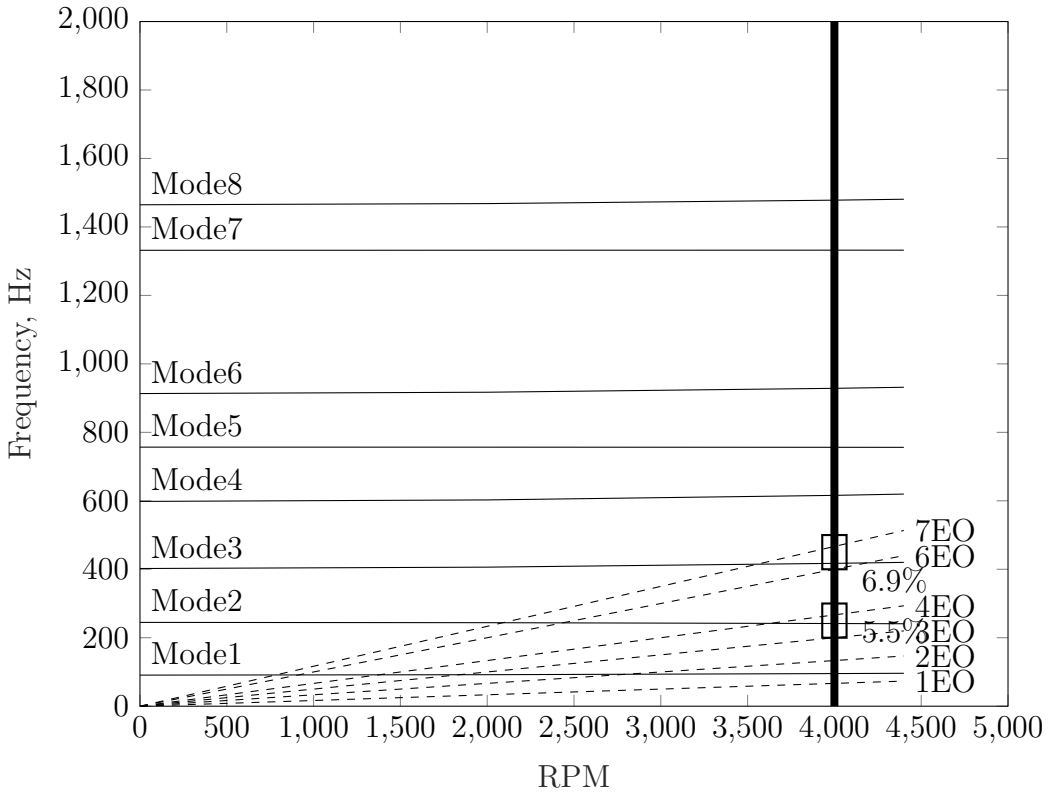

Figure 159: Campbell diagram of optimized P3S3 design.

Feasibility analysis

The analysis of the design obtained by performing optimization on the generated surrogate model resulted in a 0.22% drop in stage efficiency. Still, it demonstrated safe margins in the Goodman diagram and Campbell diagram. Thus, this design is deemed structurally satisfactory.

6.3.4 Summary of Experiment 2.2

Hypothesis 2 stated that a design that can minimize vibratory stresses could be achieved using VAM in the design framework. Experiment 2.2 was conducted to test this hypothesis. In experiment 2.2a, the transient structural analysis of an aerodynamically optimized baseline design was performed. It showed that the design demonstrated extremely high vibratory stresses and the M3 frequency coincided with 6EO frequency. Thus, the design was considered infeasible. The computational

efficiency afforded by both aerodynamic and structural tools allowed to simulate a large number of cases to generate surrogate models. Experiment 2.2b was conducted to explore the design space, and neural network fits were generated for each aero-mechanical response. An optimization problem was solved that resulted in an optimal set of design variables. The stage efficiency reduced by only 0.22%, and safe margins in Campbell and Goodman diagrams were achieved by increasing the natural frequencies and lowering the blade stresses. The experiment results established the sensitivities of various design parameters on both aerodynamic and structural responses, and using VAM helped generate a design that met the aerodynamic and structural constraints set forth. In that regard, hypothesis 2 is validated.

CHAPTER VII

SUMMARY AND CONCLUSIONS

The thesis presented in this work is that the fan stage conceptual design framework introduced and developed in this dissertation provides improvements on the existing methods for fan design under distortion. It is computationally efficient, optimizes for several aerodynamic effects considered necessary for distortion, and introduces an efficient method for transient structural analysis of rotor blades.

The developed framework consists of four main phases. A summary diagram of the framework is shown in Fig. 160. The first phase is the aerodynamic design block. The aerodynamic method leverages the existing conceptual design multi-meanline method and implements additional modeling elements on top of it to make it attractive for conceptual design for distortion. It accounts for asymmetry in the flow field by creating several circumferential sectors. Rotor incidence and deviation angles are optimized to minimize the overall stage losses. The unsteady rotor response is computed by converting the quasi-steady response using potential flow quasi-steady and unsteady airfoil behavior and the quasi-steady rotor response. The design of non-axisymmetric stators is also implemented to reduce the amount of losses in the stator row. An optimizer is wrapped around the aerodynamic framework such that the overall pressure rise is equal to the stage pressure rise. The second phase is the structural analysis preparation block. The preparation block consists of converting the cross-sectional properties to profiles, radially stacking these profiles, meshing them, and generating the input files for the third phase - the structural analysis block. A transient structural analysis of rotor blades is performed using VAM. VAM can solve the 2-D cross-sectional and 1-D non-linear analysis in a computationally efficient manner, generating the 3-D

displacements, stresses, and strains and making it suitable in the level of conceptual design. The final phase is the aero-structural optimization block. In this block, the stage design parameters are varied in order to maximize the aerodynamic performance while satisfying the structural constraints for the safe operation of the fan stage.

Experiments 1.1 - 1.3 established the importance of parametric blade angle optimization, unsteady rotor response, and non-axisymmetric stators' design. Experiment 1.4 evaluated the effectiveness of the overall framework in recovering the losses due to distortion. Experiment 2.1 successfully identified VAM as a suitable tool for conceptual design optimization. Experiment 2.2 showed that the aerodynamically optimized designs need not necessarily satisfy the structural constraints and demonstrated the required trade-off in aerodynamic performance to satisfy structural constraints. The remainder of the chapter will detail the hypotheses presented, contributions, and recommendations for future work.

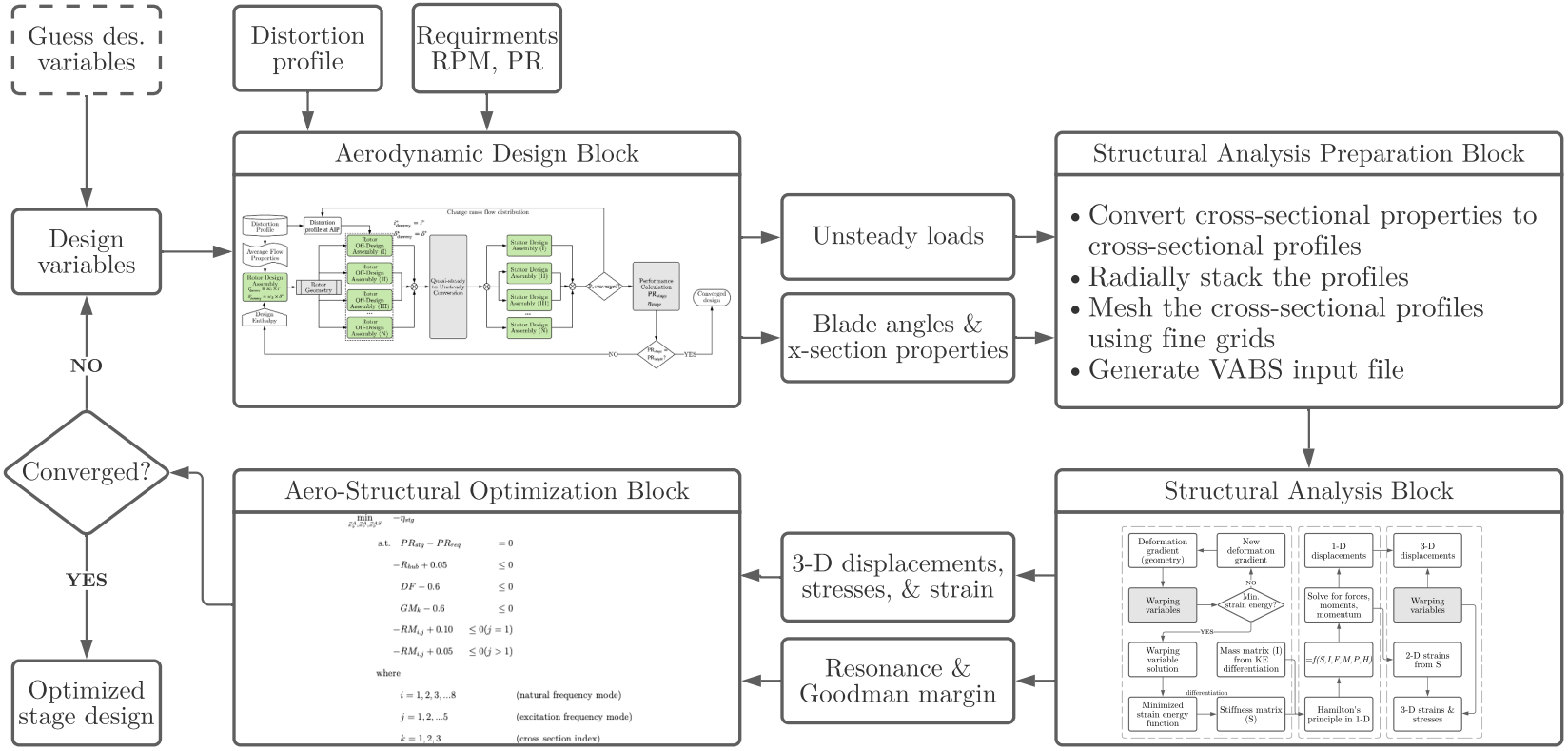

Figure 160: A summary of the overall framework.

7.1 Review of Hypotheses

The absence of an aerodynamic design methodology in the conceptual design of the fan stage for distorted inflows established the research question 1.

Research Question 1: *What is an appropriate design framework to maximize the stage efficiency of a fan in presence of flow asymmetry?*

Research question 1 motivated the analysis of current design methods on three aspects: rotor loss variation, unsteady rotor response, and non-axisymmetric stator design. Three sub-hypotheses were established to define hypothesis 1. The first was regarding the rotor blade angle optimization.

Hypothesis 1.1: *If the fan is designed for an averaged flow, the minimum loss design incidence for non-uniform flow departs from its optimal value for uniform flow*

This hypothesis's validity was tested on ten different flow conditions characterized by the presence of total pressure, swirl, and mixed distortions. A high-level set of design variables similar to those found in the literature for BLI analysis was used. The experiment was conducted to evaluate whether the rotor losses can be reduced by changing the blade incidence angle away from the design incidence angle when designing for an averaged flow. Experiment 1.1 established the importance of blade angle optimization to minimize losses in the fan stage in the presence of non-uniform flow. By parametrically varying the blade incidence angle, an optimal value can be obtained at which both the rotor and stator losses can be alleviated.

The experiments observed that the losses were lower for some angle away from the design incidence. On average, 15% - 20% of the rotor losses could be recovered through this process. The recovery was only seen in cases where some total pressure distortion

was present. An insightful observation was that when the co-swirl and counter-swirl magnitudes were equal, the rotor losses were minimum at design incidence for the averaged flow. This behavior was observed because any variation in incidence angle to minimize the loss in one sector would be offset by the increased losses in another. Another important observation was regarding the difference in loss behaviors for various cross-sections. While only one parameter was used to control the entire span's incidence variation in this dissertation, higher losses were observed in the hub region for the cases concerned. As a result, in some sectors, the tip and the mid regions had to experience increased losses. This observation emphasizes the need to consider separate scalars for each cross-section in the span-wise direction.

Hypothesis 1.2 was regarding the effect of unsteady rotor response and was stated as follows:

Hypothesis 1.2 *The necessity of including unsteady rotor response will be dependent on the intensity of distortion. At high distortion intensities, the effect of unsteady response on pressure rise and the blade normal force will be non-negligible*

This hypothesis was also tested on a set of 10 flow conditions used in experiment 1.1. Flow profiles of low, mid, and high intensities were used to represent lower, typical, and upper bounds for distortion. Experiment 1.2 was carried out to test this hypothesis to specifically evaluate two parameters: (i) difference in the rotor quasi-steady and unsteady blade normal force and (ii) difference in the rotor quasi-steady and unsteady pressure ratio.

Experiment 1.2 showed the importance of including unsteady rotor response. The experiments observed that the differences in blade normal forces and pressure profile at the rotor exit increase with increasing intensity of distortion. An insightful observation was that comparison on the relative unsteadiness between two flow profiles could not

be made based on the differences in the normal blade force. For example, the cases with pure swirl distortion was found to have a larger amount of required turning than other cases. The implication of hypothesis 1.2 is that when computing blade forces for structural analysis or using the rotor exit flow profile to design stators, using the quasi-steady response will likely give non-optimal solutions at higher distortion intensities.

Hypothesis 1.3 was made regarding the required degree of asymmetry in the stators and was stated as follows:

Hypothesis 1.3 *If the distortion intensity is higher, a larger increase in the level of required stator asymmetry will be observed. The stator asymmetry will also be observed higher for total pressure distortion than swirl distortion*

Hypothesis 1.3 was also tested on the same set of flow conditions and design variables used in experiments 1.1 and 1.2. At any iteration of the design, the rotor's design was guided by an averaged flow definition. Still, the stators' design was guided by the rotor performance in the distorted flow field - the rationale being that stators have to match to the incoming flow.

The results of experiment 1.3 showed that variation as large as 20° was observed in the stator blade angles along the circumference for cases with mixed distortion. A linear increase in total pressure distortion intensity resulted in a linear increase in the required stator asymmetry. It implies that the rotor inlet's mass flow deficit is the leading cause of flow angle asymmetry at the rotor exit. This finding was further evidenced when analyzing the stator angles for pure swirl distortion cases. No significant variation ($< 4°$) was observed in the blade angles for pure swirl distortion cases.

Hypothesis 1 was an implied hypothesis of hypotheses 1.1 - 1.3. It was stated as

follows:

Hypothesis 1 *If hypotheses 1.1 - 1.3 are true, then the fan stage design framework that incorporates the parametric variation of rotor blade angles, unsteady rotor response, and non-axisymmetric stators will be able to recover a significant portion of the losses in distortion that a fan designed for uniform flow experiences*

Hypothesis 1 was tested for all flow conditions used in experiments 1.1 - 1.3 for the same set of design parameters. Experiment 1.4 was performed to test hypothesis 1. The design was modified on a step-by-step basis to evaluate each modeling element's contribution to the recovery of the overall losses. Experiment 1.4 showed that optimizing incidence and deviation angles, designing non-axisymmetric stators, and modeling rotor unsteady response contributed to the recovery of around 45% - 65% of the losses, on average. An insightful observation from this experiment was that any modeling element's contribution depends on both the intensity and type of distortion. For example, the effect of modeling unsteady rotor response was important only in mid and high intensities, in agreement with the results seen in experiment 1.2.

Similarly, rotor blade angle optimization was deemed important to be included for lower intensities of distortion. Non-axisymmetric stators had a relatively constant effect in all distortion types and levels. In some cases (especially in high distortion cases), it was observed that including unsteady response reduced in percentage contribution at higher intensities. It was discovered that including the unsteady modeling effects asked for more turning from the stators and led to a larger increase in diffusion. It could be argued that in addition to the blade angles, stator chords could also be designed in an asymmetric manner. It has been argued in previous studies, and the argument is strengthened based on the observations from this experiment.

Research question 2 was motivated to understand the influence of distortion on

rotor structural constraints and what design improvements could ensure structural safety. The absence of a computationally efficient transient structural analysis method established research question 2.1.

Research Question 2.1: *How can transient analysis of rotor blades be performed in a computationally efficient manner?*

Hypothesis 2.1 was formed from understanding past studies treating fan rotor blades as beam-like structures and the Variational Asymptotic Method's current capability to analyze beam-like structures in a computationally efficient manner.

Hypothesis 2.1: *Variable Asymptotic Method (VAM) will be able to correctly predict the stresses and displacements acting on rotor blade-like structures and can be used as a computationally efficient model for transient structural analysis of rotor blades*

Hypothesis 2.1 was tested on four cases comprising tip loads and distributed loads under rotating and stationary conditions in experiments 2.1a - 2.1d. In all experiments, eigenvalues, hub stresses, and tip displacements were compared between VABS/GEBT and COMSOL, the 3-D FEA method used for this work. In all cases, it was observed that except for the torsional mode, all eigenvalues were within a 5% difference between the two modeling software. Similarly, the tip displacements in the transverse direction closely matched as well. The principal tensile stress and the time at which the peak stress occurred also matched for the tip loaded cases. A peak difference in 12% was observed in one case. During the simulation of distributed loads, difficulties arose in converging solutions in COMSOL with non-linearities. However, it was also observed that the inclusion of non-linearities with a relatively coarser grid brought the COMSOL solution closer to the one predicted by VABS/GEBT. Similar trends were observed

for the rotating case as well. From different scenarios run in experiment 2.1, VAM's confidence for transient analysis of fan rotor blades is strengthened.

Research question 2 stated the following:

Research Question 2: *How will the inclusion of structural analysis affect the design of the fan stage?*

Hypothesis 2 was formulated regarding the effects of time-varying loads on the rotor's structural integrity and was stated as follows.

Hypothesis 2: *Using VAM in the design framework will allow for rapid exploration of design space and generate a design that minimizes the amount of vibratory stresses with safe margins for operation represented in the Goodman and Campbell diagrams while also reducing the penalty in stage efficiency*

Hypothesis 2 was tested for a high-intensity case that included both total pressure and swirl distortions. The results of experiments 2.2a and 2.2b conducted to test this hypothesis showed that the aerodynamically optimized design led to large vibratory stresses for the rotor blade inhibiting its ability to operate smoothly for its desired life cycle. Similarly, close margins between natural frequency and engine order excitation were also observed. After the baseline design demanded changes, design space was explored in search of a design that maximized aerodynamic efficiency while satisfying structural constraints. Several design parameters like hub to tip ratio, thickness distribution, tip chord, and area ratios were important parameters to control the magnitude of vibratory stresses present in the structure. An optimal set of design variables was found that made the design safe in terms of the Goodman and Campbell diagrams' parameters. The realized trade-off in aerodynamic stage efficiency was

0.22%, suggesting that sound structural design can be obtained without a significant loss in the fan stage's aerodynamic performance.

7.2 Summary of Contributions

The major contributions of this thesis are as follows:

- The development of an aerodynamic design framework for the conceptual design of fan stages for circumferential inlet distortion is the primary contribution of this work. The design framework accounts for asymmetry in the flow field, optimizes the rotor blade angles in the presence of incidence swings, computes unsteady rotor response from the quasi-steady response, and designs non-axisymmetric stators. This method uses existing conceptual design tools and can easily integrate with cycle analysis tools like NPSS, allowing designers to replace fan maps with this design framework. This provides a huge advantage over map based methods since map based methods do not enable any design capability and also fail to account for the effects mentioned here that were able to recover 45% to 65% of the losses in distortion and ensure that the designs are safe to operate under those conditions as well.

- Some insights were also gained into the problem of designing a fan stage for flow distortion. First, it was observed that the losses in the distorted flow field mostly occur in the rotor. In general, 1/4th to 1/3rd of the losses arise in stators, and 2/3rd to 4/5th of the losses arise in rotors, based on the intensity and type of distortion. However, designing non-axisymmetric stators helped recover stator losses and rotor losses by allowing the incidence and deviation angles to re-optimize and relieve some losses in the rotors. Second, it was also observed that the distortion losses could not be superposed based on either the intensity or the type of distortion. Third, another useful insight was the understanding that rotor losses could be reduced further by allowing for the

design incidence and deviation angles to have variation in the span-wise direction. Finally, the necessity of including any modeling effect is dependent on a case-by-case basis. For example, at low intensities of distortion, not including unsteady response did not provide a significant difference. Similarly, rotor incidence and deviation optimization proved to be the most useful at low intensities. For pure swirl distortion cases, they seemed to provide a minimal effect in the design improvement.

- This is also the first reported work of using the Variational Asymptotic Method for the transient structural analysis of fan rotor blades. A parametric analysis environment is setup where any blade profile can mesh, 2-D cross-sectional analysis is performed with VABS, and 1-D non-linear analysis with time-varying loads is performed with GEBT. VAM's computational efficiency makes it an extremely useful tool for the conceptual level analysis of the designed blades. This method's reasonable accuracy provides an argument for using this method not only in the conceptual design, but also in the later stages of the design process.

- Finally, some insights were gained regarding the sensitivities of the design parameters on the structural performance. Fan design parameters such as hub to tip ratio, thickness distribution, chord length, loading distribution, and taper type were found to have the most significant effects on the alternating stresses and the design's natural frequencies. The presence of engine order excitations becomes imminent during the ingestion of non-uniform flows. So, it was essential to maintain sufficient margins between the natural frequencies and the lower engine order frequencies. Trade-offs within the structural performance parameters were also observed, further emphasizing the need for such analysis from the early design phase. In the final design, increasing the number of blades

also increased to increase the solidity and reduced the loading per blade, but any weight trade-off analysis was not performed.

7.3 Recommendations for Future Work

While the elements of the framework discussed here are sufficient to show the merits of the method, the physics of inlet distortion is complex. There are three main avenues in the view of the current author that could be tackled to improve the method described in this work.

7.3.0.1 Model Refinement

Several modeling elements could be added to refine the model and/or strengthen the validity of the results achieved here. While some cases were analyzed to verify that the aerodynamic model provided reasonable estimates, experimental/higher fidelity analysis could further increase the confidence in the developed model. The second area could be the inclusion of additional loss models. The loss models used in this work were specifically for double circular-arc airfoils. Inclusion of various airfoil types and consequent loss models would make the model more flexible. Another addition could be the inclusion of uncertainty analysis. Perturbations on certain assumed parameters may identify that while the achieved design might be optimal, it may not be robust to uncertainties. In that regard, uncertainty analyses could be performed at various levels of the design process (esp. when integrating with cycle and vehicle design) similar to the techniques used by Burgaud [16], albeit in a different field. Finally, weight analysis was also not carried out during the fan design process, making it difficult to understand the weight-efficiency trade-offs. To limit an overweight design, the number of blades in the optimization process was limited to 25, but the addition of weight model would allow for capturing the trade-offs and selecting a more optimal design.

7.3.0.2 Aero-structural Coupling

The aero-structural framework described in this dissertation does not consider a strong coupling between the aerodynamic design and structural analysis. It was assumed that the blade geometry deformation does not lead to any change in aerodynamic performance and loads. In reality, we expect the aerodynamic performance to alter due to the rotor blade deformation. Therefore, a natural extension of this work could include the strong coupling between the two disciplines. If the framework were to be extended to ensure the coupling, the effect of structural deformation has to be quantified as a change in rotor inlet and exit angles at different radial locations. Some changes have to be made in the aerodynamic design framework to account for this. The rotor design assembly should only be run in the first iteration, and any deformation changes should be analyzed in the rotor off-design assemblies. Difficulty in ensuring the stage pressure rise may be encountered in this effort since the blade geometry changes also alter the rotor exit pressure profile. In this case, the optimization using design space exploration could be replaced by a more robust gradient-based optimization technique. Sarojini et al. [138] describe a method to optimize beam structures subject to dynamic loads using the adjoint-method to obtain gradients needed for structural optimization.

7.3.0.3 Off-design Resonance Analysis and Damping Considerations

Another area for improvement could be made in the structural analysis side. Results obtained in this dissertation were performed without any damping considerations. Therefore the results predicted by VABS/GEBT could be on the slightly conservative side. This discrepancy would not be significant in the off-resonance condition but might lead to non-negligible differences in the conditions near resonance. Some work on adding damping considerations have been performed in the Ph.D. thesis by

Gupta [67]. In the structural analysis domain, resonance analysis was performed at design speed only. However, from the Campbell diagram analysis, there were certain speeds where narrow margins could be observed, especially at lower engine order frequencies. Improvement in the method could, therefore, come from incorporating resonance analysis at critical speeds of operations.

7.3.0.4 Multiple Design Point Scenarios

The work that was accomplished for this thesis is a design point scenario. The proposed framework can generate a fan design given a design point flow profile and a stage requirement. However, an ideal scenario would be to generate an optimal design considering various flow regimes where the fan would likely operate. In the propulsion modeling domain, the concept of Multi Design Point (MDP) is widely used. The idea is to use the constraints from multiple design points to design the cycle. A similar idea can be applied to the fan design, especially in the BLI domain. Some work on turbine design using multiple design point scenarios has been performed by Hendricks [82].

It is important to identify the mission points where the flow distortion is crucial in its intensity and impact on the fan stage. MDP's concept applied to this framework would enable fan designs considering critical mission points of the aircraft. As the method stands right now, it cannot consider multiple flow distortions and design an optimal stage. If this framework were to be extended, a possible solution would be to add multiple rotor and stator off-design assemblies. Performance under these off-design conditions can be considered as constraints that will simultaneously change the design by changing the definition for rotor design and, consequently, stator design.

Once the multiple design point setup is incorporated, it provides a powerful capability to design and analyze BLI systems from a vehicle design perspective. Integrating with engine design tools like NPSS and vehicle design tools like FLOPS,

it allows for rapid sizing of the airframe, propulsor, and the fan stage simultaneously (assuming that the fidelity of modeling BLI exists in every discipline). Overall, by capturing the inherent trade-offs, it enables answering whether a BLI concept will buy itself into the system.

7.4 Final Thoughts

This work has been an intellectually stimulating experience for me. While there is certainly a lot left to be accomplished in the field of inlet distortion and fan design, I hope that the work done in this thesis will add some value to anyone invested in this field. I am excited about the future of aviation and look forward to witnessing the application of BLI materialize in commercial aircraft someday.

APPENDIX A

SUPPLEMENTARY FIGURES

Fig. 161 - Fig. 171 shows the training and validation metrics for various aero-structural responses for the test case described in Section 6.3.

A.1 Model fit for stage efficiency

Fig. 161 shows the training (left) and validation (right) metrics for stage efficiency. The actual vs. predicted plots for both training a validation points are very close to each other. R^2 values of > 0.99 are observed for both. The errors in the responses are well captured as the residual plot does not show the presence of any noticeable trends.

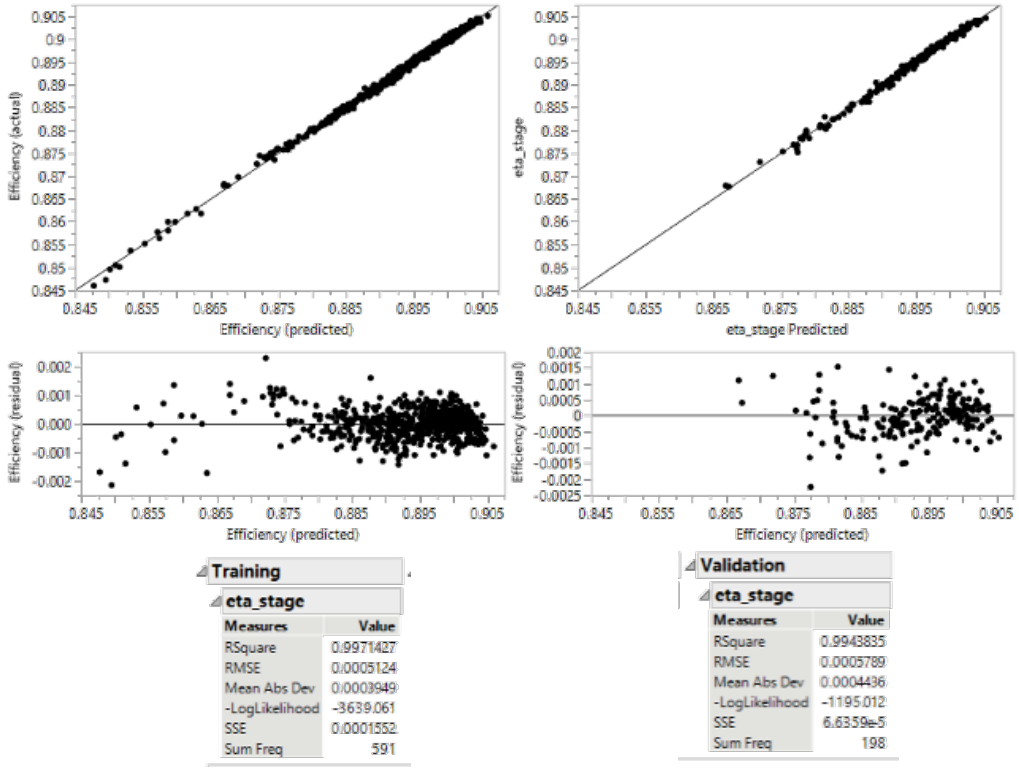

Training

eta_stage

Measures	Value
RSquare	0.9971427
RMSE	0.0005124
Mean Abs Dev	0.0003949
-LogLikelihood	-3639.061
SSE	0.0001552
Sum Freq	591

Validation

eta_stage

Measures	Value
RSquare	0.9943835
RMSE	0.0005789
Mean Abs Dev	0.0004436
-LogLikelihood	-1195.012
SSE	6.6359e-5
Sum Freq	198

Figure 161: Training and validation metrics for η_{Stg}.

A.2 Model fit for hub reaction

Fig. 162 shows the model fit parameters for hub reaction. The hub reaction ranges from 0 - 0.5. A strong fit is observed for both training and validation data. R^2 values of > 0.99 and RMSE of < 0.005 are observed for both. Similarly, the range of the residuals is an order of magnitude lower than the parameter values.

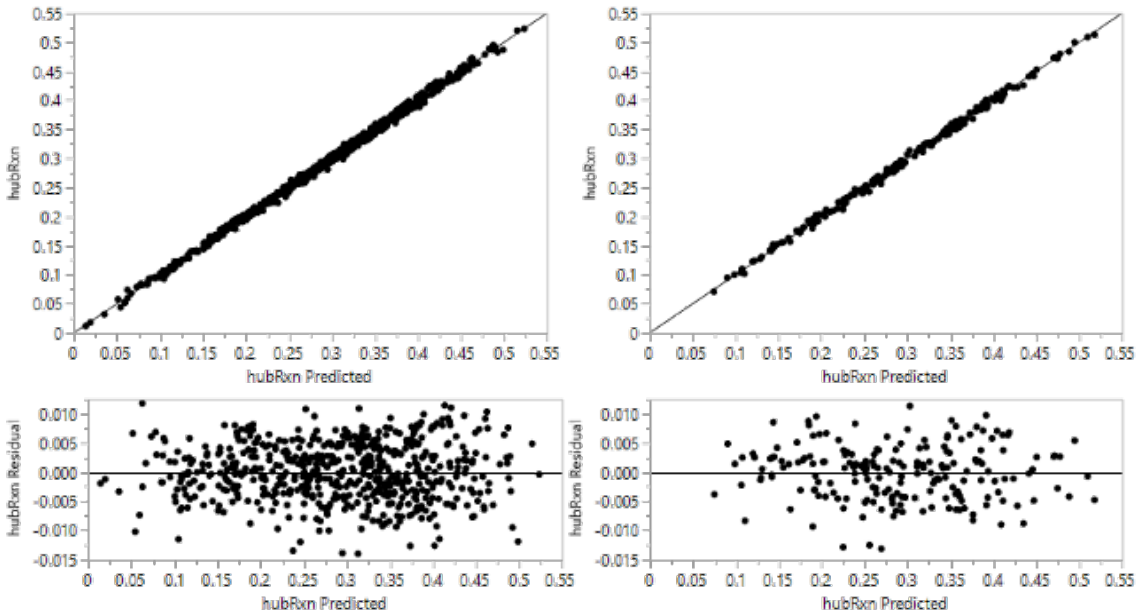

Training

hubRxn

Measures	Value
RSquare	0.9978032
RMSE	0.0048187
Mean Abs Dev	0.003941
-LogLikelihood	-2314.545
SSE	0.0137228
Sum Freq	591

Validation

hubRxn

Measures	Value
RSquare	0.9976406
RMSE	0.0046324
Mean Abs Dev	0.0037429
-LogLikelihood	-783.2361
SSE	0.0042489
Sum Freq	198

Figure 162: Training and validation metrics for hub reaction (R_h).

A.3 Model fit for stall indicator

The stall indicator is defined using the number of stall cells when the blade rotates. Anywhere from 0 - 4 cells stalled. In Fig. 163, the confusion matrices show the actual vs. true prediction counts and ratios respectively. It can be see the predictive power for lower number of stall cells is high. This is important because we desire the stall indicator to be 0. Similar ratios are observed for both training and validation data, suggesting a good model fit.

Training

stallIndicator

Measures	Value
Mean Abs Dev	0.0961806
Misclassification Rate	0.0592217
-LogLikelihood	83.570967
Sum Freq	591

Confusion Matrix

Actual stallIndicator	Predicted Count 0	1	2	3	4
0	21	2	0	0	0
1	1	324	4	0	0
2	0	5	155	9	0
3	0	0	9	38	1
4	0	0	0	4	18

Confusion Rates

Actual stallIndicator	Predicted Rate 0	1	2	3	4
0	0.913	0.087	0.000	0.000	0.000
1	0.003	0.985	0.012	0.000	0.000
2	0.000	0.030	0.917	0.053	0.000
3	0.000	0.000	0.188	0.792	0.021
4	0.000	0.000	0.000	0.182	0.818

Validation

stallIndicator

Measures	Value
Mean Abs Dev	0.1110143
Misclassification Rate	0.0909091
-LogLikelihood	41.468993
Sum Freq	198

Confusion Matrix

Actual stallIndicator	Predicted Count 0	1	2	3	4
0	4	0	0	0	0
1	1	130	8	0	1
2	0	1	30	1	0
3	0	0	0	9	2
4	0	0	0	4	7

Confusion Rates

Actual stallIndicator	Predicted Rate 0	1	2	3	4
0	1.000	0.000	0.000	0.000	0.000
1	0.007	0.929	0.057	0.000	0.007
2	0.000	0.031	0.938	0.031	0.000
3	0.000	0.000	0.000	0.818	0.182
4	0.000	0.000	0.000	0.364	0.636

Figure 163: Training and validation metrics for stall indicator $[P(N_{st}) > 0]$.

A.4 Model fit for Goodman margin at the hub

The responses for Goodman margin at the hub were tracked, and the results are shown in Fig. 164. The actual vs. predicted plots follow the y=x line closely. R^2 values for both training and validation are > 0.99. While the results are satisfactory, in the residual plots, it is observed that the errors are higher at high margins. This is not a huge concern since the errors for Goodman margin $< 60\%$ is less than 5%.

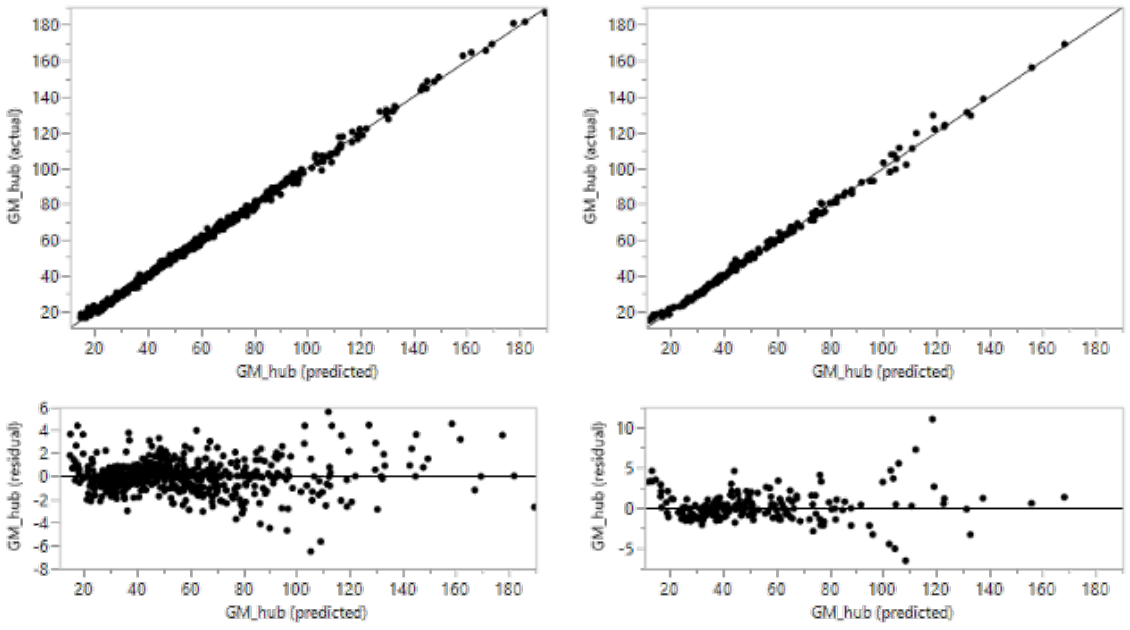

Training

CS2_margin

Measures	Value
RSquare	0.9981703
RMSE	1.3633717
Mean Abs Dev	0.9261856
-LogLikelihood	955.33173
SSE	1098.5405
Sum Freq	591

Validation

CS2_margin

Measures	Value
RSquare	0.9962024
RMSE	1.9157351
Mean Abs Dev	1.3110655
-LogLikelihood	388.8695
SSE	726.6681
Sum Freq	198

Figure 164: Training and validation metrics for Goodman margin (hub).

A.5 Model fit for Goodman margin at the mid

Unlike the model fit for the Goodman margin at the hub, the model fit for mid section was performed using classification. The results are shown in Fig. 165. Since a significant number of cases had the mean stress outside the yield limit, only 370 cases satisfied the mean stress criteria. It was observed that classifying the designs into two categories (acceptable vs. unacceptable) provided a better model fit. While the training R^2 was greater that 0.95, the validation R^2 is only slightly higher than 0.8. This is very likely due to the low number of design points available for model fit. Thus, a little error in the prediction of the Goodman margin at the mid section is expected.

Training

CS2_Y/N

Measures	Value
Generalized RSquare	0.9503781
Entropy RSquare	0.9318571
RMSE	0.0641034
Mean Abs Dev	0.0190485
Misclassification Rate	0.0035211
-LogLikelihood	6.2310957
Sum Freq	284

Confusion Matrix

Actual	Predicted Count	
CS2_Y/N	0	1
0	256	0
1	1	27

Confusion Rates

Actual	Predicted Rate	
CS2_Y/N	0	1
0	1.000	0.000
1	0.036	0.964

Validation

CS2_Y/N

Measures	Value
Generalized RSquare	0.800536
Entropy RSquare	0.7619751
RMSE	0.1261716
Mean Abs Dev	0.0405239
Misclassification Rate	0.0232558
-LogLikelihood	4.5406343
Sum Freq	86

Confusion Matrix

Actual	Predicted Count	
CS2_Y/N	0	1
0	80	1
1	1	4

Confusion Rates

Actual	Predicted Rate	
CS2_Y/N	0	1
0	0.988	0.012
1	0.200	0.800

Figure 165: Training and validation metrics for Goodman margin (mid).

A.6 Model fit for M1/1EO margin

Fig. 166 shows the model fit for the first natural mode and first engine order frequency margins. Very accurate model fit is obtained and R^2 values of > 0.99 is observed in both training and validation points.

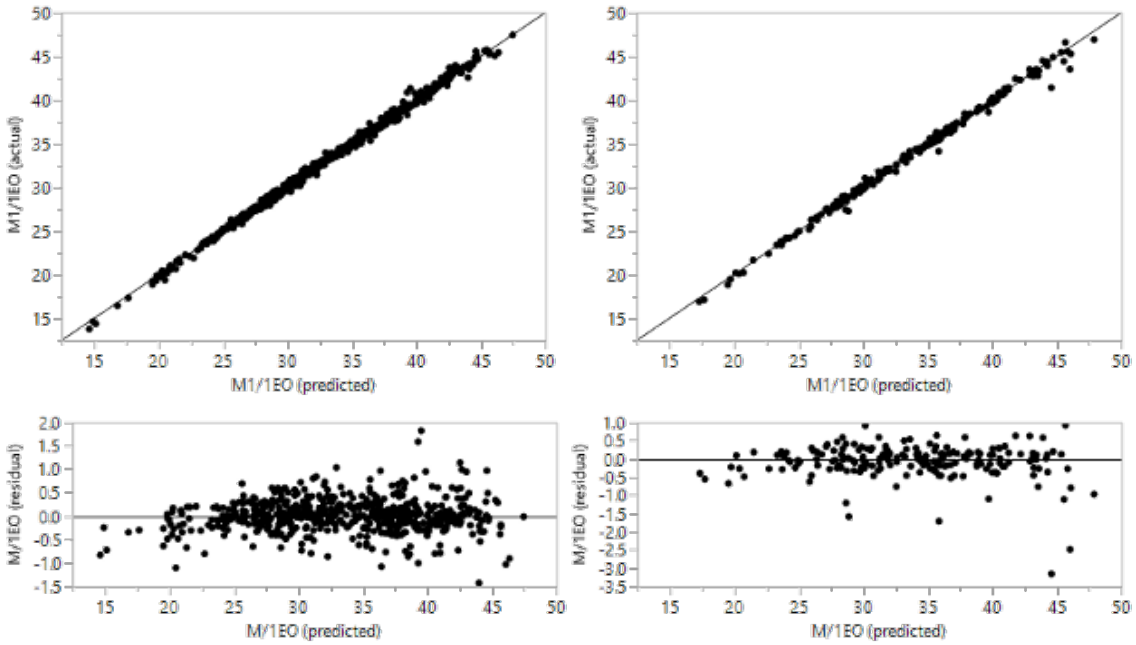

Training

M1/1EO

Measures	Value
RSquare	0.9979495
RMSE	0.3452262
Mean Abs Dev	0.2432834
-LogLikelihood	165.25468
SSE	70.436042
Sum Freq	591

Validation

M1/1EO

Measures	Value
RSquare	0.9969831
RMSE	0.4681782
Mean Abs Dev	0.2902151
-LogLikelihood	90.290796
SSE	43.399782
Sum Freq	198

Figure 166: Training and validation metrics for M1/1EO margin.

A.7 Model fit for M1/2EO margin

The model fit for M1/1EO and M1/2EO are very similar, since an increase in one leads to a decrease in the other. Fig. 167 shows the model fit for the first natural mode and second engine order frequency margins. The R^2 values for bothe the training and validation of > 0.99 is observed in both training and validation points.

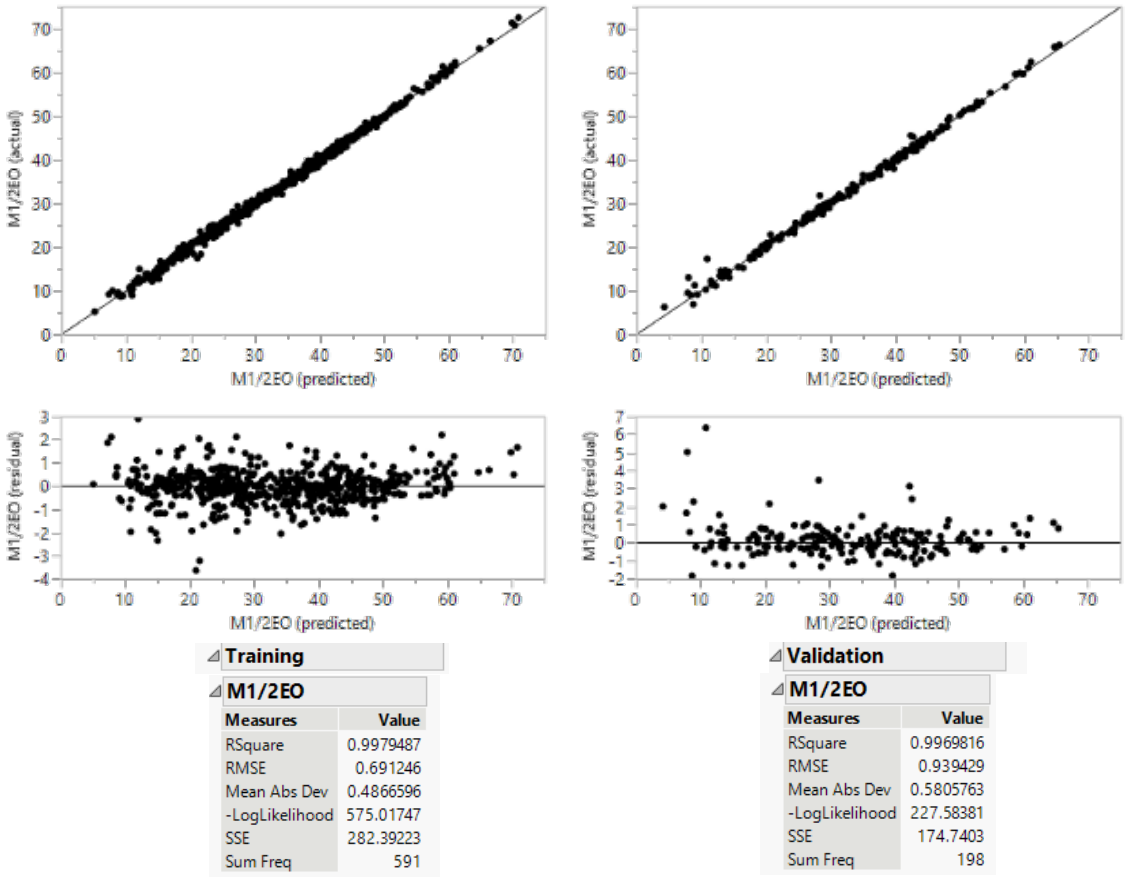

Training

M1/2EO

Measures	Value
RSquare	0.9979487
RMSE	0.691246
Mean Abs Dev	0.4866596
-LogLikelihood	575.01747
SSE	282.39223
Sum Freq	591

Validation

M1/2EO

Measures	Value
RSquare	0.9969816
RMSE	0.939429
Mean Abs Dev	0.5805763
-LogLikelihood	227.58381
SSE	174.7403
Sum Freq	198

Figure 167: Training and validation metrics for M1/2EO margin.

A.8 Model fit for M2/3EO margin

The model fit results for M2/3EO margin is shown in Fig. 168. While the R^2 values for both training and validation of > 0.99, the residual plots show that the errors mostly arise from over prediction of the frequency margins.

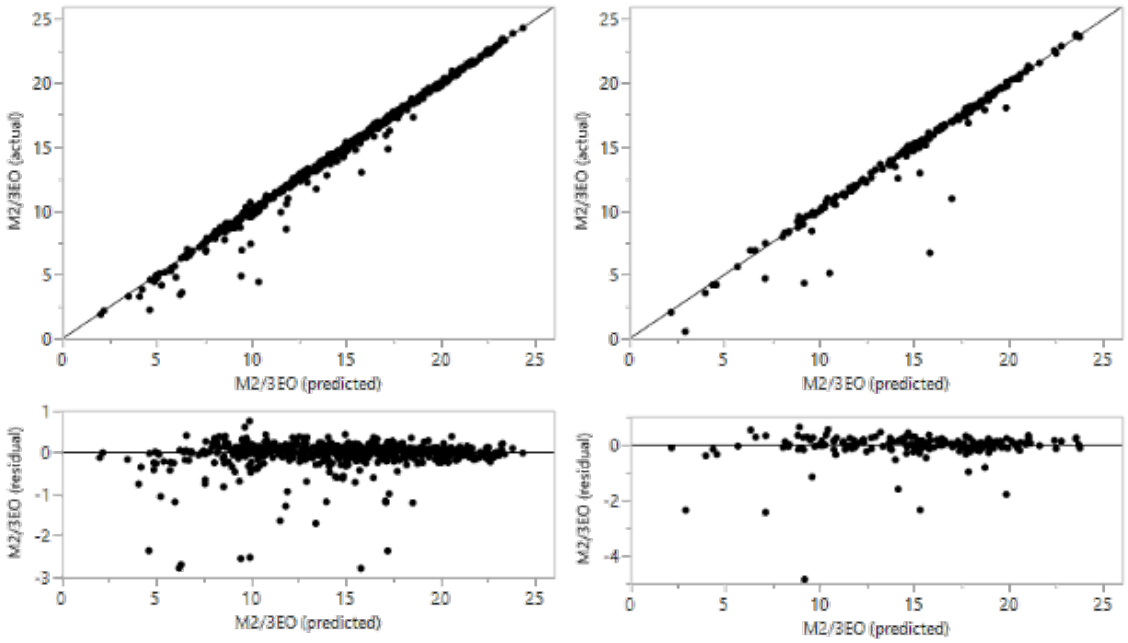

Training

M2/3EO

Measures	Value
RSquare	0.9969871
RMSE	0.505118
Mean Abs Dev	0.203636
-LogLikelihood	60.120026
SSE	150.7902
Sum Freq	591

Validation

M2/3EO

Measures	Value
RSquare	0.9909645
RMSE	1.0195665
Mean Abs Dev	0.3368619
-LogLikelihood	119.80286
SSE	205.82415
Sum Freq	198

Figure 168: Training and validation metrics for M2/3EO margin.

A.9 Model fit for M2/4EO margin

The model fit results for M2/4EO margin is shown in Fig. 169. Most errors arise through under prediction of the margins. This makes sense since M2 lies between 3EO and 4EO; under prediction of one leads to an over prediction of the other. This is not a huge concern since the R^2 values for both training and validation of > 0.99.

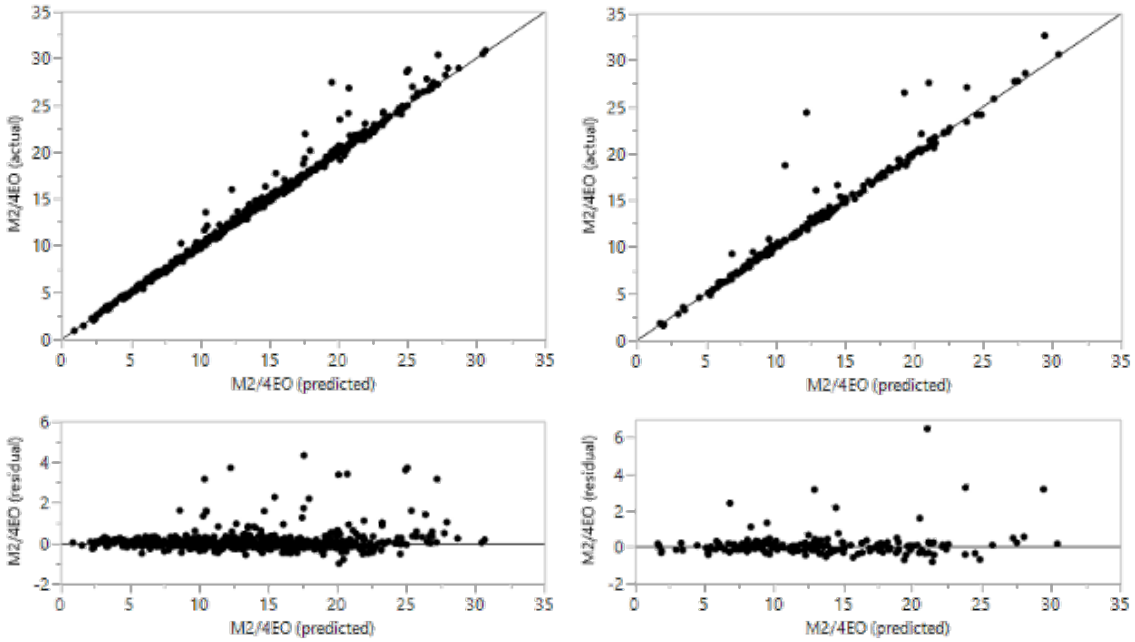

Training

M2/4EO

Measures	Value
RSquare	0.9969847
RMSE	0.6731125
Mean Abs Dev	0.2716221
-LogLikelihood	230.37403
SSE	267.77051
Sum Freq	591

Validation

M2/4EO

Measures	Value
RSquare	0.9909417
RMSE	1.3585222
Mean Abs Dev	0.4497159
-LogLikelihood	177.01356
SSE	365.42536
Sum Freq	198

Figure 169: Training and validation metrics for M2/4EO margin.

A.10 Model fit for M3/6EO margin

The model fit results for training and validation points for M3/6EO margin are shown in Fig. 170. Similar to other frequency margins, a strong fit has been obtained. While the R^2 values are slightly lower other frequency margins, they are greater than 0.97.

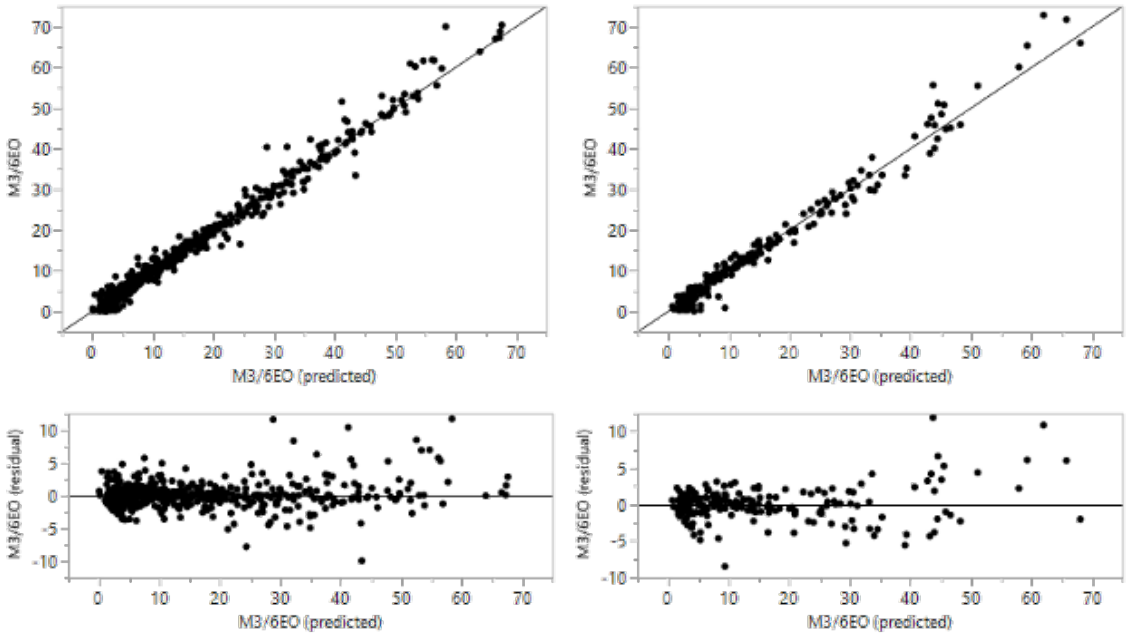

Training

M3/6EO

Measures	Value
RSquare	0.9871963
RMSE	1.9205866
Mean Abs Dev	1.1815592
-LogLikelihood	1099.2494
SSE	2179.9938
Sum Freq	591

Validation

M3/6EO

Measures	Value
RSquare	0.9776593
RMSE	2.4166135
Mean Abs Dev	1.6639685
-LogLikelihood	436.06581
SSE	1156.3241
Sum Freq	198

Figure 170: Training and validation metrics for M3/6EO margin.

A.11 Model fit for M3/7EO margin

The final response tracked was M3/7EO margin. A strong model fit for both training and validation points were obtained. R^2 values were greater than 0.99 for both. The residual plots suggest the errors are higher for higher margins, which are not significant concerns for our analysis since our goal is to ensure these margins are above a certain margin.

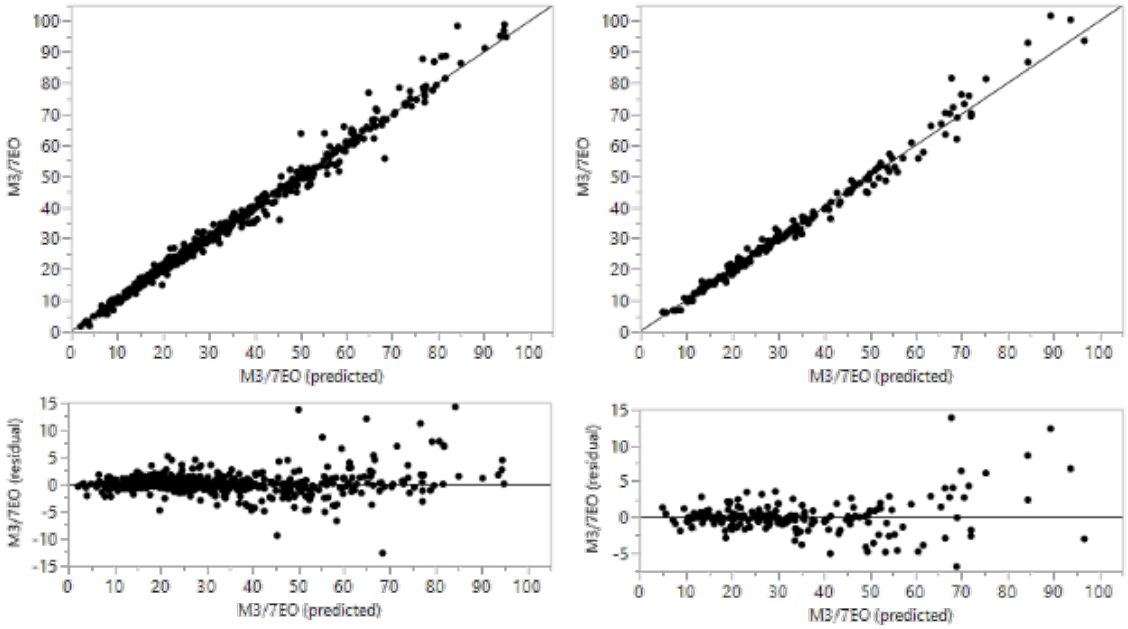

Training

M3/7EO

Measures	Value
RSquare	0.9936956
RMSE	2.0465179
Mean Abs Dev	1.1058845
-LogLikelihood	1060.1315
SSE	2475.2473
Sum Freq	591

Validation

M3/7EO

Measures	Value
RSquare	0.990332
RMSE	2.3825051
Mean Abs Dev	1.4324024
-LogLikelihood	406.39504
SSE	1123.9134
Sum Freq	198

Figure 171: Training and validation metrics for M3/7EO margin.

REFERENCES

[1] Ahuja, J. S., *A Method for Modeling Aero-Propulsive Coupling Characteristics of Boundary Layer Ingesting Aircraft in Conceptual Design*. PhD thesis, Georgia Tech, 2020.

[2] Ainley, D. and Mathieson, G. C., "A method of performance estimation for axial-flow turbines," tech. rep., Aeronautical Research Council London (United Kingdom), 1951.

[3] Altus, S. and Kroo, I., "Concurrent wing design and flight-path optimization using optimizer-based decomposition," in *7th AIAA/USAF/NASA/ISSMO Symposium on Multidisciplinary Analysis and Optimization*, p. 4920, 1998.

[4] Ashcraft, S. W., Padron, A. S., Pascioni, K. A., Stout Jr, G. W., and Huff, D. L., "Review of propulsion technologies for n+ 3 subsonic vehicle concepts," 2011.

[5] Aungier, R. H. and Cassin, I., "Axial-flow compressors: A strategy for aerodynamic design and analysis," 2003.

[6] Avcar, M. and Saplioglu, K., "An artificial neural network application for estimation of natural frequencies of beams," *International Journal of Advanced Computer Science and Applications*, vol. 6, no. 6, pp. 94–102, 2015.

[7] Bakhle, M., Reddy, T., Herrick, G., Shabbir, A., and Florea, R., "Aeromechanics analysis of a boundary layer ingesting fan," in *48th AIAA/ASME/SAE/ASEE Joint Propulsion Conference & Exhibit*, p. 3995, 2012.

[8] Bakhle, M. A., Reddy, T. S., Coroneos, R., Min, J. B., Provenza, A. J., Duffy, K. P., Stefko, G. L., and Heinlein, G., "Aeromechanics analysis of a distortion-tolerant fan with boundary layer ingestion," in *2018 AIAA Aerospace Sciences Meeting*, p. 1891, 2018.

[9] Bao, Y., Liu, D., Tang, Z., and Li, H., "Machine-learning-based methods for output only structural modal identification," *arXiv preprint arXiv:2004.07644*, 2020.

[10] Beddoes, T., "Practical computation of unsteady lift," 1982.

[11] Bendarkar, M. V., Rajaram, D., Cai, Y., Briceno, S. I., and Mavris, D. N., "Evaluating optimal paths for aircraft subsystem electrification in early design," in *AIAA Aviation 2019 Forum*, p. 2802, 2019.

[12] Berdichevskii, V., "Variational-asymptotic method of constructing a theory of shells: Pmm vol. 43, no. 4, 1979, pp. 664–687," *Journal of Applied Mathematics and Mechanics*, vol. 43, no. 4, pp. 711–736, 1979.

[13] Berrier, B. and Allan, B., "Experimental and computational evaluation of flush-mounted, s-duct inlets," in *42nd AIAA Aerospace Sciences Meeting and Exhibit*, p. 764, 2004.

[14] Buannic, N. and Cartraud, P., "Higher-order effective modeling of periodic heterogeneous beams. i. asymptotic expansion method," *International Journal of Solids and Structures*, vol. 38, no. 40-41, pp. 7139–7161, 2001.

[15] Buannic, N. and Cartraud, P., "Higher-order effective modeling of periodic heterogeneous beams. ii. derivation of the proper boundary conditions for the interior asymptotic solution," *International Journal of Solids and Structures*, vol. 38, no. 40-41, pp. 7163–7180, 2001.

[16] Burgaud, F., *A risk-value-based methodology for enterprise-level decision-making*. PhD thesis, Georgia Institute of Technology, 2017.

[17] Cai, Y., Rajaram, D., and Mavris, D. N., "Multi-mission multi-objective optimization in commercial aircraft conceptual design," in *AIAA Aviation 2019 Forum*, p. 3577, 2019.

[18] Callahan, G. M. and Stenning, A., "Attenuation of inlet flow distortion upstream of axial flow compressors," *Journal of Aircraft*, vol. 8, no. 4, pp. 227–233, 1971.

[19] Campbell, W., "Protection of turbine disk wheels from axial vibration," in *Proceedings of the Cleveland Spring Meeting*, 1924.

[20] Carta, F. O., "Analysis of unsteady aerodynamic effects on an axial-flow compressor stage with distorted inflow," tech. rep., Purdue Univ Lafayette in Project Squid Headquarters, 1972.

[21] Celestina, M. L. and Long-Davis, M. J., "Large-scale boundary layer ingesting propulsor research," 2019.

[22] Chen, H., Yu, W., and Capellaro, M., "A critical assessment of computer tools for calculating composite wind turbine blade properties," *Wind Energy*, vol. 13, no. 6, pp. 497–516, 2010.

[23] Committee, S. S.-. and others, "Arp 1420, february 2002," gas turbine inlet flow distortion guidelines," revision b," *Society of Automotive Engineers*.

[24] Cousins, W., "A theory for the prediction of compressor blade aerodynamic response," in *34th AIAA/ASME/SAE/ASEE Joint Propulsion Conference and Exhibit*, p. 3308, 1998.

[25] Cousins, W. T., *The dynamics of stall and surge behavior in axial-centrifugal compressors*. PhD thesis, Virginia Tech, 1997.

[26] Cousins, W. T. and Davis Jr, M. W., "Evaluating complex inlet distortion with a parallel compressor model: Part 1—concepts, theory, extensions, and limitations," in *Turbo Expo: Power for Land, Sea, and Air*, vol. 54617, pp. 1–12, 2011.

[27] Cousins, W. T., Voytovych, D., Tillman, G., and Gray, E., "Design of a distortion-tolerant fan for a boundary-layer ingesting embedded engine application," in *53rd AIAA/SAE/ASEE Joint Propulsion Conference*, p. 5042, 2017.

[28] Cousins, W., Jones, M., and Belling, T., "Surge and stall characteristics of axial-centrifugal compressors: The enhancement to engine stability," in *AGARD CONFERENCE PROCEEDINGS AGARD CP*, pp. 29–29, AGARD, 1996.

[29] Craig, H. and Cox, H., "Performance estimation of axial flow turbines," *Proceedings of the Institution of Mechanical Engineers*, vol. 185, no. 1, pp. 407–424, 1970.

[30] Cumpsty, N. and Greitzer, E., "Ideas and methods of turbomachinery aerodynamics: a historical view," *Journal of propulsion and power*, vol. 20, no. 1, pp. 15–26, 2004.

[31] Cumpsty, N. A., *Compressor aerodynamics*. No. BOOK, Longman Scientific & Technical, 1989.

[32] Davis Jr, M. W. and Cousins, W. T., "Evaluating complex inlet distortion with a parallel compressor model: Part 2—applications to complex patterns," in *Turbo Expo: Power for Land, Sea, and Air*, vol. 54617, pp. 13–23, 2011.

[33] Dean, R. C., "On the necessity of unsteady flow in fluid machines," *Journal of Basic Engineering*, vol. 81, no. 1, pp. 24–28, 1959.

[34] Defoe, J., Narkaj, A., and Spakovszky, Z., "A body-force based methodology for predicting multiple-pure-tone noise: Validation," in *16th AIAA/CEAS Aeroacoustics Conference*, p. 3747, 2010.

[35] Del Rosario, R., "Propulsion technologies for future aircraft generations: Clean, lean, quiet, and green," 2011.

[36] Denton, J., "Throughflow calculations for transonic axial flow turbines," *Journal of Engineering for Power*, vol. 100, no. 2, pp. 212–218, 1978.

[37] Doulgeris, G., Khaleghi, H., Kalfas, A., and Pilidis, P., "Development of a method for enhanced fan representation in gas turbine modeling," *International Journal of Rotating Machinery*, vol. 2011, 2011.

[38] Drela, M., "Development of the d8 transport configuration," in *29th AIAA Applied Aerodynamics Conference*, p. 3970, 2011.

[39] Dunham, J., "Non-axisymmetric flows in axial compressors," *Mechanical Engineering Science Monograph, MESM*, 1965.

[40] Dunham, J. and Came, P., "Improvements to the ainley-mathieson method of turbine performance prediction," *Journal of Engineering for Power*, vol. 92, no. 3, pp. 252–256, 1970.

[41] EHRICH, F., "Circumferential Inlet Distortions in Axial Flow Turbomachinery," *Journal of the Aeronautical Sciences*, vol. 24, no. 6, pp. 413–417, 1957.

[42] Ehrich, F., "Circumferential inlet distortions in axial flow turbomachinery," *Journal of the Aeronautical Sciences*, vol. 24, no. 6, pp. 413–417, 1957.

[43] Elham, A., La Rocca, G., and Van Tooren, M., "Development and implementation of an advanced, design-sensitive method for wing weight estimation," *Aerospace Science and Technology*, vol. 29, no. 1, pp. 100–113, 2013.

[44] Ellington, C. P., Van Den Berg, C., Willmott, A. P., and Thomas, A. L., "Leading-edge vortices in insect flight," *Nature*, vol. 384, no. 6610, p. 626, 1996.

[45] Felder, J., Kim, H., Brown, G., and Kummer, J., "An examination of the effect of boundary layer ingestion on turboelectric distributed propulsion systems," in *49th AIAA aerospace sciences meeting including the new horizons forum and aerospace exposition*, p. 300, 2011.

[46] Ferrar, A. and O'Brien, W., "Fan response to total pressure distortions produced by boundary layer ingesting serpentine inlets," in *48th AIAA/ASME/SAE/ASEE Joint Propulsion Conference & Exhibit*, p. 3996, 2012.

[47] Ferrar, A. M., *Measurements of Flow in Boundary Layer Ingesting Serpentine Inlets*. PhD thesis, Virginia Tech, 2011.

[48] Fidalgo, V. J., Hall, C., and Colin, Y., "A study of fan-distortion interaction within the nasa rotor 67 transonic stage," *Journal of Turbomachinery*, vol. 134, no. 5, p. 051011, 2012.

[49] Florea, R. V., Matalanis, C., Hardin, L. W., Stucky, M., and Shabbir, A., "Parametric analysis and design for embedded engine inlets," *Journal of Propulsion and Power*, vol. 31, no. 3, pp. 843–850, 2015.

[50] Florea, R. V., Voytovych, D., Tillman, G., Stucky, M., Shabbir, A., Sharma, O., and Arend, D. J., "Aerodynamic analysis of a boundary-layer-ingesting distortion-tolerant fan," in *ASME Turbo Expo 2013: Turbine Technical Conference and Exposition*, pp. V06BT38A006–V06BT38A006, American Society of Mechanical Engineers, 2013.

[51] Frost, D., *A streamline curvature through-flow computer program for analysing the flow through axial-flow turbomachines*. Citeseer, 1970.

[52] Gearhart, W. S. and Henderson, R. E., "Selection of a propulsor for a submersible system," *Journal of Aircraft*, vol. 3, no. 1, pp. 84–90, 1966.

[53] Giles, G. L., "Equivalent plate analysis of aircraft wing box structures with general planform geometry," *Journal of Aircraft*, vol. 23, no. 11, pp. 859–864, 1986.

[54] Giuliani, J. E., Chen, J. P., Beach, T. A., and Bakhle, M. A., "Numerical simulation of boundary layer ingesting inlet/fan interaction," in *50th AIAA/ASME/ SAE/ASEE Joint Propulsion Conference*, p. 3731, 2014.

[55] Giuliani, J. E., *Jet Engine Fan Response to Inlet Distortions Generated by Ingesting Boundary Layer Flow*. PhD thesis, The Ohio State University, 2016.

[56] Gladin, J. C., *A sizing and vehicle matching methodology for boundary layer ingesting propulsion systems*. PhD thesis, Georgia Institute of Technology, 2015.

[57] Gong, Y., *A computational model for rotating stall and inlet distortions in multistage compressors*. PhD thesis, Massachusetts Institute of Technology, 1999.

[58] Gorton, S., Owens, L., Jenkins, L., Allan, B., and Schuster, E., "Active flow control on a boundary-layer-ingesting inlet," in *42nd AIAA Aerospace Sciences Meeting and Exhibit*, p. 1203, 2004.

[59] Gray, J. S., Mader, C. A., Kenway, G. K., and Martins, J., "Approach to modeling boundary layer ingestion using a fully coupled propulsion-rans model," in *58th AIAA/ASCE/AHS/ASC Structures, Structural Dynamics, and Materials Conference*, p. 1753, 2017.

[60] Greitzer, E., "Upstream attenuation and quasi-steady rotor lift fluctuations in asymmetric flows in axial compressors," in *Turbo Expo: Power for Land, Sea, and Air*, vol. 79801, p. V001T01A030, American Society of Mechanical Engineers, 1973.

[61] Greitzer, E., "Axial compressor stall phenomena," *Journal of Fluids Engineering*, vol. 102, no. 2, pp. 134–151, 1980.

[62] Greitzer, E. and Griswol, H., "Compressor-diffuser interaction with circumferential flow distortion," *Journal of Mechanical Engineering Science*, vol. 18, no. 1, pp. 25–38, 1976.

[63] Greitzer, E. and Strand, T., "Asymmetric swirling flows in turbomachine annuli," *Journal of Engineering for Power*, vol. 100, no. 4, pp. 618–629, 1978.

[64] Gülçat, Ü., *Fundamentals of modern unsteady aerodynamics*. Springer, 2010.

[65] Gunn, E. and Hall, C., "Aerodynamics of boundary layer ingesting fans," in *ASME Turbo Expo 2014: Turbine Technical Conference and Exposition*, pp. V01AT01A024–V01AT01A024, American Society of Mechanical Engineers, 2014.

[66] Gunn, E. J. and Hall, C. A., "Nonaxisymmetric stator design for boundary layer ingesting fans," *Journal of Turbomachinery*, vol. 141, no. 7, p. 071010, 2019.

[67] Gupta, M., *Enhancements in Analysis of Beam-Like Structures using Asymptotic Methods*. PhD thesis, Georgia Institute of Technology, 2019.

[68] Gupta, M. and Hodges, D. H., "Modeling thin-walled beams using vam," in *58th AIAA/ASCE/AHS/ASC Structures, Structural Dynamics, and Materials Conference*, p. 1832, 2017.

[69] Gupta, M., Pokhrel, M., Hodges, D. H., and Mavris, D. N., "Application of variational asymptotic method for structural analysis of fan rotor blades in boundary layer ingesting flow field," in *AIAA Scitech 2020 Forum*, p. 0133, 2020.

[70] Gupta, M., Sarkar, K., and Hodges, D. H., "3-d stress-strain histories for composite beams in nonlinear transient structural analysis," in *AIAA Scitech 2019 Forum*, p. 1026, 2019.

[71] Gupta, M., Sarkar, K., and Hodges, D. H., "Dynamic analysis of nonlinear composite beams with 3-d structural damping," in *AIAA Scitech 2019 Forum*, p. 0211, 2019.

[72] Gupta, M., Sarojini, D., Shah, A., and Hodges, D. H., "Dimensional reduction technique for analysis of aperiodic inhomogeneous structures," in *2018 AIAA/ASCE/AHS/ASC Structures, Structural Dynamics, and Materials Conference*, p. 0698, 2018.

[73] Gupta, M., Sarojini, D., Shah, A., and Hodges, D. H., "Beam theory for asymptotic analysis of aperiodic and inhomogeneous structures," *AIAA Journal*, vol. 57, no. 10, pp. 4155–4168, 2019.

[74] Hajela, P., "Reduced complexity structural modeling for automated airframe synthesis," 1987.

[75] Hall, D. K., Huang, A. C., Uranga, A., Greitzer, E. M., Drela, M., and Sato, S., "Boundary layer ingestion propulsion benefit for transport aircraft," *Journal of Propulsion and Power*, vol. 33, no. 5, pp. 1118–1129, 2017.

[76] Hall, D. K., *Analysis of civil aircraft propulsors with boundary layer ingestion*. PhD thesis, Massachusetts Institute of Technology, 2015.

[77] Hall, D., Greitzer, E., and Tan, C., "Analysis of fan stage conceptual design attributes for boundary layer ingestion," *Journal of Turbomachinery*, vol. 139, no. 7, p. 071012, 2017.

[78] Halliday, D., Resnick, R., and Walker, J., *Fundamentals of physics extended*. John Wiley & Sons, 2010.

[79] Hardin, L., Tillman, G., Sharma, O., Berton, J., and Arend, D., "Aircraft system study of boundary layer ingesting propulsion," in *48th AIAA/ASME/SAE/ASEE Joint Propulsion Conference & Exhibit*, p. 3993, 2012.

[80] Henderson, R. E. and Horlock, J., "An approximate analysis of the unsteady lift on airfoils in cascade," 1972.

[81] Hendricks, E. S., "A review of boundary layer ingestion modeling approaches for use in conceptual design," 2018.

[82] Hendricks, E. S., *A multi-level multi-design point approach for gas turbine cycle and turbine conceptual design*. PhD thesis, Georgia Institute of Technology, 2017.

[83] Hodges, D. H., "Nonlinear composite beam theory," 2006.

[84] Hodges, D. H. and Dowell, E., "Nonlinear equations of motion for the elastic bending and torsion of twisted nonuniform rotor blades," 1974.

[85] Horlock, J., Greitzer, E., and Henderson, R., "The response of turbomachine blades to low frequency inlet distortions," 1977.

[86] Hsiao, E., Naimi, M., Lewis, J. P., Dalbey, K., Gong, Y., and Tan, C., "Actuator duct model of turbomachinery components for powered-nacelle navier-stokes calculations," *Journal of Propulsion and Power*, vol. 17, no. 4, pp. 919–927, 2001.

[87] Jennions, I. and Stow, P., "The importance of circumferential non-uniformities in a passage-averaged quasi-three-dimensional turbomachinery design system," in *ASME 1985 Beijing International Gas Turbine Symposium and Exposition*, pp. V001T02A020–V001T02A020, American Society of Mechanical Engineers, 1985.

[88] Jennions, I. and Stow, P., "A quasi-three-dimensional turbomachinery blade design system: Part i—throughflow analysis," *Journal of Engineering for Gas Turbines and Power*, vol. 107, no. 2, pp. 301–307, 1985.

[89] Jones, S. M., "Development of an object-oriented turbomachinery analysis code within the npss framework," 2014.

[90] Joo, W. and Hynes, T., "The simulation of turbomachinery blade rows in asymmetric flow using actuator disks," *Journal of turbomachinery*, vol. 119, no. 4, pp. 723–732, 1997.

[91] Kacker, S. and Okapuu, U., "A mean line prediction method for axial flow turbine efficiency," *Journal of engineering for power*, vol. 104, no. 1, pp. 111–119, 1982.

[92] Kallas, S. and Geoghegan-Quiin, M., "Flightpath 2050: Europe's vision for aviation: Report of the high level group on aviation research," 2011.

[93] Kármán, T. v., "Airfoil theory for non-uniform motion," *Journal of the Aeronautical Sciences*, vol. 5, no. 10, pp. 379–390, 1938.

[94] Kim, J.-S. and Wang, K., "Vibration analysis of composite beams with end effects via the formal asymptotic method," *Journal of Vibration and Acoustics*, vol. 132, no. 4, p. 041003, 2010.

[95] Kurzke, J., "Effects of inlet flow distortion on the performance of aircraft gas turbines," *Journal of Engineering for Gas Turbines and Power*, vol. 130, no. 4, p. 041201, 2008.

[96] Lee, B., Liou, M.-F., and Liou, M.-S., "Aerodynamic conceptual design of boundary layer ingestion propulsor systems: A quasi-2d through flow analysis method and multi-fidelity propulsor design framework," 2018.

[97] Lee, B., Liou, M.-F., and Liou, M.-S., "Conceptual aerodynamic design of a tail-cone thruster system under axi-symmetric inlet distortion," in *Turbo Expo: Power for Land, Sea, and Air*, vol. 50992, p. V02AT39A015, American Society of Mechanical Engineers, 2018.

[98] Lee, B. J. and Liou, M.-F., "Aerodynamic design and optimization of fan stage for boundary layer ingestion propulsion system," 2018.

[99] Letcher, T., *A Matlab Implementation of the Streamline Curvature Method for Axial Turbomachinery*. PhD thesis, Ohio State University, 2008.

[100] Li, X., Grecov, D., Guo, Z., and Hou, Z., "Influence of unsteady and kinematic parameters on aerodynamic characteristics of a pitching airfoil," *Journal of Aerospace Engineering*, vol. 32, no. 1, p. 04018120, 2019.

[101] Lieblein, S., Schwenk, F. C., and Broderick, R. L., "Diffusion factor for estimating losses and limiting blade loadings in axial-flow-compressor blade elements," tech. rep., National Advisory Committee for Aeronautics Cleveland OH Lewis Flight Propulsion Lab, 1953.

[102] Liu, Y., Elham, A., Horst, P., and Hepperle, M., "Exploring vehicle level benefits of revolutionary technology progress via aircraft design and optimization," *Energies*, vol. 11, no. 1, p. 166, 2018.

[103] Longley, J. and Greitzer, E., "Inlet distortion effects in aircraft propulsion system integration," 1992.

[104] Lucas, J. R., O'Brien, W. F., and Ferrar, A. M., "Effect of bli–type inlet distortion on turbofan engine performance," in *ASME Turbo Expo 2014: Turbine Technical Conference and Exposition*, p. V01AT01A037, American Society of Mechanical Engineers, 2014.

[105] Lusk, J. T., *Wing and Fuselage Optimization Considering Alternative Material*. PhD thesis, University of Kansas, 2008.

[106] Marble, F. and Rannie, W., "Unsteady flows in axial turbomachines," 1957.

[107] Marble, F. E., "Three-dimensional flow in turbomachines," 1964.

[108] Marien, T., Welstead, J. R., and Jones, S. M., "Vehicle level system impact of boundary layer ingestion for the nasa d8 concept aircraft," in *2018 AIAA Aerospace Sciences Meeting*, p. 0271, 2018.

[109] Marsh, H., "Throughflow calculations in axial turbomachinery—a technical point of view," in *AGARD Propulsion and Energetics Panel, 47th Meeting, Paper*, no. 2, 1976.

[110] Maute, K., Nikbay, M., and Farhat, C., "Coupled analytical sensitivity analysis and optimization of three-dimensional nonlinear aeroelastic systems," *AIAA journal*, vol. 39, no. 11, pp. 2051–2061, 2001.

[111] Mazzawy, R. S., "Multiple segment parallel compressor model for circumferential flow distortion," *Journal of Engineering for Power*, vol. 99, no. 2, pp. 288–296, 1977.

[112] Mehdizadeh, F. and Trépanier, J.-Y., "Development and validation of a new boundary condition for intake design under distortion,"

[113] Meher-Homji, C. B., Gabriles, G., and others, "Gas turbine blade failures-causes, avoidance, and troubleshooting.," in *Proceedings of the 27th turbomachinery symposium*, Texas A&M University. Turbomachinery Laboratories, 1998.

[114] Mennicken, M., Schoenweitz, D., Schnoes, M., and Schnell, R., "Conceptual fan design for boundary layer ingestion," *Proceedings of the ASME Turbo Expo*, vol. 2C-2019, pp. 1–14, 2019.

[115] Mennicken, M., Schönweitz, D., Schnoes, M., and Schnell, R., "Conceptual fan design for boundary layer ingestion," in *Turbo Expo: Power for Land, Sea, and Air*, vol. 58578, p. V02CT41A009, American Society of Mechanical Engineers, 2019.

[116] Min, J. B., Reddy, T. S., Bakhle, M. A., Coroneos, R. M., Stefko, G. L., Provenza, A. J., and Duffy, K. P., "Cyclic symmetry finite element forced response analysis of a distortion tolerant fan with boundary layer ingestion," in *2018 AIAA Aerospace Sciences Meeting*, p. 1890, 2018.

[117] Novak, R., "Streamline curvature computing procedures for fluid-flow problems," *Journal of Engineering for Power*, vol. 89, no. 4, pp. 478–490, 1967.

[118] Oates, G. C., "Actuator disk theory for incompressible highly rotating flows," *Journal of Basic Engineering*, vol. 94, no. 3, pp. 613–621, 1972.

[119] Pachidis, V., Pilidis, P., Templalexis, I., Korakianitis, T., and Kotsiopoulos, P., "Prediction of engine performance under compressor inlet flow distortion using streamline curvature," *Journal of Engineering for Gas Turbines and Power*, vol. 129, no. 1, pp. 97–103, 2007.

[120] Pearson, H. and McKenzie, A., "Wakes in axial compressors," *The Aeronautical Journal*, vol. 63, no. 583, pp. 415–416, 1959.

[121] Perovic, D., Hall, C., and Gunn, E., "Stall inception in a boundary layer ingesting fan," in *ASME Turbo Expo 2015: Turbine Technical Conference and Exposition*, pp. V02AT37A031–V02AT37A031, American Society of Mechanical Engineers, 2015.

[122] Peters, A., Spakovszky, Z. S., Lord, W. K., and Rose, B., "Ultrashort nacelles for low fan pressure ratio propulsors," *Journal of Turbomachinery*, vol. 137, no. 2, p. 021001, 2015.

[123] Plas, A., Crichton, D., Sargeant, M., Hynes, T., Greitzer, E., Hall, C., and Madani, V., "Performance of a boundary layer ingesting (bli) propulsion system," in *45th AIAA aerospace sciences meeting and exhibit*, p. 450, 2007.

[124] Plas, A. A. P., *Performance of a boundary layer ingesting propulsion system.* PhD thesis, Massachusetts Institute of Technology, 2006.

[125] Pokhrel, M., Gladin, J., Denney, R. K., and Mavris, D., "An approach for fan stage conceptual design with non-axisymmetric stators in presence of distortion," in *AIAA AVIATION 2020 FORUM*, p. 2643, 2020.

[126] Pokhrel, M., Sarojini, D., and Mavris, D., "Conceptual level optimization of a fan stage under distortion considering aero-structural constraints," in *AIAA AVIATION 2020 FORUM*, p. 3115, 2020.

[127] Pokhrel, M., Shi, M., Ahuja, J., Gladin, J., and Mavris, D. N., "Conceptual design of a bli propulsor capturing aero-propulsive coupling and distortion impacts," in *AIAA Scitech 2019 Forum*, p. 1588, 2019.

[128] Pope, A., "On airfoil theory and experiment," *Journal of the Aeronautical Sciences*, vol. 15, no. 7, pp. 407–410, 1948.

[129] Provenza, A. J., Duffy, K. P., and Bakhle, M. A., "Aeromechanical response of a distortion-tolerant boundary layer ingesting fan," *Journal of Engineering for Gas Turbines and Power*, vol. 141, no. 1, 2019.

[130] Rajagopal, A., *Advancements in rotor blade cross-sectional analysis using the variational-asymptotic method*. PhD thesis, Georgia Institute of Technology, 2014.

[131] Rajaram, D., Cai, Y., Chakraborty, I., and Mavris, D. N., "Integrated sizing and optimization of aircraft and subsystem architectures in early design," *Journal of Aircraft*, vol. 55, no. 5, pp. 1942–1954, 2018.

[132] Rajaram, D., Puranik, T. G., Ashwin Renganathan, S., Sung, W., Fischer, O. P., Mavris, D. N., and Ramamurthy, A., "Empirical assessment of deep gaussian process surrogate models for engineering problems," *Journal of Aircraft*, pp. 1–15, 2020.

[133] Rajaram, D., Puranik, T. G., Renganathan, A., Sung, W. J., Pinon-Fischer, O. J., Mavris, D. N., and Ramamurthy, A., "Deep gaussian process enabled surrogate models for aerodynamic flows," in *AIAA Scitech 2020 Forum*, p. 1640, 2020.

[134] Reid, C., "The response of axial flow compressors to intake flow distortion," in *ASME 1969 gas turbine conference and products show*, pp. V001T01A029–V001T01A029, American Society of Mechanical Engineers, 1969.

[135] Sachdeva, C., Gupta, M., and Hodges, D. H., "Modeling of initially curved and twisted smart beams using intrinsic equations," *International Journal of Solids and Structures*, vol. 148, pp. 3–13, 2018.

[136] Saravanamuttoo, H. I., Rogers, G. F. C., and Cohen, H., *Gas turbine theory*. Pearson Education, 2001.

[137] Sarojini, D., Gupta, M., Hodges, D. H., and Mavris, D. N., "An efficient method to dimensionally reduce aperiodic inhomogeneous 3-d structures to 1-d beam-like structures," in *AIAA Scitech 2020 Forum*, p. 0272, 2020.

[138] Sarojini, D., Rajaram, D., Solano, D., and Mavris, D. N., "Adjoint-based structural optimization for beam-like structures subjected to dynamic loads," in *AIAA Scitech 2020 Forum*, p. 0273, 2020.

[139] Schutte, J., Tai, J., and Mavris, D., "Multi design point cycle design incorporation into the environmental design space," in *48th AIAA/ASME/SAE/ASEE Joint Propulsion Conference & Exhibit*, p. 3812, 2012.

[140] Shin, J., "Nasa aeronautics: Strategic implementation plan," *NASA NP-2017–01-2352-HQ*, 2017.

[141] Silvester, M. and Hetherington, R., "Three-dimensional compressible flow through axial flow turbomachines, published in numerical analysis-an introduction," 1966.

[142] Smith, A., "The jet airplane utilizing boundary layer air for propulsion," *Journal of the Aeronautical Sciences*, vol. 14, no. 2, pp. 97–109, 1947.

[143] Smith, L., "The radial-equilibrium equation of turbomachinery," *Journal of Engineering for Power*, vol. 88, no. 1, pp. 1–12, 1966.

[144] Stenning, A. H., "Inlet distortion effects in axial compressors," *Journal of Fluids Engineering, Transactions of the ASME*, vol. 102, no. 1, pp. 7–13, 1980.

[145] Strazisar, A. and Powell, J., "Laser anemometer measurements in a transonic axial flow compressor rotor," 1981.

[146] Tanida, Y., "Inlet airflow distortion in turbomachinery," *Zeitschrift für angewandte Mathematik und Physik ZAMP*, vol. 23, no. 4, pp. 645–654, 1972.

[147] Theodorsen, T. and Mutchler, W., "General theory of aerodynamic instability and the mechanism of flutter," 1935.

[148] Thollet, W., Dufour, G., Carbonneau, X., and Blanc, F., "Assessment of body force methodologies for the analysis of intake-fan aerodynamic interactions," in *ASME Turbo Expo 2016: Turbomachinery Technical Conference and Exposition*, pp. V02CT39A036–V02CT39A036, American Society of Mechanical Engineers, 2016.

[149] Thollet, W., Dufour, G., Carbonneau, X., and Blanc, F., "Body-force modeling for aerodynamic analysis of air intake–fan interactions," *International Journal of Numerical Methods for Heat & Fluid Flow*, vol. 26, no. 7, pp. 2048–2065, 2016.

[150] Valencia, E., Hidalgo, V., Nalianda, D., Laskaridis, P., and Singh, R., "Discretized miller approach to assess effects on boundary layer ingestion induced distortion," *Chinese Journal of Aeronautics*, vol. 30, no. 1, pp. 235–248, 2017.

[151] Wagner, H., "Über die entstehung des dynamischen auftriebes von tragflügeln," *ZAMM-Journal of Applied Mathematics and Mechanics/Zeitschrift für Angewandte Mathematik und Mechanik*, vol. 5, no. 1, pp. 17–35, 1925.

[152] Wang, Q. and Yu, W., "Geometrically nonlinear analysis of composite beams using wiener-milenković parameters," *Journal of Renewable and Sustainable Energy*, vol. 9, no. 3, p. 033306, 2017.

[153] Welstead, J. and Felder, J. L., "Conceptual design of a single-aisle turboelectric commercial transport with fuselage boundary layer ingestion," in *54th AIAA Aerospace Sciences Meeting*, p. 1027, 2016.

[154] Wiart, L., Atinault, O., Grenon, R., Paluch, B., and Hue, D., "Development of nova aircraft configurations for large engine integration studies," in *33rd AIAA Applied Aerodynamics Conference*, p. 2254, 2015.

[155] Williams, D., "Review of current knowledge on engine response to distorted inflow conditions," tech. rep., ROLLS-ROYCE LTD BRISTOL (ENGLAND), 1987.

[156] Wislicenus, G. F., "Hydrodynamics and propulsion of submerged bodies," *ARS Journal*, vol. 30, no. 12, pp. 1140–1148, 1960.

[157] Wu, C.-H., "A general theory of three-dimensional flow in subsonic and supersonic turbomachines of axial-, radial, and mixed-flow types," tech. rep., National Aeronautics and Space Administration Washington DC, 1952.

[158] Xu, J. and Kroo, I., "Aircraft design with active load alleviation and natural laminar flow," *Journal of Aircraft*, vol. 51, no. 5, pp. 1532–1545, 2014.

[159] Yao, J., Gorrell, S. E., and Wadia, A. R., "High-fidelity numerical analysis of Per-Rev-Type inlet distortion transfer in multistage fans-Part I: Simulations with selected blade rows," *Journal of Turbomachinery*, vol. 132, no. 4, pp. 1–10, 2010.

[160] Yao, J., Gorrell, S. E., and Wadia, A. R., "High-fidelity numerical analysis of per-rev-type inlet distortion transfer in multistage fans—part i: simulations with selected blade rows," *Journal of Turbomachinery*, vol. 132, no. 4, 2010.

[161] Yeh, H., "An actuator disc analysis of inlet distortion and rotating stall in axial flow turbomachines," *Journal of the Aerospace Sciences*, vol. 26, no. 11, pp. 739–753, 1959.

[162] Yu, W. and Blair, M., "Gebt: A general-purpose nonlinear analysis tool for composite beams," *Composite Structures*, vol. 94, no. 9, pp. 2677–2689, 2012.

[163] Yu, W., Hodges, D. H., and Ho, J. C., "Variational asymptotic beam sectional analysis–an updated version," *International Journal of Engineering Science*, vol. 59, pp. 40–64, 2012.

[164] Yu, W., Hodges, D. H., Volovoi, V., and Cesnik, C. E., "On timoshenko-like modeling of initially curved and twisted composite beams," *International Journal of Solids and Structures*, vol. 39, no. 19, pp. 5101–5121, 2002.

[165] Yutko, B., Titchener, N., Courtin, C., Lieu, M., Wirsing, L., Hall, D., Tylko, J., Chambers, J., Roberts, T., and Church, C., "Design and development of the commercial d8 transport aircraft," in *31st Congress of the International Council of the Aeronautical Sciences*, 2018.

[166] Zierke, W. C., "Unsteady force calculations in turbomachinery," tech. rep., Pennsylvania State University, University Park Applied Research Lab, 1991.